A NUMERICAL AND EXPERIMENTAL STUDY OF THE SCALAR TRANSPORT AT A TURBULENT LIQUID FREE SURFACE

by

Boo Cheong Khoo

B.A., University of Cambridge (1980)
M.Eng., National University of Singapore (1984)

Submitted to the Department of Mechanical Engineering
in Partial Fulfillment of the Requirements
for the Degree of

DOCTOR OF PHILOSOPHY

at the
MASSACHUSETTS INSTITUTE OF TECHNOLOGY
November 1988

Signature of Author _____
Department of Mechanical Engineering
November 1988

Certified by _____
Professor Ain A. Sonin
Thesis Supervisor

Accepted by _____
Professor Ain A. Sonin
Chairman, Department Committee on Graduate Studies

A Numerical and Experimental Study of the Scalar Transport at a Turbulent Liquid Free Surface

by

Boo Cheong Khoo

Submitted to the Department of Mechanical Engineering in partial fulfillment of the requirements for the degree of Doctor of Philosopy

Abstract

An experimental study was carried out on the fundamental relationship between the gas absorption rate at a turbulent free surface and the parameters which define the turbulence on the liquid side. Measurements were carried out in a system similar to that used by Sonin, Shimko and Chun (1986) to study vapour condensation on surfaces with zero shear. In this apparatus the turbulence intensity can be varied over a broad range, and the macroscale can be changed by using test cells of different size. The present study focused on transport at high Schmidt numbers (230-1600) and was conducted with CO_2 as the transfer agent and water or water-glycerol mixture as the liquid. The results revealed that the rate equation has two asymptotes, one for low and the other for high eddy Reynolds number. At the lower Reynolds numbers, the transport coefficient increases linearly with V' and is proportional to $Sc^{-1/2}$; at the higher Reynolds numbers, the rate of increase of the coefficient with V' is sufficiently higher, and the Schmidt number dependence subsides. The break point between the two regions is characterised by a critical eddy Reynolde number which is Schmidt number dependent.

None of the features of the experimental correlation are explained by any of the numerous simple models which have been postulated for free surface transport. This led us to attempt a rigorous numerical analysis of both the turbulence distribution and passive scalar transport in the region near the liquid interface. Computational were made for the layer between the free surface and a depth of one macroscale. The effect of the turbulence in the bulk of the liquid was represented by a Dirichlet-type boundary condition applied at the bottom of this layer: at that plane, an unsteady velocity field was imposed which simulated isotropic turbulence with specified V' and macroscale. The Navier-Stokes and scalar conservation equations were solved until both the turbulence and the temperature distributions in the domain attained statistically steady states. Two eddy Reynolds number cases were computed, 1000 and 100, with the Schmidt number in the range 1 - 50 (higher values of Schmidt number would have limited the Reynolds number to uncomfortably low values for simulating turbulence). The solutions showed that some fundamental difficulties arise when one tries to replace an

outer turbulence field with a Dirichlet-type boundary condition at some plane near the transfer surface: a physically unrealistic (but computational correct) boundary layer forms near that plane, and the turbulence distribution in the computational domain shows unrealistic features. Nevertheless, the computed transport coefficient agreed surprisingly well with the experimental data of Brown (1989) for the Schmidt number range 1.5-5.

Thesis Supervisor: Professor Ain A. Sonin
Thesis Committee: Professor Antony T. Patera
Professor Joseph H. Haritonidis

Acknowledgement

My deepest appreciation goes to my thesis advisor, Professor Ain A. Sonin who provided me with invaluable guidance and yet afforded me plenty of academic freedom to explore and satisfy my curiosity. His presence has been the most important aspect of my education here in M.I.T., to face the frontier of science with confidence.

I would also like to express my appreciation to my thesis committee, Professors Antony T. Patera and Joseph H. Hartonidis: to Professor Patera for providing me with the rich intricacies of computational techniques and implementation, and to Professor Hartonidis for offering helphful insights into the experiments.

The present and former members of the Fluid Mechanics Laboratory have given me much help and made my stay here more enjoyable. Special thanks goes to Dick Fenner for his seemingly unlimited ideas for design simplification. Thanks also to Claire Sasahara and Leslie Regan who selflessly helped me with the administrative chores.

I would also like to acknowledge the Singapore Government for funding my study here at M.I.T., and NASA Lewis Research Centre for supporting part of my experimental expenses (under Grant No. NAG3-731) and for providing time on their Cray for the numerical simulation.

Finally, I would like to profess my belief in God who provided me with a supportive family, my wife Peck-Ha and son Ivan who have been a source of joy and comfort in many occasions.

Table of Contents

Page

Title page 1

Abstract 2

Acknowledgements 4

Nomenclature 7

List of Tables 13

List of Figures 14

1. INTRODUCTION 22

2. MODELS OF AND CORRELATIONS FOR SURFACE TRANSPORT 25

Part I

3. EXPERIMENT 31
   - 3.1 Apparatus for Gas Absorption Rate 31
   - 3.2 LDA System for Velocity Measurement 34
   - 3.3 Velocity Measurement with High Speed Video Camera System 36

4. RESULTS AND DISCUSSIONS 40
   - 4.1 Turbulence Characteristics 40
     - 4.1.1 RMS Velocity Correlation 40
     - 4.1.2 An attempt to measure Surface RMS Velocity on the Free Surface 41
     - 4.1.3 The Turbulence Macroscale 42
     - 4.1.4 Eulerian Time Spectrum 43
   - 4.2 Mass Transfer Rate 44
   - 4.3 Comparison with Other Results 51
     - 4.3.1 Turbulence Imposed from Within the Liquid .. 52

4.3.2 Turbulence Imposed via Shear at the Interface 61
5. CONCLUSIONS FOR EXPERIMENTS 68
5.1 LDA Calibration of Turbulence in Test Cell 68
5.2 Gas Absorption Rate Correlation 69

Part II

6. NUMERICAL SIMULATION 71
6.1 Background and Overview 71
6.2 Discretized Equations 72
6.3 Boundary Conditions 75
6.4 Mesh Size Considerations 81
7. RESULTS AND DISCUSSIONS II 84
7.1 Approach to Steady State 84
7.1.1 Time Evolution of Stanton number 84
7.1.2 Energy Transfer Across Each Plane 85
7.2 Velocity Characteristics 87
7.2.1 Ensemble Averaging of the RMS Velocity in the Steady State 87
7.2.2 RMS Velocity Profile 88
7.2.3 Energy Spectra 90
7.3 Temperature Profiles 91
7.4 Turbulent Diffusivity 93
7.5 The Condensation Stanton number and Comparison with Experiment 94
8. CONCLUDING REMARKS ON COMPUTATION 98

References 100

Tables 110

Figures 120

Appendix 212

General Nomenclature, Part I

Note : SI units are used throughout, unless otherwise stated

A	gas-liquid interfacial area
C	species concentration
C_s	saturated condition of the gas in the liquid
C_p	specific heat of liquid in constant pressure
d	nozzle diameter
D	diameter of test cell
D	molecular diffusivity of gas in the liquid
k	average turbulent kinetic energy per unit mass
K_*	mass/heat transfer coefficient corresponding to the 'break' velocity as defined in equation 4.2.5
K_L	mass/heat transfer coefficient (equation 1.1)
$L_{k-\varepsilon}$	length scale in k-ε model analysis
P	pressure
ΔP	pressure difference across the nozzle
Pr, Pr_b	bulk Prandtl number
Q	volumetric flow rate circulating through system
r	radial coordinate measured from the cylinder axis

$R_{uu}(t)$ Eulerian autocorrelation, defined as
$< u(t'+t)u(t') > / < u^2 >$

$R_{ww}(t)$ Eulerian autocorrelation, defined as
$< w(t'+t)w(t') > / < w^2 >$

Re_s system Reynolds number, $(Q/Dd)(D/\nu)$, where $D \equiv$ test cell diameter

Re_Λ eddy Reynolds number, $V'\Lambda/\nu$

$(Re_\Lambda)_*$ break Reynolds number, $V_*\Lambda/\nu$

Sc Schmidt number, ν/D

St Stanton number, K_L/V'

t time

U_{*w} friction velocity based on shear stress at interface and water density

u(t) local horizontal component of the fluctuating velocity (measured as azimuthal)

v'(t) local vertical or horizontal component of fluctuating velocity

w(t) local vertical component of the fluctuating velocity

V' rms value of the local horizontal or vertical component of turbulent velocity in the system; in rate correlations, V' is used to indicate the rms value of either component at the "interface" obtained by extrapolating from the bulk, disregarding surface damping.

V_* rms velocity in the 'break' region, as defined in equation 4.2.5

V volume of water in the system

z coordinate measure vertically upwards from the nozzle exit in the test section

z_s height of interface above nozzle

Greek symbols

α thermal/molecular diffusivity of liquid

ε viscous dissipation rate per unit mass

Λ integral length scale of turbulent eddies as defined in equation 4.1.6

μ liquid dynamic viscosity

ν liquid kinematic viscosity

ρ liquid density

σ surface tension

τ turbulence macroscale time

$\Phi(Re_s)$ function used in figures 3.3.1 and 3.3.2

$\Psi_{uu}(f)$ Eulerian time spectrum in the horizontal direction

$\Psi_{ww}(f)$ Eulerian time spectrum in the vertical direction

Subscript

b	bulk liquid condition
s	evaluated at interfacial condition
*	conditions at the 'break' region (see section 4.2)

Additional nomenclature for Part II

l_s	smallest length scale in the velocity field
L_x, L_y	size of computational domain in the horizontal directions
Pe	Peclet number
Q(z)	total heat flux across plane at elevation z; used as dimensionless quantity, non-dimensionalised w.r.t. $U(T_s-T_b)$ in figures 7.1.6 - 7.1.9, 7.1.14 - 7.1.16
Re_b	eddy Reynolds number, $U\Lambda/\nu$, which is based on the rms velocity at the lower surface
S_{uu}	dimensionless longitudinal power spectrum on a horizontal plane in the x-direction, non-dimensionalised w.r.t. U^2
S_{vv}	dimensionless longitudinal power spectrum on a horizontal plane in the y-direction, non-dimensionalised w.r.t. U^2
S_{ww}	dimensionless transverse power spectrum on a horizontal plane in the z-direction, non-dimensionalised w.r.t. U^2
T	dimensionless temperature, $(T"-T_b)/(T_s-T_b)$
T"	dimensional temperature

T_s, T_1 saturation temperature at the interface

T_b, T_2 bulk temperature within the liquid

$\underset{\sim}{u}$ dimensionless vector velocity (u,v,w) non-dimensionalised w.r.t. to U

u,v velocity component in the horizontal directions, non-dimensionalised w.r.t. to U

u_{rms} dimensionless rms velocity in the x-directions, non-dimensionalised w.r.t. to U

v_{rms} dimensionless rms velocity in the y-directions, non-dimensionalised w.r.t. to U

w_{rms} dimensionless rms velocity in the z-directions, non-dimensionalised w.r.t. to U

U rms velocity at the lower surface of computational domain, serve as reference velocity used for non-dimensionalisation

w dimensionless velocity in the vertical direction, non-dimensionalised w.r.t. to U

x,y horizontal coordinates

z vertical coordinate

Greek symbols

α' defined as $2\pi/L_x$

α_{art} artificial diffusivity replacing the molecular diffusivity in the energy equation for region near the lower boundary (see section 6.3)

α_T turbulent diffusivity; used as dimensionless quantity, non-dimensionalised w.r.t. $U\Lambda$ in figures 7.4.1 - 7.4.4, 7.4.6 - 7.4.8

β defined as $2\pi/L_y$

Π dimensionless dynamic pressure, $P/\rho U^2 + 0.5|\underset{\sim}{u}.\underset{\sim}{u}|$

Δ grid spacing in the computational domain

Δt dimensionless time increment, non-dimensionalised w.r.t. Λ/U

τ' time constant as defined in equation 7.4.2; used as dimensionless quantity, non-dimensionalised w.r.t. Λ/U in figure 7.4.5

List of Tables

Table	Title
1	Major conceptual models for transport across a free surface
2	LDA measurement of turbulence macroscale time (τ) and length (Λ=V'τ) in the system with diameter of 0.152m at 0.03m beneath the interface
3	Operating conditions of the mass transfer experiments
4	Conditions at the "break" point as defined in equation 4.2.1
5	Mass transfer result for $Re_\Lambda < (Re_\Lambda)_*$
6	Summary of comparison with experiments where turbulence is imposed form within the liquid
7	Summary of comparison with experiments where turbulence is induced by shear at the interface
8	Parameters associated with the numerical simulations for case A and case B
9	Computed St vs Pr for case A and comparison with experiment
10	Computed St vs Pr for case B and comparison with experiment

List of Figures

Figure	Title
3.1.1	Schematic diagram of the test system
3.1.2	System flow rate calibration curve, Q/Dd vs $\Delta P^{1/2}$
3.2.1	Schematic diagram of the test section used in velocity measurement by the LDA
3.3.1	The function $\Phi(Re_s)$ in the correlation for V' by Shimko (1985) used by Sonin et al (1986)
3.3.2	The function $\Phi(Re_s)$ in the correlation for V' by Brown (1989)
4.1.1	Horizontal rms velocity profile for Re_s=29140
4.1.2	Horizontal rms velocity profile for Re_s=40120
4.1.3	Horizontal rms velocity profile for Re_s=57690
4.1.4	Vertical rms velocity profile for Re_s=29140
4.1.5	Vertical rms velocity profile for Re_s=40120
4.1.6	Vertical rms velocity profile for Re_s=57690
4.1.7	Azimuthal rms and mean velocity at 5mm beneath the interface as a function of radius for Re_s=40120
4.1.8	Surface rms velocity vs Q/Dd at height z/D=3.67

4.1.9 Surface rms velocity vs Q/Dd at height z/D=4.17

4.1.10 Surface rms velocity vs Q/Dd at height z/D=4.50

4.1.11 Eulerian autocorrelation for the horizontal velocity at the centreline 30mm beneath the interface for Re_s=25000

4.1.12 Eulerian autocorrelation for the horizontal velocity at the centreline 30mm beneath the interface for Re_s=35200

4.1.13 Eulerian autocorrelation for the horizontal velocity at the centreline 30mm beneath the interface for Re_s=50300

4.1.14 Eulerian autocorrelation for the horizontal velocity at the centreline 30mm beneath the interface for Re_s=70500

4.1.15 Eulerian autocorrelation for the vertical velocity at the centreline 30mm beneath the interface for Re_s=25000

4.1.16 Eulerian autocorrelation for the vertical velocity at the centreline 30mm beneath the interface for Re_s=35200

4.1.17 Eulerian autocorrelation for the vertical velocity at the centreline 30mm beneath the interface for Re_s=50300

4.1.18 Eulerian autocorrelation for the vertical velocity at the centreline 30mm beneath the interface for Re_s=70500

4.1.19 Eulerian time spectrum $\Psi_{uu}(f)$ for the horizontal

velocity at the centreline 30mm beneath the interface for Re_s=25000

4.1.20 Eulerian time spectrum $\Psi_{ww}(f)$ for the vertical velocity at the centreline 30mm beneath the interface for Re_s=25000

4.1.21 Eulerian time spectrum $\Psi_{uu}(f)$ for the horizontal velocity at the centreline 30mm beneath the interface for Re_s=50300

4.1.22 Eulerian time spectrum $\Psi_{ww}(f)$ for the vertical velocity at the centreline 30mm beneath the interface for Re_s=50300

4.2.1 Mass transfer coefficient K_L vs V' for Sc=230

4.2.2 Mass transfer coefficient K_L vs V' for Sc=377

4.2.3 Mass transfer coefficient K_L vs V' for Sc=525

4.2.4 Mass transfer coefficient K_L vs V' for Sc=1600

4.2.5 Mass transfer coefficient K_L vs V' for Sc=525 with smaller test-section

4.2.6 Mass transfer coefficient K_L vs V' for Sc=525 with both test-sections

4.2.7 Dimensionless plot of $StSc^{0.5}$ vs Re_Λ

4.2.8 Dimensionless plot of $(K_L-K_*)/(V'-V_*)$ vs Re_Λ for $Re_\Lambda < (Re_\Lambda)_*$

4.2.9 Plot of St vs $Re_\Lambda/(Re_\Lambda)_*$ for equations 4.2.10(a) and 4.2.10(b)

4.2.10 Plot of K_L vs V' for Sc=525 with prediction given by equations 4.2.8 and 4.2.9

4.2.11 Plot of K_L vs V' for Sc=1600 with prediction given by equations 4.2.8 and 4.2.9

4.3.1 Dimensionless plot of $StSc^{0.5}$ ve Re_I for system of submerged oscillating grid as means of generating turbulence (Isenogle (1985))

4.3.2 Dimensionless plot of $StSc^{0.5}$ ve Re_H for system of submerged oscillating grid as means of generating turbulence (Ho (1987))

6.3.1 Plot of f(r) vs r for isotropic turbulence cube

6.3.2 Profile of α_{art}/α for case A

6.3.3 Profile of α_{art}/α for case B

6.4.1 Diagram showing the grid arrangement for case A

6.4.2 Diagram showing the grid arrangement for case B

7.1.1 Time evolution of computed St for case A (Pr=1.0)

7.1.2 Time evolution of computed St for case A (Pr=1.5)

7.1.3 Time evolution of computed St for case A (Pr=2.2)

7.1.4 Time evolution of computed St for case A (Pr=3.15)

7.1.5 Time evolution of computed St for case B (Pr=3.15)

7.1.6 Total heat flux profile in the steady state for

case A (Pr=1.0)

7.1.7 Total heat flux profile in the steady state for case A (Pr=1.5)

7.1.8 Total heat flux profile in the steady state for case A (Pr=2.2)

7.1.9 Total heat flux profile in the steady state for case A (Pr=3.15)

7.1.10 Turbulent heat flux profile in the steady state for case A (Pr=1.0)

7.1.11 Turbulent heat flux profile in the steady state for case A (Pr=1.5)

7.1.12 Turbulent heat flux profile in the steady state for case A (Pr=2.2)

7.1.13 Turbulent heat flux profile in the steady state for case A (Pr=3.15)

7.1.14 Total heat flux profile in the steady state for case B (Pr=3.15)

7.1.15 Total heat flux profile in the steady state for case B (Pr=10.0)

7.1.16 Total heat flux profile in the steady state for case B (Pr=50.0)

7.1.17 Turbulent heat flux profile in the steady state for case B (Pr=3.15)

7.1.18 Turbulent heat flux profile in the steady state for case B (Pr=10.0)

7.1.19 Turbulent heat flux profile in the steady state for case B (Pr=50.0)

7.2.1 Computed rms velocity profile in the x-direction for case A

7.2.2 Computed rms velocity profile in the y-direction for case A

7.2.3 Computed rms velocity profile in the z-direction for case A

7.2.4 Computed rms velocity profile in the x-direction for case B

7.2.5 Computed rms velocity profile in the y-direction for case B

7.2.6 Computed rms velocity profile in the z-direction for case B

7.2.7 Longitudinal power spectrum S_{uu} for case A

7.2.8 Longitudinal power spectrum S_{vv} for case A

7.2.9 Transverse power spectrum S_{ww} for case A

7.2.10 Longitudinal power spectrum S_{uu} for case B

7.2.11 Longitudinal power spectrum S_{vv} for case B

7.2.12 Transverse power spectrum S_{ww} for case B

7.3.1 Mean temperature profile in the steady state for case A (Pr=1.0)

7.3.2 Mean temperature profile in the steady state for

case A (Pr=1.5)

7.3.3 Mean temperature profile in the steady state for case A (Pr=2.2)

7.3.4 Mean temperature profile in the steady state for case A (Pr=3.15)

7.3.5 Mean temperature profile in the steady state for case B (Pr=3.15)

7.3.6 Mean temperature profile in the steady state for case B (Pr=10.0)

7.3.7 Mean temperature profile in the steady state for case B (Pr=50.0)

7.4.1 Turbulent diffusivity profile in the steady state for case A (Pr=1.0)

7.4.2 Turbulent diffusivity profile in the steady state for case A (Pr=1.5)

7.4.3 Turbulent diffusivity profile in the steady state for case A (Pr=2.2)

7.4.4 Turbulent diffusivity profile in the steady state for case A (Pr=3.15)

7.4.5 Plot of time constant τ' vs Pr for both case A and case B

7.4.6 Turbulent diffusivity profile in the steady state for case B (Pr=3.15)

7.4.7 Turbulent diffusivity profile in the steady state for case B (Pr=10.0)

7.4.8 Turbulent diffusivity profile in the steady state for case B (Pr=50.0)

7.5.1 Plot of St vs Pr for both case A and case B

1. INTRODUCTION

Transport of heat or mass across across the free surface of a turbulent liquid plays a central role in many fields of engineering. Chemical engineers are interested in maximising the rates of gas absorption to or desorption from liquid solvents (Higbie, 1935; Ratbun et al, 1984). The sanitation engineer is interested in increasing the oxidation of the sludge in the sewage treatment plant (Downing, 1960; Tchobanoglous, 1979). The environmentalist is concerned with the reaeration of streams and rivers (Streeter et al, 1925; Ratbun, 1977), with how the gaseous pollutants spread through absorption and desorption by turbulent bodies of water (Brtko et al, 1976 & 1978; Munz et al, 1982), and with the formation of acid rain when water droplets pass through clouds of pollutants like sulphur dioxide (Matteson et al, 1984). Mechanical and nuclear engineers are concerned with steam condensation rates on cold, turbulent water, a process which is particular important in certain nuclear power plant accident scenarios. Direct condensation of vapour on cold liquid is basically a heat transfer process, since it is limited by the rate at which the latent heat can be removed from the surface. More recently, NASA has focused on direct condensation as a central problem in pressure control during the handling and transfer of cryogenic liquids (such as hydrogen and oxygen) under zero-gravity conditions (Merino et al, 1980; Aydelott et al, 1985).

The transport rate is usually limited by the turbulent transport on the liquid side, and is defined in terms of a transport coefficient, K_L:

$$K_L \equiv j/\Delta C \quad \text{(mass transfer)} \qquad 1.1$$
$$\equiv q/\rho c_p \Delta T \quad \text{(heat transfer or condensation)}$$

where j is the molar flux , ΔC is the molar concentration difference between the surface and the bulk of the liquid, or equivalently, q is the thermal flux, ΔT is the temperature difference between the surface and the bulk of the liquid, and ρ and c_p are the density and specific heat capacity of the liquid, respectively. Assuming negligible resistance in the gaseous phase, K_L is a function of liquid properties and the parameters which control the turbulence on the liquid side.

Despite the significant body of work that has been published in this area since the early contributions of Lewis (1924) and Higbie (1935) to gas absorption, no consensus exists as yet on a single universal model, or even a single empirical correlation, for the transport rate (eg. see the review in Sonin et al, 1986). Our work in this laboratory has been aimed at developing a better fundamental understanding of the transport process at a free, turbulent interface, in the hope that this will lead to a more universal model for the transport rate. We have developed an experimental apparatus in which an easily controlled, steady turbulence can be imposed from below on a shear-free liquid surface, and transport rates measured and correlated in terms of turbulence intensity, turbulence length scale, and liquid-side Prandtl or Schmidt number. Our hope was that a careful investigation of the dependence of the transport coefficient on these parameters would guide us toward a more general and accurate model for the transport process.

Our earlier work with this system dealt with vapour condensation on a liquid (Sonin et al, 1986; Helmick et al, 1988; see also Brown, 1989) and showed that the transport coefficient was directly proportional to the rms value of the fluctuating velocity on the liquid side (at least at low Richardson number) and to the negative one-third power of the bulk liquid Prandtl number, approximately. These results are not explained by any of the available models which might have been thought to be applicable. (Each of these models is

based on some particular simplfying assumptions about the turbulent transport process - see Sonin et al, 1986.)

The objective of the present work was to try to advance the state of the art in three ways. First, since most of the available simple models for the transport rate were based on simplifications appropriate for high Schmidt number, we embarked on an experimental study of high Schmidt number gas absorption in our experimental system at turbulence conditions similar to those of the condensation studies. The results of this investigation are described in section 4.2. Second, we undertook a more detailed study of the turbulence structure in our experimental system, using a laser doppler velocimeter. The transport rate is controlled in large measure by the structure of the turbulence in the region very close to the surface, where measurements are very difficult. Our new measurements offer some insight into the larger-scale structure of the turbulence in our type of system, however, and give a more rational basis for the correlation of the data (see section 4.1). Third, we attempted a numerical simulation of the turbulence field and passive scalar distribution near a shear-free surface, with turbulence imposed from below. The full, unsteady Navier-Stokes equations and the energy equation are solved using a spectral Fourier expansion in the two horizontal directions, and a Legendre spectral element technique in the vertical direction. The computational domain, "extracted" from the full flow, is restricted to a single-macroscale neighbourhood of the interface, with the top boundary representing the free surface conditions, and the bottom boundary simulating the "far-field" isotropic turbulence. Two statistically steady calculations at eddy Reynolds number of 100 and 1000 and Prandtl numbers ranging from 1 to 50 are presented. The computed transport rates are then compared to the experimental steam condensation results of Brown (1989).

2. MODELS OF AND CORRELATIONS FOR SURFACE TRANSPORT

A turbulent liquid surface can be viewed as being continually replaced with fresh elements of fluid from the bulk. Higbie (1935) postulated that during the periods of direct exposure to the surface, transport occur by transient molecular diffusion into the fluid elements. If a typical eddy has a residence time τ at the surface, the liquid-side transfer coefficient can be expressed as

$$K_L \sim (D/\tau)^{0.5} \qquad 2.1$$

where D is the molecular diffusivity. The problem is thus reduced to that of expressing τ in terms of the properties of the turbulence on the liquid side.

The above expression can also be derived differently. The Reynolds-averaged turbulent diffusion equation can be written as

$$\partial\overline{C}/\partial t = \partial/\partial z\ ((D + D_T)\partial\overline{C}/\partial z) \qquad 2.2$$

where z is the distance measured from the interface into the liquid, $D_T(z)$ is the turbulent diffusivity and $\overline{C}$ is the Reynolds averaged species concentration. The turbulent diffusivity is defined by the equation

$$< w'C' > = - D_T\partial\overline{C}/\partial y \qquad 2.3$$

where w' is the fluctuating part of the normal velocity component, C' is the fluctuating part of the concentration and the symbol < > represents ensemble average. For the region very near the free surface, where the transport resistance is greatest, Levich (1962) has argued that

$$D_T = z^2/\tau' \qquad 2.4$$

where τ' is a quantity with dimension of time. The statistically steady solution of equation 2.2 is (King, 1966)

$$K_L = (2/\pi)(D/\tau')^{0.5} \qquad 2.5$$

Equation 2.1 (with an exact equality sign) is identical to equation 2.5 if we make the identification $\tau=\pi\tau'/2$.

Numerous models have been proposed for relating τ to the properties of the turbulence on the liquid side. Table 1 (see also Sonin et al, 1986) is a summary of five major models. We shall give a brief outline of each below.

Fortescue and Pearson (1967) proposed the large-eddy model which assumes that the large (macroscale) eddies are responsible for bringing fresh fluid to the surface and removing the 'enriched' liquid into the bulk. The characteristic time scale of these large eddies is given by

$$\tau \sim L/V' \qquad 2.6$$

where L is an integral length scale and V' is the turbulence intensity near the interface. Based on equation 2.1 or 2.5, K_L can be expressed as

$$K_L \sim (DV'/L)^{0.5} \qquad 2.7$$

Fortescue and Pearson obtained some experimental support for their model in an experiment where turbulence was produced by a grid in an open channel flow, and the mass transfer across the free surface was measured. It should be pointed out, however, that they made numerous corrections to their 'raw' mass transfer data (of the order of 10% - 20%) to account for the entrance effect immediately downstream of the grid and the end region of the channel, where a weir was positioned to maintain a constant water height.

Lamont and Scott (1971) suggested that the transfer is controlled not by the large eddies, but by eddies of Kolmogorov microscale size, which 'piggy-back' on the large eddies that sweep by the surface. The appropriate time scale τ is then the Kolmogorov time scale, that is

$$\tau \sim (\nu L/V'^3)^{0.5} \qquad 2.8$$

and K_L is obtained as

$$K_L \sim (\nu D^2/L)^{0.25} V'^{0.75}. \qquad 2.9$$

Lamont and Scott measured the absorption rates from small gas bubbles transported in turbulent pipe flow. Their data could be correlated with the energy dissipation rate ϵ, and thus suggested the importance of small eddies in the transport process. They also made some quantitative comparison of their model with the data of Fortescue and Pearson and agreement was off by a factor of at least two. Subsequently, Prasher et al (1973), in a separate experiment where an impeller was used to generate turbulence in an enclosed vessel, provided data which supported the small-eddy model.

Meanwhile, Theofanous et al (1976) made use of several sets of available experimental data to try and combine the large and small eddy models into a more generalised model. They suggested that there was a critical turbulence Reynolds number (based on the turbulence intensity and the macroscale) of 500, below which the large-eddy model is more suitable, and above which the small-eddy model appeared to be preferable. However, considering the large scatter in the data with respect to their suggested correlation and the numerous assumptions made to relate the experimental flow parameters to V' and L, their conclusions should be taken cautiously.

Earlier, Levich (1962) had taken a different tack, and argued that the length scale of the eddies near the surface is controlled by surface tension and curvature. Equating the surface tension force with the inertia force, he suggested that the length scale of the eddies which control the interfacial transport rate is

$$L \sim \sigma/\rho V'^2 \qquad 2.10$$

where σ is the surface tension of the liquid, from which it follows that the time scale L/V' of these eddies is

$$\tau \sim \sigma/(\rho V'^3). \qquad 2.11$$

Levich 's argument yields K_L as

$$K_L \sim (\rho D V'^3/\sigma)^{0.5}. \qquad 2.12$$

J. T. Davies and collaborators (1972) have obtained mass transfer data for flows down an inclined plane, with and without roughened surfaces. They also studied gas absorption between a free turbulent jet of liquid and a gas. Davies claims approximate agreement with the model put forth by Levich.

A still different correlation has emerged from studies of transport at surfaces where turbulence is imposed by interfacial shear. Based on their own experimental data, Ueda et al (1977) suggested that the length scale of eddies near such interfaces is dominated by the viscous inner layer scaling law, just as it is near a solid wall. This suggests a time scale τ of the form

$$\tau \sim \nu/V'^2 \qquad 2.13$$

Upon substitution into 2.1, K_L becomes

$$K_L \sim (D/\nu)^{0.5} V', \qquad 2.14$$

Finally, an entirely different model was proposed very early by Kishinevsky (1955) who argued that transport is completely dominated by turbulent diffusivity, D_T, even right at the surface. In this model, D_T replaces D in equation 2.1, and with the time scale $\tau \sim L/V'$, yields K_L as

$$K_L \sim V' \qquad 2.15$$

which is entirely independent of the molecular diffusivity. Kishinevsky and Serebryansky (1956) supported this model with data from an experiment where turbulence was produced by a mechanical stirrer operating at very high speed (1700 r.p.m.) below the liquid interface. They acknowledged, however, that at lower turbulence intensities, the effect of molecular diffusivity would play an ever increasing role. Unfortunately, the threshold of turbulence intensity above which equation 2.15 is applicable was not established.

The five models given above are by no means the only ones that have been proposed. They are provided here to illustrate the diverse concepts which previous investigators have proposed for the transport mechanism. Each model has claimed some support from experiments. We note, however, that other experiments have yielded data that do not conform to any of these models. Prominent examples are (a) the class of flows where the turbulence in the liquid is generated by means of a submerged oscillating grid (see Isenogle, 1985, and Ho, 1987) and (b) thin-film flows (see Won et al, 1982, and Bin, 1983). Data taken in systems where the turbulence is created by mechanical stirrers operating at a much lower speed than in Kishinevsky and Serebryansky 's tests, also do not agree well with any of these proposed models (see the experiments of Davies et al, 1979, and Luk, 1986). For flows in which turbulence is generated by a strong wind blowing above the interface, the data show two different transport regimes, as found for example in Merlivat et al (1983) and Broecker et al (1984). None of the model discussed above is

capable of predicting these regimes. Further development of analytical models has been held back in large measure because of the lack of understanding of, or data on, the turbulence structure near a free surface.

From table 1, we can see that the various models suggest Reynolds number exponent from -0.5 to 0.5, while the Schmidt number appears always to be -0.5 power except for the fully turbulent model of Kishinevsky. It should be mentioned that most of these models were proposed for fairly large Schmidt or Prandtl numbers and most of the experiments were carried out with gas as the transfer agent to achieve the high Schmidt number.

Our hope in this work was to shed some light on which, if any, of these models are correct, and to better define K_L in terms of easily measured parameters, general enough for wide application, irrespective of how the turbulence is generated.

Part I

3. EXPERIMENT

3.1 Apparatus for Gas Absorption Rate Measured

Sonin et al (1986) have shown that an axisymmetric confined jet in a cylinder partially filled with water gives a bulk-flow-free and reasonably uniform turbulence at the free surface, provided the surface is at distances greater than 3D from the jet nozzle, D being the diameter of the cylinder. The turbulence decays with elevation from the nozzle and is relatively isotropic in a horizontal plane. The system has the added characteristic of possessing a constant integral length scale that appears to be 'locked' to D.

Our apparatus was similar to the system of Sonin et al. It consisted of a vertical, axisymmetric nozzle in a pyrex tube partially filled with water, as shown in figure 3.1.1. A centrifugal pump circulated the water through a closed-loop system. The total volume of water in the system was kept to a minimum to minimise the time required for each mass transfer experiment. (As in any mass transfer experiment, the amount of dissolved CO_2 in the system reached a readily measurable value only after a fairly long time.) A heat exchanger was used to maintain the bulk water temperature constant.

The turbulence intensity in the water was controlled by varying the momentum flux through the nozzle and the water level in the test section (see Sonin et al, 1986). Two different test section diameters were used, 0.152m and 0.038m. The respective nozzles had diameters of 0.0064m and 0.0016m. For the larger system, the flow rate Q was calibrated against the pressure drop ΔP across the nozzle. ΔP was measured with a Kistler model RP15 pressure

transducer linked to a Dynascience model CD10 Carrier Demodulator whose output voltage can be read from a Dana model 3800B multimeter. The calibration is shown in figure 3.1.2 , and is given as

$$(Q/Dd)/\Delta P^{0.5} = 0.171 \pm 5\% \qquad 3.1.1$$

where Q is the volumetric flow rate through nozzle, ΔP is the pressure drop in voltage as registered by the pressure transducer , D is the diameter of the test section and d is the diameter of the nozzle. In the smaller system, the flow rates were determined using a calibrated Fisher Rotameter inserted in the flow loop.

CO_2 , which was used in all the mass transfer measurements, was introduced just above the interface and exhausted at a higher station. Our aim was to prevent the build up of any noncondensable gases, notably air, next to the interface. Air, being lighter than CO_2, would tend in any case to be exhausted out of the test section. The gas space was continually flushed with CO_2 and maintained at 1 psi above atmospheric pressure. In order to ensure that the CO_2 coming into the test section did not induce 'extra' turbulence at the interface, a large inlet tube was used to reduce inflow velocity. The interface remained perfectly still before and after the valve controlling the supply of CO_2 was turned off. Also, the incoming CO_2 was preheated by passing the gas through a copper tubing, immersed in a water-glycerol mixture bath so that it was at the same temperature as the bulk water in the test section. In this way, we were able to maintain a gas temperature within $\pm 0.5^{o}C$ of the water temperature, thereby ensuring a known gas temperature at the interface, which was important since the saturated concentration of CO_2 in water is highly dependent on temperature (which has a variation of about 3% for every degree Celsius change in temperature).

For each test, the system was first allowed to run for at least 20 minutes with CO_2 inflow to reach the desired steady operating condition. Five different samples (50 ml each) of the bulk water were then taken to determine the initial average concentration of dissolved CO_2. The water level in the test cell was then reduced precisely to the desired z_s/D level, z_s being the height of interface above the inlet nozzle. The system was restarted and run for a time ranging from 5 to 12 hours, depending on the turbulence intensity imposed. At the end of the run, 7 samples were taken for determinating the average final concentration. The amount of dissolved CO_2 in the samples was determined using an Orion Research carbon dioxide electrode (model 95-02) which has an accuracy of $\pm 5\%$. The electrode was calibrated against two known samples of dissolved CO_2 (supplied by Orion Research); the output (in millivolts) was measured with a very high input-impedance Keithley 602 electrometer. In the electrode, dissolved CO_2 diffuses through a gas-permeable membrane and affects the level of hydrogen ions in the internal filling solution of the electrode according to the reaction

$$CO_2 + H_2O \rightleftharpoons H^+ + HCO_3^- \qquad 3.1.2$$

The pH in the internal filling solution is then related to the hydrogen ion concentration by the Nernst equation

$$E = E_o + S \ln[H^+] \qquad 3.1.3$$

where E is the measured electrode potential, E_o is the reference potential (a constant), $[H^+]$ is the hydrogen ion concentration and S is the electrode slope obtained by calibration mentioned above. By virtue of 3.1.2, the electrode response to the CO_2 is also Nernstian,

$$E = E_o + S \ln[CO_2] \qquad 3.1.4$$

where $[CO_2]$ is the CO_2 concentration. Calibration of the electrode were carried out twice; first for the measurement of the initial samples and second for the measurement of the final samples.

The governing equation for the transfer of CO_2 into the liquid volume of the test system is

$$VdC/dt = K_L A(C_s - C) \qquad 3.1.5$$

where V is the volume of water in the system, A is the area of the interface, C is the bulk concentration of CO_2 in water, C_s is the saturated concentration of CO_2 at the interface, K_L is the mass transfer coefficient (m/s), and t is the time in seconds. Upon integrating 3.1.5, we have, if K_L is constant,

$$K_L = V/(At)\ \ln((C_s - C_i)/(C_s - C_f)) \qquad 3.1.6$$

where C_i is the initial concentration of CO_2, C_f is the final concentration of CO_2 and t is the time duration of the run. With C_i and C_f measured, equation 3.1.6 gives the mass transfer coefficient K_L. After each run, the system was flushed thoroughly with tap water before a new run is initiated.

3.2 LDA System for Velocity Measurement

The turbulence in the system was investigated using a back-scattered two-color LDA. Both the vertical and horizontal components of velocity were measured. The LDA consisted of a Lexel model 95 ion laser as the source and DISA-made optics, namely, 55X20/21 cover and retarder, 55X22 beam waist adjuster, 55X25 beam splitter, 55X28 beam displacer, 55X29 Bragg cell, 55X32 beam translator, two 55X12 expanders, and a 55X57 310mm focal length achromatic

front lens. The receiving optics consisted of a 55X31 pinhole section, 55X34 PM optics, 55X30 backscatter section, 55X35 color separator, 55X36 and 55X37 interference filters. Signals from the PM and the Bragg cell were fed to the 55N10 frequency shifter and 55L90a counter processor. Finally the counter was linked to a portable DEC MINC-11 mini-computer via a DEC DRV11-J parallel-line interface. Data was collected by a series of assembly-code routines addressed to the mini-computer, which in turn drove the interface-card. The internal oscillator of the computer was used to time the arrival of each validated doppler signal for autocorrelation purpose.

A window of flat plexiglass was attached into a specially machined slot in the cylindrical test section, as shown in figure 3.2.1. The slot measured 53mm in width and was located at 72mm from the axis of the test section, which had a radius of 76.2mm. Provided velocity measurements were not made too far away from the centreline, the perturbation of the cylindrical geometry was minimial. The usage of two beam expanders in series resulted in a very small 40μm x 40μm x 600μm measuring volume. The test section was mounted on a traversing table which provided movement in three orthogonal linear directions and rotation on a horizontal plane. Instead of adjusting the laser beams for intersection at the various position in the flow field, we would shift the test section. This left the optical system stationary, and avoided frequent optical realignment of the laser beams.

The centrifugal pump for the test cell was housed in a specially made sound-proof box and rested on vibration absorbers to minimise any transmission of vibration to the LDA. It was connected to the test section by an eight feet long stainless steel flexible hose. Prelimary tests of the LDA system were carried out with a plexiglass disk filled with water rotating at a known angular velocity, mounted on the test cell stand. Laser reading of velocity were recorded without the pump running, and were found to check against

the actual velocity to within $\pm$ 3%. The rms value of the velocity fluctuations was also noted and found to be about 5% of the mean. Subsequently, tests were carried out with the centrifugal pump running. We found that the rms velocity fluctuations did not differ significantly with or without the pump running; this implied that the precautions taken to minimise pump vibrations were successful.

Seedlings for the back-scattered LDA were provided in the form of aluminium particles of size 3 μm. This gave us a signal-to-noise ratio of about 5. We also tried TiO_2 particles of size 1 μm but found that the SNR was not as good. More information about the LDA system and its set-up is given in Appendix 1.

3.3 Velocity Measurement with High Speed Video Camera System

Sonin et al (1986) were the first to use a confined jet apparatus to study transport across a free, turbulent liquid surface. They characterised the rms velocity V' at the interface by extrapolating the value of V' from the bulk region to the surface. The velocity measurements were made using 3mm polypropelene spheres (which have a small negative buoyancy) as 'seedlings' for the high speed video camera system. The video tapes were then replayed frame by frame on a grid-covered monitor to determine the displacement, and vertical and horizontal components of particle velocity were computed. Sonin et al also used the k-ε model of turbulence to give an approximate analytical description of the turbulence in the region z/D > 3 (z is the distance above the inlet nozzle) where the mean circulatory flow is small compared to the fluctuating velocity. Assuming the average turbulence kinetic energy k is a function of z only, they reduced the high-Reynolds number form of the k-ε model to

$$0 = d/dz(C_\mu/\sigma_k \; k^{0.5} L_{k-\varepsilon} dk/dz) - k^{1.5}/L_{k-\varepsilon} \qquad 3.3.1$$

where $L_{k-\varepsilon}$ is the k-ε model length scale, and the coefficients are $C_\mu = 0.09$ and $\sigma_k = 1.0$. The solution of equation 3.3.1, subject to the boundary condition of $k \rightarrow 0$ as $z \rightarrow \infty$ and to the assumption that the length scale $L_{k-\varepsilon}$ is 'locked' to the tube diameter, D,

$$L_{k-\varepsilon} = \beta D \qquad 3.3.2$$

where β is a constant, is

$$k^{0.5} = k_o^{0.5} \exp\{-\beta^{-1}(\sigma_k/6C_\mu)^{0.5} (z/D - z_o/D)\} \qquad 3.3.3$$

where k_o is the magnitude at $z=z_o$. Using arguments based on dimensional analysis, Sonin et al further obtained for their system,

$$V' = Q/Dd \; F(Re_s, z/D) \qquad 3.3.4$$

where Re_s is the system Reynolds number, defined as $Q/d\nu$, and V' is the rms velocity in either the horizontal or vertical direction since it was found that flow is essentially isotropic in a horizontal plane, provided z is not too close to the interface. Equation 3.3.3 suggests that the dependence on z/D should be an exponential decay. Sonin et al were able to fit their experimental data to the function

$$V' = Q/Dd \; \Phi(Re_s) \; e^{-1.2z/D} \qquad 3.3.5$$

$$\text{for} \quad 3.1 < z/D < 4.2$$

where $\Phi(Re_s) = 21.8$ for $Re_s > 25000$

$= $ as in figure 3.3.1 for $Re_s < 25000$

and

$$L_{k-\varepsilon} = 1.1D \qquad 3.3.6$$

The data used in the correlation function $\Phi(Re_s)$ for $Re_s <$ 25000 were obtained using the smaller test-section of diameter 0.0381m. Subsequently, Brown (1989) made more measurements of V' for Re_s < 15000 with the same test section of diameter 0.038m and essentially the same experimental procedure as Sonin et al. However, he used much smaller (0.1-1.0mm diameter) polystyrene beads as seedlings, compared to the 3mm polypropelene spheres used formerly, and a nozzle with a smoother inlet region. Brown 's data is summarised in figure 3.3.2, and shows a substantially smaller value of $\Phi(Re_s)$ than Sonin et al found in the lower Reynolds number range. Brown 's data should be more reliable because of the smaller size seedlings, which would follow the fluid motions more faithfully, and the larger sample size of 200 readings each versus the sample size of 60 readings in Sonin et al. Nevertheless, there is still a considerable scatter in Brown 's data. If we assume a constant $\Phi(Re_s)$ through the whole range, 4000 < Re_s < 70000, a value of 23.5 is obtained by least square fit. This would make the LDA results (refer to figure 3.3.2 and see section 4.1.1 for more details) somewhat lower than the average. The LDA results, which we tend to trust more than the video data, show better agreement with the correlation of $\Phi(Re_s)$=21.8, which is the least square value for data in the range 30000 < Re_s < 70000. A closer examination of Brown 's data shows that one cannot rule out the possibility that $\Phi(Re_s)$ increases slightly as Re_s decreases. Until more data are available, especially in the range 15000 < Re_s < 30000, we shall adopt as our correlation

$$\Phi(Re_s) = 24.5 \quad (Re_s < 15000) \qquad 3.3.7$$
$$= 21.8 \quad (30000 < Re_s < 70000)$$

The value 24.5 is the least square fit in the lower Reynolds number range.

It should be noted that the LDA (in our particular set-up) was only capable of providing measurement up to 2mm and 5mm beneath the interface for the horizontal and vertical components of velocity respectively. To measure the surface velocity directly, we mounted the video camera vertically facing the interface from above. Air bubbles were introduced into the system. They floated on the interface and appeared as very bright spots due to the reflection of the synchronised lightings provided. (The lightings were synchronised with the frame speed of the camera.) This conveniently addressed the problem of depth of field resolution. Only the bubbles at the interface appear as bright spots in contrast to those beneath the interface. A transparent 'Scriptel' digitizing tablet was mounted against the monitor during the playbacks and the positions of the bubbles were recorded directly via the tablet through its interface to the laboratory VAX 11/750 computer for further processing. Each "data point" of rms velocity was based on about 200 measurements. These results are discussed in the next section.

4. RESULTS AND DISCUSSIONS I

4.1 Turbulence Characteristics

4.1.1 RMS Velocity Correlation

Both horizontal and the vertical velocity components were measured with the LDA near the interface. Figures 4.1.1 to 4.1.6 show data taken at the axis of the test section to depths up to 30mm. The interface was kept at a height of z/D=3.67, where z is the height above the nozzle and D is diameter of the test-section. The horizontal rms velocities are shown in figures 4.1.1, 4.1.2, and 4.1.3 for three system Reynolds numbers $Re_s \equiv Q/(d\nu)$ = 29140, 40120, and 57690 respectively. The corresponding plots for the vertical rms velocities are given in figures 4.1.4, 4.1.5, and 4.1.6. Each rms value is computed from at least 5 samples, with each sample composed of 10,000 data points. Also shown as a broken line in each figure is the correlation proposed by Sonin et al (1986) based on an independent method (see equation 3.3.5 with $\Phi(Re_s)$ = 21.8) for points sufficiently far below the interface to be unaffected by it.

Overall our LDA data show agreement with the correlation of Sonin et al (equations 3.3.5 and 3.3.7) for locations far from the interface. This is to be expected since that correlation was based on the data taken far below the interface. Nearer the interface, we expect the vertical rms velocity to be damped and the horizontal rms velocity to increase due to the transfer of momentum from the vertical to the horizontal component. Based on figures 4.1.1 to 4.1.6, the presence of the free surface starts to affect the rms velocity at a depth of about 0.13D, irrespective of Re_s. We shall call this layer the 'damped layer'.

Figure 4.1.7 shows the azimuthal rms velocity at 5mm beneath the interface as a function of radius for

$Re_s = 4.01 \times 10^4$. As expected, the rms value tends to decrease as one approaches the wall. It drops gradually to about 85% of the centreline value at r=0.4D, and more dramatically between 0.4D and the wall at 0.5D.

Also shown in figure 4.1.7 is the mean azimuthal velocity as a function of r/D. As expected, its value (bounded by ± 0.01 m/s) is much smaller than the rms value of fluctuating velocity. This is also true for the mean velocities, both horizontal and vertical, measured for all the test points in figures 4.1.1 to 4.1.6. All were below the ± 0.01 m/s bound (not shown). This supports the existence of an essentially bulk-free-flow test region, as postulated by Sonin et al (1986).

The mass transfer across a turbulent liquid interface will depend on the turbulence state imposed on the liquid side. We assume that the latter is characterised by a macroscale, an rms velocity, and the liquid density ρ and kinematic viscosity ν. For the characteristic velocity, we take the value of V' extrapolated from the bulk to the free surface (see figure 4.1.1 to 4.1.6). For the macroscale, we choose the quantity Λ defined in section 4.1.3 below.

4.1.2 An attempt to measure Surface RMS Velocity on the Free Surface directly

An attempt was made to determine the actual turbulent velocity fluctuations on the free surface itself by measuring the motion of air bubbles floating on it. Air was introduced into the test cell at a depth near the inlet nozzle. The bubbles were broken up into much smaller ones by the eddies as they rose towards the free surface. We recorded the movement of these bubbles using a video camera, limiting the range of bubble sizes to between 1 mm and 5mm in diameter, to obtain the rms velocity v" defined as

$$v'' = [< (v_r^2 + v_\theta^2) >]^{1/2} \qquad 4.1.1$$

where v_r is the radial component of velocity, v_θ is the tangential component of velocity, and $< >$ represents the ensemble average. Figures 4.1.8, 4.1.9 and 4.1.10 show the plot of v" against Q/Dd for z/D = 3.67, 4.17 and 4.5 respectively. Each point represents an ensemble average of 200 measurements. Also shown on each figure is a solid line representing equation 3.3.5. Surprisingly, the data are close to equation 3.3.5, though we would expect them to lie close to the LDA-obtained horizontal rms velocity extrapolated to the surface and multiplied by a factor of $\sqrt{2}$ to account for the two-dimensional measurement of the rms value of bubble motion, as opposed to the one-dimensional component measured with the LDA. We have no explanation for the low v" observed except the most obvious: i.e., one may question whether the air bubbles truly follow the fluid motions on the free surface. The analysis of bubble motions at the interface and its dynamics is still a research topic and we will have to defer the explanation to future work.

4.1.3 The Turbulence Macroscale

Since our measurements were restricted to a single point at any given time, we were unable to determine the more conventional macroscale which is based on the two-point autocorrelation function. However, we can define an Eulerian time macroscale

$$\tau = {}_0\int^{\infty} R_{uu}(t)\,dt \quad \text{or} \quad {}_0\int^{\infty} R_{ww}(t)\,dt \qquad 4.1.2$$

where

$$R_{uu}(t) = < u'(t'+t)u'(t') > / < u'^2 > \qquad 4.1.3$$

$$R_{ww}(t) = < w'(t'+t)w'(t') > / < w'^2 >$$

are the Eulerian autocorrelations defined at a point, u' and w' being the horizontal and vertical fluctuating velocity components, respectively, and the symbol < > represents the ensemble average. Based on this Eulerian time macroscale and the local rms velocity, we can define an Eulerian length macroscale

$$\Lambda \equiv V'\tau \qquad 4.1.4$$

Figures 4.1.11, 4.1.12, 4.1.13 and 4.1.14 show the autocorrelation correlation function $R_{uu}(t)$, taken at the centreline at a depth of 30mm for four system Reynolds number, Re_s =25000, 35200, 50300 and 70500. Figures 4.1.15, 4.1.16, 4.1.17 and 4.1.18 show the corresponding $R_{ww}(t)$ for the vertical component of velocity respectively. Each autocorrelation plot was derived from four samples of 10^4 data points each, collected at about 100 Hz. We specifically adjusted the Doppler frequency counter to the 'combined mode' so that each Doppler burst yielded one frequency data after validation. Table 2 summarises all the results for both $R_{uu}(t)$ and $R_{ww}(t)$, τ and Λ. The data imply that the system possesses a Reynolds-number invariant length macroscale (large eddy size),

$$\Lambda = V'\tau \simeq 0.24D \qquad 4.1.5$$

In what follows, we adopt this length scale as the characteristic size of the turbulent eddies and Reynolds number based on Λ as the eddy Reynolds number.

4.1.4 Eulerian Time Spectrum

Based on our measurement of both the horizontal and vertical velocities with respect to time, it is interesting to examine the behaviour of the corresponding Eulerian time

spectrum. Using the definition of the Eulerian time spectrum (e.g. Tennekes and Lumley, 1972),

$$\Psi_{uu}(f) = \int_{-\infty}^{\infty} \exp(-i2\pi ft)\, R_{uu}(t)\, dt \qquad 4.1.6$$

$$\Psi_{ww}(f) = \int_{-\infty}^{\infty} \exp(-i2\pi ft)\, R_{ww}(t)\, dt$$

where f is the frequency in Hertz, we plot the Eulerian time spectrum/energy spectrum for the horizontal and vertical directions, in figures 4.1.19 and 4.1.20 respectively. The system Reynolds number (Re_s) is 25000. The corresponding plots for the horizontal and vertical energy spectrum for Re_s = 50300 are depicted in figures 4.1.21 and 4.1.22 respectively. All the four figures show that at sufficiently high frequency, the spectrum decays approximately as $f^{-5/3}$. This follows the prediction of the spectral decay in the inertial subrange, as discussed by Tennekes and Lumley (1972). The experimental result of Hannoun et al (1988), whose turbulence is generated by means of a submerged oscillating grid, gives similar decay rate in the region far away from the grid, where turbulence is expected to be homogeneous. Also, for each system Reynolds number, both components of energy spectrum are quite identical, which confirms again that our flow is indeed approximately isotropic in turbulence, provided one is not too close to the interface.

4.2 Mass Transfer Rate

All mass transfer data were obtained using CO_2 as the transfer agent. Schmidt numbers of 230, 377, 525 and 1600 were used. The lower three Schmidt numbers were obtained simply by operating at bulk water temperatures of 40°C, 29°C and 23°C respectively. The molecular diffusivities of CO_2 in water were taken from Davidson et al (1957) and Hayduk et al

(1974), while the saturated condition of CO_2 at the interface (required in equation 3.1.6) were taken from Cox et al (1962) and Harned et al (1943). To achieve Sc=1600, a mixture of glycerol and water at 25°C was used as the solvent. These liquids were pre-mixed in the proportion of 21% by volume of glycerol. After each mixing, samples were taken to determine the kinematic viscosity using a 'Cannon-Fenske-Routine' viscometer placed in a precision temperature controlled viscosity bath (model 74944, manufactured by Precision Scientific Company) maintained at a temperature of 25°C ± 0.1°C. The density of the mixture was also measured directly. The diffusion coefficient and the saturated condition of CO_2 at the mixture interface were obtained from Brignole et al (1981). After each run, the mixture was discarded and the whole system flushed with tap water. A new mixture was then made for the next run, and the procedure repeated to obtained the relevant data as described above. The mean Schmidt number of 1600 has a ±10% uncertainty. All the parameters are tabulated in Table 3.

Results for K_L, the mass transfer coefficient, in m/s, versus V' are plotted dimensionally in figure 4.2.1, 4.2.2, 4.2.3 and 4.2.4 respectively, for the four values of Sc. The most significant features of these plots is the appearance of a 'break', which separates two linear regions. This break has not been noted by previous researchers, most of whom used a single power law (or polynomial function) to fit all their dimensional or non-dimensional data. Breaks of one kind or another have, however, been noted by Theofanous et al (1976), McCready et al (1984) and in experiments involving the generation of turbulence by strong wind blowing above the interface (eg. see Merlivat et al (1983)). We shall defer discussion of these other data to section 4.3.

If V_* is the rms velocity corresponding to the 'break' point, we expect that

$$V_* = V_*(D, \rho, \nu, \Lambda) \qquad 4.2.1$$

where D is the molecular diffusivity, ρ is the density of the liquid, ν is the kinematic viscosity of the liquid, and Λ is the macroscale length, as defined in 4.1.5. Dimensional analysis then shows that a break Reynolds number $(Re_\Lambda)_* \equiv V_* \Lambda/\nu$ must be a function only of the Schmidt number, ie.

$$(Re_\Lambda)_* \equiv V_* \Lambda/\nu = f(Sc) \qquad 4.2.2$$

This scaling law suggest that the 'break' velocity is inversely proportional to the turbulence macroscale Λ if Sc is constant. In order to check this conclusion, we performed a set of mass transfer experiments at a bulk water temperature of 23°C (Sc = 525) in a smaller test cell with diameter D_s=0.038m, four times smaller than the former system. Using the relation 4.1.5, the macroscale Λ_2 associated with the smaller test cell would be four times smaller than the macroscale Λ_1 (0.037m) associated with the larger system. Equation 4.2.2 would imply that the break velocity $(V_*)_2$ associated with the small system should be four times larger than the corresponding break velocity of the large system at the same Schmidt number.

Figure 4.2.5 shows the plot of K_L versus V' for D_s=0.038m. The relationship is linear, and passes through the break velocity of the large system, V_*=0.073 m/s, without a break. This feature is shown more clearly in the following figure, 4.2.6. Our scaling analysis thus appears to be confirmed. We were not able to obtain data for the small system at or beyond its break velocity because the interface became quite wavy before such high velocities could be reached. Throughout all our experiment, we deliberately kept the turbulence intensity below the value where the induced surface waves had amplitudes of more than a few mm high. The gradient of the linear profile, dK_L/dV', of the small system has a somewhat higher value (by 20%) than the corresponding large system. By using similar

scaling arguments as employed in Sonin et al (1986), we can established, in simplest form, that

$$K_L = K_L(V', \Lambda, \nu, D, \rho) \qquad 4.2.3$$

whence, upon dimensional analysis, we obtain

$$St = St(\ Re_\Lambda,\ Sc\ ) \qquad 4.2.4$$

where St is a Stanton number,

$$St \equiv K_L/V' = j/V'\Delta C,$$

and Re_Λ is the eddy Reynolds number,

$$Re_\Lambda \equiv V'\Lambda/\nu.$$

Here j is the molar flux transport across the interface and ΔC is the molar concentration difference between the surface and the bulk of the liquid. At velocities below the break velocity, our data shows that K_L/V' is constant, which implies that St is independent of Re_Λ. This, in turn, implies that, for velocities below the break, dK_L/dV' for the smaller system (figure 4.2.5) should be the same as for the large system (figure 4.2.3). The apparent difference seen in figure 4.2.6 can possibly be attributed to the uncertainty involved in the $\Phi(Re_s)$ calibration (see section 3.3).

With data from four tests with different Sc, we can try to establish the function f(Sc) in equation 4.2.2 empirically. The data suggest (see Table 4) that the break point Reynolds number is given by

$$(Re_\Lambda)_* \simeq 3.5\text{x}10^4\ Sc^{-0.4} \qquad 4.2.5$$

$$\text{for} \qquad 230 < Sc < 1600$$

where the break point (denoted by *) is defined as the intersection point of the two linear regions (see figures 4.2.1 to 4.2.4).

Although equation 4.2.5 is derived for the indicated range of high Schmidt number, we obtain some idea of whether it might apply also at much lower Schmidt number by referring to the data of Sonin et al (1986) and Brown (1989) for condensation heat transfer at Prandtl numbers in the range 1.5 to 6.6. These data show a linear relation between K_L and V', with no break point, for rms velocities as large as 0.15 m/s. This result is at least consistent with 4.2.5, which predicts that at Sc=10, say, the break Reynolds number is 1.4×10^4, which is much higher than the maximum Reynolds numbers in the experiments described by Sonin et al and Brown.

In principle the possibility exists that a 'break' observed in our data might be the result of surface contamination with monolayers or even dust. The break point might then signal the condition where the turbulence intensity becomes strong enough to actually break up the surface contamination. Contamination might arise in our system from oil leakage from the pump, etc. J. T. Davies and co-workers have done extensive work on gas absorption through monolayers and found that monolayer resistance can cause a profound effect. Davies et al (1964) postulated that a monolayer acts not only as a direct physical barrier to transport at the interface, but also offers "hydrodynamic resistance" by damping out the eddies in the vicinity of the interface, and thereby causing a drastic reduction in the transport rate compared to the clean surface condition. Their experimental data showed that the greatest reduction in transport rate occured when the turbulence intensity in the liquid was fairly low, which suggested that the cause was the inability of the surface-clearing eddies to break up the surface film. Above a certain turbulence intensity, the corresponding percentage reduction in K_L became smaller. At

very high turbulence intensity, the effect of monolayers was reduced to the layer's resistance (physical barrier) to transport. They found that the effect of even a small amount of contamination, of order one ppm could be measured with suitable contaminants.

In view of this, we carried out a series of experiment designed to check if there was any change in surface tension before and after the mass transfer experiment (monolayers generally alter the surface tension). Care was taken to test only water taken from very near the interface. Our Cenco tensiometer registered at most a $\pm$ 0.0001 N/m variation in the surface tension of the water, which was measured as 0.0728 N/m (20^{o}C) irrespective of the test conditions. Orridge (1970) has studied the effect of 0.1 ppm of sodium sulfosuccinate as surfactant on the flow down an inclined plane. He registered a 15% reduction in CO_2 transfer rate with accompanying 0.0011 N/m decrease in surface tension. Our maximum $\pm$ 0.0001 N/m variation in surface tension thus suggests the absence of significant surface-seeking surfactants in our test. In addition, Orridge 's result also shows a maximum reduction of 50% in the transport rate when the surfactants were increased to 10 ppm, with an accompanying decrease in surface tension of 0.009 N/m. Typically the slope dK_L/dV' increases in our experiment by a much greater factor — at least 4 — as the break point is traversed. This suggests that monolayer contamination is most likely ruled out as the reason for the 'break' observed in our data.

As discussed in chapter 2, most models for interfacial transport suggest that Stanton number, St, is proportional to the -0.5 power of Sc, i.e.

$$St \propto Sc^{-0.5} \qquad 4.2.6$$

the only exception being Kishinevsky model which predicts an independence of Sc. This provides us with the motivation to

ascertain if $Sc^{-0.5}$ dependence is reasonable at least for those data with V' < V_*. Table 5 gives the Stanton number, or slope dK_L/dV', for $Re_\Lambda < (Re_\Lambda)_*$. The data can be correlated well with

$$StSc^{0.5} \simeq 0.0092 \pm 0.0018 \quad [\ Re_\Lambda < (Re_\Lambda)_*\ ] \qquad 4.2.7$$

A non-dimensional plot of $StSc^{0.5}$ versus Re_Λ (figure 4.2.7) indicates the approximately constant region of about 0.0092.

For the 'post-break' region V' > V_*, we plot $(K_L - K_*)/(V'-V_*))$ against Re_Λ in figure 4.2.8, excluding those data very near the 'break' region, as any slight scatter of the data in that region would makes its effect felt disproportionately due to the denominator, $V'-V_*$. The results of figure 4.2.8 suggest that for V' >> V_*, the Stanton number can be approximated as being roughly constant, or at most a very weak function of both Re_Λ and Sc. It is likely that Kishinevsky and Serebryansky's (1956) data lies in the 'post-break' region, as evidenced by their very high stirring rate of about 1700 rpm to generate the turbulence.

To summarise, our data on mass transfer can be correlated as

$$StSc^{0.5} \simeq 0.010 \pm 0.0018 \quad [\ Re_\Lambda < 3.5\text{x}10^4 Sc^{-0.4}\ ] \qquad 4.2.8$$

and

$$(K_L - K_*)/(V'-V_*) \simeq 0.0020 \pm 0.0003 \quad [Re_\Lambda > 3.5\text{x}10^4 Sc^{-0.4}] \qquad 4.2.9a$$

where equation 4.2.9 is viewed as an approximation. Equivalently, using 4.2.5 and 4.2.8, 4.2.9a can be expressed as

$$St \simeq 0.0020 + (0.010\ Sc^{-0.5} - 0.0020)(Re_\Lambda)_*/Re_\Lambda \qquad 4.2.9b$$

$$\text{for } Re_\Lambda Sc^{0.4} > 3.5\text{x}10^4$$

Note that up to this point, the velocity used to define St is the nominal rms velocity, which is taken at the centreline of the test-cell. The actual turbulence intensity decreases as the radial distance increases (see figure 4.1.7). If we use a simple smooth curve fit for figure 4.1.7, we find that the mean velocity is about 25% less than the centreline velocity. This implies that if we base both St and Re_Λ on the local rms velocity, equations 4.2.8 and 4.2.9b become

$$StSc^{0.5} \simeq 0.013 \pm 0.002 \quad [\ Re_\Lambda < 2.7\times10^4 Sc^{-0.4}\ ] \qquad 4.2.10(a)$$

$$St \simeq 0.0025 + (0.013\ Sc^{-0.5} - 0.0025)(Re_\Lambda)_*/Re_\Lambda \qquad 4.2.10(b)$$

$$\text{for}\quad Re_\Lambda > 2.7\times10^4\ Sc^{-0.4}$$

and the break Reynolds number, $(Re_\Lambda)_*$, is given as

$$(Re_\Lambda)_* \simeq 2.7\times10^4\ Sc^{-0.4} \qquad 4.2.11$$

Equations 4.2.10(a) and (b) are applicable for $500 < Re_\Lambda < 8000$ and $230 < Sc < 1600$. Plotted in figure 4.2.9 is the functional form of equations 4.2.10(a) and (b) for the same four Schmidt numbers as in our experiment. Figures 4.2.10 and 4.2.11 show respectively the experimental data for the Sc of 525 and 1600 with the prediction given by equations 4.2.8 and 4.2.9 for comparison.

4.3 Comparison with Other Results

One feature that stands out in our transport rate correlation is the fact that there are two regimes of behaviour, separated "break point" characterised by a Schmidt-number-dependent critical Reynolds number. Most of the previously published work show no such break point. The

burden falls on us to explain the apparent discrepancy. The basic difficulty here is that of deducing the parameters V' and Λ for the data in the literature, so that previous data can be rationally compared with the present data. The means of generating turbulence are numerous : vertically oscillating grid, flow down an inclined plane, wind driven shear flow, falling film flow and many others. Comparison is possible only with those data where empirical relationships exist for converting the respective flow parameters to V' and Λ.

We shall attempt to show that the data of most previous investigations have fallen into either one or the other of the two regions demarcated by the break Reynolds number (see equation 4.2.3). The discussion will be divided into two sections. The first will cover those experiments where turbulence is generated within the liquid and diffuses towards the interface. These are summarised in in Table 6. The second will deal with cases where turbulence is imposed from above the interface. These are summarised in Table 7.

Before we embark on these comparison, however, it is worth pointing out that the two-regime behaviour in our data is distinctly different from that postulated by Theofanous et al (1976) or that obtained by McCready and Hanratty (1984). Theofanous et al postulated a break at Re ~ 500, with $K_L \sim (V')^{1/2}$ at lower Re and $K_L \sim (V')^{3/4}$ at higher Re. McCready and Hanratty found, in experiments with wind-induced turbulence in channel, that the mass transfer coefficient changed from a $(V')^2$ dependence at Re < 50 to a V' dependence at Re > 50, (ie. they found a very different behaviour from that suggested by Theofanous et al). Our break is different from both of these. It occurs at much higher Reynolds number, and separates two linear regions of K_L versus V'.

4.3.1 Turbulence Imposed from Within the Liquid

First consider the mass transfer data obtained in inclined channel flow without surface shear. This type of turbulence generation is similar to ours in that the turbulence is imposed from beneath the interface.

Plate and Friedrich (1984) have indicated that for a channel flow without surface shear,

$$\sigma_u \simeq U_{*w} \qquad 4.3.1$$

$$U_{*w} \simeq 0.1U_w \qquad 4.3.2$$

where σ_u is the rms value of the horizontal turbulence component at 1 cm beneath the surface, U_{*w} is the friction velocity, and U_w is the mean velocity in the channel. They managed to get an empirical fit for the experimental data of Krenkel et al (1963) and Eloubaidy et al (1969), which can be expressed as

$$K_L = 1.78\text{x}10^{-5}\, U_{*w}\, h/R$$

where h is the height of water in the channel and R is the hydraulic radius. Taking $R \simeq 2h$ for a wide channel and $(Sc)_{O_2} \simeq 500$, we have

$$(K_L/V')Sc^{0.5} \simeq 0.020 \qquad 4.3.3$$

which is identical to our 4.2.10(a) except that the constant differ by a factor of about 1.5. We have to keep in mind some possible error in using the approximation 4.3.1 for the comparison. Noting that the largest shear velocity and water height were U_{*w}=0.038m/s and h=0.145m respectively, we have, on estimating the macroscale Λ_h in a channel as 0.1h (see Appendix 2 for a detailed derivation),

$$[(V'\Lambda_h/\nu)Sc^{0.4}]_{max} \simeq 6600 \qquad 4.3.4$$

which is about a factor of four smaller than our break Reynolds number (4.2.11). Hence the 'single-regime' behaviour of their data is consistent with our results.

Next, we consider the flow behind a grid in an open channel as found in Fortescue and Pearson (1967). Unlike our correlation (4.2.10), their data seem to exhibit a better fit with a correlation that implies $K_L \sim V'^{0.5}$ (see also expression 2.7). They made numerous corrections to their 'raw' experimental data to take into account the entrance effect immediately downstream of the grid and the end region where they placed a weir to maintain constant water height. An estimate of these corrections was put at least between 10% to 20%, a figure that is not too small and may be at least in part responsible for the discrepancy with our correlation. Nevertheless, their data only show a 'single-regime' behaviour and we would like to test if their maximum Reynolds number is below our $(Re_\Delta)_*$. Fortescue et al assumed that the turbulence induced by the grid is given by

$$v'/U = 0.086/(X/M - 10)^{0.5} \qquad 4.3.5$$

where v' is the local rms velocity, U is the flow velocity in the channel, M is the ratio of mesh size to diameter of grid and X is the distance from grid downstream, and is applicable througout the channel length. From 4.3.5, we can compute the mean rms velocity V' as

$$V'/U = 0.172M(L/M - 10)^{0.5}/L \qquad 4.3.6$$

where L is the length of the channel. After substituting the appropiate quantities, one obtains

$$V'/U \simeq 0.02 \qquad 4.3.7$$

V' obtained in this way is most likely too low. If we treat the flow like that of an inclined channel, we would have V'

$\simeq 0.1U$ (equation 4.3.2). This raises the issue of the validity of the assumption made with respect to equation 4.3.5 and its application by Fortescue and Pearson throughout the channel length. In fact, equation 4.3.5, which was first proposed by Batchelor and Townsend (1948), was clearly intended to be used only in the region close to the grid, not further than a channel depth, say. Fortescue and Pearson, on the other hand, used it for distances much larger than the channel depth. This may imply that the flow conditions of Fortescue and Pearson were more similar to those of 'open channel flow' than to 'grid' flow, especially in the region further away from the grid. However, the difference they observed in the gas absorption results when the entrance length between the grid and the open-channel section was varied suggests that the grid-induced turbulence should not be discounted entirely in favour of the turbulence due to the shear stress on the channel floor. Nevertheless, it is very difficult (due to the absence of any revelant measurements) to relate the turbulence intensity in their system to the mean flow parameters. If we make the assumption that $V' \sim \beta U$, where β is some constant whose value is of order 0.1, but dependent on the actual grid configuration, then our correlation (equation 4.2.10(a)) can be reduced to the form

$$K_L \simeq 0.013\ Sc^{-0.5}\beta U$$

Since Fortescue and Pearson data were obtained with the water height remaining about constant and at a single operating condition of $20^{o}C$, our correlation implies the following functional form

$$K_L \simeq \text{const.}\ Re_{FP}$$

where $Re_{FP} \equiv 4Q/\nu w$ (Q and w being the volumetric flow rate and the wetted perimeter respectively), for comparison. The

experimental data of Fortescue and Pearson were plotted in linear dimensions of K_L vs Re_{FP} in their figure 12 and logarithmically in figure 14. Comparing these two figures, we can deduce the location of the origin for the linear plot (which lacks a scale for the ordinate in the paper). With this information, it turns out that the data in their linear plot can be approximated by straight lines through the origin. This observation is true for the two sets of data obtained with different grid configurations, which suggests rather good agreement, at least in the functional form, with our correlation (made with the above assumption about V'). If we take β as 0.2, these data also suggests that, for Sc $\simeq$ 570,

$$StSc^{0.5} \simeq 0.033$$

which agrees only very roughly with our correlation equation 4.2.10(a) (within a factor of three for the constant). For the largest Re_{FP} of 10000 achieved in their experiment, we can calculate

$$[(V'D_h/\nu)Sc^{0.4}]_{max} \simeq 6300 \qquad 4.3.8$$

where D_h is the approximately the height of water in the channel and we have taken β as 0.2. The value computed in 4.3.8 is smaller than our break Reynolds number even though we are using D_h instead of some macroscale compatible with our Λ (which should be some fraction of D_h). In other words, their data lies in the pre-critical region.

A submerged oscillating grid has been used by a number of researchers to generate 'homogeneous' turbulence which decays as the free surface is approached. Isenogle (1985), following up work of Dickey et al (1984), made numerous measurements in such a system of both the horizontal and vertical rms velocities at various depths beneath the interface, under various operating conditions. He also

carried out measurement of the integral length scale, L_I, defined as

$$L_I \equiv {}_0\int^{\infty} f(r)\, dr \qquad 4.3.9$$

where $f(r) = \langle u(r_0)u(r_0 + r) \rangle / \langle u^2(r_0) \rangle$

u is the fluctuating velocity

r_0 is the reference location

r is the mean separation distance

$\langle \quad \rangle$ is the ensemble average

which is compatible with, though not exactly equal to, our integral length scale Λ. By using the absolute turbulent velocity $Q \equiv \langle (u^2 + v^2 + w^2)^{0.5} \rangle$ and L_I extrapolated to the interface, we were able to replot Isenogle's mass transfer data as in figure 4.3.1. It is interesting to note that when Re_I ($\equiv QL_I/\nu$) exceeds about 600, $K_L Sc^{0.5}/Q$ levels off to a value of about 0.01. If we assume that the total kinetic energy does not change significantly in the 'damped' layer next to the interface, then we can relate our V' (which is extrapolated from the bulk to the interface) to Q in the form $V' \simeq Q/\sqrt{3}$. In this case, the data of Isenogle can be re-correlated as $K_L Sc^{0.5}/V' \simeq 0.017$ for $Re(\equiv V'L_I/\nu) > 400$, which agrees rather well with our correlation (equation 4.2.10(a)). For $Re < 400$, $K_L Sc^{0.5}/V'$ shows some indication of rising above 0.017. Our data did not stretch to such low Reynolds numbers. Note, however, that the rise at $Re < 400$ is quite different from that data of McCready and Hanratty (1984), who observed a decrease in K_L/V' at $Re < 50$. In Isenogle's data

$$(Re_I Sc^{0.4})_{max} \simeq 10400 \qquad 4.3.10$$

which is smaller than our break Reynolds number. A single-regime behaviour in his case is thus consistent with our results.

In an independent finding, Ho (1987) made measurements of the average mass transfer of O_2 onto a turbulent liquid. The turbulence was induced by an oscillating grid beneath the interface. Ho's apparatus was the same as that used by Brumley et al (1984) who reportedly found that, provided one is not too close to the interface to be influenced by its presence, the dimensionally consistent relationship of Toly and Hopfinger (1976)

$$V = 0.25\ f\ S^{1.5} M^{0.5} / z' \qquad 4.3.11$$

$$L_{TH} = 0.1\ z' \qquad 4.3.12$$

is a fairly good approximation of the velocity field. Here, V is the rms horizontal/vertical velocity, L_{TH} is the macroscale length scale, f is the grid frequency, S is the stroke amplitude, M is the mesh size of grid, and z' is the distance from the virtual origin (which is close to the centre of oscillation). We therefore took the rms velocity and length scale at the interface as being given by 4.3.11 and 4.3.12, respectively. We reduced Ho's mass transfer data, which were collected at a fixed temperature of $20^{o}C$, to the form $StSc^{0.5}$ versus Re_H ($\equiv VL_H/\nu$). The results are plotted in figure 4.3.2. Although there is some scatter in the plot, a mean value of $StSc^{0.5} = 0.0156$, which is indepedent of Re_H, is found to be a fairly good representation. This compares favourably to our correlation 4.2.10(a). Next, we calculate that for Ho's data,

$$(Re_H Sc^{0.4})_{max} \simeq 3100 \qquad 4.3.13$$

which is very much smaller than our break Reynolds number. A single-regime behaviour in Ho's data is thus consistent with ours.

Finally, Thomas (1979) did experiments on steam condensation at a shear-free turbulent interface, using a

vertical jet system somewhat like ours, but with a much shallower test cell with z_s/D ranging from 0.3 to 1.3. His system produced a bulk radial flow under the interface, with the radial velocity at the surface varying inversely with r, i.e. the flow was distinctly different from our bulk-free flow condition. Thomas made some measurements of the mean velocity near the interface and, on the assumption that the rms velocity V' was about one-quarter of the radial mean velocity at the surface, suggested the following relations

$$V' \simeq 1.5U_n d/s \quad \text{for} \quad 0 < r < 0.3s \qquad 4.3.14$$
$$V' \simeq 0.65U_n d/s \quad \text{for} \quad 0.3s < r < R$$

and

$$l_T \simeq 0.039s \quad \text{for} \quad 0 < r < 0.3s \qquad 4.3.15$$
$$l_T \simeq 0.045r \quad \text{for} \quad 0.3s < r < R$$

Here U_n is the velocity at the nozzle, d is the nozzle diameter, s is the depth of nozzle beneath the interface, l_T is the integral scale of the turbulence, and R is the radius of the test-cell. Using the above relations to obtain the integrated mean rms velocity, Thomas's heat transfer data can be interpreted approximately as

$$StPr^{0.5} \simeq 0.010 \qquad 4.3.16$$

The corresponding correlation of Orridge (1970), who used a very similar set-up, but with even shallower depth of nozzle beneath the interface, for the gas absorption of O_2 and CO_2, can be expressed as

$$StSc^{0.5} \simeq 0.004 \qquad 4.3.17$$

We have implicitly assumed that the velocity and length scale relations of Thomas (4.3.14 and 4.3.15) are applicable

to Orridge's experiments, though Orridge's data are for smaller z_s/D than Thomas. Both equations 4.3.16 and 4.3.17 clearly bear strong a resemblance to our 4.2.10(a).

The highest nozzle Reynolds number achieved in Thomas 's run is around 80000. Assuming the macroscale Λ_T associated with Thomas 's system to be the mean value of the integral scale of eddies (as defined in 4.3.15), we can deduced that

$$[(V'\Lambda_T/\nu)Pr^{0.4}]_{max} \simeq 14000 \qquad 4.3.18$$

The equivalent result of Orridge experiment is

$$[(V'\Lambda_T/\nu)Sc^{0.4}]_{max} \simeq 8200 \qquad 4.3.19$$

The single-regime behaviour in both Thomas and Orridge tests is thus expected.

All the data we have referred to thus far lie in the 'pre-critical' region. The only experiments that we are aware of which may be in our 'post-critical' region are those of Kishinevsky and Serebryansky (1956). Kishinevsky and Serebryansky used a mechanical stirrer to generate turbulence in a cylindrical test cell. The stirring rate was kept constant at 1700 rpm and mass transfer were collected for 3 different gases, namely nitrogen, oxygen and hydrogen, at 20°C. In order to relate their data ot ours, we follow the suggestion by McManamey et al (1973) who suggests that for turbulence generated by a stirrer,

$$V' \sim 0.55NL \qquad 4.3.20$$

where V' is the turbulence fluctuation near the interface, N is the stirring speed (revolutions per second), and L is the length (tip to tip) of the stirrer blade, and

$$\Lambda_K \sim 0.3L \qquad 4.3.21$$

where Λ_K is the characteristic eddy dimension (macroscale). Note that subsequent hot wire measurement of the velocity field in a stirrer vessel by Davies et al (1979) supported the correlation of 4.3.20. In this way, we are able to restate Kishinevsky et al result as

$$St \sim 0.0045 \qquad 4.3.22$$

which is less than a factor of three higher than our correlation (4.3.10(b)). As to whether their data belong to the post-critical region, we compute

$$(V'\Lambda_K/\nu)Sc^{0.4} \sim 54000,\ 66000,\ 71000 \qquad 4.3.23$$

respectively for H_2, O_2 and N_2. These values are well above our break Reynolds number which lends further credibility to our postulation.

4.3.2 Turbulence Imposed via Shear at the Interface

In this section, we will look at data taken under conditions where the liquid-side turbulence is generated by imposeing a mean shear stress at the interface. Although strictly speaking, it does not follow that our correlation should apply in these cases, it is of interest to test whether that might be the case.

Jensen and Yuen (1982) made measurements in a water channel of turbulence intensity near the interface in the presence of a cocurrent steam flow and found that

$$V' \simeq 2.9U_{*_W} \qquad 4.3.24$$

where V' is the longitudinal (flow-wise) rms velocity at interface, and U_{*_W} is the interfacial shear velocity based on the water density. Their experiment on cocurrent steam condensation yielded an expression of the form

$$StPr^{0.5} \simeq 0.048 \qquad 4.3.25$$

where Pr is the Prandtl number based on bulk water temperature. Equation 4.3.25 differs from our correlation (4.2.10(a)) only in that the constant is larger. Note that the Prandtl number dependence was assumed, not determined empirically. The largest Reynolds number (based on the mean water velocity V and height of water in the channel h) reached in Jensen and Yuen 's data was 6800. If we assume $U_{*w} \sim 0(V)$ (which is an overestimate) and make use of 4.3.24, we arrive at

$$[(V'h/\nu)Pr^{0.4}]_{max} \sim 31000 \qquad 4.3.26$$

This value is of the same order as our break Reynolds number, even though we have used h to represent the macroscale length and taken $U_{*w} \sim V$ (overestimates). Their data exhibited a single-regime behaviour, with K_L proportional to V'.

Aisa et al (1981) measured the transfer of O_2 and CO_2 from a moving stream into a channel of constant water height for a range of Schmidt number, $400 < Sc < 750$. Using 4.3.24, we can readily reduce their correlation function to the form

$$StSc^{0.5} \simeq 0.034 \qquad 4.3.27$$

For their experiment,

$$[(V'M/\nu)Sc^{0.4}]_{max} \simeq 40000 \qquad 4.3.28$$

where M is the height of water in the channel. According to this estimate, their maximum Reynolds number is again of the same order as our break Reynolds number. We must bear in mind, however, that we have used M as an estimate for the macroscale (M is definitely larger than Λ), and that hence the results of Aisa et al would be expected to fall in the 'pre-break' regime, as indeed they seem to have done.

McCready and Hanratty (1984) conducted a series of experiment similar to Aisa et al. They obtained results similar to 4.3.27 for large Re (Re > 50, which is based on interfacial shear velocity and height of water). The largest Reynolds number reached in their experiment was

$$U_{*_w}M/\nu = 1000 \qquad 4.3.29$$

where U_{*_w} is the interfacial shear velocity based on water density. This corresponds to (with 4.3.24 and Sc=440)

$$[(V'M/\nu)Sc^{0.4}]_{max} \simeq 33100 \qquad 4.3.30$$

which is of the same order as our break Reynolds number even though we are using M instead of the appropriate length scale (some fraction of M) for the computation. Evidently, only a single-regime behaviour is found. However, for Re < 50, their data indicates that K_L begins to show marked variation from the correlation mentioned above (4.3.27). Davies (1972, pp 194) made measurements of flow down an inclined plane and found that flow was essentially laminar for Reynolds number (based on mean velocity u, and height of water) below 500. If we used the approximation $u \simeq 0(10U_{*_w})$ which can be deduced from Mattingly 's (1977) wind imposed shear flow experiments, then the departure from 4.3.27 for McCready et al data at Re < 50 can be attributed to the flow turning laminar. Another explanation for the deviation was put forward by McCready et al that at very low Re, the water height became exceedingly thin, allowing the lower solid boundary to exert an increasing influence on the turbulence near the interface. The occurrence of capillary waves is not uncommon. In such a scenario, the 'lower boundary effect' manifests itselt as the dependence of the mass transfer coefficient on more parameters besides Re.

The only experimental data which have previously shown the existence of two regimes are for cases where the

turbulence in the liquid is generated by a strong wind blowing above the interface (eg. see figure 11 of Broecker et al (1978) which show two different linear regimes when K_L is plotted against the wind velocity). In all these cases, at the higher wind speed, the linear relation between K_L and the wind speed appears to break down and K_L increases more rapidly with further increases in wind speed. This has been attributed by some to the effect of small bubbles produced by wave breaking and the presence of large gravity waves and capillary waves (eg. see Merlivat et al (1983) and Broecker et al (1984)). In order to make further comparison with our result, we shall continue to use 4.3.24 of Jensen and Yuen (1982). However, the determination of a relevant macroscale, compatible with our Λ, is more problematic. The macroscale in a shear-imposed flow is most likely dependent on the shear stress at both the interface and the channel floor, and the water height. Since there is no reported work on macroscale determination in this class of flow, we have to make some order of magnitude estimate for comparison.

For flow conditions where the amplitude of the gravity waves are relatively small, and capillary waves and wave breaking are absent, Sivakumar 's (1984) correlation for O_2 absorption can be reduced to the form

$$StSc^{0.5} \simeq 0.016 \qquad 4.3.31$$

Here we have used equation 4.3.24 to obtain V' from U_{*w}. Sivakumar took measurement of the mean water velocity as a function of depth for a constant water height of 0.3m, with the nominal wind speed varying from 2.6 m/s to 10.2 m/s blowing above the interface. We can estimate a macroscale l_s from the expression

$$\Delta u / l_s \simeq \partial u / \partial y |_{interface} \qquad 4.3.32$$

where Δu is the mean velocity at the interface and y is the vertical coordinate. Equation 4.3.32 defines a length scale about equal to the Prandtl mixing length. Our criteria for the 'break' condition (equation 4.2.11) can thus be expressed as

$$[(V' l_s/\Lambda)Sc^{0.4}]_{break} \simeq 25000 \qquad 4.3.33$$

which is of the same order as our break Reynolds number. This has two important implications. One, it shows that Sivakumar 's data before the break lies essentially in the 'pre-critical' region. Secondly, this provide a possible explanation for the existence of two regimes. We have to bear in mind that the 'post-critical' region in our flow was <u>not</u> accompanied by any wave breaking nor the formation of bubbles. Perhaps with the further increase in wind speed, both wave breaking and formation of bubbles become more prevalent, introducing more complications. If this is the case, the 'pre-critical' region can change either at the break Reynolds number as defined in 4.2.11, or, at the conditions where wave breaking occurs, depending on which happens first.

Merlivat and Memery (1983) obtained data for N_2O and Ar absorption in a wind-driven channel with h=0.3m. At lower wind speeds, their results can be interpreted as

$$StSc^{0.5} \simeq 0.050 \qquad 4.3.34$$

A break occurred when the wind velocity was about 10 m/s, with K_L incresing more rapidly with V' at the higher speeds. This enable us to use Sivakumar data for the determination of a macroscale l_m according to 4.3.32. With V' in their break region, we calculate

$$[(V' l_m/\Lambda)Sc^{0.4}]_{break} \simeq 16000 \qquad 4.3.35$$

which implies that the above correlation 4.3.34 lies in the 'pre-critical' region.

Deacon (1977) also obtained correlation of the form

$$(K_L/V')Sc^{0.67} \simeq 0.027 \qquad 4.3.36$$

for the region of the lower wind velocity where the interface is relatively unruffled. For the wind speed very much higher than 5 m/s, he found that K_L is in rough proportion to the square of the wind speed.

To overcome the problem of limited fetch experienced in a linear tunnel, Jahne et al (1979) made measurements of gas exchange in a circular wind-water tunnel and got relation of the form,

$$(K_L/V')Sc^{0.5} \simeq 0.007 \qquad 4.3.37$$

For this case, we are not able to use Sivakumar data for a fair estimate of the macroscale since the water height used were quite different. If we take the macroscale l_J to be 20%, say, of the water height of 0.1m, we can compute

$$[(V'l_J/\Lambda)Sc^{0.4}]_{break} \simeq 15000 \qquad 4.3.38$$

which suggests that the correlation 4.3.37 is in the 'pre-critical' region.

In conclusion, our postulation of two regimes for the mass transport correlation is not inconsistent with the previously published data. Furthermore, all the correlations obtained by previous workers for the 'pre-critical region' (equations 4.3.3, 4.3.16, 4.3.17, 4.3.25, 4.3.27, 4.3.31, 4.3.34, 4.3.36 and 4.3.37) have forms similar to our equation 4.2.10(a), though the constant in general differs (at most by a factor of four). For the 'post-critical region', the only previously available data, equation 4.3.22

compares favourably with our 4.2.10(b). It was pointed out by Sonin et al (1986) that the way in which turbulence is being generated might have some bearing on the value of the constant. The important outcome of the brief comparison (a more extensive comparison is possible only if we could relate the flow parameters in other experiments to V' and Λ) suggests that St may be expressed as

$$StSc^{0.5} \simeq A \qquad [\ (V'\Lambda/\nu)Sc^{0.4} < 2.7\times10^{4}\ ] \qquad 4.3.39$$

$$St \simeq B + (ASc^{-0.5}-B)(Re_{\Lambda})_{*}/Re_{\Lambda} \qquad [\ Re_{\Lambda} > (Re_{\Lambda})_{*}\ ] \qquad 4.3.40$$

where A and B are constants to be determined. Equations 4.3.39 and 4.3.40 may apply to a wider class of flow conditions, irrespective of how turbulence is induced in the liquid.

5. CONCLUSIONS FOR EXPERIMENTS

5.1 LDA Calibration of Turbulence in Test Cell

(a) The rms velocities measured with the LDA at the system centreline agree fairly well with the correlation of Sonin et al 's (1986) (equations 3.3.5 and 3.3.7), provided one is not too close to the interface. The interface distorts the turbulence intensity to a depth of about 0.1D. As one approaches the interface from below, the horizontal rms velocity increases and the vertical rms velocity decreases. This is the result of a transfer of momentum from the vertical to the horizontal directions.

(b) With the interface at 3.67 system diameters above the nozzle, the rms value of the turbulence intensity near the interface is overwhelmingly large compared with any vertical bulk flow velocity in the same region.

(c) As a result of wall effects, the average value of V' is about 25% below the centreline value.

(d) The integral length scale based on the Eulerian autocorrelation and the respective local rms velocity V' yields a length scale Λ,

$$\Lambda = V'\tau = 0.24D \qquad 5.1$$

which does not depend on V'. This is consistent with the postulation of Sonin et al (1986) that the macroscale is 'locked' to the system diameter D at locations greater than about 3D away from the nozzle. Sonin et al also used the k-ε model to fit their experimental results and obtained an associated length scale $L_{k-\varepsilon} = 1.1D$, where $L_{k-\varepsilon} \equiv 1.5V'^{1.5}/\varepsilon$, ε being the dissipation rate per unit mass. The

fact that $L_{k-\varepsilon}$ is significantly larger than Λ is consistent with what is found in most turbulent flows.

5.2 Gas Absorption Rate Correlation

Our mass transfer data for Sc between 230 and 1600 suggest a 'two-regime' behaviour with respect to the eddy Reynolds number, the two regimes being separated by a "break" Reynolds number, $(Re_\Lambda)_*$, given approximately by

$$(Re_\Lambda)_* \simeq 2.7\times10^4\ Sc^{-0.4} \qquad 5.2$$

where the Reynolds number is based on Λ and the local (average) rms value V' of one velocity component. At Reynolds numbers below $(Re_\Lambda)_*$, the transfer coefficient K_L is directly proportional to V' and inversely proportional to $Sc^{1/2}$ (see below), while at Reynolds number above $(Re_\Lambda)_*$, K_L is proportional to V' with a much higher proportionality coefficient, and essentially independent of Sc.

For flow with $Re_\Lambda Sc^{0.4} < 2.7\times10^4$, a correlation

$$StSc^{0.5} \simeq 0.013 \pm 0.002 \qquad 5.3$$

is found for the shear-free interface with turbulence imposed from below. Here $St \equiv K_L/V' = j/V'\Delta C$ where j is the molar flux transfer across the interface and ΔC is the molar concentration difference between the surface and the bulk of the liquid. This expression is similar in form (though the constant on the right hand side differs from case to case) to the correlations which have been obtained by other researchers for various other methods of producing liquid-side turbulence, such as with flow down an inclined plane, wind-induced interfacial shear and submerged oscillating grids. It is shown that, with a few exceptions, these previous correlations have been obtained at Reynolds number

lower than our break Reynolds number. In the few cases where the Reynolds number exceeded $(Re_\Lambda)_*$, a two-regime behaviour had in fact been observed.

For flow with $Re_\Lambda > 2.7 \times 10^4 Sc^{-0.4}$, our correlation for a shear-free interface has the form

$$St \simeq 0.0025 + (0.013\, Sc^{-0.5} - 0.0025)(Re_\Lambda)_*/Re_\Lambda$$

This relation is in approximate agreement with the data of Kishinevsky and Serebryansky (1956).

Part II

6. NUMERICAL SIMULATION

6.1 Background and Overview

The major obstacle to the formulation of a general model for transport at a turbulent free surface has been our lack of understanding of the turbulence structure at a free surface. Very little information, either theoretical or experimental, is available for the distribution of the turbulence on the liquid side, very near the interface, where the major resistance to transport occurs. The transport models which have been proposed to date have all been based on simplified conjectures about what aspects of the liquid-side turbulence control the transport, and their diversity and shortcomings can be traced directly to the oversimplified input assumptions.

Detailed velocity measurements sufficiently close to the free interface are not easy to obtain, because the region of interest in mass transfer problems is often less than a millimetre from the interface. Usually, particularly at the higher turbulence intensities, the surface moves with an amplitude larger than the thickness of entire region of interest. (Even the resolution of a LDA with a typical measuring volume of 40μm x 40μm x 600μm is barely adequate, although the main difficulty is usually not resolution but beam reflections from the moving free surface). Recently Brumley et al (1984) made some detailed velocity measurement, using a split-film anemometer probe mounted in front of a mechanical, rotating arm, in a system where turbulence was generated by means of a submerged oscillating grid. Even then, the Reynolds number had to be limited to fairly low values, since the surface turbulence had to be low enough to ensure that the interface was essentially flat).

In order to make further progress towards developing a theoretical decription of the free surface transport process in general, and of our mass and heat transfer data in particular, we undertook a direct numerical simulation of the turbulence and passive scalar transport (species concentration or temperature) near a free surface. The unsteady Navier-Stokes equations were numerical computed from some initial conditions until an approximately statistically steady state was reached. Because the computational domain had to be at least of the order of the turbulence macroscale in size, and the computation had to resolve features down to the Kolmogorov microscale, the Reynolds number based on rms velocity and macroscale was limited to values which only approach those of our experiments. For similar reasons, the Prandtl number had to be limited to low values, Pr $\sim$ 0(10), which explains why we refer to the energy equation instead of the species concentration equation, where typically Sc $\sim$ 0(100 - 1000). To conserve computational time, the energy equation was solved for a number of Prandtl numbers after the velocity field was updated from each time step. The computation was continued in time until <u>both</u> the velocity and the temperature profiles reach approximately statistically steady states. The Reynolds-averaged heat transport rate and the rms values of the vertical and horizontal components of velocity fluctuations were then computed, and the results compared with the experimental data of Brown (1989) on condensation heat transfer at a free surface.

6.2 <u>Discretized Equations</u>

The time dependent incompressible Navier Stokes equation in its rotational form is given by

$$(1/\mathrm{Re})\nabla^2 \underset{\sim}{u} - \nabla \Pi = \partial \underset{\sim}{u}/\partial t + \underset{\sim}{\omega} \times \underset{\sim}{u} \qquad 6.2.1$$

$$\nabla.\underset{\sim}{u} = 0 \qquad 6.2.2$$

where $\underset{\sim}{u}$ is the velocity non-dimensionalised w.r.t. U, U is the rms velocity at the bottom boundary of the computational domain, $\underset{\sim}{\omega}$ is the vorticity, $\nabla\times\underset{\sim}{u}$, Π is the dynamic pressure, $P/\rho U^2 + 0.5|\underset{\sim}{u}.\underset{\sim}{u}|$ and Re is the Reynolds number, $U\Delta/\nu$. Temporal discretisation of 6.1.1 by an implicit Crank-Nicolson method in time gives a semi-discrete system of the form,

$$(1/2Re)\nabla^2(\underset{\sim}{u}^{n+1} + \underset{\sim}{u}^{n}) - \nabla\Pi = (1/\Delta t)(\underset{\sim}{u}^{n+1} - \underset{\sim}{u}^{n}) + \underset{\sim}{\omega}\times\underset{\sim}{u} \qquad 6.2.3$$

$$\nabla.\underset{\sim}{u}^{n+1} = 0 \qquad 6.2.4$$

Similarly, the energy equation can be expressed as follows,

$$(1/2Pe)\nabla^2(T^{n+1} + T^{n}) = (1/\Delta t)(T^{n+1} - T^{n}) + \underset{\sim}{u}.\nabla T \qquad 6.2.5$$

where T is the non-dimensional temperature, defined as the local-to-bulk temperature differential non-dimansionalised with the subcooling ΔT, Pe is the Peclet number, $U\Delta/\alpha$, and α is the molecular diffusivity.

Using spectral Fourier expansions in the horizontal x and y directions and Gauss-Lobatto Lagrangian interpolations in the vertical z direction, we can express $\underset{\sim}{u}$ and T in the form,

$$\underset{\sim}{u}(x,y,z) = \sum_{-M}^{M-1}\sum_{-N}^{N-1} \underset{\sim}{u}_1(m,n,z)e^{i\alpha' mx}e^{i\beta ny}$$

$$\underset{\sim}{u}(m,n,z) = \sum_{0}^{NN} \underset{\sim}{u}_{11}(m,n,j)h_j(z)$$

$$T(x,y,z) = \sum_{-M}^{M-1}\sum_{-N}^{N-1} T_1(m,n,z)e^{i\alpha' mx}e^{i\beta ny}$$

$$T(m,n,z) = \sum_{0}^{NN} T_{11}(m,n,j)h_j(z)$$

where $i = \sqrt{-1}$,

$\alpha' = 2\pi/L_x$, L_x is the extent of x domain,

β $= 2\pi/L_y$, L_y is the extent of y domain, and $h_j(r)$ is the elemental Lagrangian interpolants.

This effectively decouples the problem into a one dimensional problem to be solved for each wavenumber, $-M < m < M-1$, and $-N < n < N-1$.

The next step is the variational discretisation of both the Navier-Stokes and energy equations. This process is described by Maday and Patera (1987), who give the fully discretised equations as

$$-(A + \sigma_1 B)u_i^{n+1} + D_i^H \Pi_i = (A + \sigma_2 B)u_i^n + 2Bf_i \qquad 6.2.6$$

$$D_i u_i^{n+1} = 0 \qquad 6.2.7$$

where A and B are stiffness and mass matrices as defined in Maday and Patera (1987), D_i is the del operator, D_i^H is the Hermittian matrix of D_i, f_i represents 3^{rd} order Adam-Bashforth treatment of the explicit term $\underset{\sim}{\omega}\times\underset{\sim}{u}$, σ_1 represents $(\alpha^2m^2 + \beta^2n^2)/Re + 2/\Delta t$, and finally σ_2 is $-(\alpha^2m^2 + \beta^2n^2)/Re + 2/\Delta t$. From 6.2.6 and 6.2.7, Π is evaluated first followed by u_i^{n+1}. Due to the highly symmetric forms of the equations involved, we use the method of 'fast direct Poisson solvers' as described by Patera (1986), to solve for Π_i and u_i^{n+1}. T_i^{n+1} is then evaluated from the energy equation which is discretised as,

$$-(A_1 + \sigma_{11}B_1)T_i^{n+1} = (A_1 + \sigma_{21}B_1)T_i^n + 2B_1g_i \qquad 6.2.8$$

where A_1 and B_1 are stiffness and mass matrices similar in form to A and B, σ_{11} represents $(\alpha^2m^2 + \beta^2n^2)/Pe + 2/\Delta t$, σ_{21} is $-(\alpha^2m^2 + \beta^2n^2)/Pe + 2/\Delta t$, and finally g_i is the 3^{rd} order Adam-Bashforth treatment of the explicit term $\underset{\sim}{u}\times\nabla T$. In all the above representations, we have assumed that the appropriate boundary conditions are taken into account in the respective matrices. The implementation of

the boundary condition would be described in the next section.

In the computation, the velocity field was updated at every time step using the discretised Navier-Stokes equations. At the end of each time step, the velocity field was "frozen", and the temperature fields were evaluated for each of the various specified Prandtl numbers. The velocity field was then obtained for the next time step, and the procedure repeated until an approximately steady state was reached for both the velocity and temperature fields.

6.3 Boundary Conditions

The problem we are addressing is one which involves an essentially horizontal liquid interface with negligible surface shear. The turbulence in the liquid is imposed from below (eg. by some mixing or shear flow below the surface). We consider the simplest case where the turbulence is isotropic in a horizontal plane, though - the source of turbulence being below the interface - its intensity necessarily decreases in the liquid with increasing elevation. For our computational domain, we take a rectangular box with horizontal and vertical sides equal to Λ. (Λ being defined in 4.1.5). On the top horizontal surface, we impose a stress-free condition

$$\partial u/\partial z = 0 \qquad 6.3.1$$

$$\partial v/\partial z = 0 \qquad 6.3.2$$

where u and v are the horizontal velocities and z is the distance measured vertically upwards, and assume that the interface remains horizontal,

$$w = 0 \qquad 6.3.3$$

where w is the vertical velocity.

On the sides of our domain, we impose a periodic boundary condition, which is automatically taken care of with the spectral Fourier expansion in the x and y directions.

The specification of the boundary condition for the bottom boundary (henceforth called the lower boundary) is not so straightforward. We must impose a time and space dependent velocity field which simulates at least some minimum statistical properties - which we take as V' and Λ - of the real turbulence for which the computation is aimed. This is done as follows. First - separately from the computation - we generate a "forgery" of isotropic turbulence, with zero mean flow and satisfying $\nabla.\underset{\sim}{u}=0$, in a cube of the same size Λ as our computational domain. This cube of isotropic turbulence is generated following the method of Orszag (1969) based on a random number generator and a knowledge of the turbulent energy spectrum, E(k). The turbulence so generated has a zero mean flow and satisfies the incompressible continuity equation (ie. $\nabla.\underset{\sim}{u}=0$). The sides of the cube take on periodic boundary conditions, consistent with our assumed boundary conditions.

The cube of turbulence thus generated is characterised by a spatial longitudinal velocity correlation f(r) and a lateral velocity correlation g(r) (see Hinze (1975) for definitions), but is "frozen" in time. In order to introduce an appropriate time dependence, we identify the lower boundary of our computational domain with a horizontal plane which moves vertically upward through the cube with a certain speed c. The speed c must be chosen so that the Eulerian autocorrelation $R_{ww}(t)$ for a point on the lower boundary (ie. for a point moving vertically upward through the cube of isotropic turbulence, at a speed c) matches f(r). In other words,

$$R_{ww}(ct) = f(r) \qquad 6.3.4$$

or equivalently

$$c \int_0^{\infty} R_{ww}(t')\, dt' = \int_0^{\infty} f(r)\, dr \qquad 6.3.5$$

The relation between c and V' is given below in equation 6.3.12.

As for the specification of the energy spectrum E(k), which is required in Orszag's simulation of the isotropic turbulence cube, the simplest expression is (Tennekes and Lumley, 1972),

$$E(k) = 1.5\, \varepsilon^{2/3}\, k^{-5/3} \qquad 6.3.6$$

where ε is the viscous dissipation rate per unit mass and k is the wave number. For our case, ε can be further expressed as

$$\varepsilon = (1.5V'^2)^{1.5}/L_{k-\varepsilon} \qquad 6.3.7$$

where V' is the rms velocity and $L_{k-\varepsilon}$ is the length scale associated with the k-ε model. Sonin et al (1986) estimated that $L_{k-\varepsilon} = 1.1D$ (equation 3.3.6) and from our experiment, $\Lambda = 0.24D$ (equation 4.1.5), so that ε can be rewritten as

$$\varepsilon = (1.5V'^2)^{1.5}/4.583\Lambda \qquad 6.3.8$$

Mesh size consideration (see the following section for more details) and the memory capacity of the Cray XMP/24 computer allowed us to have 32 Fourier modes in the two horizontal directions, thus giving minimum wave number k_{min} and maximun wave number k_{max} as

$$k_{min} = 2\pi/\Lambda \qquad 6.3.9$$

$$k_{max} = 2\pi/\Lambda * 15\sqrt{3} \qquad 6.3.10$$

Upon substituting 6.3.8 into 6.3.6, and integration of 6.3.6 with the limits imposed by 6.3.9 and 6.3.10, we find

$$1.5\ V'^2 > \int_{k_{min}}^{k_{max}} E(k)\ dk \qquad 6.3.11$$

which violates the principle of energy conservation. To overcome this problem, we replace 6.3.6 with a modified energy spectrum, E(k),

$$E(k) = (1.5\ \varepsilon^{2/3} k^{-5/3})(1 + B' e^{-(k-k_o/\sigma)}) \qquad 6.3.11$$

where $k_o = k_{min}$, $\sigma = 2k_o$ and B' is a constant to be determined by satisfying the requirement $1.5\ V'^2 = \int_{k_{min}}^{k_{max}} E(k)\ dk$. B' is found to be 2.784. The above modification of E(k) will bias the energy distribution at the lower wave numbers (longer length scales) relative to the higher wave numbers (shorter length scales). However, any small eddies that are specified at the lower boundary will in any case most likely be damped out by viscosity inside the domain before reaching the top surface. Thus we expect that the smaller turbulence scales at the top boundary will be the result of the breakdown of the larger eddies, which contain the kinetic energy, and not the result of eddies transferred up from the lower surface where the turbulence is specified.

With the cube of isotropic turbulence thus generated using the above-mentioned specification of E(k), we can calculate the longitudinal spatial correlation, f(r), as shown in figure 6.3.1. Note that, since the cube has periodic boundary condition, f(r) decreases initially from 1.0 at r=0 and subsequently increases again to 1.0 at $r=\Lambda$. In order to evaluate $\int_0^\infty f(r)\ dr$ as required in equation 6.3.5 for the computation of speed c, we approximate the integral by truncating at $r=0.5\Lambda$. With this approximation, c is obtained as

$$c = 0.232 V_b \qquad 6.3.12$$

where V_b is the rms velocity in the cube, or equivalently, the rms velocity of the lower boundary of the computational domain.

It should be noted that because we specify a Dirichlet boundary conditions at the lower surface, irrespective of the flow conditions that are actually developed within the computational domain, we expect an artificial boundary layer to form at this boundary. This is in contrast to the real flow which does not have a boundary layer at this surface. This boundary layer is simply an artifice of the way we simulate the effect of the turbulence in the bulk of the liquid via a Dirichlet boundary condition. Resolution of this artificial normal boundary layer would require the placement of a fine grid spacing in the vicinity of the lower boundary, subject to the constraint,

$$\Delta < \nu/W_{max} \qquad 6.3.13$$

where Δ is the grid spacing in the z direction, ν is the kinematic viscosity and W_{max} is the maximum vertical velocity at the lower surface.

Expression 6.3.13, together with the requirement that the mesh be sufficiently fine near the upper boundary to resolve the thermal boundary layer (see below), puts an upper limit on the Reynolds number which can be handled by a given computer. We performed complete calculations for the two cases, case A and case B (see Table 8). In case A, which has a high Reynolds number of 1000, the artificial boundary layer was not resolved. In case B, which has a Reynolds number of 100, both the artificial boundary layer at the lower surface and the thermal boundary layer at the interface were fully resolved.

In the energy equation, we apply a constant temperature T_1 at the top surface (this simulates vapour condensation, where the interface is at a constant saturation temperature). With respect to the sides of the

domain, the temperature takes periodic boundary condition. In the real case, the lower surface has a time-varying temperature distribution due to the turbulent heat flux $< w'T' >$ (which dominates the molecular heat flux $\alpha\partial T/\partial z$),

$$< w'T' > \; >> \; \alpha\partial\bar{T}/\partial z \qquad 6.3.14$$

where $\bar{T}$ is the average temperature, α is the molecular diffusivity, T' is the fluctuating component of temperature, w' is the fluctuating component of vertical velocity and the symbol $< \; >$ represents ensemble average. Since the true boundary condition at the lower surface is part of the solution, we simplify the problem by approximating the lower boundary temperature as a constant temperature, T_2, but provide an artificial diffusivity $\alpha_{art}(z)$ at the lower surface, making sure that $\alpha_{art}(z)$ is large compared with the molecular diffusivity in that region. Its primary purpose is to represent the turbulent heat flux,

$$\alpha_T\partial\bar{T}/\partial z\,|_{\text{lower surface}} = -<w'T'>|_{\text{lower surface}} \qquad 6.3.15$$

which allows the passage of the heat flux with a very small mean temperature gradient. In typical turbulent flows with heat transfer,

$$\alpha_{turb} \sim 0.01U\Lambda \qquad 6.3.16$$

where U and Λ are the characteristic velocity and macroscale of the flow. For our computation, the function $\alpha_{art}(z)/\alpha$ for case A is plotted in figure 6.3.2 while the counterpart for case B is given in the following figure 6.3.3. In each case, $\alpha_{art}(z)/\alpha$ takes the form of a parabolic equation such that it approaches the value of unity smoothly at 0.7Λ and 0.8Λ from the interface for case A and case B respectively. At the lower boundary, for case A,

$$\alpha_{art}/U\Lambda = 0.2,\ 0.13,\ 0.09,\ 0.06 \qquad 6.3.17$$

respectively for Pr of 1.0, 1.5, 2.2 and 3.15, while for case B

$$\alpha_{art}/U\Lambda = 0.6,\ 0.20,\ 0.04 \qquad 6.3.18$$

respectively for Pr of 3.15, 10.0 and 50.0.

6.4 Mesh Size Considerations

A "rigorous" solution of the basic equations must resolve the largest and the smallest length scales of the velocity as well as the temperature. Townsend (1951) has shown that for turbulent flow, most of the viscous dissipation occurs at wave numbers below k_{max}, where

$$0.3 < k_{max}/k_\eta < 0.5 \qquad 6.4.1$$

k_η being the wavenumber corresponding to the Kolmogorov length,

$$k_\eta = (\varepsilon/\nu^3)^{1/4} \qquad 6.4.2$$

where ε is the energy dissipation per unit mass and ν is the kinematic viscosity. The maximum dissipation rate occurs at $k/k_\eta \simeq 0.2$. For our flow, we shall adopt a maximum wavenumber $k_{max} = 0.4k_\eta$. In equation 6.4.2, we set

$$\varepsilon = (1.5U^2)^{1.5}/L_{k-\varepsilon} \qquad 6.4.3$$

where $L_{k-\varepsilon}$ is the k-ε lengthscale associated with the flow and U is the characteristic velocity which is taken to be the rms velocity at the lower boundary. We can, on using the relation established earlier $L_{k-\varepsilon} = 1.1D$ (equation 3.3.6) and $\Lambda = 0.24D$ (equation 4.1.5), further express k_{max} as

$$k_{max} = 0.318\ Re_b^{0.75}/\Lambda \qquad 6.4.4$$

where Re_b is the Reynolds number based on the rms velocity at the lower boundary. Finally, the smallest length scale associated with the flow, l_s, is given as

$$l_s = 2\pi/k_{max} \simeq 19.75\Delta/Re_b^{0.75} \qquad 6.4.5$$

(An expression similar to 6.4.5 can be derived independently using the relation $l_s \sim 13\eta$, where η is the Kolmogorov microscale, as proposed by Pope and Whitelaw (1976)). To resolve the smallest scales of turbulent velocity, the grid spacing throughout the domain must satisfy

$$\Delta < l_s \qquad 6.4.6$$

Next, we have to make an estimate of the thermal boundary layer δ in the vicinity of the interface so that appropriate resolution can be applied. δ can be nominally express as

$$\delta \sim \alpha/K_L \qquad 6.4.7$$

where α is the molecular diffusivity and K_L is the turbulent heat transfer coefficient. It can be further restated as follows

$$\delta \sim (\alpha/\nu)(\nu/V'\Delta)(V'/K_L)\Delta \qquad 6.4.8$$

$$\delta/\Delta = (1/Pr)(1/Re_\Delta)(1/St) \qquad 6.4.9$$

and Re_Δ is based on extrapolated velocity at the interface. From the steam condensation experiments by Brown (1989), in the limit of zero Richardson number,

$$St \sim 0.0172\ Pr^{-0.33}, \qquad 6.4.10$$

whence

$$\delta/\Lambda \sim 58.1/Re_{\Lambda}Pr^{0.66} \qquad 6.4.11$$

Since our computational domain is Λ, we can further express

$$\delta/\Lambda \sim 77.3/Re_{b}Pr^{0.66} \qquad 6.4.12$$

where Re_b is the Reynolds number based on the rms velocity at the lower boundary. We have implicitly made use of the rms velocity correlation of 3.3.5, which was determined experimentally, to relate Re_{Λ} to Re_b. Hence to resolve the thermal diffusion layer, the vertical spacing near the interface must be much smaller than δ.

Finally, the computational domain L_D must be able to accomodate the largest size eddy Λ. This is done by making $L_D = \Lambda$.

With all the constraints mentioned above and in section 6.3, we performed the complete calculations for the following two cases: case A with a higher Re_b of 1000 and Pr of 1.0, 1.5, 2.2 and 3.15, and case B with a lower Re_b of 100 and Pr of 3.15, 10.0 and 50.0. The higher range of Pr was chosen for case B since, from expression 6.4.5, a low Re_b of 100 and Pr of 0(1) would have made $\delta/\Lambda \sim 0(1)$ which violates the assumption - implicit in the use of an artificial (turbulent) diffusivity at the lower boundary - that $\delta << \Lambda$. The assumption is that δ/Λ is small enough not to be overly influence by the specification of $\alpha_{art}(z)$ at the lower surface. The grids in the z direction for the above-mentioned two cases are given in figures 6.4.1 and 6.4.2 respectively, both showing a very fine grid spacing near the interface for the resolution of δ. Note that the grid spacing is also finer at the inner boundary compared to the middle portion of the computational domain for figure 6.4.2. The horizontal x and y directions have 32 Fourier modes each. Table 8 shows all the parameters associated with the implementation of the two cases A and B.

7. RESULTS AND DISCUSSIONS II

The numerical simulations were carried out for two conditions, identified as case A and case B. In case A, the eddy Reynolds number Re_b (based on the rms velocity at the lower boundary) was 1000 and the grid mesh spacing is shown in figure 6.4.1. Re_b for case B was 100; the grid mesh is shown in figure 6.4.2. For both cases, computations were carried out with the NASA Lewis Research Centre Cray XMP/24 computer. The computations were started with the initial velocity distribution in the computational domain equated to that in the cube of isotropic turbulence which was used to generate the lower boundary condition (see section 6.3). The initial temperature distribution was taken as a step function with a value of unity at the interface and zero throughout the domain. Computations were allowed to run for a period of at least 10 eddy turnovers (an eddy turnover is defined as Λ/U, where U is the reference rms velocity at the lower surface) to ensure that a satisfactory statistically-steady state had been reached for both the velocity and temperature distributions. In terms of Cray time, case A took over 10 hours of CPU time. Case B, which had a finer mesh to resolve the artificial boundary layer at the lower surface, required close to 30 CPU hours.

7.1 Approach to Steady State

7.1.1 Time Evolution of Stanton number

Since we started our computations from arbitrary initial states and allowed the calculations to proceed until a so-called 'steady' state was reached, it was necessary to track the time evolution of a quantity which is a good representation of the flow. We selected the Stanton number, $St \equiv K_L/U$, based on the rms velocity at the lower boundary

and on the average value of K_L over the interface, because of its inherent dependence on both the velocity and the temperature fields. (In general, the velocity field and the temperature field will not reach steady state at the same time; and hence it is convenient to use as a "marker" a quantity which depends on both).

Case A

The spatially-averaged St is shown versus time in figures 7.1.1, 7.1.2, 7.1.3 and 7.1.4 for Pr of 1.0, 1.5, 2.2 and 3.15, respectively. The time evolution for St in the very early periods is not shown because our initial conditions (mentioned above) are artificial and the initial value of St is not a characteristic value of St. The dotted lines in each plot indicate those regions where the computed data were not retrieved from NASA Lewis for post-processing. Nevertheless, we can see that St has stopped varying on the average after about 7 eddy turnovers, implying that an approximately steady state has been reached.

Case B

The average St (averaged spatially over the interface) vs time is shown in figure 7.1.5 for Pr=3.15. Again, the dotted lines represent those sections where the computed data were not retrieved from NASA. The plot reveals that in this case, St has reach an approximately steady level after the 6 eddy turnover periods.

7.1.2 Energy Transfer Across Each Plane

Case A

If the deduction that a steady state has been reached after the 7 eddy turnovers can be made from the plots of the time evolution of St, then the mean temperature profile should remains approximately invariant with respect to time

(see section 7.3), and the heat flux should be the same across each horizontal plane of the computational domain. The total heat flux, Q(z), can be defined as

$$Q(z) = \alpha \partial \bar{T}/\partial z - \langle w'T' \rangle \qquad 7.1.1$$

where α is the molecular diffusivity, $\partial \bar{T}/\partial z$ is the mean temperature gradient at height z, T' is the fluctuating component of temperature and w' is the fluctuating component of the vertical velocity. The first term on the right in 7.1.1 represents the molecular heat flux, while the second term represents the heat flux due to the turbulent eddy motion (turbulent heat flux).

Figures 7.1.6, 7.1.7, 7.1.8 and 7.1.9 show the ensemble-averaged total heat flux (Q(z) is first averaged spatially over each plane and then time average at each z over the last 3 eddy turnover periods) for the Prandtl numbers of 1.0, 1.5, 2.2 and 3.15, respectively. In each case, Q(z) is approximately invariant with distance, which reaffirms that a steady state exist.

The turbulent part of the heat flux, $\langle w'T' \rangle$, is shown next, in figures 7.1.10, 7.1.11, 7.1.12 and 7.1.13. It is important to note that as one moves further away from the interface, turbulent heat flux dominates progressively over the molecular heat transfer. This is clear from a comparison of figures 7.1.6, 7.1.7, 7.1.8 and 7.1.9 with 7.1.10, 7.1.11, 7.1.12 and 7.1.13 respectively; note that the magnitude of the turbulent heat transfer approaches that of the total heat transfer at locations away from the upper interface. However, in the vicinity of the lower surface, the 'molecular' heat transfer predominates again at the expense of the explicit turbulent heat transfer. This is because we have artificially specified a variable molecular diffusivity, $\alpha_{art}(z)$, to represent the turbulent heat flux $\langle w'T' \rangle$ in that region (see section 6.3 for details). This action was necessary because of the Dirichlet boundary conditions for temperature at the lower surface.

Case B

The ensemble-averaged heat flux (averaged spatially over each plane first, then time average at each z over the last 3 eddy turnovers) across each horizontal plane for Prandtl numbers 3.15, 10.0 and 50.0 are depicted in figures 7.1.14, 7.1.15 and 7.1.16, respectively. These figures show constant values across each plane, implying that a statistically steady state has been reached.

The corresponding turbulent heat flux for Prandtl numbers 3.15, 10.0 and 50.0 are plotted in figures 7.1.17, 7.1.18 and 7.1.19, respectively. As in case A, and as expected, the turbulent heat flux approaches the total heat flux sufficiently far from the interface, except in the region where an artificial molecular diffusivity has been introduced.

7.2 Velocity Characteristics

7.2.1 Ensemble Averaging of the RMS Velocity in the Steady State

For a stationary flow, ensemble averaging is equivalent to time averaging. The "ensemble-averaged" rms velocity at a given plane was computed by first determining the fluctuating component of velocity with respect to the spatial mean at each horizontal plane, followed by taking the rms of the fluctuating velocity at each plane, and finally by time-averaging (over the "steady state" period) the rms velocity thus computed at each plane. This ensemble average is somewhat different from the way the rms value is defined in an experiment. In a LDA measurements, the rms velocity at a particular point is calculated by first determining the time series mean, followed by computation of the rms quantity with respect to the time series mean. There is no reason why the two process of calculating rms velocity

should be significantly different in principle. We chose to use our sequence of averaging because it would required an enormous amount of memory space for a computer to store data for every time step and for every location so that the more conventional ensemble average can be evaluated. To spot check whether our ensemble averaging produced results in agreement with the conventional ensemble averaging, we took a limited time series of velocity at a particular position on each plane, and found that the resulting rms velocity profile was indeed approximately the same as the rms velocity we computed (to within about 30%; the differences depended on the point examined, and could be explained by the relatively short time-wise averaging period).

7.2.2 RMS Velocity Profile

Case A

The ensemble-averaged rms velocities in the two horizontal directions and the vertical direction are plotted in figures 7.2.1, 7.2.2 and 7.2.3, respectively. The ensemble averages were taken over a period of the last three eddy turnovers. As mentioned earlier in section 6.3, the fact that the grid spacing near the lower surface was not fine enough to resolve the artificial boundary layer has probably resulted in the observed increase in the rms velocity from about 1.0 at the inner boundary to about 1.5 at the first grid location of the computational domain. All the three components of rms velocity then decrease with elevation from a high value of about 1.5 to about 0.2 at a distance of only 0.4Δ from the lower surface. This sharp drop in rms velocity is not found in the experimental results (see figures 4.1.1 to 4.1.6). It is probably attributable to the way we imposed the velocity boundary condition at the lower boundary of the computational domain, and aggravated by not having a fine mesh to resolve the

normal boundary layer (see the discussion in section 6.2). However, as will be seen below, there is still a large decline in the rms velocity in case B, where the artificial boundary layer was resolved, as one moves from the lower surface to about 0.6Λ from the interface. This decline is therefore most likely caused by our artificial boundary condition at the lower surface. We simulate V' and Λ at that boundary. However, not only is the application of a Dirichlet boundary condition artificial, but so is the fact that our imposed turbulence has random phasing. Isotropic turbulence in a spatial domain can be decomposed into wave numbers of different magnitude and phases between each wave number. In Orszag's (1969) scheme of generating isotropic turbulence, which we adopted for the specification of the lower boundary condition, only the amplitudes of the wavenumbers are considered and the phase between each wavenumber is completely ignored. This might present a problem if the phase differences between the wavenumbers are also important. This problem is compounded by the fact that the Dirichlet boundary condition prevents information exchange from the flow inside the domain to the flow at the lower boundary, which results in the formation of an artificial boundary layer. The result of all this may be that the flow within the domain requires more spatial distance than one Λ for its evolution into a more "universal" turbulence.

It is interesting to note, however, that our computed rms velocity profiles bear a strong resemblance to the experimental data of Brumley and Jirka (1984), who used a submerged oscillating grid to generate their turbulence. Their resultant rms velocity exhibits a sharp decline in magnitude with distance measured away from the oscillating grid, towards the free surface. It should be noted that their oscillating grid is in fact a Dirichlet boundary condition, and that it takes some distance from the grid for the flow to develop characteristics pertaining to isotropic

turbulence, with an accompanying large drop in energy. The rate of decline in the rms velocity subsequently becomes much more gradual, similar to our computed results. However, there are some fundamental difference between the turbulence induced by an oscillating grid and our case, notably the issue of length scales.

Case B

The use of a sufficiently fine mesh to resolve the artificial boundary layer in the vicinity of the lower boundary eliminates the surge in rms velocity at the location next to the lower surface. This is clearly shown in the horizontal rms velocity plots of figure 7.2.4 and 7.2.5 and the vertical rms velocity in figure 7.2.6. However, there is still a fairly sharp decline in magnitude close to the lower surface, as in the experiments of Brumley and Jirka. The rms velocities decrease from about 1.0 at the lower surface to about 0.15 at 0.4Δ from the inner surface. As discussed above, this is probably caused by our velocity boundary condition at the inner surface.

It is interesting to note that the ratio of the highest rms value near the inner surface to the rms value in the region close to the interface are $1.5/0.1 \simeq 15.0$ and $1.0/0.06 \simeq 16.6$ for case A and B respectively. This suggest that the turbulence intensity decreases by roughly the same ratio irrespective of the imposed eddy Reynolds number Re_b.

7.2.3 Energy Spectra

Case A

To show further quantitative similarity between the experimental data of Brumley et al (1984) and our calculations, we compare the respective longitudinal (S_{uu}, S_{vv}) and transverse (S_{ww}) power spectra (see Tennekes and Lumley, 1972, for definitions). Both of Brumley et al 's

spectra exhibited -5/3 power dependence at the higher wave numbers at locations sufficiently remote from the free surface. The longitudinal power spectra, S_{uu} and S_{vv}, are proportional respectively to u^2 and w^2 when expressed in terms of their Fourier-transformed wave number components, and the transverse power spectrum S_{ww} is proportional to w^2 when expressed in terms of its wave numbers. Figures 7.2.7, 7.2.8 and 7.2.9 show the graphs of our computed u^2, v^2 and w^2 (ensemble averaged over the last three eddy turnovers) plotted against wave number k (defined nominally as $2\pi k/\Lambda$ where k is an integer) for different depths of 0.04Λ, 0.155Λ and 0.5Λ beneath the interface. These figures show a -5/3 exponent in the high wave number region except for the case where the depth is 0.04Λ. It is likely that the the proximity of the interface has caused the deviation from the -5/3 power dependence, as is also seen in the data of Brumley et al (1984).

Case B

The equivalent power spectral densities S_{uu}, S_{vv} and S_{ww} for case B are plotted in figures 7.2.10, 7.2.11 and 7.2.12. These are ensemble average values taken over a period of the last three eddy turnovers. The interesting feature of these figures is that they do not exhibit -5/3 exponent decays. From the rms velocity profiles in figures 7.2.4 to 7.2.6, it is to be noted that the local eddy Reynolds number at depth 0.09Λ, 0.5Λ and 0.6Λ from the interface (ie. the locations where S_{uu}, S_{vv} and S_{ww} are evaluated) are of order 10. The local Reynolds number is thus probably too low for the presence of an inertial subrange where a -5/3 power exponent can be expected (see Tennekes and Lumley, 1972).

7.3 Temperature Profiles

Case A

The ensemble averaged ("mean") temperature at a given elevation was obtained by first averaging the temperature at that elevation, and then averaging over a period of the last three eddy turnovers. The mean temperature is plotted in figures 7.3.1, 7.3.2, 7.3.3 and 7.3.4 for the Prandtl numbers of 1.0, 1.5, 2.2 and 3.15 respectively. As expected, the slopes of the temperature profile at the interface are steeper for the higher Prandtl numbers.

One feature stands out, and needs comment: the presence of a slight drop in the profile at about 0.7Λ from the interface. This happens also to be the location of the last spectral element. The 'bump' in the profile can, however, be attributed to the artificially introduced molecular diffusivity $\alpha_{art}(z)$ which overwhelms the molecular diffusivity α in the energy equation (see figure 6.3.2). Recall that the artificial diffusivity $\alpha_{art}(z)$ was introduced at the lower boundary to overcome the difficulties with Dirichlet boundary condition for the temperature in the energy equation (see section 6.3 for more details).

Case B

The corresponding mean temperature profile for Prandtl numbers of 3.15, 10.0 and 50.0 are shown in figures 7.3.5, 7.3.6 and 7.3.7 respectively. These profiles show increasingly steep gradients at the interface with increasing Prandtl number. As in case A, the profile for Pr=3.15 shows a slight drop at the beginning of the last two spectral elements located next to the lower surface, where we have replace the molecular diffusivity α with a varying artificial diffusivity $\alpha_{art}(z)$. In the other figures, the temperature profile show smoother 'transition'.

Overall, the slight drop in the temperature profile is more prominent in case A than in case B. There are two probable causes. First, the distance over which $\alpha_{art}(z)$ was imposed near the lower surface was smaller in case B than in

case A (0.2Λ vs 0.3Λ). This allows a longer spatial distance for the development of the temperature profile with α in case B. Second, the grid spacing in case B is much finer near the lower surface for resolution of the artificial boundary layer; in case A (figures 7.2.1 to 7.2.3), the boundary layer was not resolved, and a sharp numerically-induced increase of rms velocity takes place near the lower surface.

7.4 Turbulent Diffusivity $\alpha_T(z)$

Case A

The turbulent diffusivity $\alpha_T(z)$ is defined as

$$\alpha_T(z) = -\langle w'T' \rangle(z) \; / \; \partial\bar{T}/\partial z \qquad 7.4.1$$

where the symbol $\langle \quad \rangle$ represent ensemble average (ie. time average) and $\bar{T}$ is the mean temperature. If we use a Taylor expansion for the term, $\langle w'T' \rangle(z)$, near the interface and apply the interfacial boundary conditions $w' = T' = 0$, $\partial u/\partial z = \partial v/\partial z = 0$, we can deduced that

$$\alpha_T(z) \simeq z^2/\tau' + \ldots\ldots + \qquad 7.4.2$$

where $$\tau' = -[(\partial\bar{T}/\partial z) \; / \; \langle \partial w'/\partial z \; \partial T'/\partial z \rangle]_{z=0}$$

is independent of z, and has the dimension of time. Being an expansion in z, 7.4.2 with only the first non-zero term is valid only in the region very close to the interface.

Figures 7.4.1, 7.4.2, 7.4.3 and 7.4.4 show plots of ensemble-averaged $\alpha_T(z)$ (based on first averaging w'T' spatially over each horizontal plane and then time averaging over the last three eddy turnovers, and separately dividing by the mean temperature gradient $\partial\bar{T}/\partial z$ taken over each plane before the time averaging) versus z for Prandtl number of

1.0, 1.5, 2.2 and 3.15 respectively. The broken lines represent the z^2 dependence. All four plots provide indications that $\alpha_T(z) \simeq \text{const.}z^2$ up to a depth of about 0.3Λ beneath the interface. Also shown in the following figure, 7.4.5, is τ' versus Pr for both case A and case B. The graph shows that τ' is at most a slightly increasing function of Pr for case A and essentially independent of Pr for case B. The magnitude of τ' differs by roughly one order between case A and B. It may be concluded therefore, that $\alpha_T(z)$ near the interface is a property of the turbulence field, and insensitive to the heat flux.

Case B

Figures 7.4.6, 7.4.7 and 7.4.8 show corresponding plots $\alpha_T(z)$ (evaluated in the same way as in case A) vs z in log-log scale for Prandtl numbers of 3.15, 10.0 and 50.0 respectively. The dotted line shows a z^2 dependence. These figures also show that $\alpha_T(z) \simeq \text{const.}z^2$ near the interface. For the lower Pr, the z^2 dependence extends over a wider spatial range. This is not unexpected, since the thermal boundary layer increases with decreasing Pr for a given Reynolds number flow.

7.5 The Condensation Stanton number and Comparison with Experiment

The condensation Stanton number, St, is defined as

$$St = -\alpha \, \partial\bar{T}/\partial z|_{interface} \; / \; V'\Delta T \qquad 7.5.1$$

where α is the molecular diffusivity, $\partial\bar{T}/\partial z$ is the mean temperature gradient evaluated at the interface, V' is the rms velocity near the interface and ΔT is the difference in temperature between the interface and the bulk. Sonin et al (1986), Helmick et al (1988) and Brown (1989) measured the

Stanton number for steam condensation on subcooled water. Expressing their Stanton number in terms of the rms velocity component (either vertical or horizontal) extrapolated from the bulk to the surface, ignoring the damping near the interface. The data of Brown, which corrected the previous data and established the Prandtl number dependence, can be correlated as

$$St = 0.0215\ Pr^{-0.33} \qquad 7.5.2$$

$$\text{for} \quad 500 < Re_{\Delta} < 12000$$
$$1.5 < Pr < 4.7$$

provided that buoyancy effects are negligible.

This equation can, in principle, be compared directly with case A, which corresponds to Re_{Δ}=1000 and, the flow being assumed incompressible, negligible buoyancy effects. An ambiguity arises, however, in determining the velocity V' on which St is to be based. Brown's experimental correlation is based on the extrapolation of V' from the bulk region to the interface, ignoring the damped layer. This value of V' (termed V'_s) is not very different in the experiments from the value of V' at $z=\Delta$ (see figures 4.1.1 to 4.1.6). In the computation, however, the profile of V' is such that a value extrapolated to the surface is clearly very different (by an order of magnitude, approximately) from the value of V' at $z=\Delta$. What is more, an attempt at making an extrapolation produces nonsensical results, since the extrapolation is controlled by the rate of decay of V' <u>within</u> the damped layer rather than outside it, as in the data of Brown. In what follows, we base our St on the value of V' at $z=\Delta$, ie. the rms velocity imposed at the lower boundary of the computational domain.

Based on the rms velocity at the lower surface (ie. the reference velocity used for normalisation), our computed ensemble-averaged Stanton number (based on the time average

of the mean temperature gradient at the interface for the last three eddy turnovers, divided by the rms velocity) for Re = 1000 agrees remarkably well with the experimental values (within about 15%). Results of the computed St vs Pr are tabulated in Table 9 together with the values from equation 7.5.2 for comparison.

This remarkable agreement is probably in some measure fortuitous, since we were not been able to simulate the rms velocity profiles well (see figures 7.2.1 to 7.2.3). The rms velocity can be viewed as the sum of the energy contribution from eddies of all sizes. That the St based on the rms velocity at the lower surface, and <u>not</u> the rms velocity in the vicinity of the interface, agrees so well with the experimental results suggests that perhaps only the large scale eddies play a pivotal role in the transport process across the free interface. If this is true, it still leaves unclear how the transport rate is related to the motion of these large eddies. The large-eddy model of Fortescue and Pearson (1967) clearly does not agree with the data. Fortescue and Pearson 's model is based on the existence of a characteristic eddy renewal time τ' which has a constant value of $0.20\Delta/U$. This disagrees with our computed τ' (figure 7.4.5) not only in magnitude but also in the functional dependence on Reynolds number.

From figure 7.5.1, we can see that the computed results imply an exponent of Pr of -0.37, which is close to Brown's experimental value of -0.33.

One of the reason why case B was computed was to check whether the agreement of the Stanton number in case A with experiment was a coincidence. The computed St for case B, based again on the rms velocity at the lower surface, are tabulated versus Pr in Table 10. Also shown are the experimental quantities, evaluated by extrapolating equation 7.5.2 to Re = 100. The agreement between the computed and the experiment is within about 20%.

Bearing in mind that the Prandtl number exponent of -0.33 in equation 7.5.2 was established using data for Pr < 5.0, and that our experimental mass transfer data of Sc >230 suggests an exponent of -0.5 (equation 4.2.10(a)), it is interesting to see whether any trend exist for the negative Prandtl number exponent to increase in the 3 data points corresponding to Pr=3.15, 10.0 and 50.0. Assumming the functional form between St and Pr as

$$St = \beta Pr^{\beta} \qquad 7.5.3$$

the lower two Prandtl number values imply β = -0.40 while the higher two imply Pr β = -0.49.

8. CONCLUDING REMARKS ON COMPUTATION

We have attempted a numerical simulation of the turbulence field and passive scalar distribution near a shear-free surface, with turbulence imposed from below. The full, unsteady Navier-Stokes equations and the energy equation are solved using a spectral Fourier expansion in the two horizontal directions, and a Legendre spectral element technique in the vertical direction. The computational domain, "extracted" from the full flow, is restricted to a single-macroscale neighbourhood of the interface, with the top boundary representing the free surface conditions, and the bottom boundary simulating the "far-field" isotropic turbulence. Two statistically steady calculations at eddy Reynolds number of 100 and 1000 and Prandtl numbers ranging from 1 to 50 are presented. Near the free surface, the computed turbulent diffusivity shows a distance-squared dependence, in agreement with the Taylor-series-expansion result appropriate for the free surface boundary conditions. The computed Stanton number (based on the rms velocity at the lower artificial boundary of the extracred domain) is found to agree with the experimental steam condensation results (Brown, 1989) to within better than 20%.

Despite this good agreement with experiment, our calculations are plagued by several serious problems that are, no doubt, endemic to the extracted-subdomain approach. First there are numerical difficulties associated with the need to resolve the (physically unrealistic) boundary layer which forms at "far-field" boundary, where we have applied artificial Dirichlet boundary conditions. Second, the use of random-phase simulated turbulent conditions at the "far-field" boundary can yield unreasonable (here, very low) turbulent intensities in the interior. If these problems can be addressed, extracted-subdomain calculations can result in significant computational savings, in that single-macroscale

domains can be used to investigate (assumed local) turbulent characteristics.

References.

Aisa L., Caussade B., Goerge J. and Masbernat L. (1981),'Exchanges de gaz dissous en ecoulenments stratifies de gaz et de liquide', Int. J. Heat/Mass Transfer, Vol 24, No. 6, pp 1005.

Aydelott J. C. and Rudland R. S. (1985),'Technology requirements to be addressed by NASA Lewis Research Centre Cryogenic Fluid Management Program', NASA Technical Memorandum 87048/AIAA paper 85-1229.

Aydelott J. C., Carney M. J. and Hobstein J. I. (1985),'NASA Lewis Research Centre low-gravity fluid management technology program', NASA Technical Memorandum 87145/AIAA GNOS Paper 85-002.

Barchilon M and Curtet R. (1964),'Some details of the flow structure of an axisymmetric confined jet with backflow', J. Basic Eng., Vol 86 , pp 777-787.

Batchelor G. K. and Townsend A. A. (1948), Proc. Royal Society, Vol. 193A, pp 539.

Battino R. (1965),'The solubility of gases in liquid', Chemical Reviews, Vol 66, pp 395-463.

Bin A. K. (1983),'Mass transfer into a turbulent liquid flow', AIChE J., Vol 25, No.3, pp 405-415.

Boadway J.D. and Karahan E. (1981),'Correction of LDA readings for refraction at cylindrical interface', DISA information No. 26.

Brignole E. A. and Echarte R. (1981),'Mass Transfer in laminar liquid jets', Chem. Eng. Sci., Vol 36, pp 695-703.

Broecker H., Petermann J. and Siems W. (1978),'The influence of wind on CO_2-exchange in a wind-wave tunnel, including effects of monolayers', J. Mar. Res., Vol 36, pp 595-610.

Broecker H. and Siems W. (1984),'The role of bubbles for gas transfer from water to air at higher windspeeds', of 'Gas transfer at water surfaces, pp 229-236'. (See Brutsaert and Gerhard, 1984).

Brown J. S. (1989), S. M. Thesis, Dept. of Mech. Eng., M. I. T. ; in progress

Brtko W. H. and Kabel R. L. (1976),'Pollution transfer into water bodies', Water, Air and Soil Pollution, Vol 6, pp 71 95.

Brtko W. J. and Kabel R. L. (1978),'Transfer of gas at natural air-water interfaces', J. Phys. Oceanogr., Vol 8, pp 543-556.

Brumley B. H. and Jirka G. H. (1987),'Near surface turbulence in a grid stirred tank', JFM, Vol 183, pp 235-263.

Brutsaert W. and Gerhard H. J. editors (1984),'Gas Transfer at Water Surfaces', D. Reidel Publishing Company.

Chun J. H., Shimko M. A. and Sonin A. A. (1986),'Vapour condensation onto a turbulent liquid - II. Condensation burst instability at high turbulence intensities', Int. J. Heat Mass Transfer, Vol 29, No. 9, pp 1333-1338.

Cox J. D. and Head A. J. (1962),'Solubility of carbon dioxide in hydrofluoric acid solutions', Trans. Faraday Society, Vol 58, pp 1839-1845.

Danckwerts P. V. (1951),'Significance of liquid film coefficients in gas absorption', Ind. Eng. Chem., Vol 43, No.6, pp 1460-1467.

Davidson J. F. and Cullen E. J. (1957),'The determination of diffusion coefficients', Trans. Instn. Chem. Engrs., Vol 35, pp 51.

Davies J. T. (1972),'Turbulence Phenomena', Academic Press.

Davies J. T., Kilner A. A. and Ratcliff G. A. (1964),'The effect of diffusivities and surface films on gas absorption', Chem. Eng. Sci., Vol 19, pp 583-590.

Davies J. T. and Lozano F. J. (1979),'Turbulence characteristics and mass transfer at air-water interfaces', AIChE J., Vol 25, pp 405-415.

Deacon E. L. (1977),'Gas transfer to and across an air-water interface', Tellus, Vol 29, pp 363-374.

Dobbins W. E. (1962),'Mechanism of gas absorption by turbulent liquids', presented at International Conference on Water Pollution Research, London, England, pp 61-96.

Downing A. L. (1960),'Aeration in the activated sludge process', Journal of the Institute of Public Health Engineers.

Eloubaidy A. F., Plate E. J. and Gessler J. (1969),'wind waves and the reaeration coefficient in open channel flow', Report No. 69.70 AFE 2, Dept. of Civil Eng., Colo. State Univ., Ft. Collins, Colo., U.S.A.

Ferrell R. T. and Himmelblau D. M. (1967),'Diffusion coefficient of nitrogen and oxygen in water', J. Chem. Eng. Data, Vol 12, pp111-115.

Fortescue G. E. and Pearson J. R. A. (1967),'On gas absorption into a turbulent liquid', Chem. Eng. Sci., Vol 22, pp 1163-1176.

Hannoun I. A., Fernando H. J. S. and List E. J. (1988),'Turbulence structure near a sharp density interface', JFM, Vol 189, pp 189-209.

Harned H. S. and Davis R. (1943),'The ionization constant of carbonic acid in water and the solubility of carbon dioxide in water and aqueous salt solution', J. Amer. Chem. Soc., Vol 65, pp 2030-2041.

Hayduk W. and Laudie H. (1974),'Prediction of diffusion coefficient for non-electrolytes in dilute aqueous solutions', AIChE J., Vol 20, No. 3, pp 611-615.

Helmick M. R. (1988),'Vapour condensation on a turbulent liquid interface for application in low gravity environment', S. M. Thesis, Dept. for Mech. and Nuclear Eng., M. I. T.

Helmick M. R., Khoo B. C., Brown J. B. and Sonin A. A. (1988),'Vapour condensation rate at a turbulent liquid interface, for application to cryogenic hydrogen', AIAA 26th Aerospace Science Meeting, Reno, Nevada.

Henstock W. H. and Hanratty T. J. (1979),'Gas absorption by a liquid layer flowing on a wall of a pipe', AIChE J., Vol 25, No. 1, pp 122-131.

Higbie R. (1935),'The rate of absorption of a pure gas into a still liquid during a short periods', Trans. AIChE, Vol 31, pp 365-389.

Hinze J. O. (1975),'Turbulence', 2nd Edition, McGraw Hill, New York.

Ho A. W. K. (1987),'A study of oxygen transfer at the air water interface of a grid agitated tank', M Sc Thesis, Cornell University, New York.

Isenogle S. S. (1985),'A laboratory study of gas transfer across an air-water interface', M Sc Thesis, Dept. of Geological Sciences, Univ. of Southern California, Los Angeles, California.

Jahne B., Munnich K. O. and Siegenthaler U. (1979), 'Measurement of gas exchange and momentum transfer in a circular wind-water tunnel', Tellus, Vol 31, pp 321-329.

Jensen R. J. and Yuen M. C. (1982),'Interphase transport in a horizontal stratified concurrent flow', U. S. Nuclear Regulatory Commission Report, NUREG/CR-2334.

Jobson H. E. and Sayre W. W. (1970),'Vertical transfer in open channel flow', J. Hydraul. Div. Am. Soc. Civ. Engrs., Vol 96, pp 703-724.

King C. J. (1966),'Turbulent liquid phase mass transfer at a free gas-liquid interface', I & EC Fundamentals, Vol 5, pp 1-8.

Kishinevsky M. (1955),'Two approaches to the theoretical analysis of absorption process', Jour. Appl. Chem. of U.S.S.R., Vol 28, pp 881-886.

Kishinevsky M. and Serebryansky V. T. (1956),' The mechanism of mass transfer at the gas-liquid interface with vigorous stirring', Jour. Appl. Chem. of U.S.S.R., Vol 29, pp 29-33.

Komori S., Ueda H., Ogino F. and Muzishina T. (1982),'Turbulent structure and transport mechanism at the free surface in an open channel flow', Int. J. Heat Mass Transfer, Vol 25, No. 4, pp 513-521.

Krenkel P. A. and Orlob G. I. (1963),'Turbulent diffusion and the reaeration coefficient,' Trans. ASCE, Vol 128, pp 293-323.

Lamont J. C. and Scott D. S. (1970),'An eddy cell model of mass transfer into the surface of a turbulent liquid', AIChE J., Vol 16, No. 4, pp 513-519.

Levich V. (1962),'Physiochemical Hydrodynamics', Prentice Hall Inc, Englewood Cliffs, NJ.

Lewis W.K. and Whitman W. G. (1924),'Principles of gas absorption', Ind. Engng. Chem., Vol 16, pp 1215.

Luk S. Y. H. L. (1986),'Mass transfer in eddies close to air-water interface', AIChE J., Vol 32, No. 9, pp 1546-1554

Maday Y. and Patera A. T. (1988),'Spectral element methods for the Navier-Stokes equations', of 'State-of-the-arts surveys in computational mechanics (A. K. Noor editor)', ASME, New York.

Matteson M. J., Flack W. H. and Woo Y. R. (1984),'Absorption of gases at condensing and evaporating water surfaces', of 'Gas transfer at water surfaces, pp 47-56'. (See Brutsaert and Gerhard).

Mattingly G. E. (1977),'Experimental studies of wind effects on reaeration', ASCE, J. Hydr. Div., Vol 103, No. HY3, pp 311-323

McCready M. J. and Hanratty T. J. (1984),'Concentration fluctuation close to a gas-liquid interface', AIChE J., Vol 30, No. 5, pp 122-131.

McCready M. J. and Hanratty T. J. (1984),'A comparison of turbulent mass transfer at a gas-liquid and solid-liquid interface', of 'Gas transfer at water surface, pp 283-292'. (See Brutsaert and Gerhard, 1984).

McManamey W. J., Davis J. T., Wollen J. M. and Coe J. R. (1973),'The influence of molecular diffusion on mass transfer between turbulent liquids', Chem. Eng. Sci., Vol 28, pp 1061-1069.

Merino F., Risberg J. A. and Hill H. (1980),'Orbital refill of propulsion vehicle tankage', NASA CR-159722.

Merlivat L. and Memery L. (1983),'Gas exchange across an air-water interface : Experimental results and modelling of bubble contribution to transfer', J. Geophysical Research, Vol 88, No. C1, pp 707-724.

Monin A. S. and Yaglom A. M. (1975),'Statistical Fluid Mechanics', Vol I & II, M. I. T. Press, Cambridge, MA.

Munz C. and Roberts P.V. (1982b),'Transfer of volatile organics contaminants into a gas phase during bubble aeration', Technical Report No. 262, Civil Eng. Dept., Stanford Univ., Stanford CA.

Orridge M. A. (1970),'Gas absorption into turbulent streams of liquids', PhD Thesis in Chem. Eng., Univ. of Birmingham, England.

Orszag S. A. (1971),'On the elimination of aliasing in finite difference schemes by filtering high wave number components', J. Atm. Sci, Vol 28, pp 1074.

Orszag S. A. (1971),'Numerical integration of incompressible flows with simple boundaries: accuracy', JFM, Vol 49, pp 75-112.

Orszag S. A. (1969),'Numerical methods for the simulation of turbulence', Physics of Fluids Supplement II, pp 250-257.

Orszag S. A. and Patera A. T. (1983),'Secondary instability of wall-bounded shear flows', JFM, Vol 128, pp 347-385.

Patera A. T. (1984),'A spectral element method for fluid dynamics: Laminar flow in a channel expansion', J. Comp. Physics, Vol 54, pp 468-488.

Patera A. T. (1986),'Fast direct Poisson solvers for high-order finite element discretisations in rectangular decomposable domains', J. Comp. Physics, Vol 65, No. 2, pp 474-480.

Plate E. J. and Friedrich R. (1984),'Reaeration of open channel flow', of 'Gas transfer at water surfaces, pp 333-346'. (See Brutsaert and Gerhard).

Pope S. B. and Whitelaw J. H. (1976),'The calculation of near wake flows', JFM, Vol 73, pp 9-32.

Prasher B. D. and Wills G. B. (1973),'Mass transfer in an agitated vessel', Ind. Eng. Chem. Process Des. Develop., Vol 12, No. 3, pp 351-354.

Ratbun R. E. (1977),'Reaeration coefficients of stream-state-of-art', J. Hydr. Div., ASCE, Vol 103, pp 409-424.

Ratbun R. E. and Tai D. Y. (1984),'Volatilization of chlorinated hydrocarbons from water', of 'Gas transfer at water surfaces, pp 27-34'. (See Brutsaert and Gerhard).

Shimko M. A. (1985),'Scalar transport at a turbulent liquid free surface', S. M. Thesis, Dept. of Mech. Eng., M. I. T.

Sivakumar M. (1984),'Reaeration and wind induced turbulence shear in a contained water body', of 'Gas transfer at water surface, pp 369-377'. (See Brutsaert and Gerhard).

Sonin A. A., Shimko M. A. and Chun J. H. (1986),'Vapour condensation onto a turbulent liquid - I. The steady condensation rate as a function of liquid side turbulence', Int. J. Heat Mass Transfer, Vol 29, pp 1319-1332.

Streeter H. W. and Phelps E. B. (1925),'A study of the pollution and natural purification of the Ohio River. III. Factors concerned in the phenomena of oxidation and reaeration', Public Health Bulletin No. 146, pp 75.

Tchobanoglous G. editor (1979),'Wastewater Engineering : Treatment, Disposal and Reuse', McGrwa-Hill, New York.

Tennekes H. and Lumley J. L. (1972),'A First Course in Turbulence', M.I.T. Press, Cambridge, Massachusetts.

Theofanous T. G., Houze R. N. and Brumfield L. K. (1976),'Turbulent mass transfer at free, gas-liquid interfaces, with applications to open-channel, bubble and jet flows', Int. J. Heat Mass Transfer, Vol 19, pp 613-624.

Thomas R. M. (1979),'Condensation of steam on water in turbulent motion', Int. J. Multiphase Flow, Vol 5, pp 1-15.

Townsend A. A. (1951), Proc. Roy. Soc. London, Vol 208A, pp 534.

Ueda H., Moller R., Komori S. and Mizushima T. (1977),'Eddy diffusivity near the free surface of open channel flow', Int. J. Heat Mass Transfer, Vol 20, pp 1127-1136.

Won Y. S. and Mills A. F. (1982),'Correlation of the effects of viscosity and surface tension on gas absorption rates into freely falling-turbulent liquid films', Int. J. Heat Mass Transfer, Vol 25, No. 2, pp 223-229.

TABLE 1: MAJOR CONCEPTUAL MODELS FOR TRANSPORT ACROSS SURFACE

MODEL	ASSUMPTIONS		TRANSPORT COEFF.
	diffusivity α	time scale τ	$k = c(\alpha/\tau)^{1/2}$
1. Large-eddy model (Fortescue & Pearson)	α	Λ/v	$\frac{k}{v} = c_1 Pr^{-\frac{1}{2}} Re^{-\frac{1}{2}}$
2. Small (Kolmogorov) eddy model (Lamont & Scott)	α	$(\nu\Lambda/v^3)^{1/2}$	$\frac{k}{v} = c_2 Pr^{-\frac{1}{2}} Re^{-\frac{1}{4}}$
3. Viscous inner layer model	α	ν/u^{*2}	$\frac{k}{u^*} = c_3 Pr^{-\frac{1}{2}}$
4. Levich	α	$\sigma/\rho v^3$	$\frac{k}{v} = c_5 Z Pr^{-\frac{1}{2}} Re^{\frac{1}{2}}$
5. Kishinevsky	$v\Lambda$	Λ/v	$\frac{k}{v} = c_6$

α = molecular diffusivity
v = characteristic turbulent fluctuating velocity
u^* = shear velocity
Λ = integral length scale of turbulent eddies
ν = kinematic viscosity
ρ = density
σ = surface tension

$Pr \equiv \nu/\alpha$ Prandtl no.

$Re \equiv v\Lambda/\nu$ Reynolds no.

$Z \equiv (\nu^2\rho/\sigma\Lambda)^{1/2}$ Ohnesorge no.

c_1 to c_6: constants

Table 2 : LDA measurements of turbulence macroscale time (τ) and length ($\Lambda = V'\tau$) in system with diameter of 0.152m at 0.03m beneath the interface

V' (m/s)	$\tau \equiv \int_0^\infty R(t)dt$ (s)	$\Lambda = V'\tau$ (m)
Horizontal components:		
0.062	0.58	0.0360
0.082	0.44	0.0363
0.116	0.34	0.0393
0.160	0.24	0.0283
Vertical components:		
0.062	0.58	0.0360
0.088	0.42	0.0370
0.131	0.31	0.0405
0.191	0.20	0.0382
Average Λ = 0.0365 m = 0.24 D		

Table 3: Operating conditions of the experiment.

Bulk water temperature ^{o}C	40	29	23	25 *
$\nu \times 10^{6}$ m^2/s	0.6529	0.8148	0.9325	1.840
$D \times 10^{9}$ m^2/s	2.8	2.18	1.78	1.13
Sc	230	377	525	1600
$C_{sat} \times 10^{2}$ mole/liter	2.407	3.120	3.640	2.630

ν is the kinematic viscosity of the bulk water

D is the diffusivity of CO_2 in the liquid

C_{sat} is saturation condition of CO_2 in the liquid

* water mixed with 21% by volume of glycerol

Table 4: Conditions at the 'break' point

Sc	230	377	525	1600
V_* (m/s) break velocity	0.066	0.068	0.073	0.092
$(Re_\Lambda)_*$ break Reynolds number	3851	3180	2983	1905
$(Re_\Lambda)_* Sc^{0.4}$	33900	34100	36500	36400
Average $(Re_\Lambda)_* Sc^{0.4} \simeq 3.5 \times 10^4$				

Table 5: St vs Sc for $Re_{\Lambda} < (Re_{\Lambda})_*$

Mass Transfer data for $Re_{\Lambda} < (Re_{\Lambda})_*$				
Sc	230	377	525	1600
$St = \frac{dK_L}{dV'}$	0.00060	0.000433	0.00040	0.00025
$StSc^{0.5}$	0.0091	0.0084	0.00916	0.0101
Average $StSc^{0.5} \simeq 0.0092$				

Table 6. Turbulence imposed from within the liquid

Reference	Correlation*	Range of Sc or Pr	Equivalent $(\frac{V'\Lambda}{\nu}Sc^{0.4})_{max}$	Type of Flow
Krenkel et al (1963) Eloubaidy et al (1969)	$StSc^{0.5} \simeq 0.020$ (a)	$Sc \simeq 500$	6.6×10^3	Flow down an inclined channel
Fortescue and Pearson (1967)	$StSc^{0.5} \simeq 0.033$ (d)	$Sc \simeq 570$	6.3×10^3	Grid induced turbulence in an open channel flow
Isenogle (1985) Ho (1987)	$StSc^{0.5} \simeq 0.017$ (b) $StSc^{0.5} \simeq 0.016$ (a)	$150 < Sc < 1050$ $Sc \sim 500$	1.04×10^4 3.1×10^3	Submerged oscillating grid
Thomas (1979) Orridge (1970)	$StPr^{0.5} \simeq 0.010$ (b) $StSc^{0.5} \simeq 0.004$ (b)	$Pr < 2.0$ $200 < Sc < 570$	1.4×10^4 8.2×10^3	Vertical jet in a large vessel
Kishinevsky and Serebryansky (1956)	$St \simeq 0.005$ (d)	$300 < Sc < 600$	5.4×10^4 (H_2) 6.6×10^4 (O_2) 7.1×10^4 (N_2)	Submerged mechanical stirrer operating at 1700 r.p.m.

* The letter indicates the classification of our "best estimate" of the uncertainty in the deduction of St from the given data. In most cases, the uncertainty comes from the estimation of V', which is classified as below

(a) 25%

(b) 50%

(c) 100%

(d) 200%

Table 7. Turbulence imposed via surface shear at the interface

Reference	Correlation*	Range of Sc or Pr	Equivalent $(\frac{V'\Lambda}{\nu}Sc^{0.4})_{max}$ or $(\frac{V'\Lambda}{\nu}Sc^{0.4})_{break}$ **	Source of surface shear
Jensen & Yuen (1982)	$StPr^{0.5} \simeq 0.050$ (a)	$Pr \simeq 6.2$	3.1×10^4	Cocurrent steam flow
Aisa et al (1981)	$StSc^{0.5} \simeq 0.034$ (b)	$400 < Sc < 750$	4.0×10^4	Cocurrent gas flow
McGready et al (1984)	$StSc^{0.5} \simeq 0.035$ (b)	$Sc \simeq 440$	3.3×10^4	
Sivakumar (1984)	$StSc^{0.5} \simeq 0.016$ (c)	$Sc \simeq 550$	2.5×10^4 (break)	Wind (in linear water tunnel)
Merlivat et al (1983)	$StSc^{0.5} \simeq 0.050$ (c)	$600 < Sc < 700$	1.6×10^4 (break)	
Deacon (1977)	$StSc^{0.67} \simeq 0.027$ (c)	$200 < Sc < 5000$	——	
Jahne et al (1979)	$StSc^{0.5} \simeq 0.007$ (c)	$600 < Sc < 1500$	1.5×10^4 (break)	Wind (in circular water tunnel with unlimited fetch

* caption as in Table 6

** The typical uncertainty in evaluating Λ for computing $(\frac{V'\Lambda}{\nu}Sc^{0.4})_{break}$ is order 100% to 200%

Table 8 : Parameters associated with case A and case B

	Case A	Case B
Re_b	1000.0	100.0
Pr	1.0,1.5,2.2,3.15	3.15,10.0,50.0
l_s/Λ	0.111	0.625
$(\delta/\Lambda)_{smallest}$	0.0362	0.0585
grid arrangement	fig. 6.4.1	fig. 6.4.2
$\alpha_{art}(z)/\alpha$	fig. 6.3.2	fig. 6.3.3
computational domain	Λ X Λ X Λ	Λ X Λ X Λ

Table 9 : St vs Pr for Case A

Pr	$St=K_L/V'$	
	Computed	Extrapolated from Experiment
1.0	0.0185	0.0215
1.5	0.0159	0.0188
2.2	0.01375	0.0165
3.15	0.01212	0.0146

Table 10 : St vs Pr for Case B

Pr	$St=K_L/V'$	
	Computed	Extrapolated from Experiment
3.15	0.0158	0.0147
10.0	0.0101	0.0100
50.0	0.0046	0.0058

APPARATUS FOR MASS TRANSFER

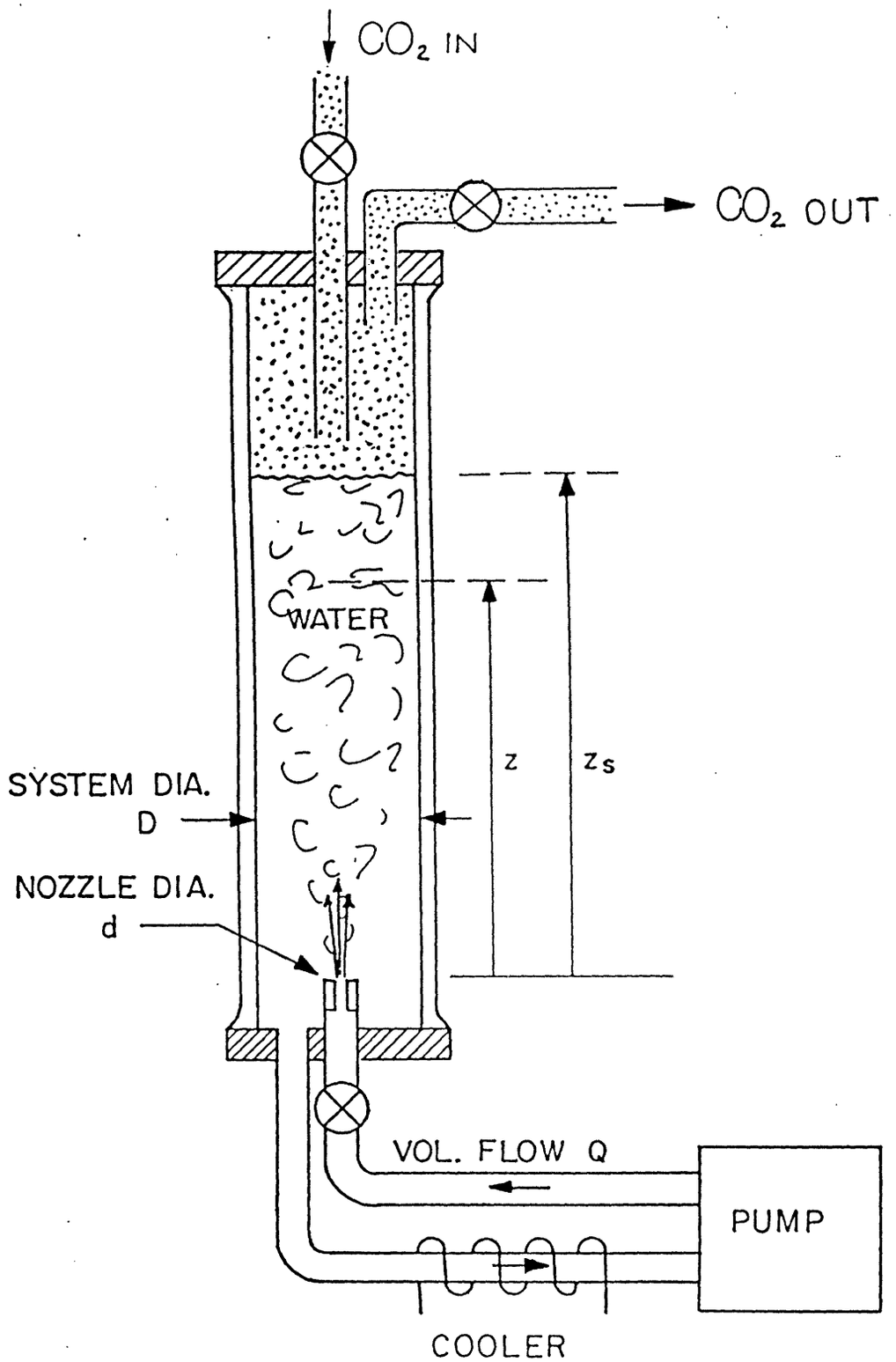

Figure 3.1.1

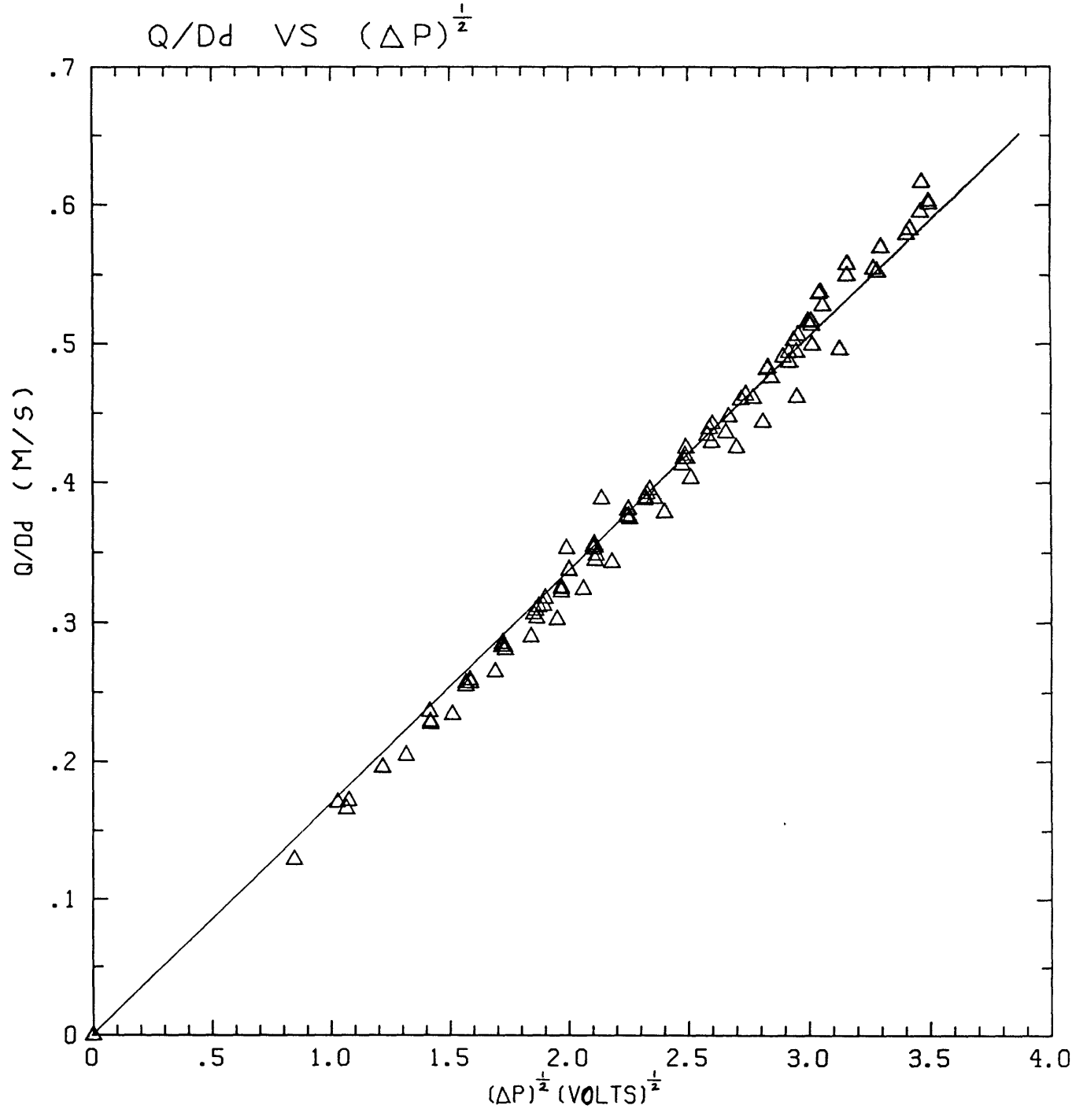

Figure 3.1.2

CYLINDRICAL SECTION FOR LDA

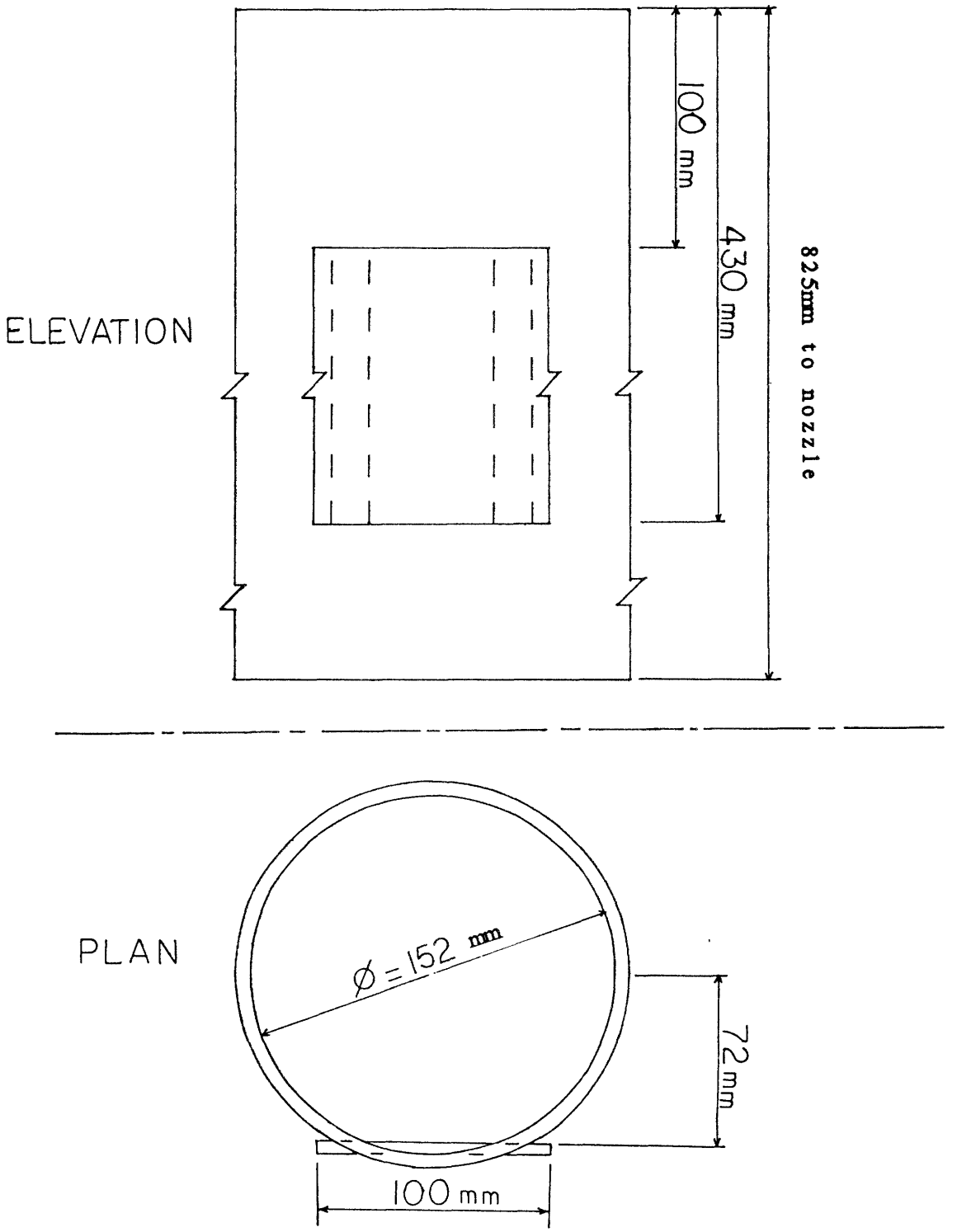

Figure 3.2.1

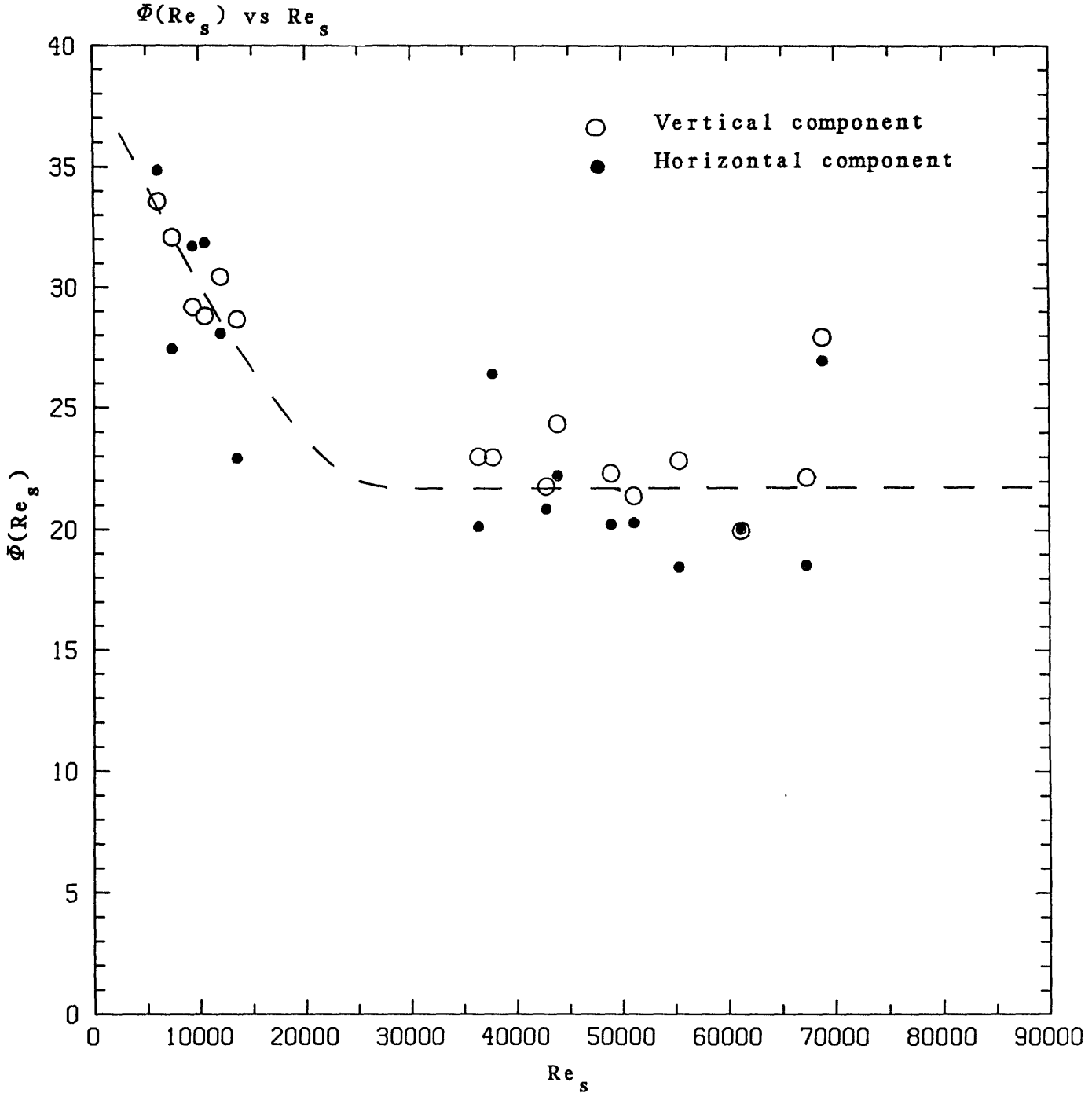
$\Phi(Re_s)$ vs Re_s
Vertical component
Horizontal component
$\Phi(Re_s)$
Re_s
0
5
10
15
20
25
30
35
40
0
10000
20000
30000
40000
50000
60000
70000
80000
90000

Figure 3.3.1

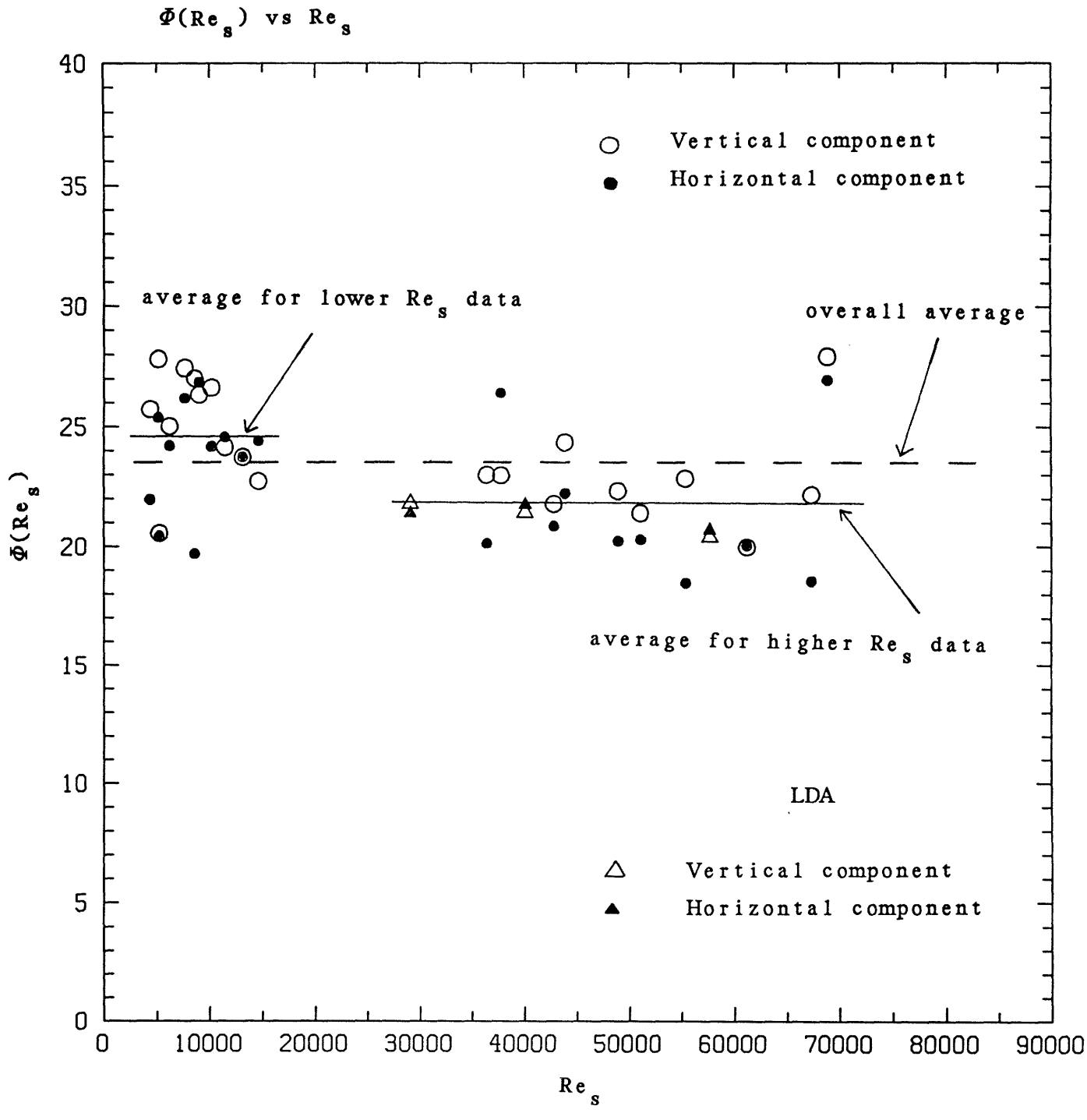
Φ(Re s) vs Re s
Vertical component
Horizontal component
average for lower Re s data
overall average
average for higher Re s data
LDA
Vertical component
Horizontal component
Φ(Re s)
Re s
0
5
10
15
20
25
30
35
40
0
10000
20000
30000
40000
50000
60000
70000
80000
90000

Figure 3.3.2

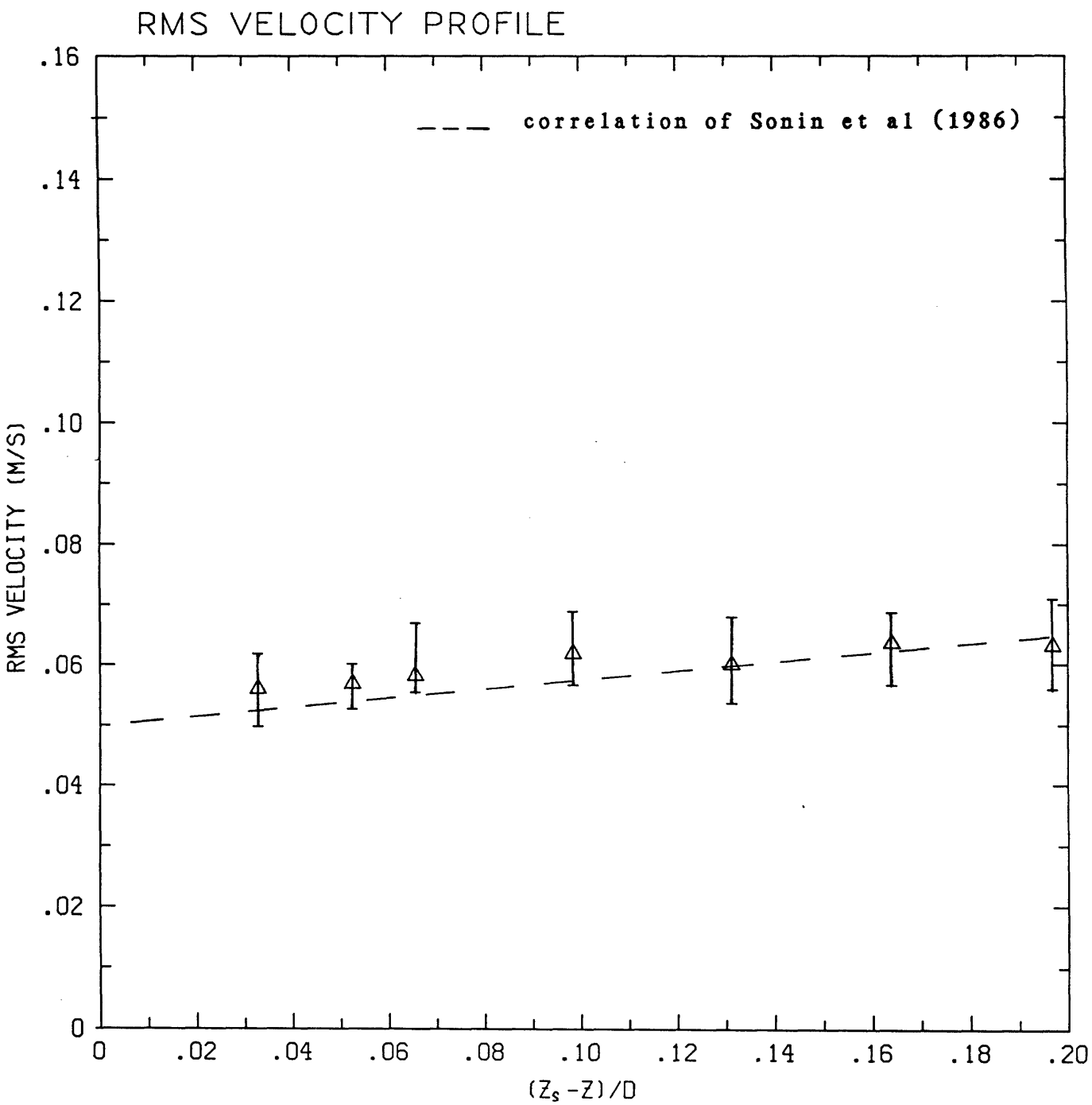
RMS VELOCITY PROFILE
correlation of Sonin et al (1986)
RMS VELOCITY (M/S)
.16
.14
.12
.10
.08
.06
.04
.02
0
0
.02
.04
.06
.08
.10
.12
.14
.16
.18
.20
(Zs -Z)/D

Figure 4.1.1

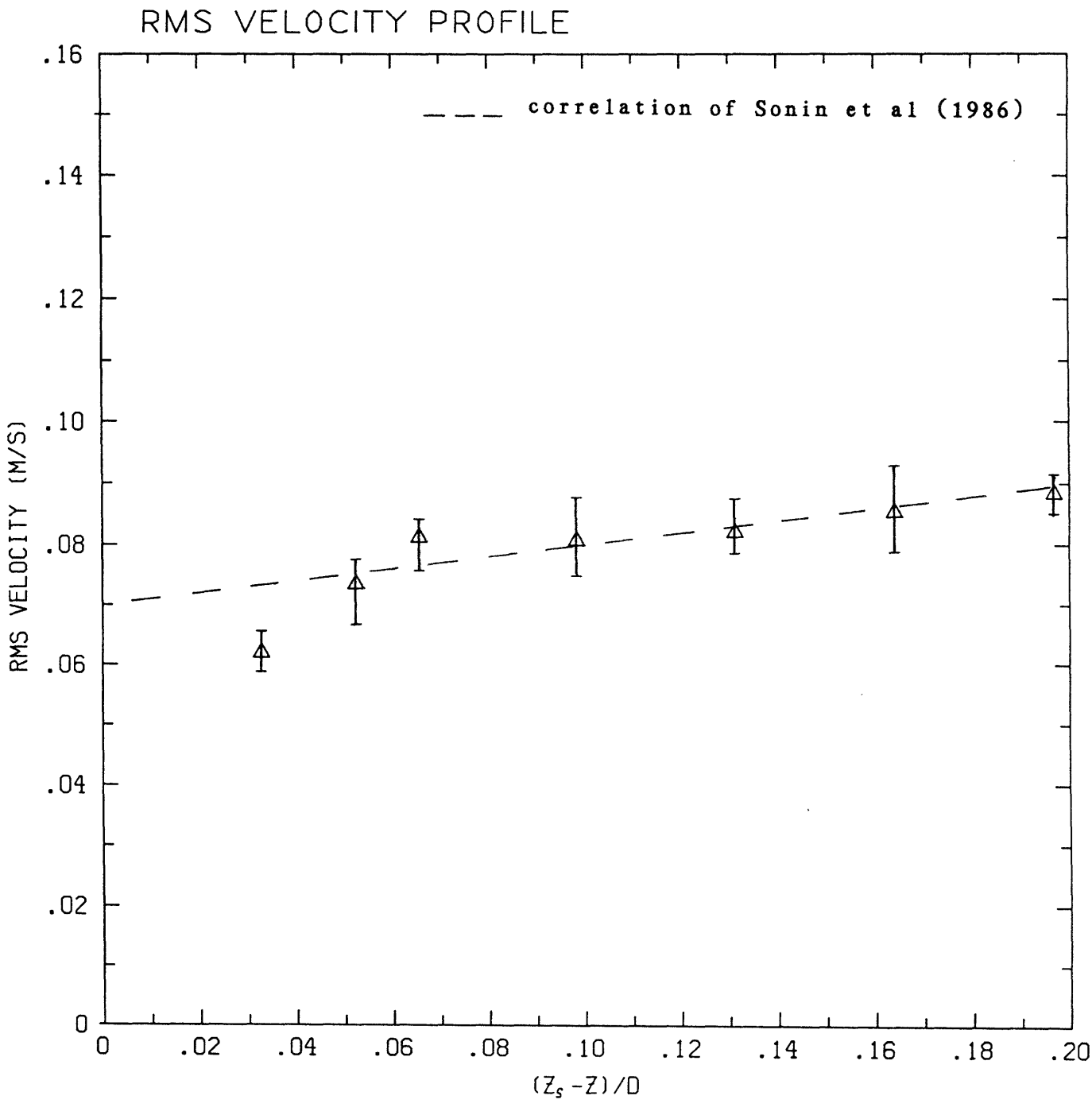
RMS VELOCITY PROFILE
correlation of Sonin et al (1986)
RMS VELOCITY (M/S)
.16
.14
.12
.10
.08
.06
.04
.02
0
0
.02
.04
.06
.08
.10
.12
.14
.16
.18
.20
(Zs -Z)/D

Figure 4.1.2

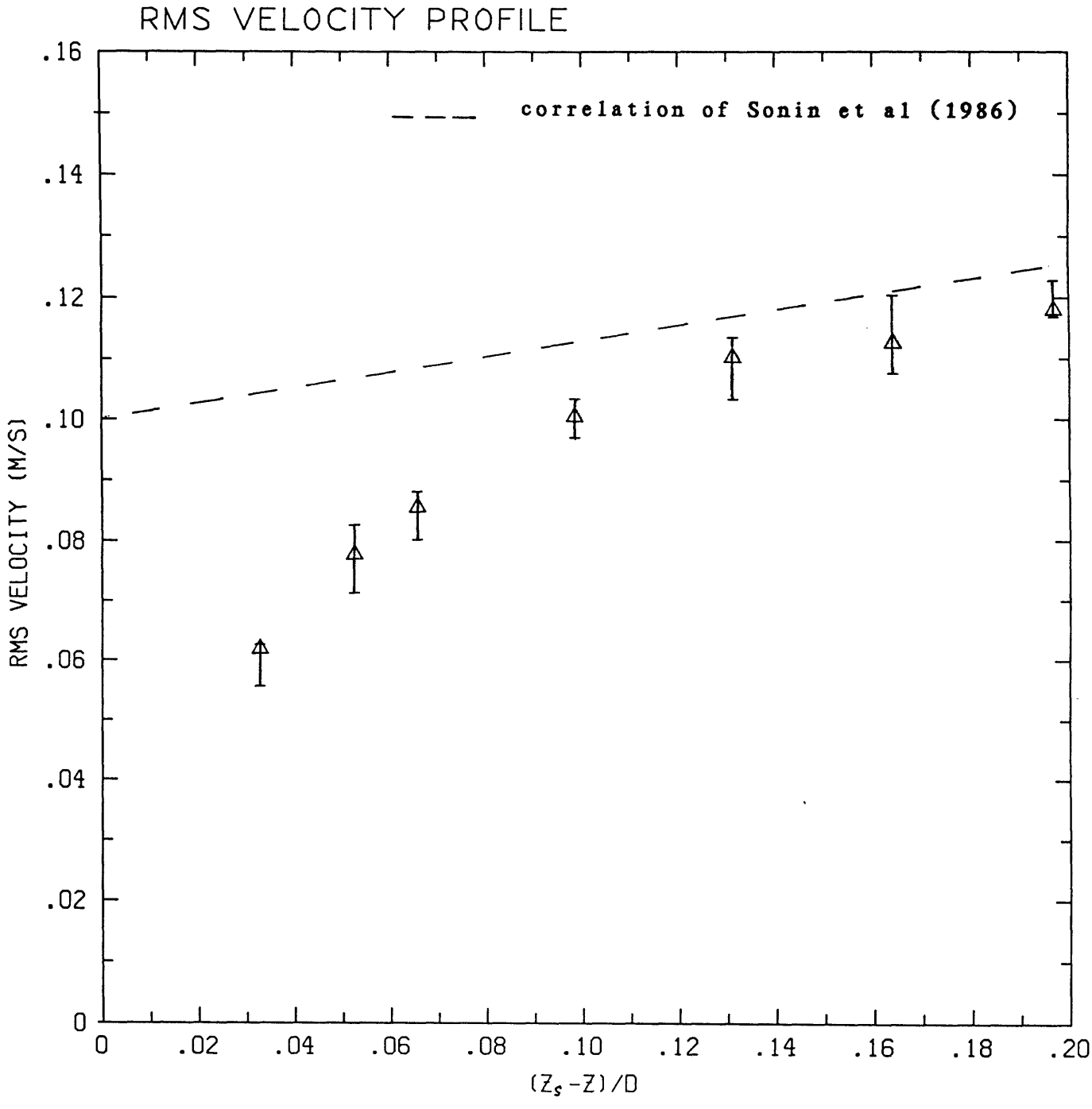
RMS VELOCITY PROFILE
correlation of Sonin et al (1986)
RMS VELOCITY (M/S)
.16
.14
.12
.10
.08
.06
.04
.02
0
0
.02
.04
.06
.08
.10
.12
.14
.16
.18
.20
(Zs-Z)/D

Figure 4.1.3

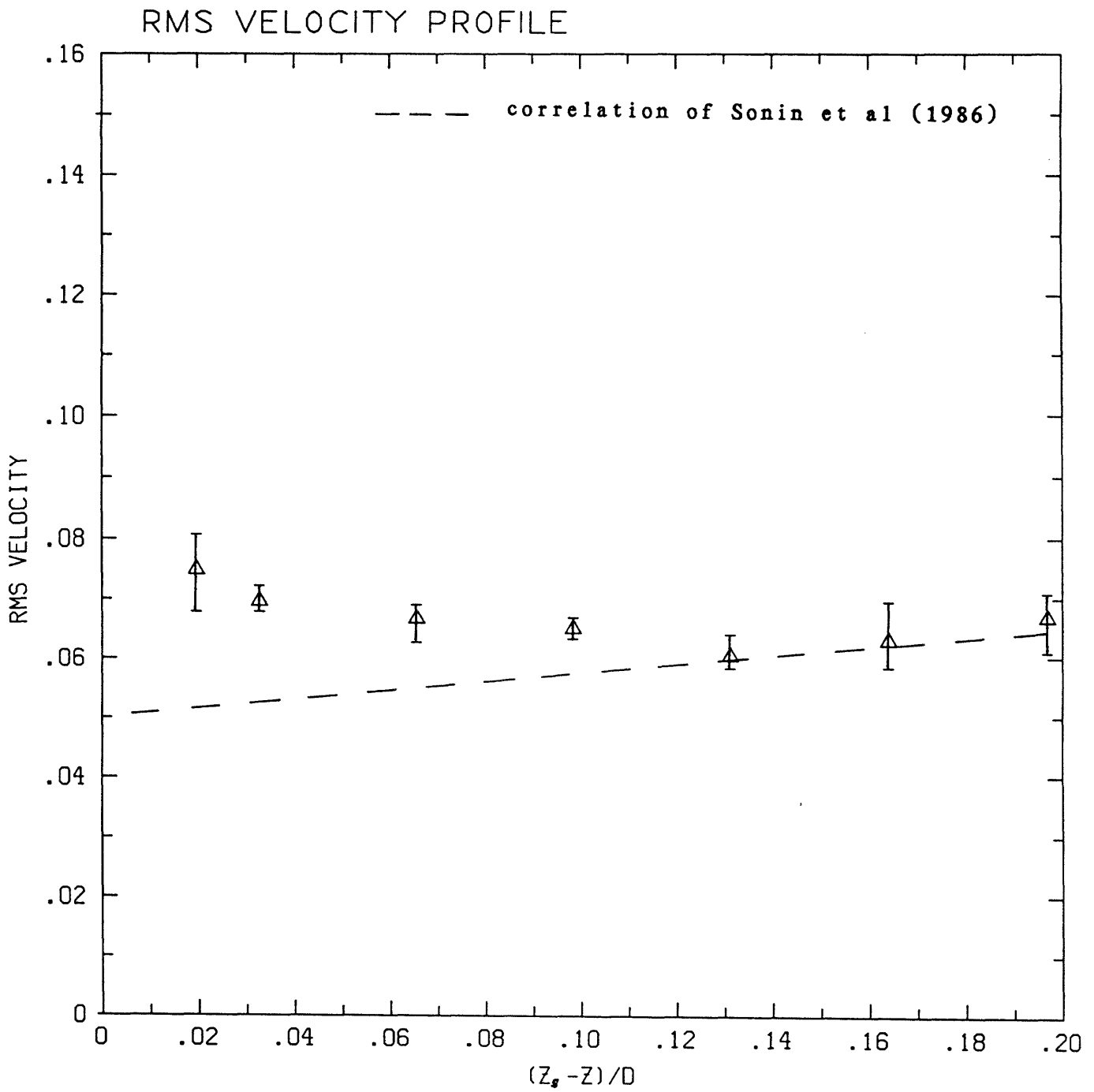
RMS VELOCITY PROFILE
correlation of Sonin et al (1986)
RMS VELOCITY
.16
.14
.12
.10
.08
.06
.04
.02
0
0
.02
.04
.06
.08
.10
.12
.14
.16
.18
.20
(Z_s -Z)/D

Figure 4.1.4

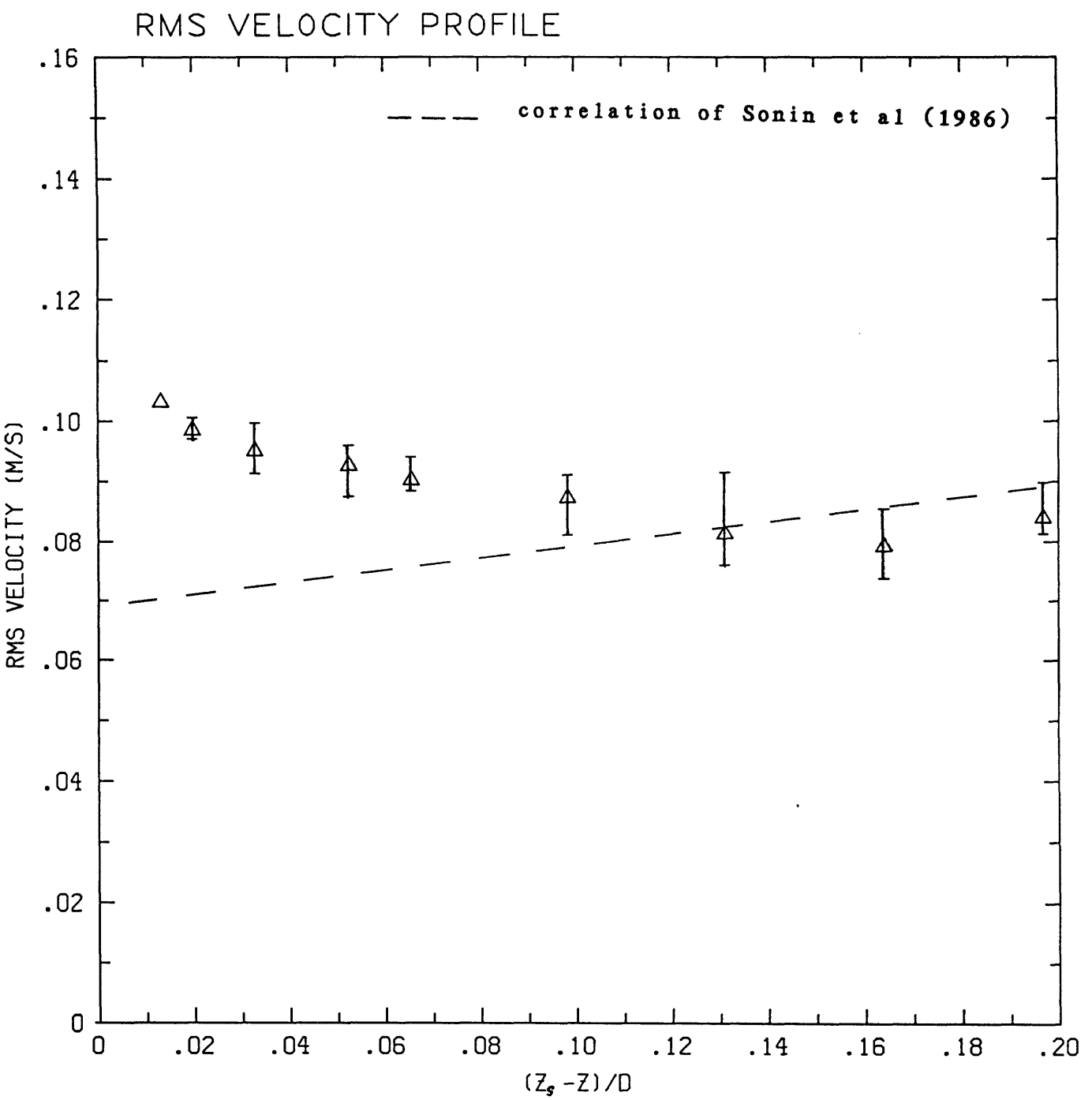
RMS VELOCITY PROFILE
correlation of Sonin et al (1986)
RMS VELOCITY (M/S)
.16
.14
.12
.10
.08
.06
.04
.02
0
0
.02
.04
.06
.08
.10
.12
.14
.16
.18
.20
(Zs -Z)/D

Figure 4.1.5

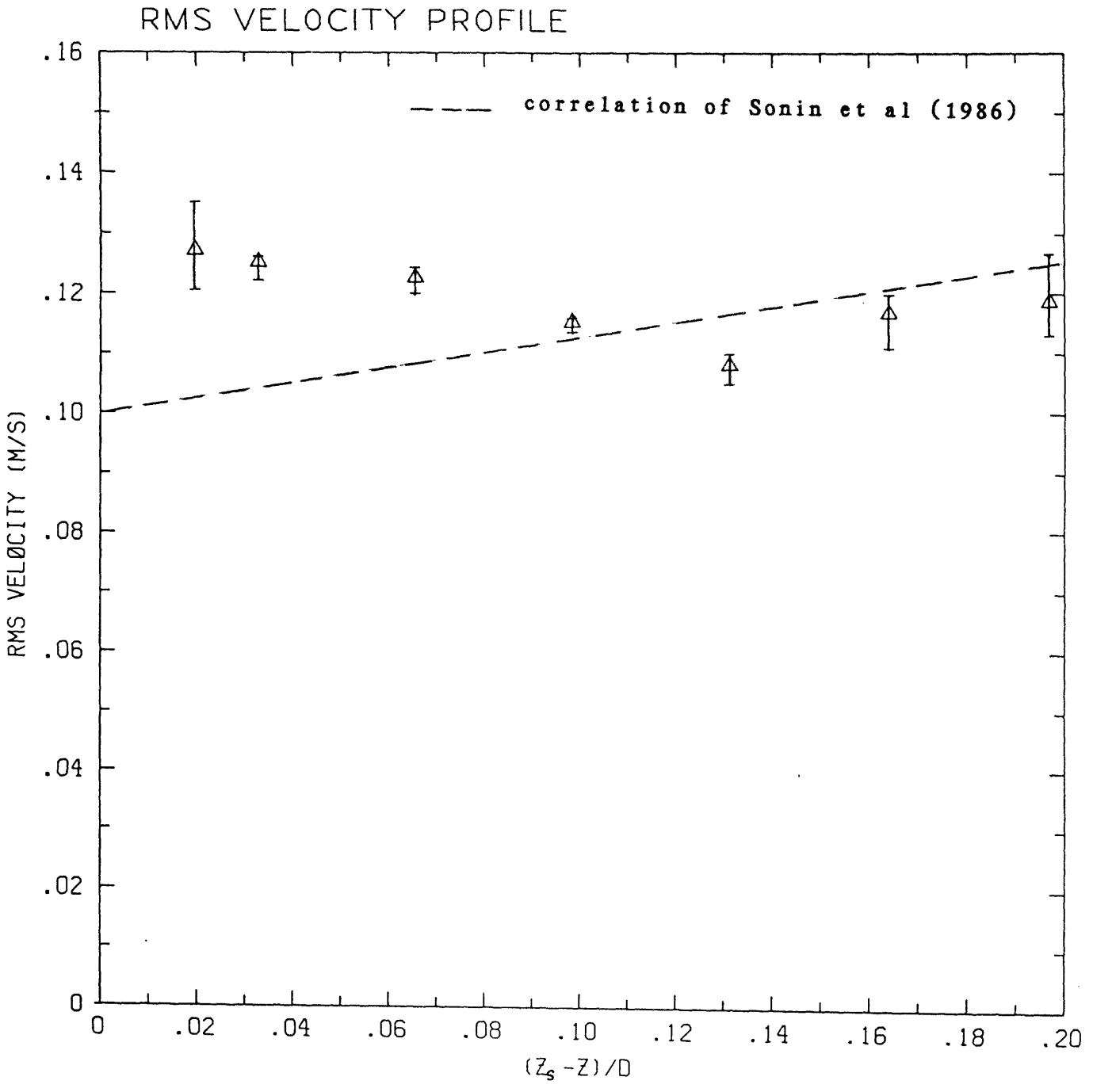
RMS VELOCITY PROFILE
correlation of Sonin et al (1986)
RMS VELOCITY (M/S)
.16
.14
.12
.10
.08
.06
.04
.02
0
0
.02
.04
.06
.08
.10
.12
.14
.16
.18
.20
(Zs -Z)/D

Figure 4.1.6

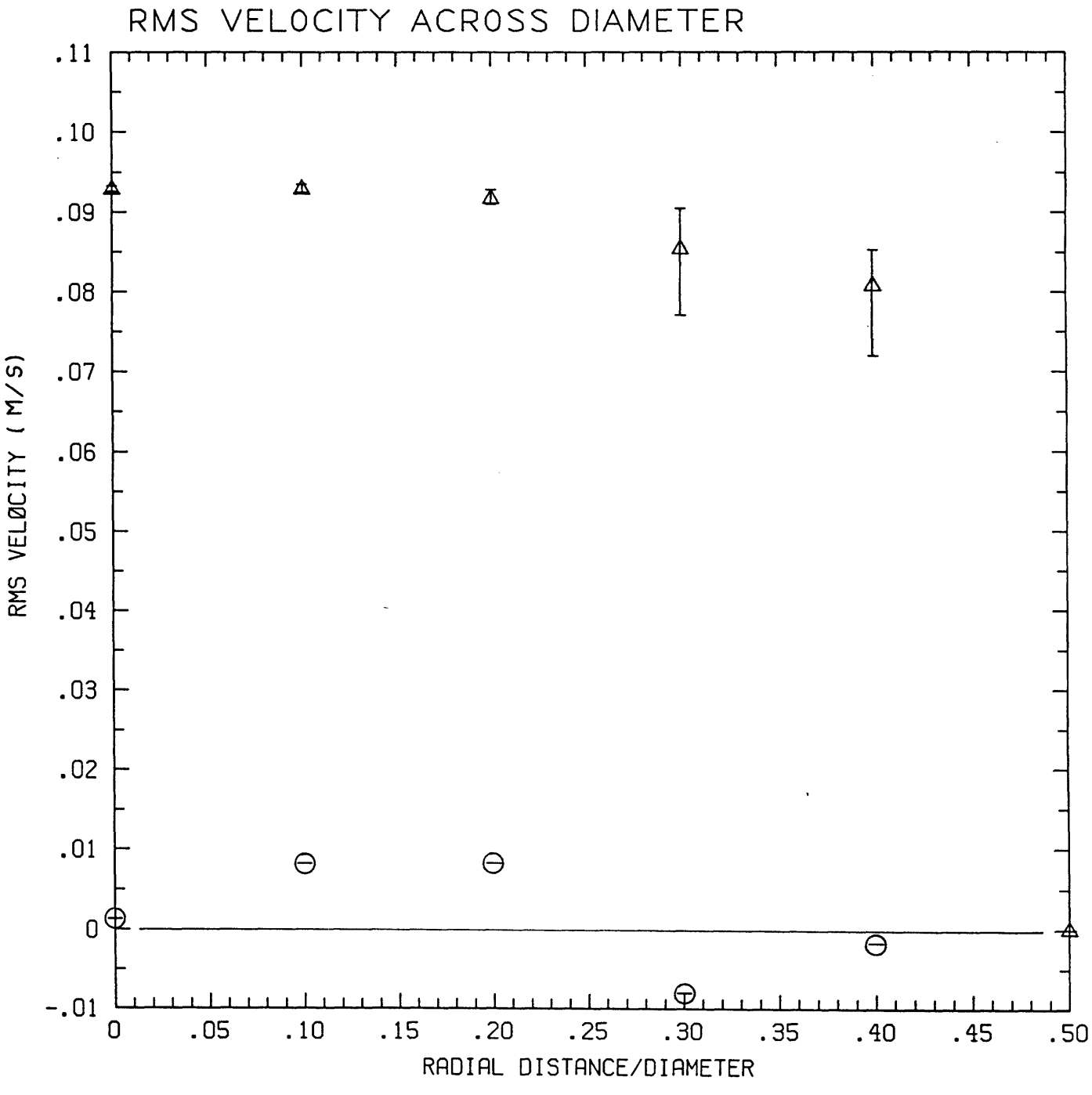
RMS VELOCITY ACROSS DIAMETER
RMS VELØCITY (M/S)
.11
.10
.09
.08
.07
.06
.05
.04
.03
.02
.01
0
-.01
0
.05
.10
.15
.20
.25
.30
.35
.40
.45
.50
RADIAL DISTANCE/DIAMETER

Figure 4.1.7

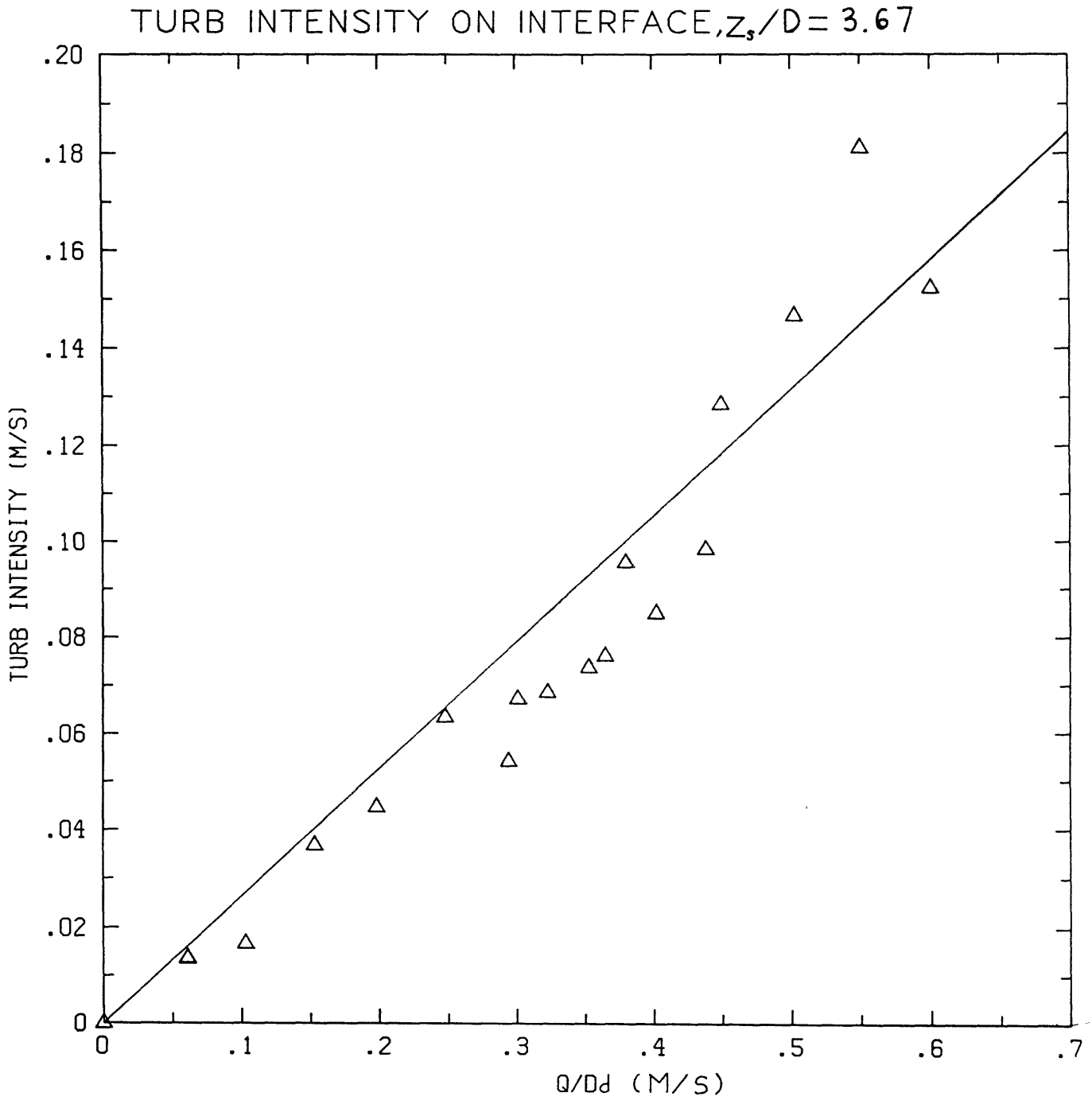
TURB INTENSITY ON INTERFACE, $Z_s/D = 3.67$
TURB INTENSITY (M/S)
.20
.18
.16
.14
.12
.10
.08
.06
.04
.02
0
0
.1
.2
.3
.4
.5
.6
.7
Q/Dd (M/S)

Figure 4.1.8

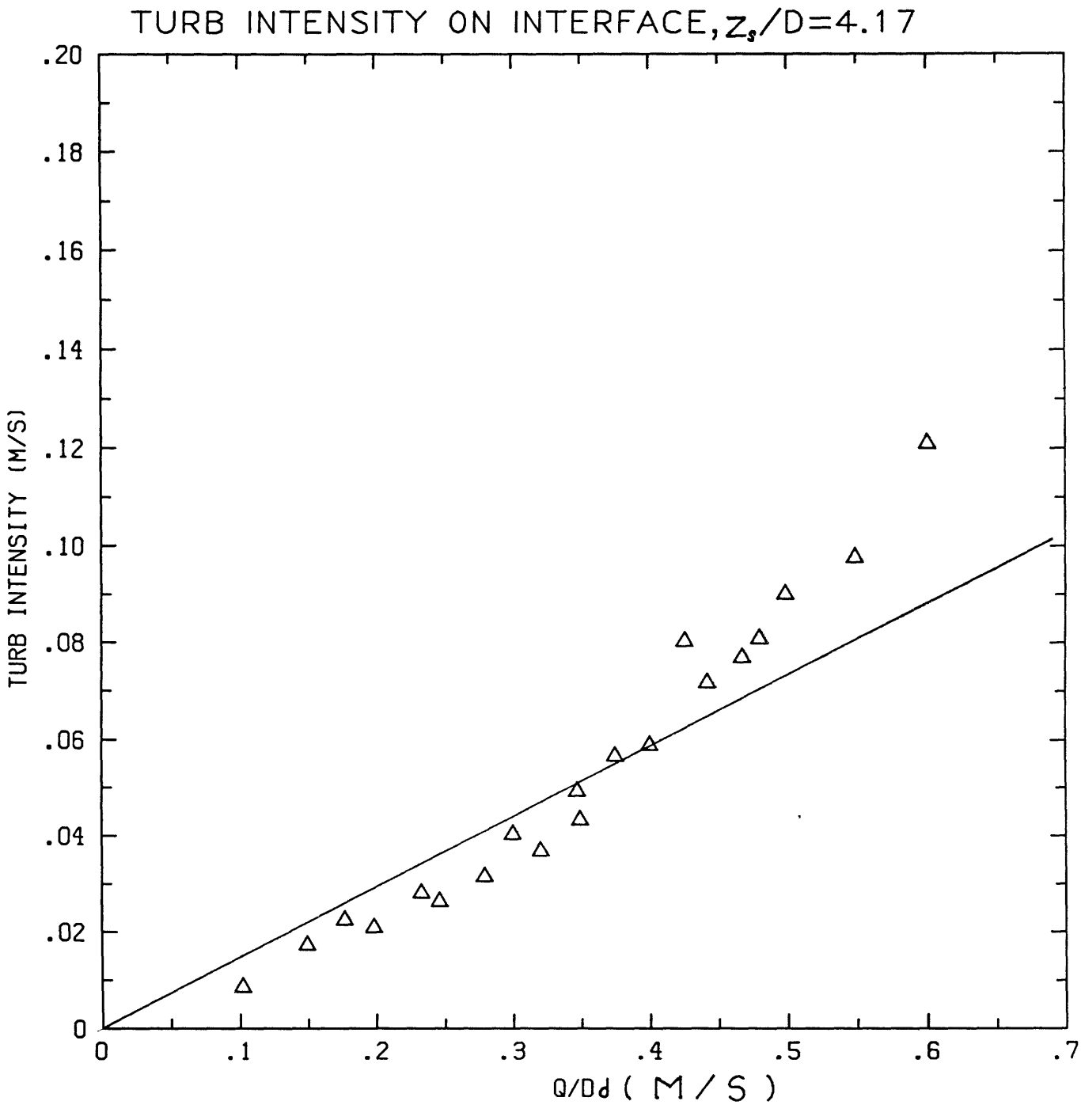
TURB INTENSITY ON INTERFACE, $Z_s/D=4.17$
TURB INTENSITY (M/S)
.20
.18
.16
.14
.12
.10
.08
.06
.04
.02
0
0
.1
.2
.3
.4
.5
.6
.7
Q/Dd (M / S)

Figure 4.1.9

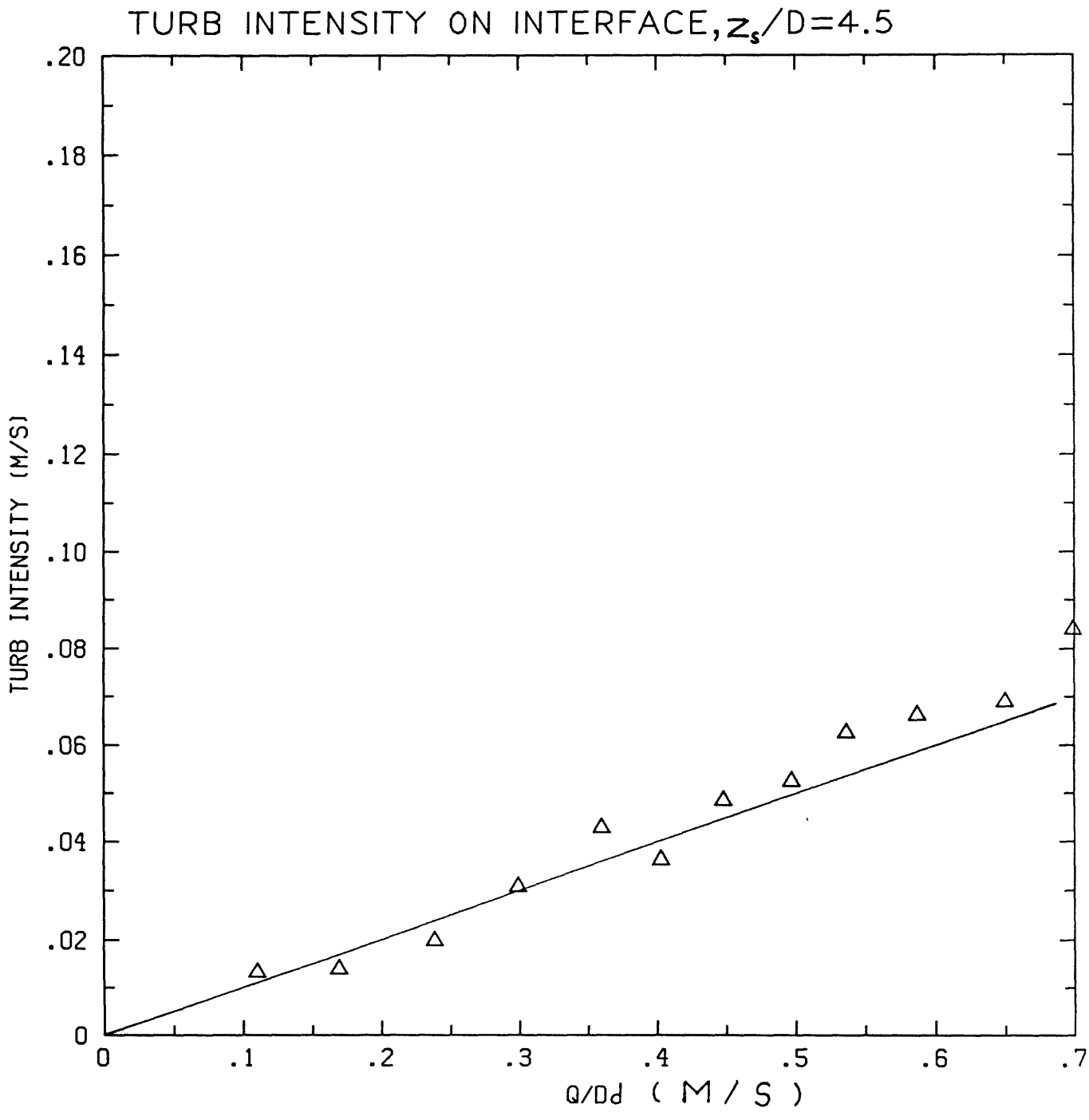
TURB INTENSITY ON INTERFACE, $z_s/D=4.5$
TURB INTENSITY (M/S)
.20
.18
.16
.14
.12
.10
.08
.06
.04
.02
0
0
.1
.2
.3
.4
.5
.6
.7
Q/Dd (M / S)

Figure 4.1.10

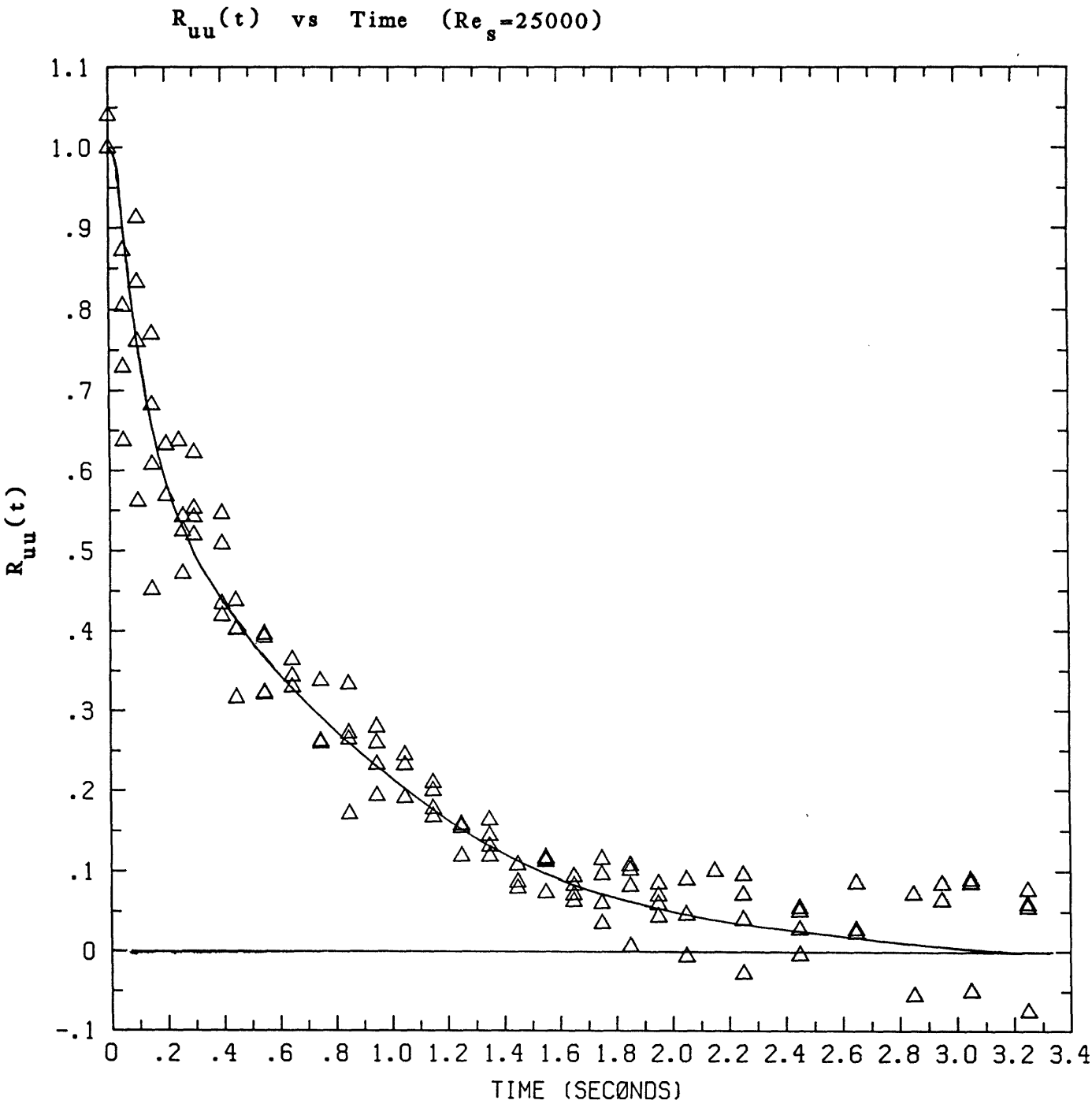
$R_{uu}(t)$ vs Time (Re_s=25000)
1.1
1.0
.9
.8
.7
.6
.5
.4
.3
.2
.1
0
-.1
$R_{uu}(t)$
0 .2 .4 .6 .8 1.0 1.2 1.4 1.6 1.8 2.0 2.2 2.4 2.6 2.8 3.0 3.2 3.4
TIME (SECØNDS)

Figure 4.1.11

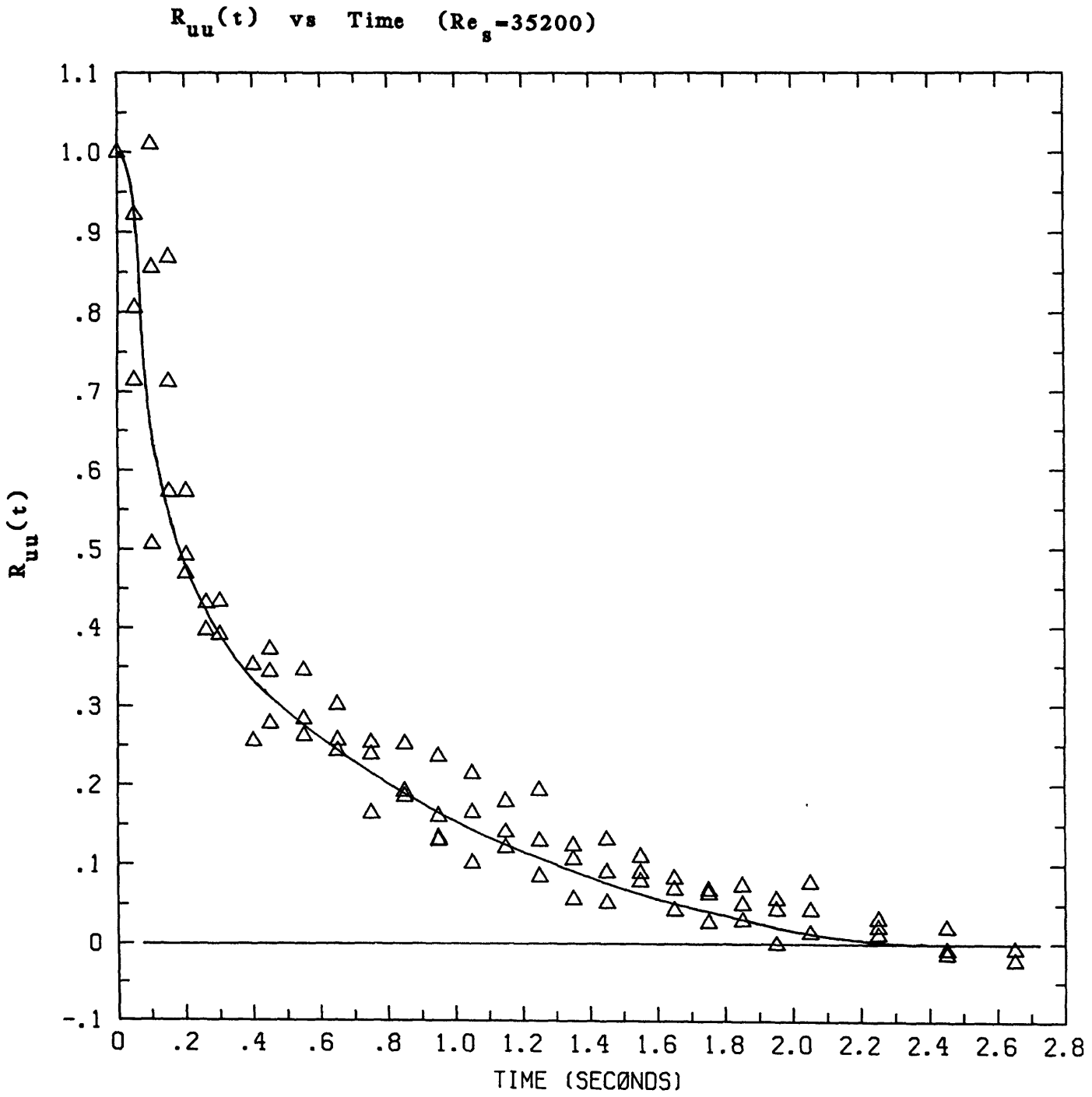
$R_{uu}(t)$ vs Time (Re_s=35200)
1.1
1.0
.9
.8
.7
.6
.5
.4
.3
.2
.1
0
-.1
$R_{uu}(t)$
0
.2
.4
.6
.8
1.0
1.2
1.4
1.6
1.8
2.0
2.2
2.4
2.6
2.8
TIME (SECØNDS)

Figure 4.1.12

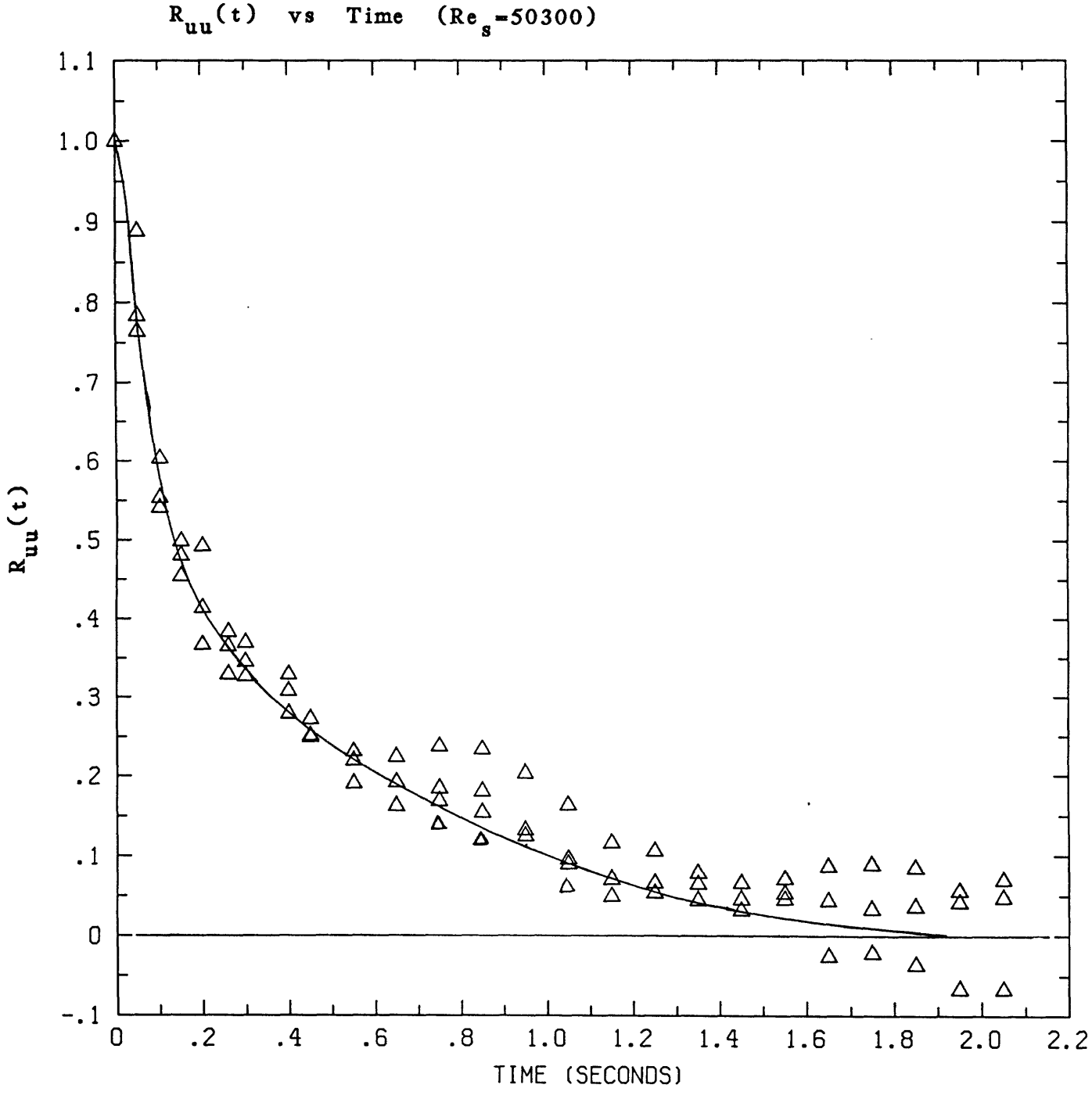
$R_{uu}(t)$ vs Time (Re_s=50300)
1.1
1.0
.9
.8
.7
.6
.5
.4
.3
.2
.1
0
-.1
$R_{uu}(t)$
0
.2
.4
.6
.8
1.0
1.2
1.4
1.6
1.8
2.0
2.2
TIME (SECONDS)

Figure 4.1.13

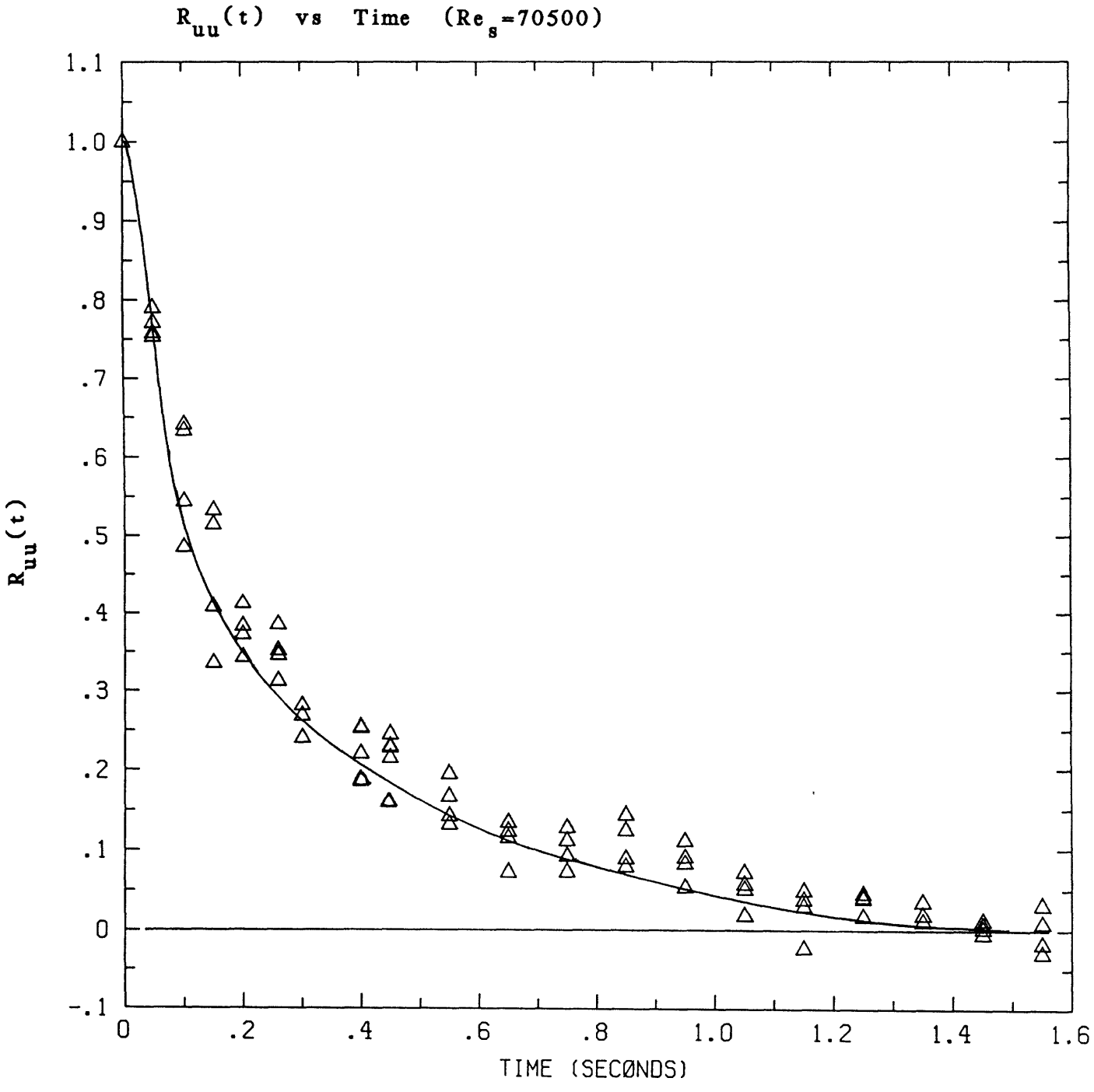
$R_{uu}(t)$ vs Time (Re_s=70500)
1.1
1.0
.9
.8
.7
.6
.5
.4
.3
.2
.1
0
-.1
$R_{uu}(t)$
0
.2
.4
.6
.8
1.0
1.2
1.4
1.6
TIME (SECØNDS)

Figure 4.1.14

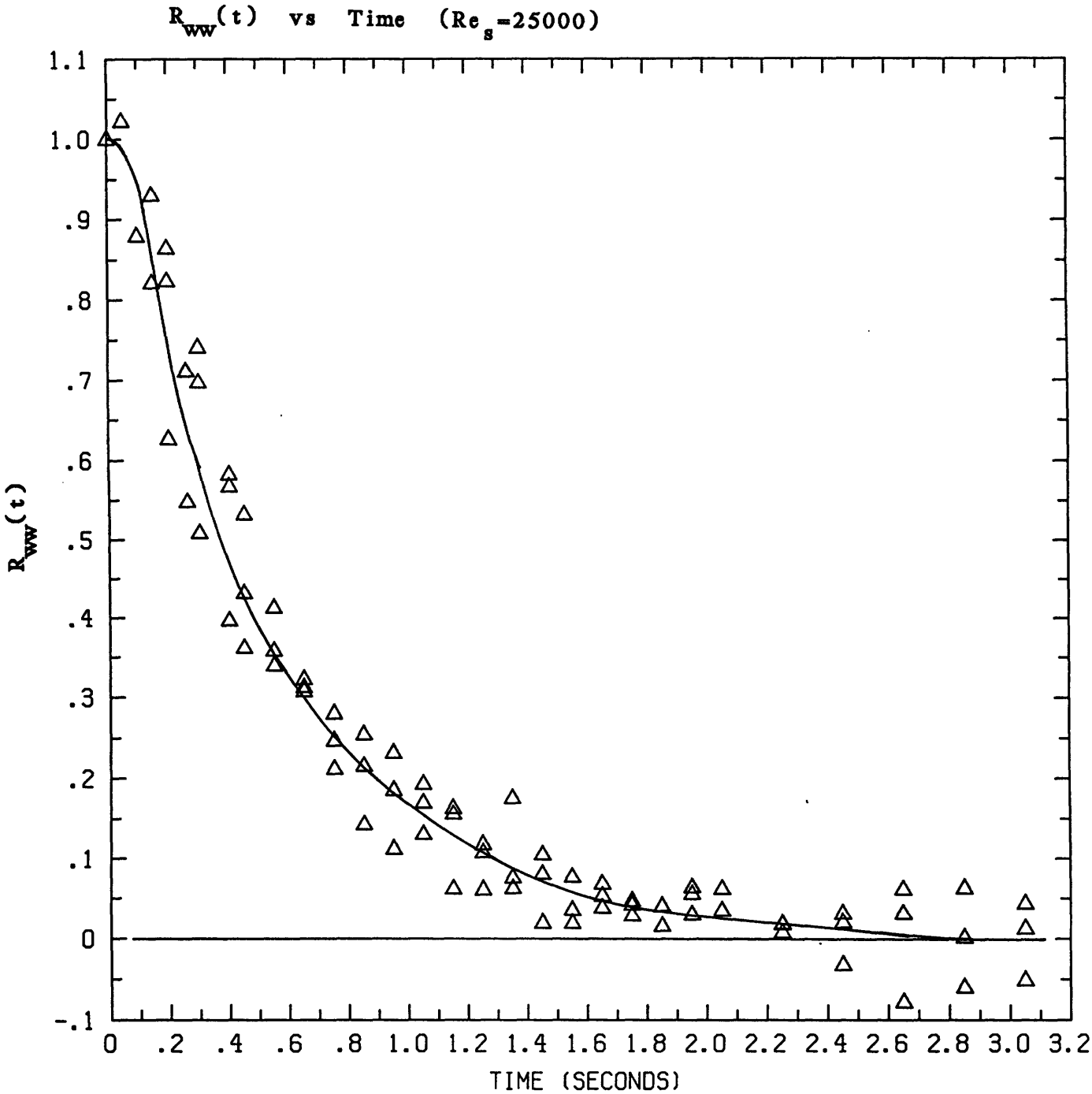
$R_{ww}(t)$ vs Time (Re_s=25000)
1.1
1.0
.9
.8
.7
.6
.5
.4
.3
.2
.1
0
-.1
$R_{ww}(t)$
0 .2 .4 .6 .8 1.0 1.2 1.4 1.6 1.8 2.0 2.2 2.4 2.6 2.8 3.0 3.2
TIME (SECONDS)

Figure 4.1.15

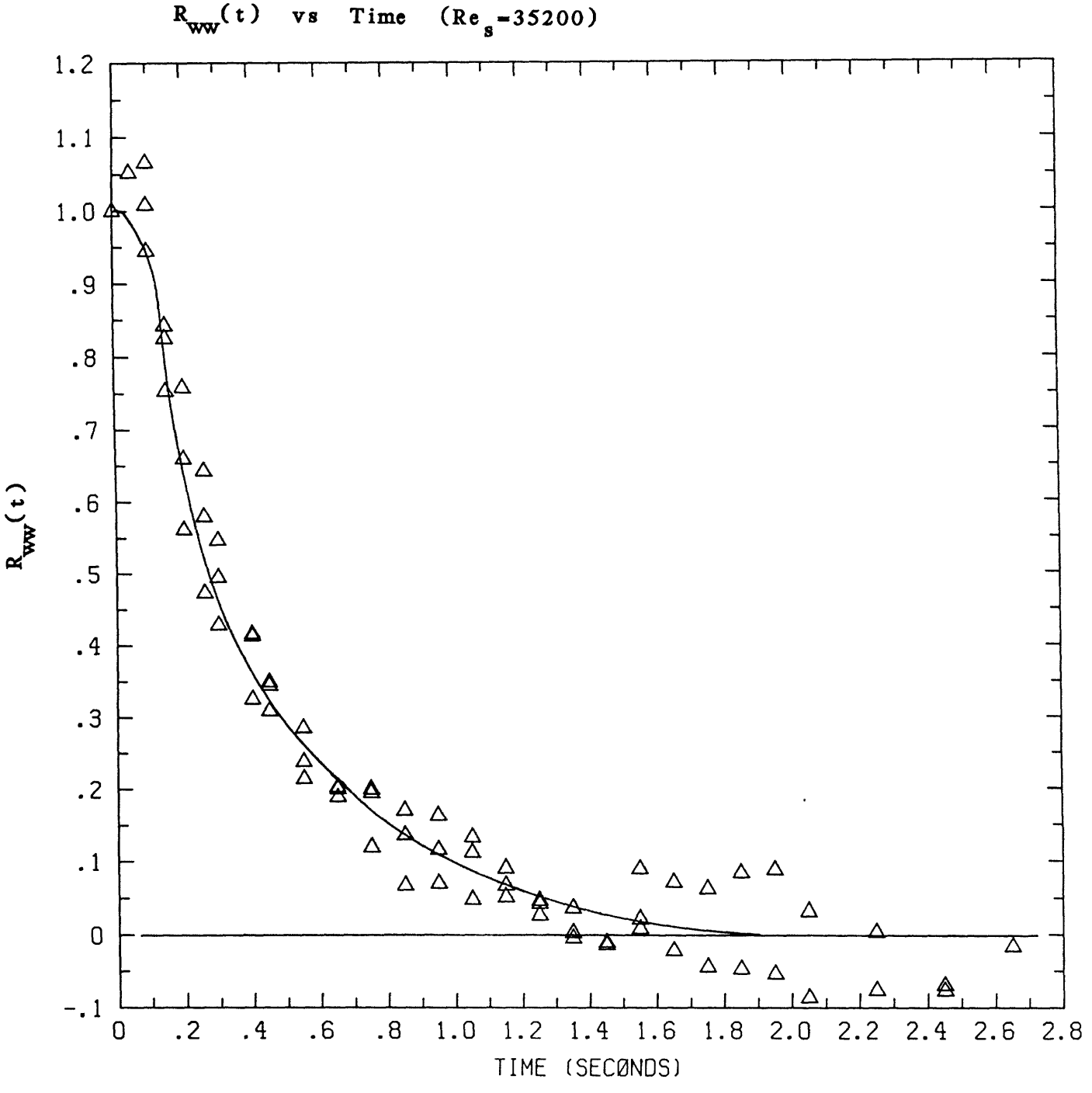
$R_{ww}(t)$ vs Time (Re_s=35200)
1.2
1.1
1.0
.9
.8
.7
.6
.5
.4
.3
.2
.1
0
-.1
$R_{ww}(t)$
0
.2
.4
.6
.8
1.0
1.2
1.4
1.6
1.8
2.0
2.2
2.4
2.6
2.8
TIME (SECØNDS)

Figure 4.1.16

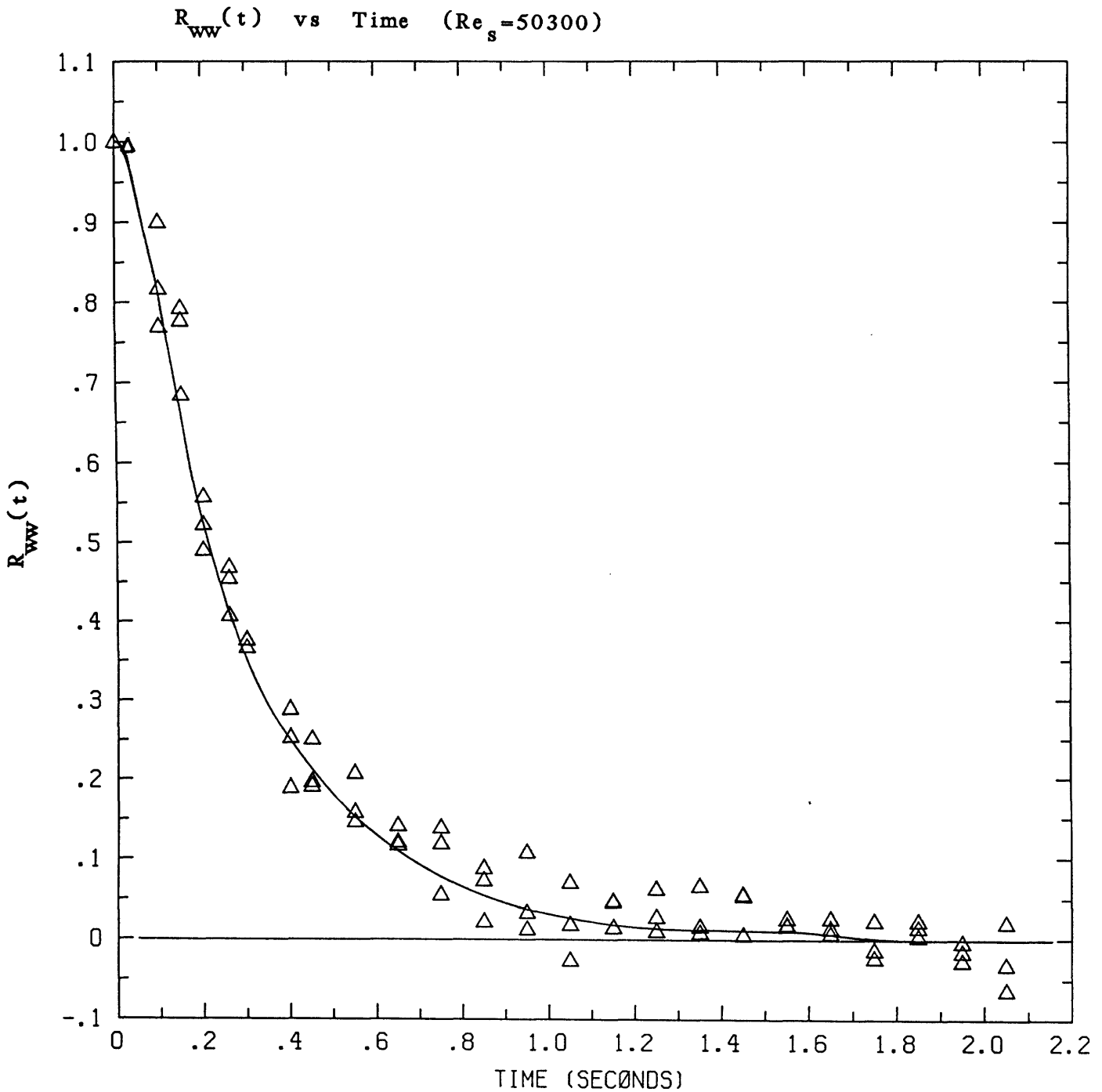
$R_{ww}(t)$ vs Time (Re_s=50300)
1.1
1.0
.9
.8
.7
.6
.5
.4
.3
.2
.1
0
-.1
$R_{ww}(t)$
0
.2
.4
.6
.8
1.0
1.2
1.4
1.6
1.8
2.0
2.2
TIME (SECØNDS)

Figure 4.1.17

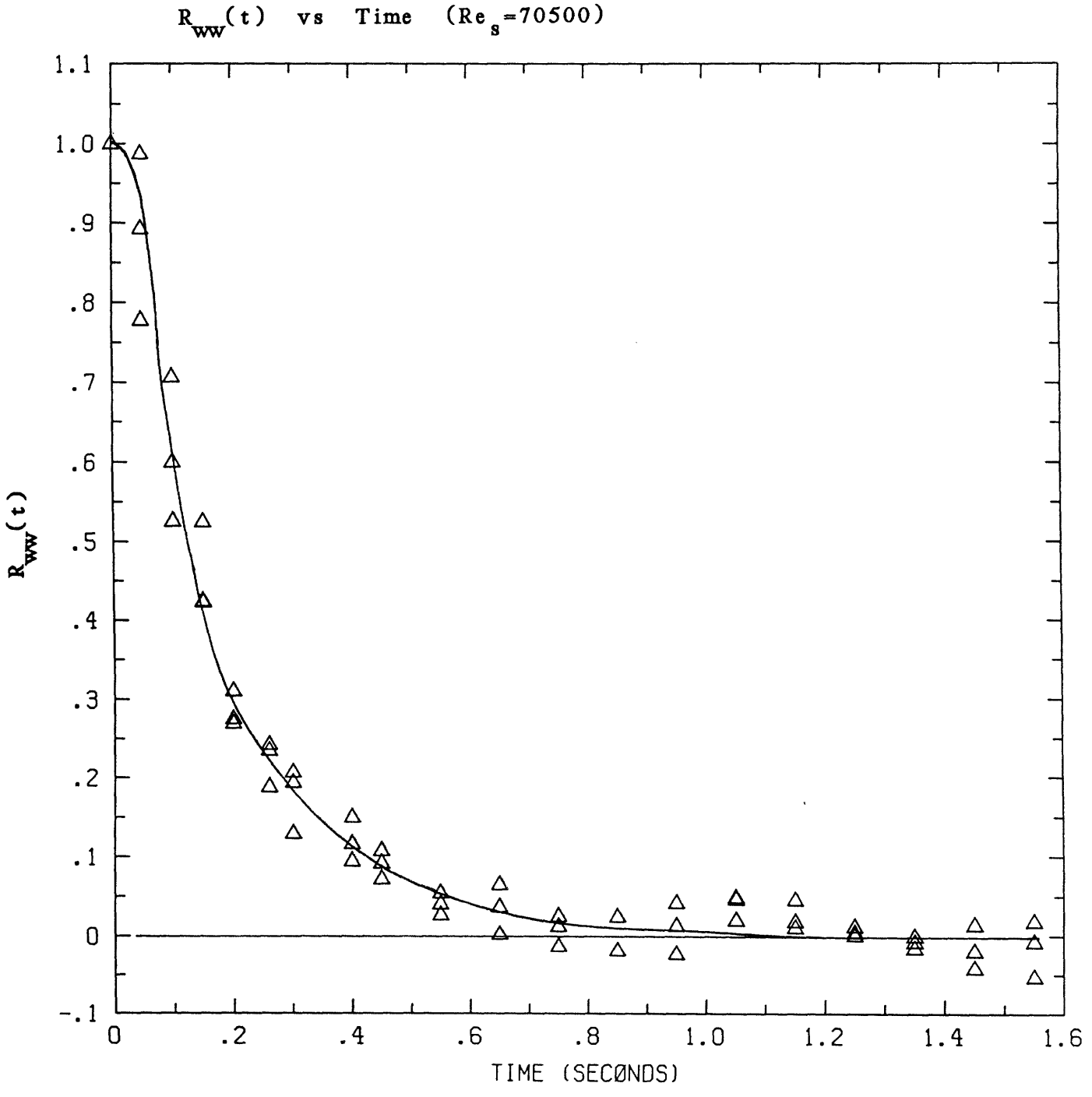
$R_{ww}(t)$ vs Time (Re_s=70500)
1.1
1.0
.9
.8
.7
.6
.5
.4
.3
.2
.1
0
-.1
$R_{ww}(t)$
0
.2
.4
.6
.8
1.0
1.2
1.4
1.6
TIME (SECØNDS)

Figure 4.1.18

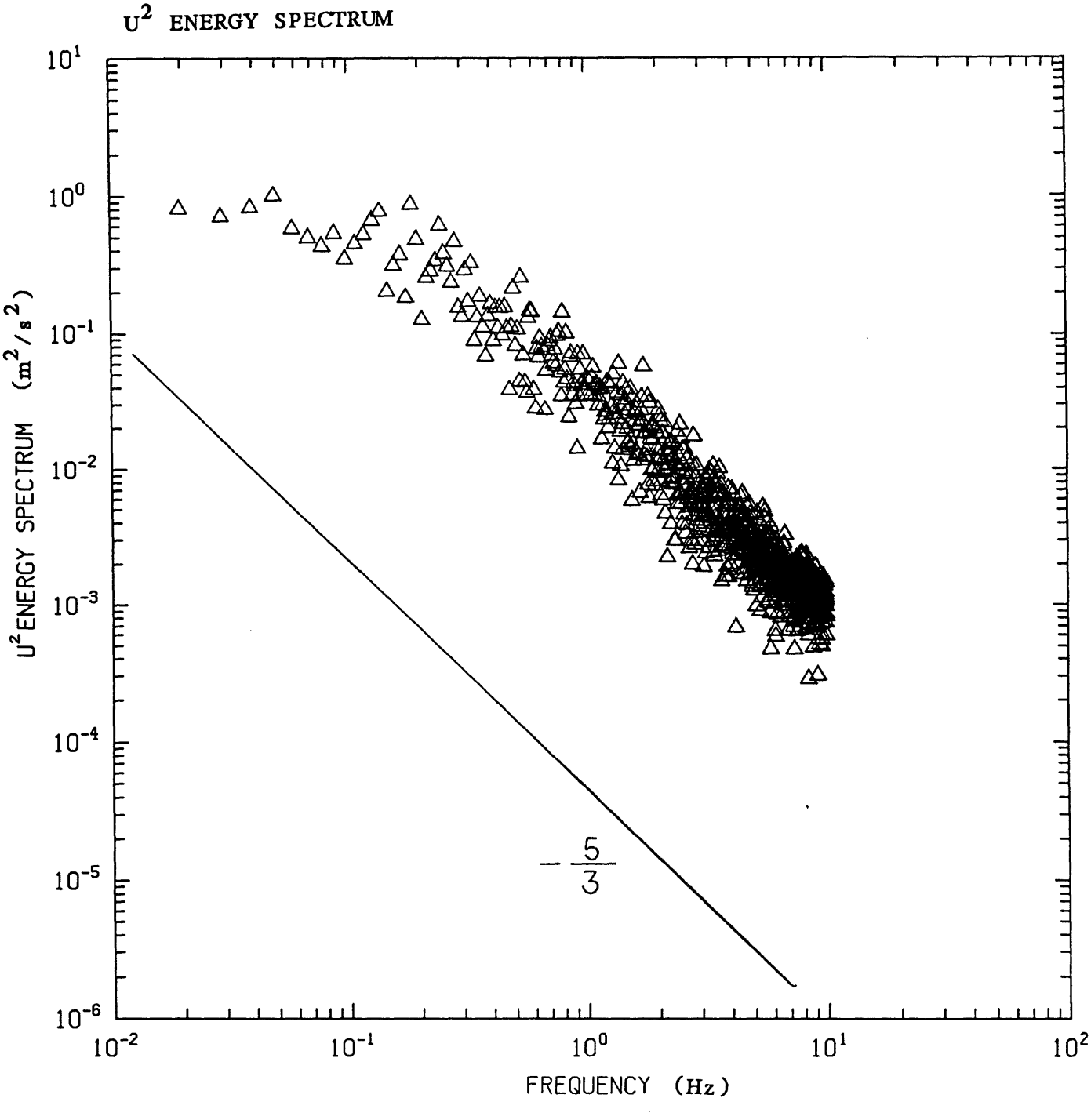
U2 ENERGY SPECTRUM
U2ENERGY SPECTRUM (m2/s2)
FREQUENCY (Hz)
10^1
10^0
10^-1
10^-2
10^-3
10^-4
10^-5
10^-6
10^-2
10^-1
10^0
10^1
10^2
-5/3

Figure 4.1.19

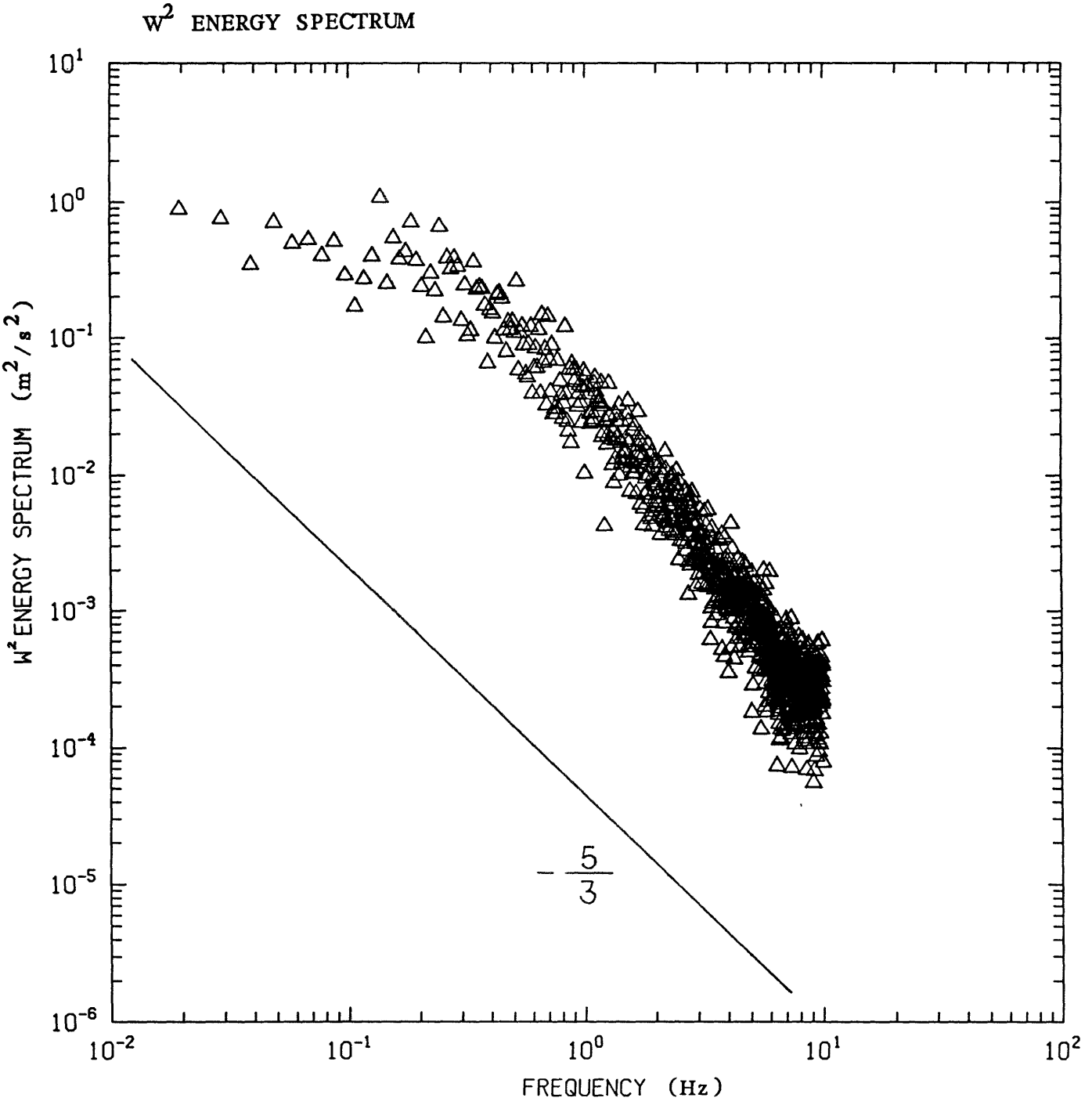
W^2 ENERGY SPECTRUM
W^2 ENERGY SPECTRUM (m^2/s^2)
FREQUENCY (Hz)
10^1
10^0
10^{-1}
10^{-2}
10^{-3}
10^{-4}
10^{-5}
10^{-6}
10^{-2}
10^{-1}
10^0
10^1
10^2
$-\frac{5}{3}$

Figure 4.1.20

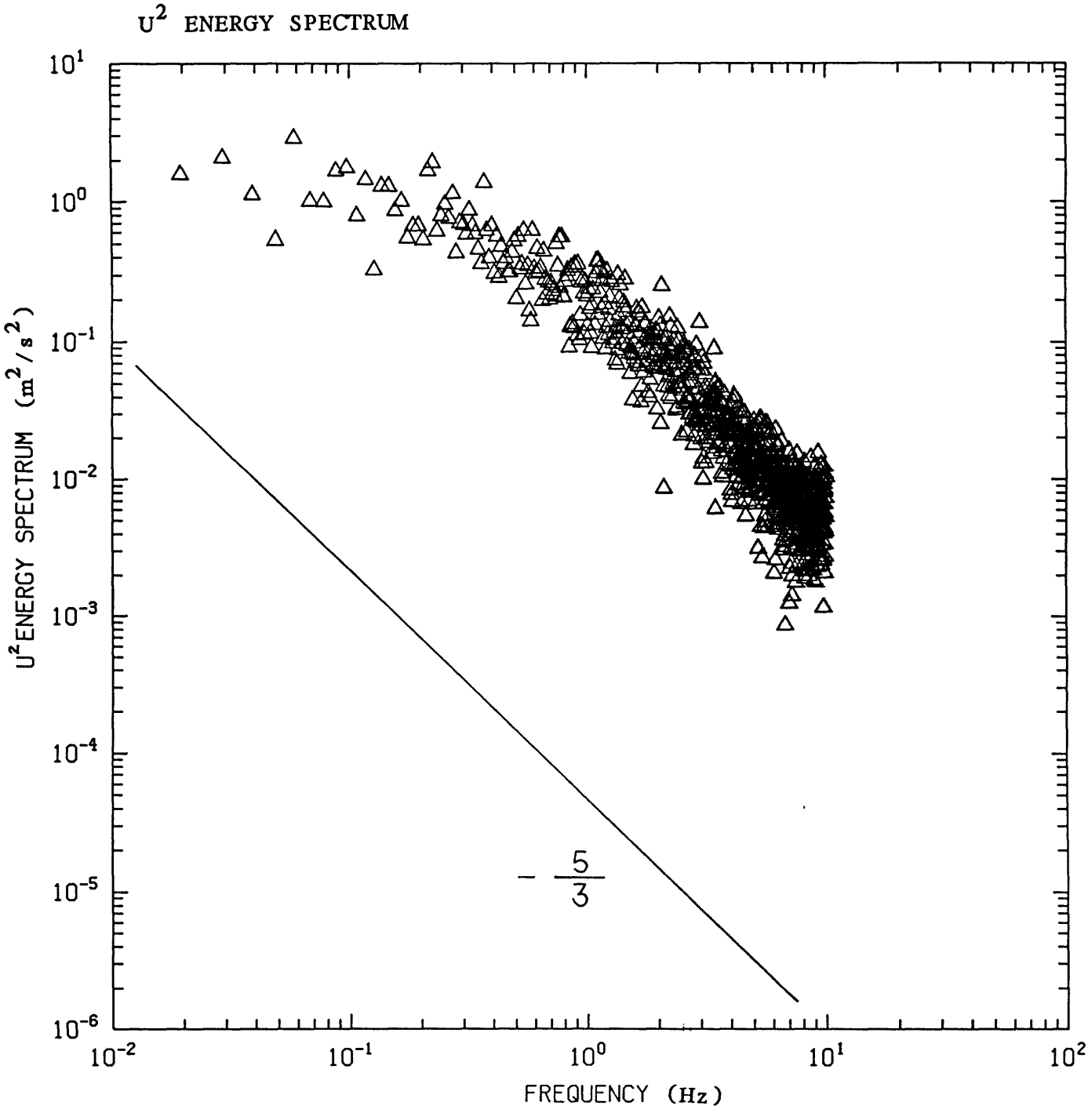
U² ENERGY SPECTRUM
U²ENERGY SPECTRUM (m²/s²)
FREQUENCY (Hz)
10¹
10⁰
10⁻¹
10⁻²
10⁻³
10⁻⁴
10⁻⁵
10⁻⁶
10⁻²
10⁻¹
10⁰
10¹
10²
- 5/3

Figure 4.1.21

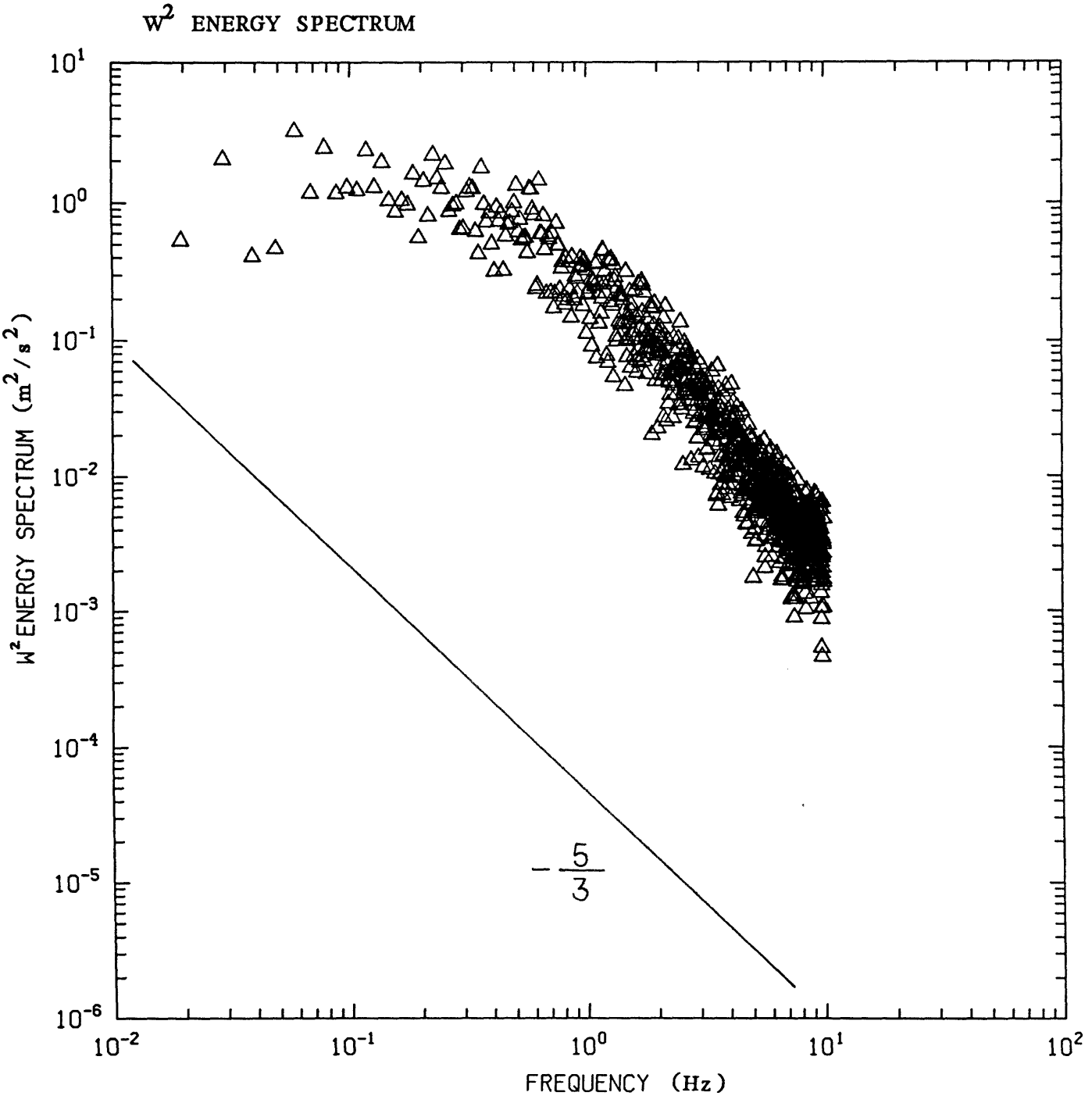
W² ENERGY SPECTRUM
W² ENERGY SPECTRUM (m²/s²)
FREQUENCY (Hz)
-5/3
10¹
10⁰
10⁻¹
10⁻²
10⁻³
10⁻⁴
10⁻⁵
10⁻⁶
10⁻²
10⁻¹
10⁰
10¹
10²

Figure 4.1.22

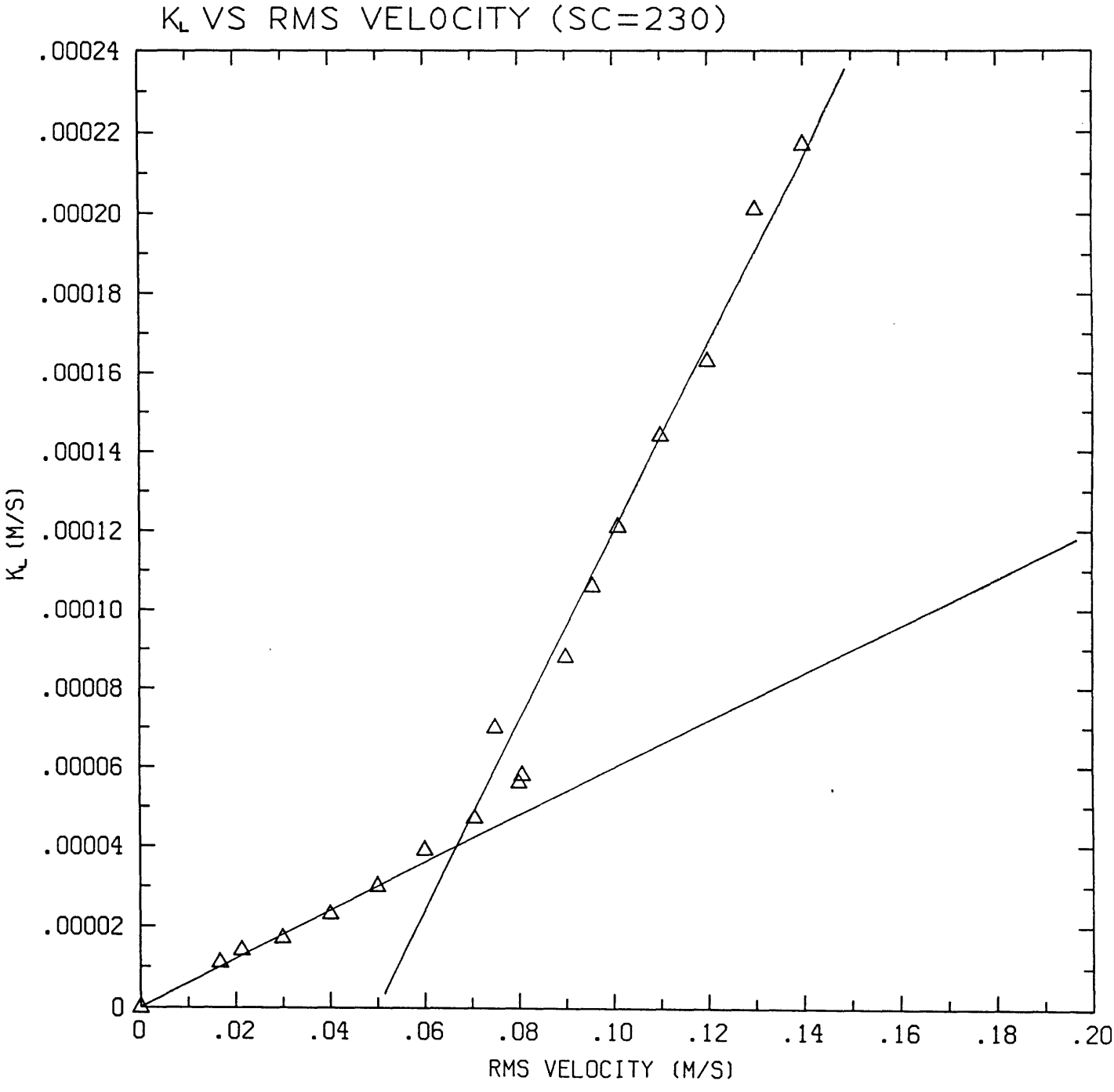
K_L VS RMS VELOCITY (SC=230)
.00024
.00022
.00020
.00018
.00016
.00014
.00012
.00010
.00008
.00006
.00004
.00002
0
K_L (M/S)
0
.02
.04
.06
.08
.10
.12
.14
.16
.18
.20
RMS VELOCITY (M/S)

Figure 4.2.1

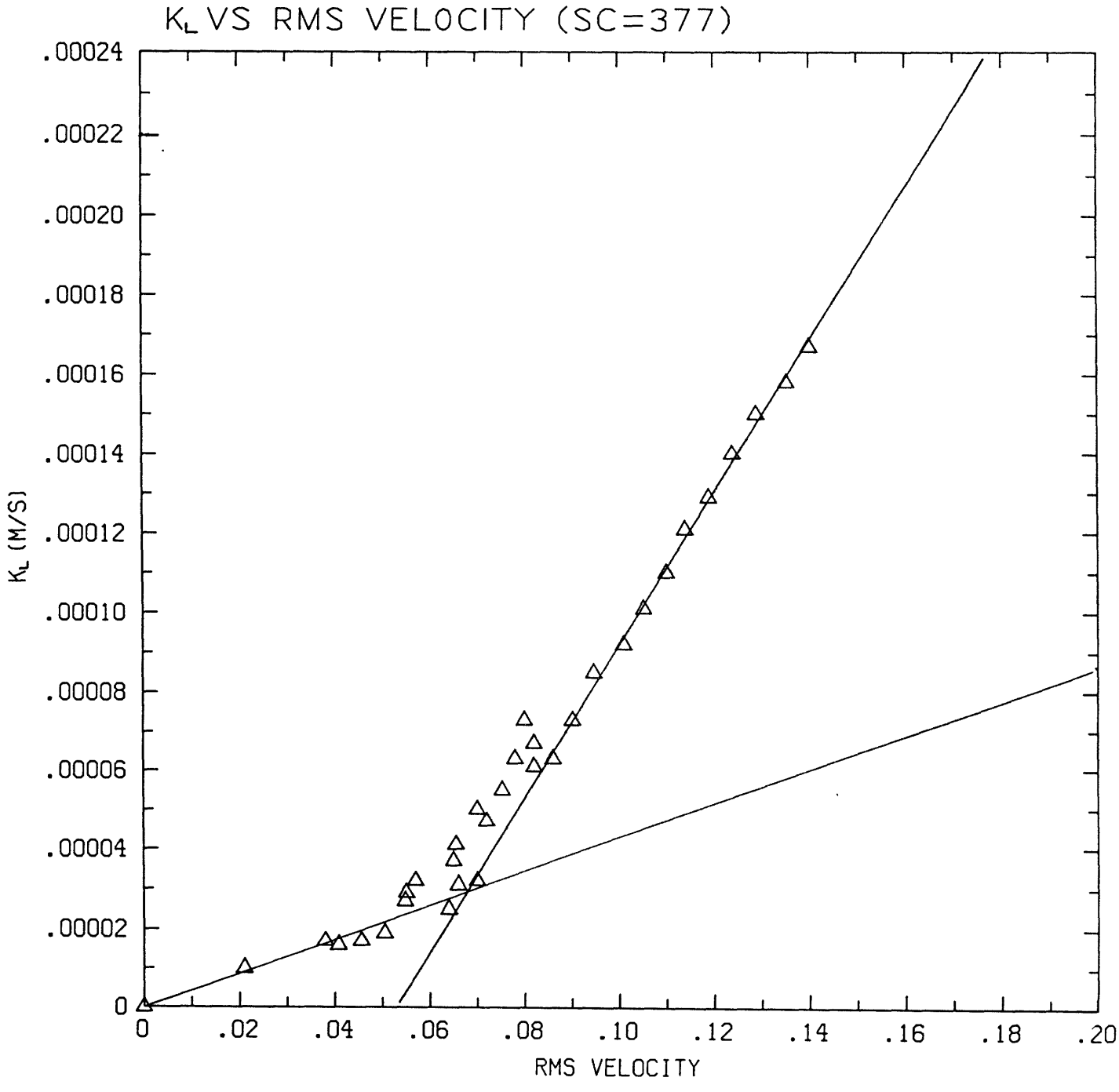
K_L VS RMS VELOCITY (SC=377)
.00024
.00022
.00020
.00018
.00016
.00014
.00012
.00010
.00008
.00006
.00004
.00002
0
K_L (M/S)
0
.02
.04
.06
.08
.10
.12
.14
.16
.18
.20
RMS VELOCITY

Figure 4.2.2

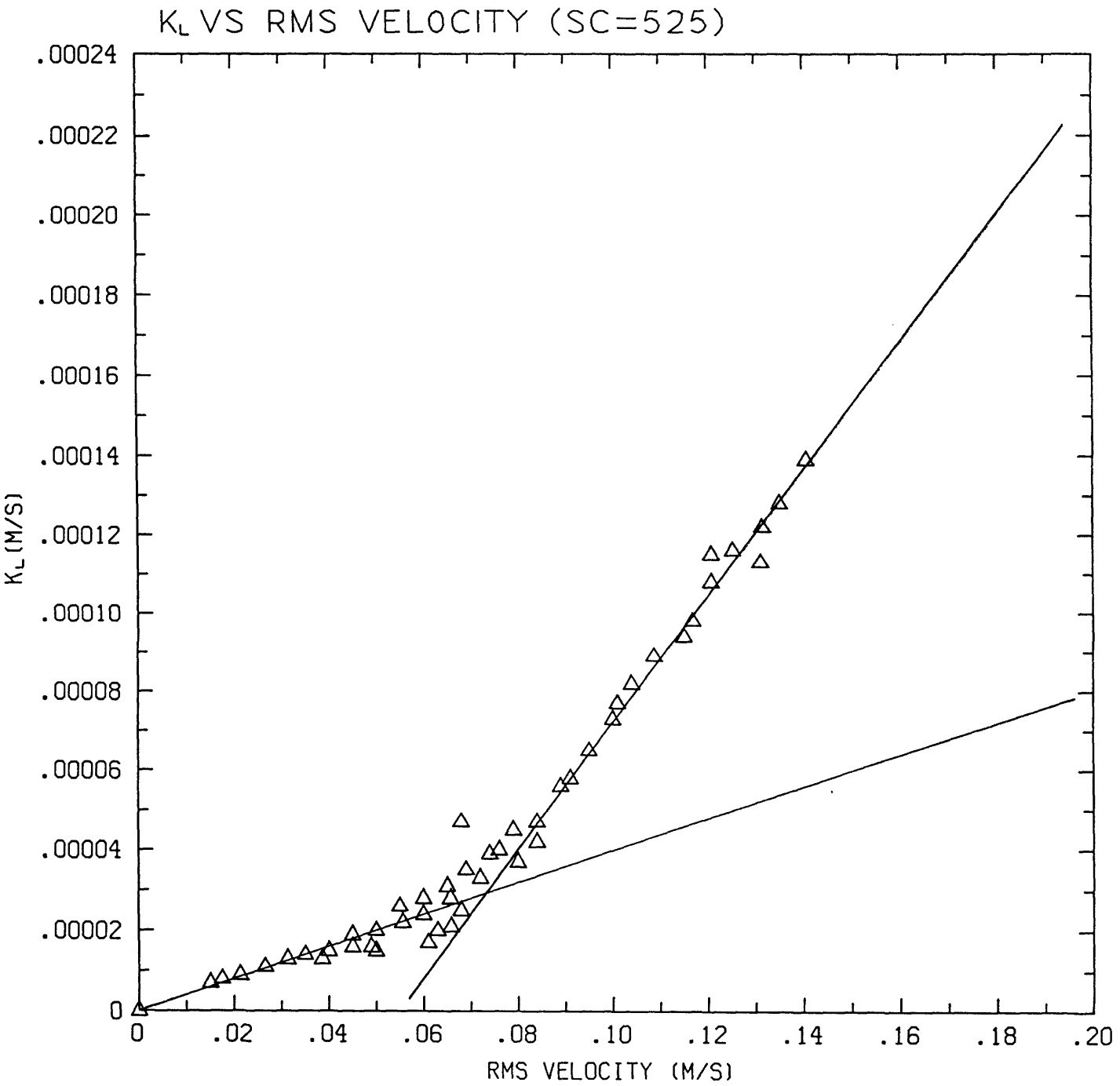
K_L VS RMS VELOCITY (SC=525)
.00024
.00022
.00020
.00018
.00016
.00014
.00012
.00010
.00008
.00006
.00004
.00002
0
K_L (M/S)
0
.02
.04
.06
.08
.10
.12
.14
.16
.18
.20
RMS VELOCITY (M/S)

Figure 4.2.3

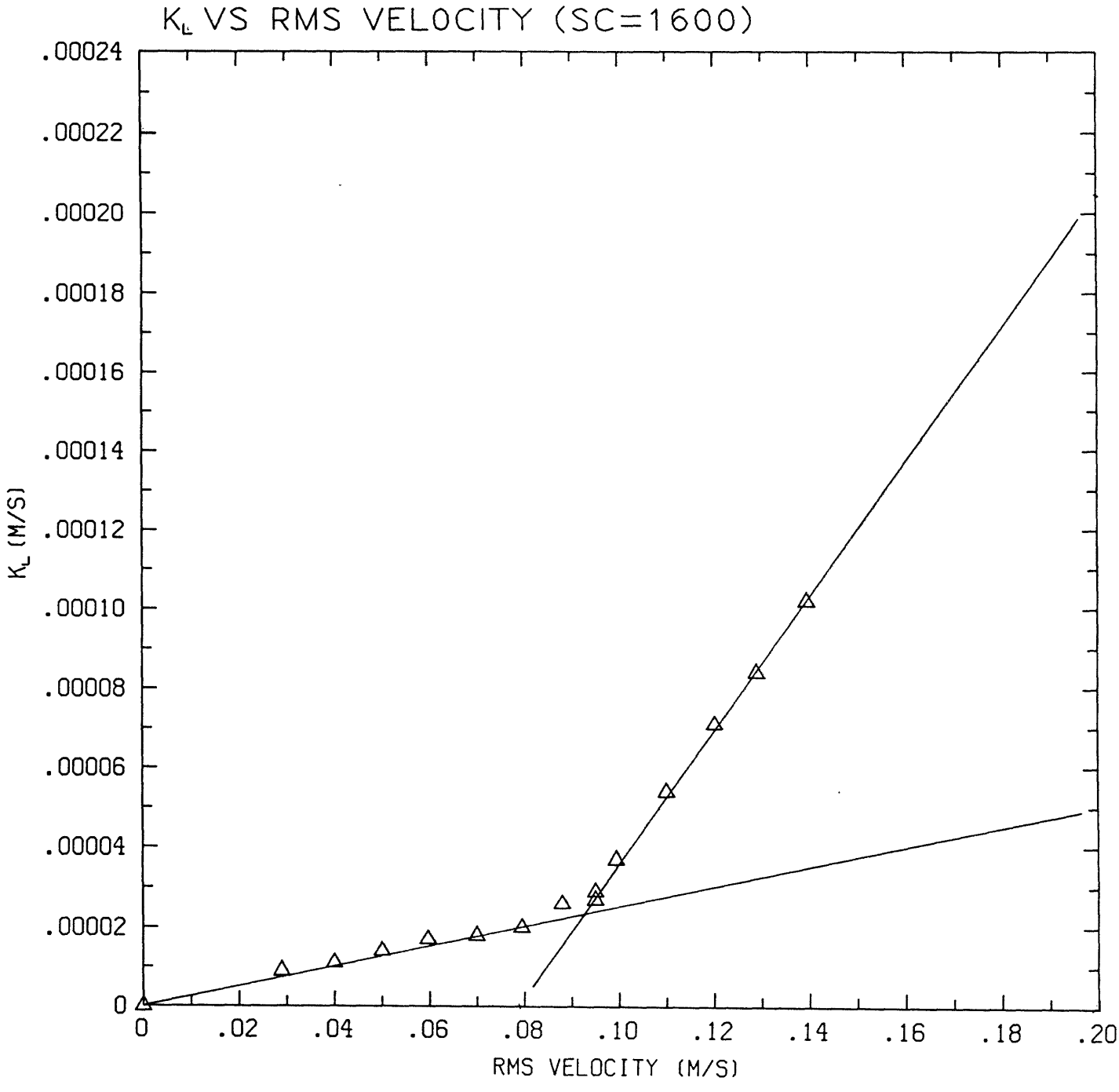
K_L VS RMS VELOCITY (SC=1600)
.00024
.00022
.00020
.00018
.00016
.00014
.00012
.00010
.00008
.00006
.00004
.00002
0
K_L (M/S)
0
.02
.04
.06
.08
.10
.12
.14
.16
.18
.20
RMS VELOCITY (M/S)

Figure 4.2.4

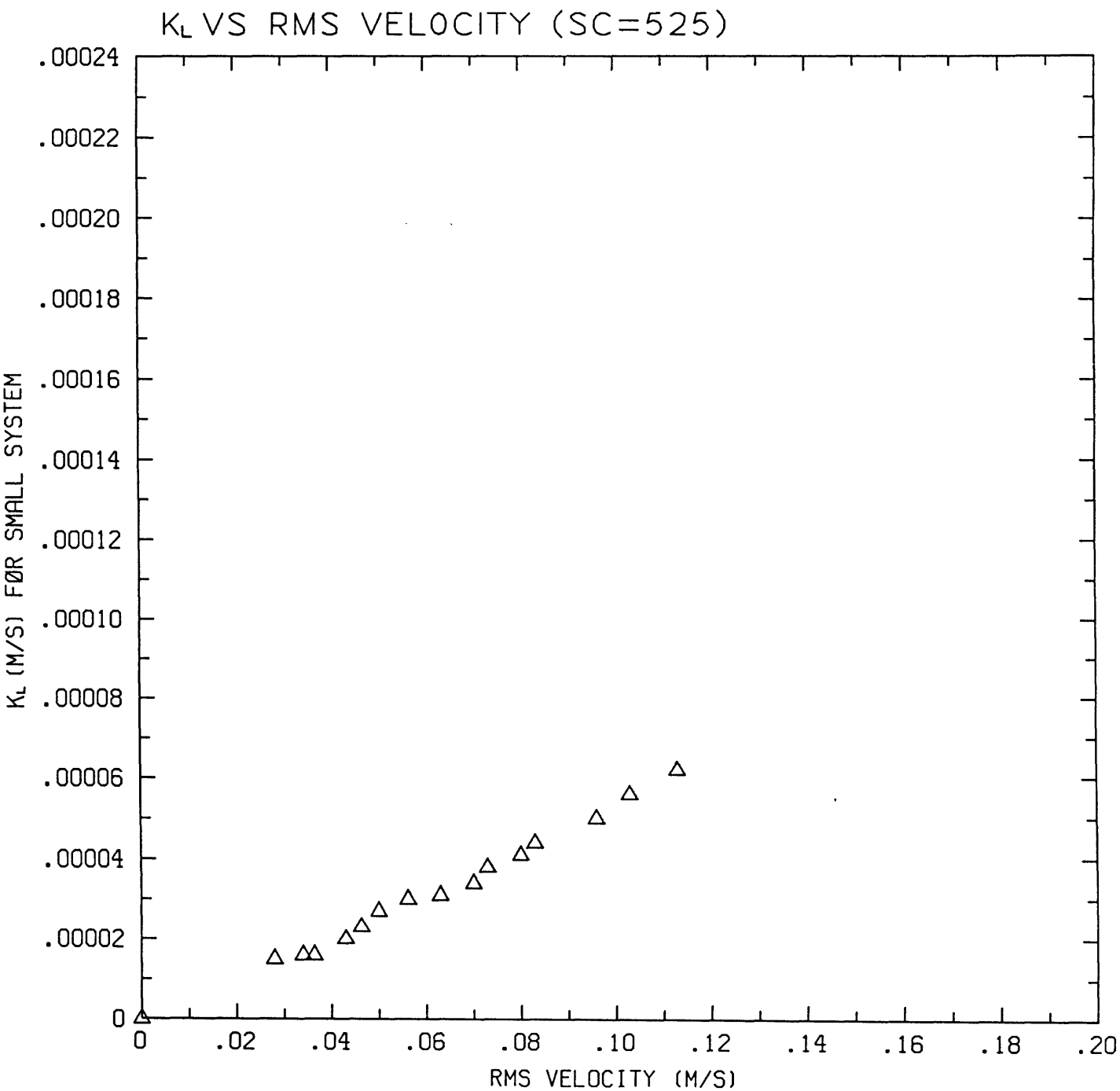
K_L VS RMS VELOCITY (SC=525)
.00024
.00022
.00020
.00018
.00016
.00014
.00012
.00010
.00008
.00006
.00004
.00002
0
K_L (M/S) FØR SMALL SYSTEM
0
.02
.04
.06
.08
.10
.12
.14
.16
.18
.20
RMS VELOCITY (M/S)

Figure 4.2.5

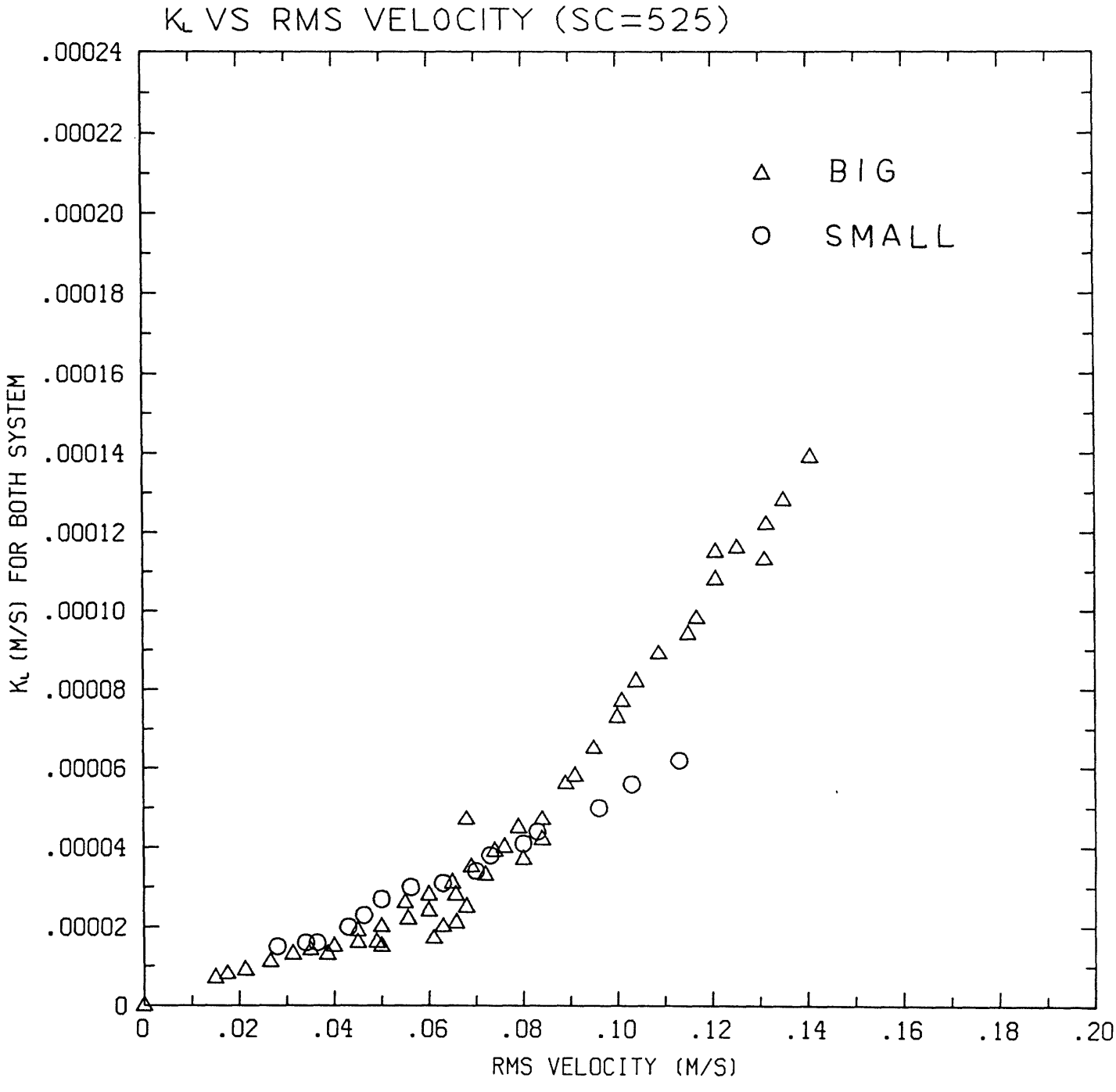
K_L VS RMS VELOCITY (SC=525)
.00024
.00022
.00020
.00018
.00016
.00014
.00012
.00010
.00008
.00006
.00004
.00002
0
K_L (M/S) FOR BOTH SYSTEM
BIG
SMALL
0
.02
.04
.06
.08
.10
.12
.14
.16
.18
.20
RMS VELOCITY (M/S)

Figure 4.2.6

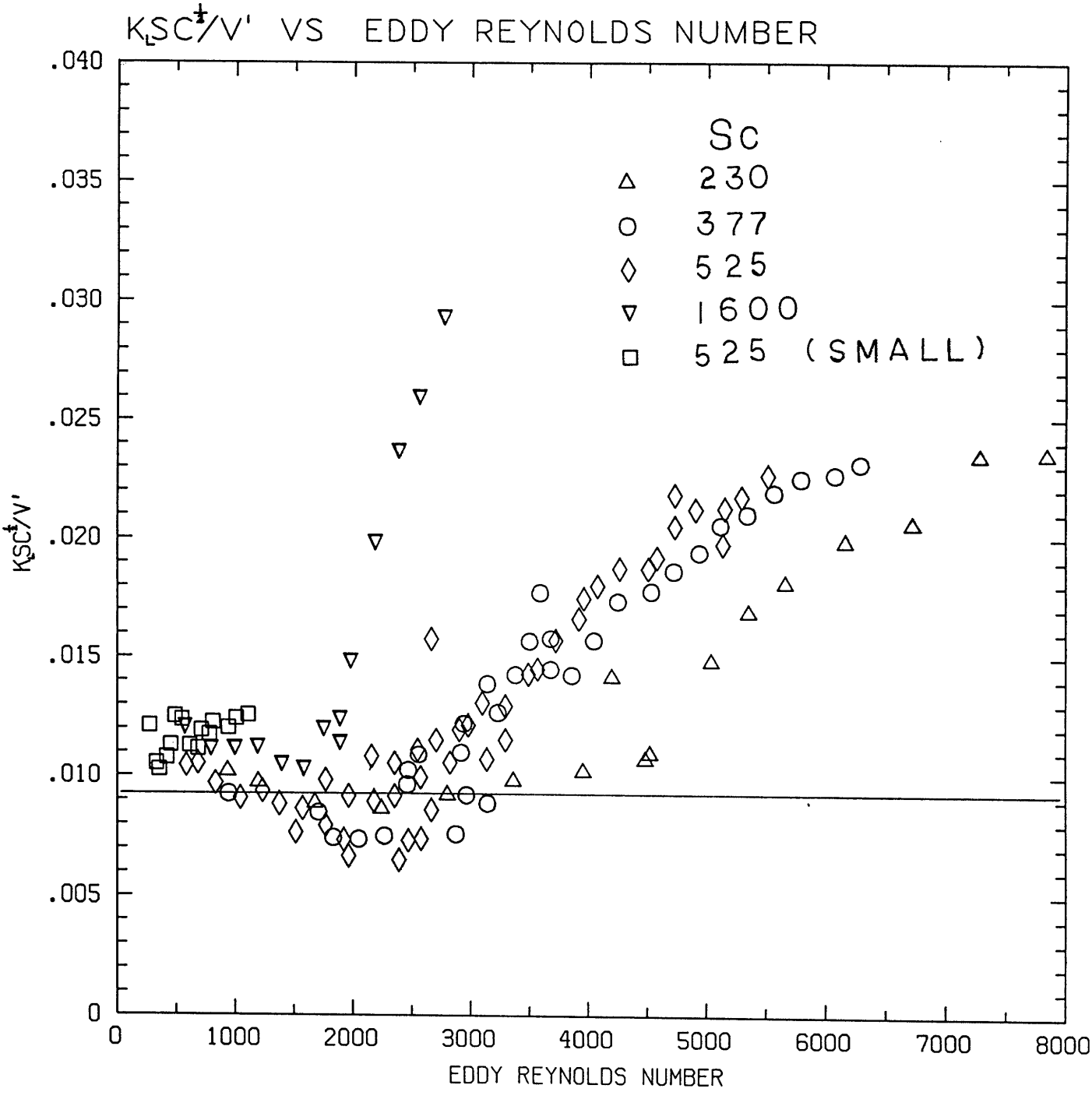
$K_L SC^{\frac{1}{2}}/V'$ VS EDDY REYNOLDS NUMBER
Sc
230
377
525
1600
525 (SMALL)
$K_L SC^{\frac{1}{2}}/V'$
.040
.035
.030
.025
.020
.015
.010
.005
0
0
1000
2000
3000
4000
5000
6000
7000
8000
EDDY REYNOLDS NUMBER

Figure 4.2.7

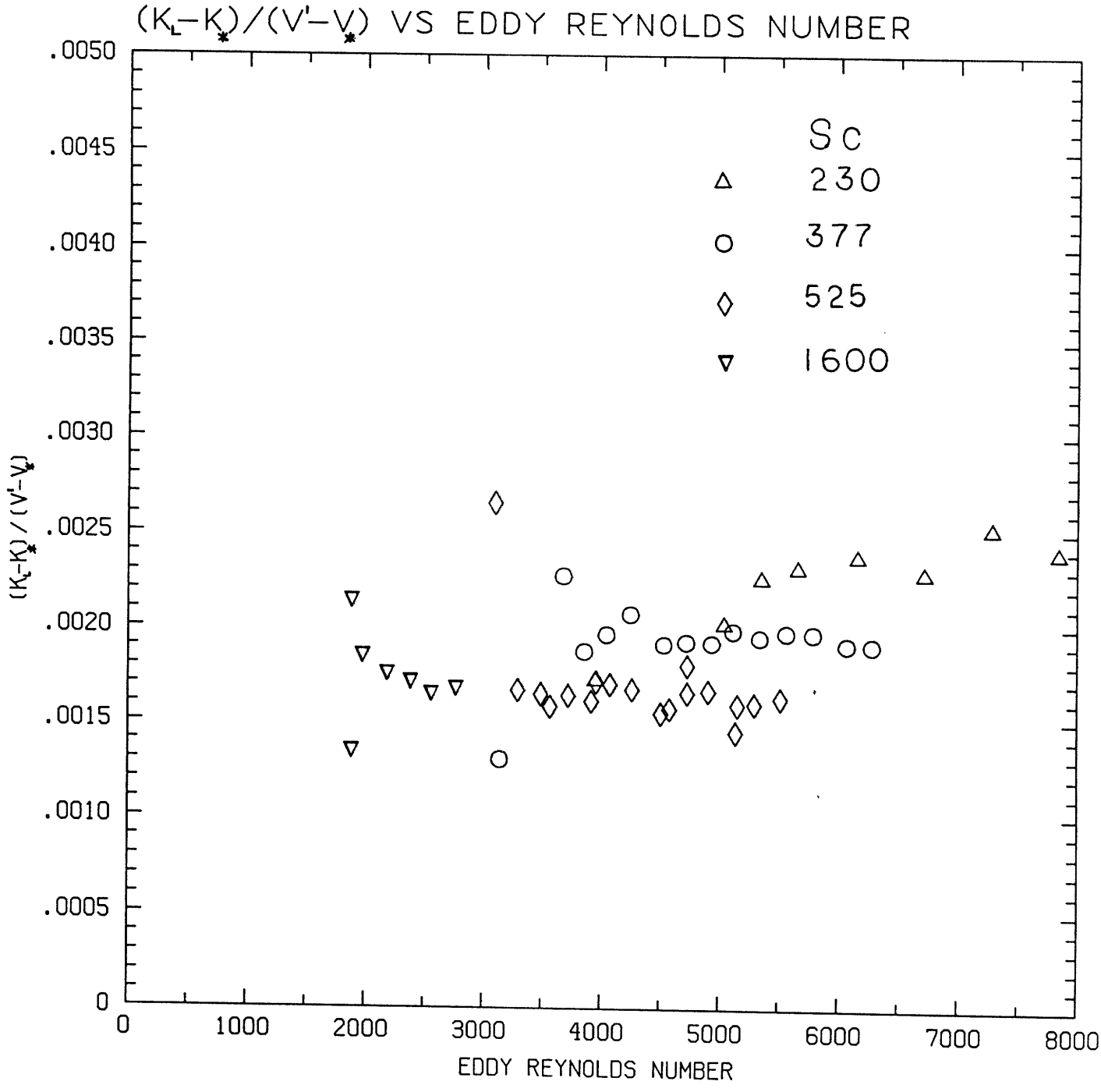
(K_L−K_*)/(V'−V_*) VS EDDY REYNOLDS NUMBER
.0050
.0045
.0040
.0035
.0030
.0025
.0020
.0015
.0010
.0005
0
(K_L-K_*) / (V'-V_*)
Sc
230
377
525
1600
0
1000
2000
3000
4000
5000
6000
7000
8000
EDDY REYNOLDS NUMBER

Figure 4.2.8

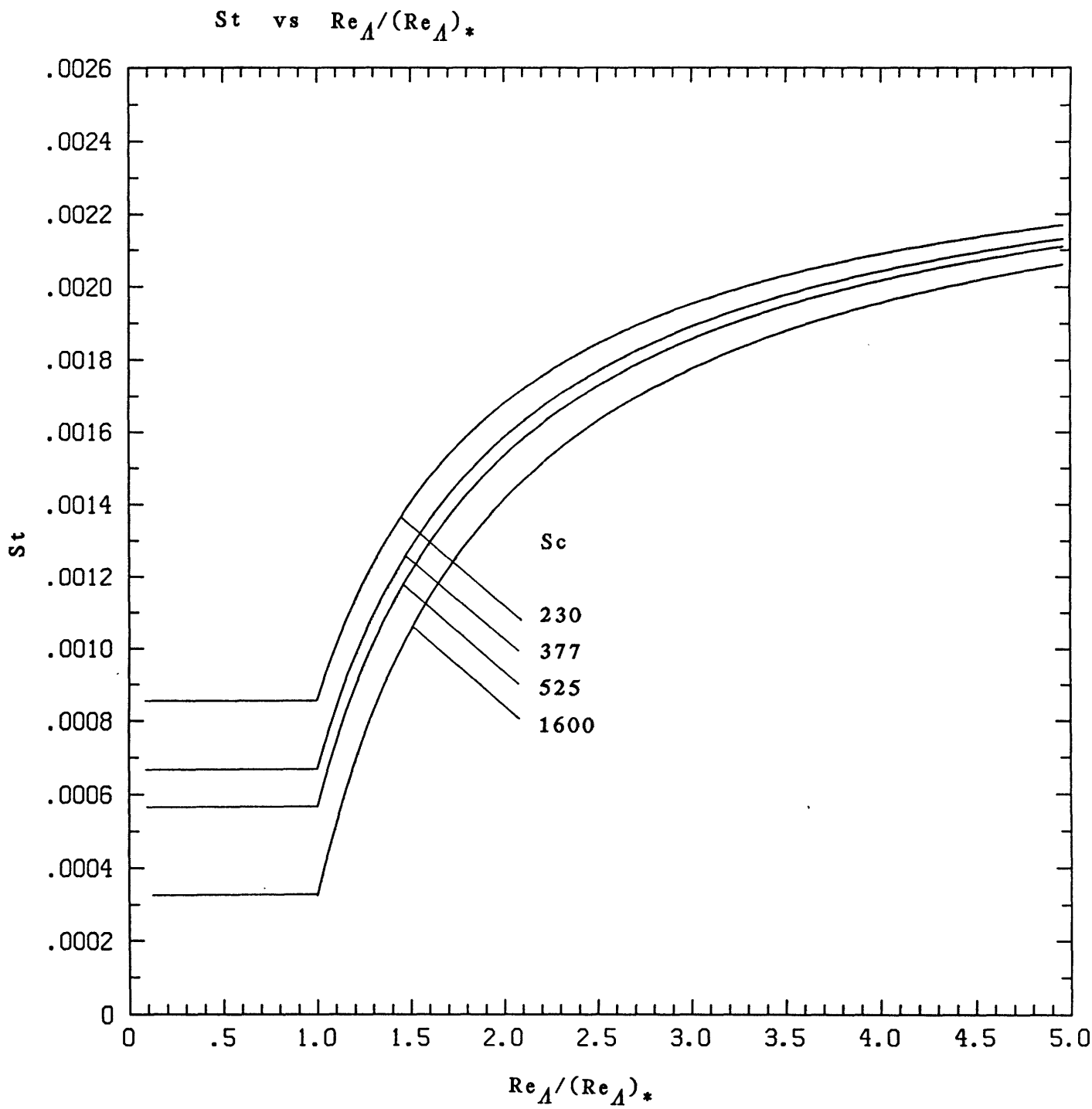
St vs $Re_\Lambda/(Re_\Lambda)_*$
.0026
.0024
.0022
.0020
.0018
.0016
.0014
.0012
.0010
.0008
.0006
.0004
.0002
0
St
Sc
230
377
525
1600
0
.5
1.0
1.5
2.0
2.5
3.0
3.5
4.0
4.5
5.0
$Re_\Lambda/(Re_\Lambda)_*$

Figure 4.2.9

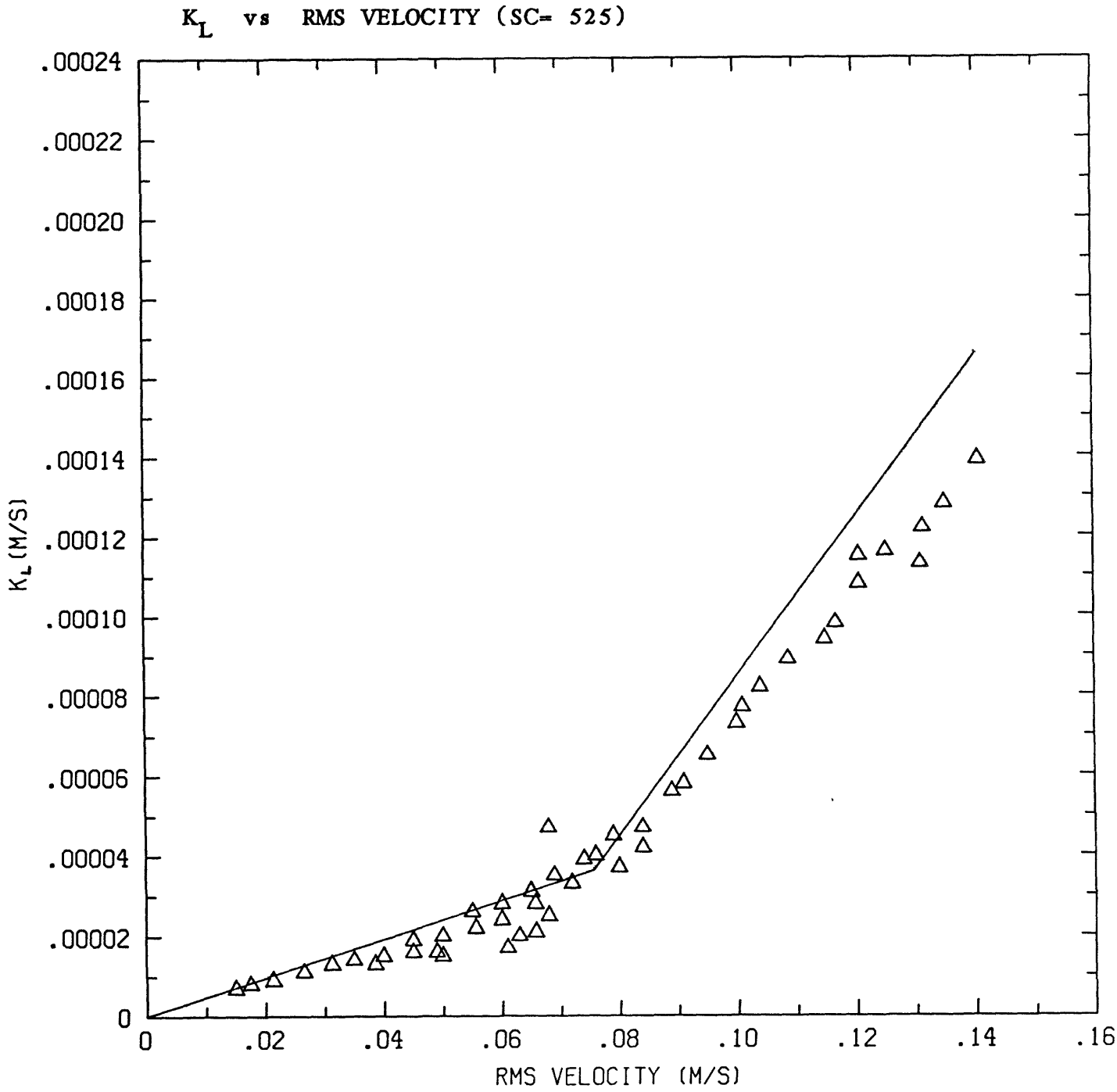
K_L vs RMS VELOCITY (SC= 525)
.00024
.00022
.00020
.00018
.00016
.00014
.00012
.00010
.00008
.00006
.00004
.00002
0
K_L (M/S)
0
.02
.04
.06
.08
.10
.12
.14
.16
RMS VELOCITY (M/S)

Figure 4.2.10

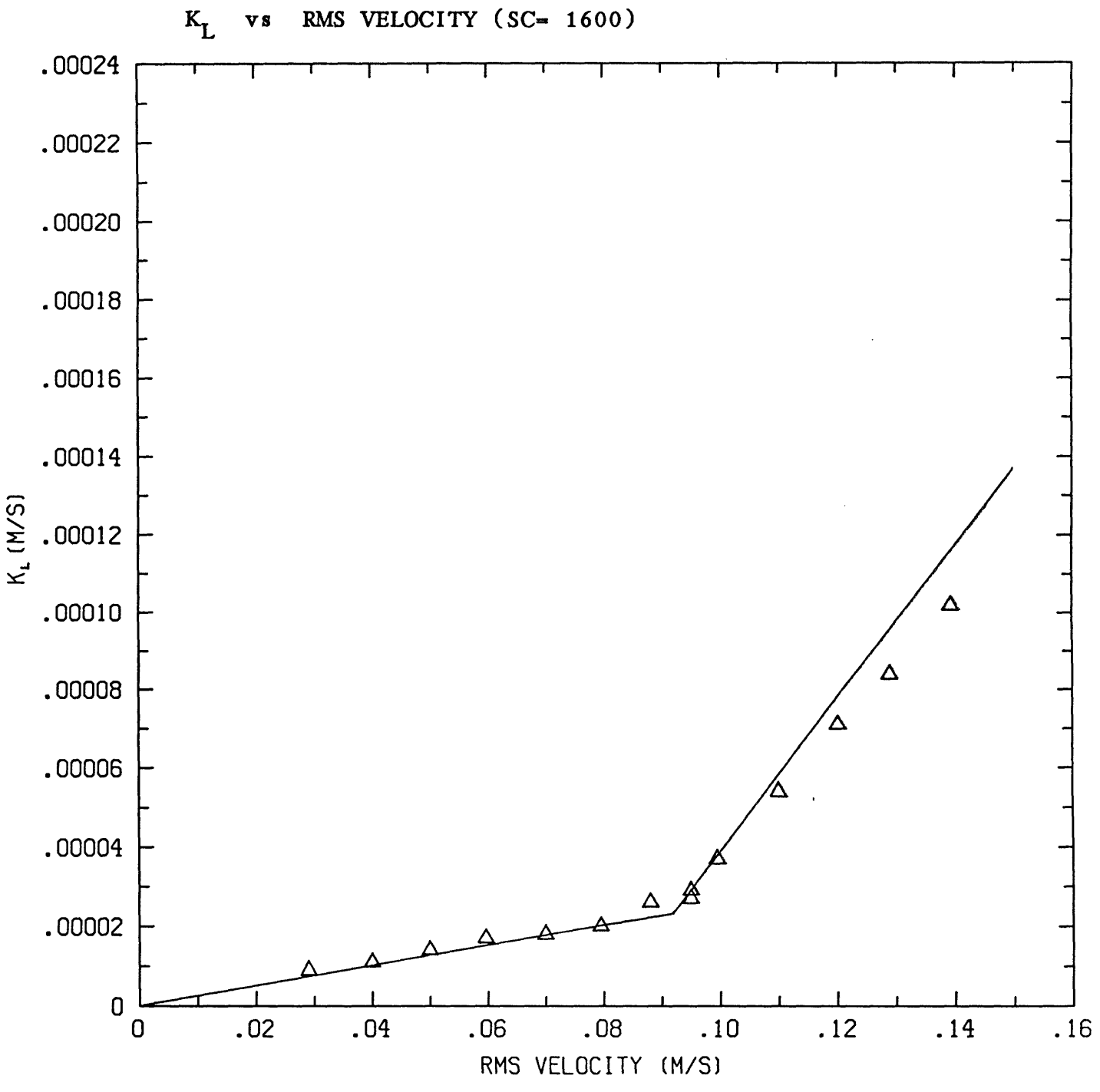
K_L vs RMS VELOCITY (SC= 1600)
.00024
.00022
.00020
.00018
.00016
.00014
.00012
.00010
.00008
.00006
.00004
.00002
0
K_L (M/S)
0
.02
.04
.06
.08
.10
.12
.14
.16
RMS VELOCITY (M/S)

Figure 4.2.11

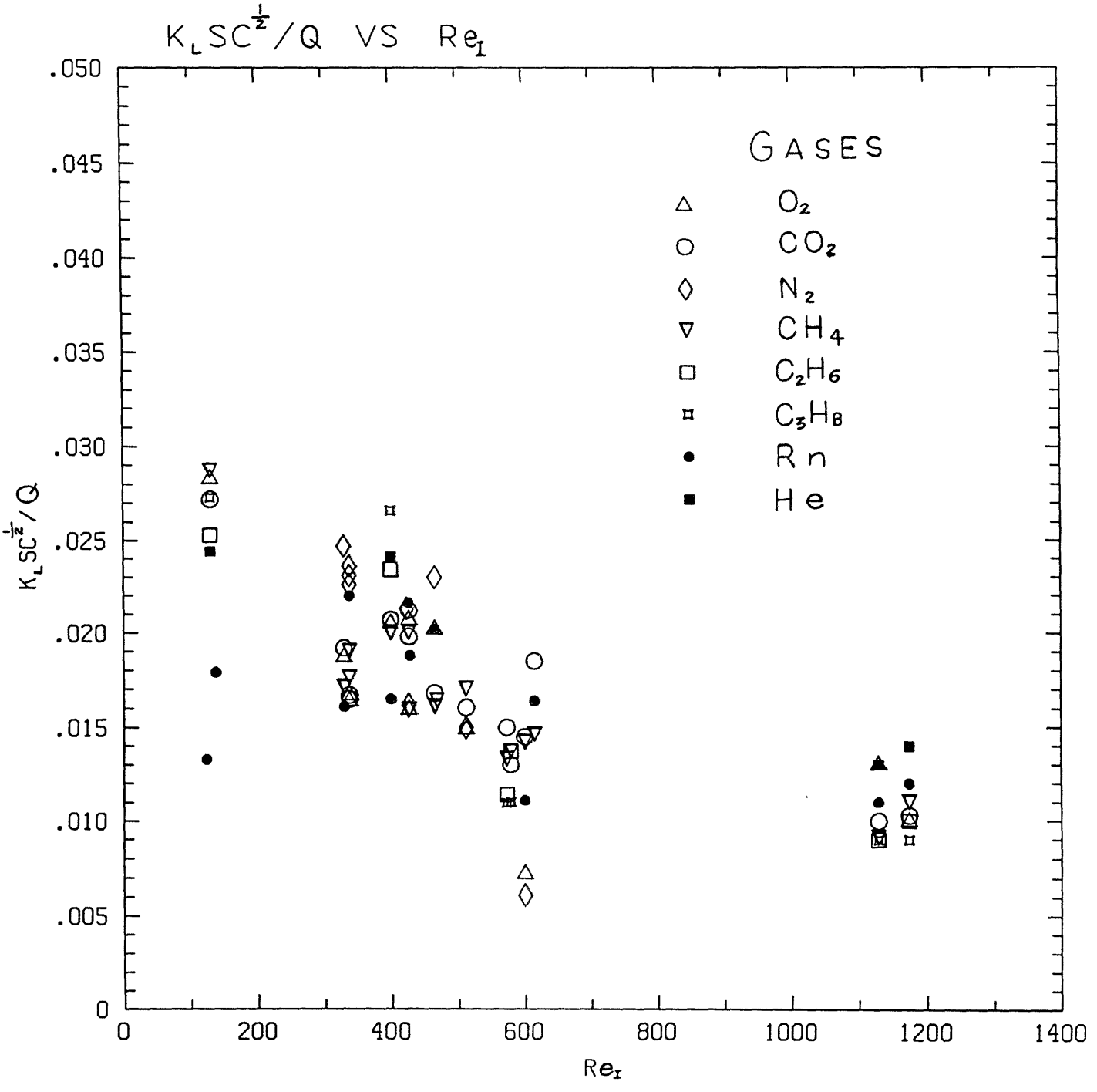
$K_L SC^{\frac{1}{2}}/Q$ VS Re_I
.050
.045
.040
.035
.030
.025
.020
.015
.010
.005
0
$K_L SC^{\frac{1}{2}}/Q$
0
200
400
600
800
1000
1200
1400
Re_I
GASES
O_2
CO_2
N_2
CH_4
C_2H_6
C_3H_8
Rn
He

Figure 4.3.1

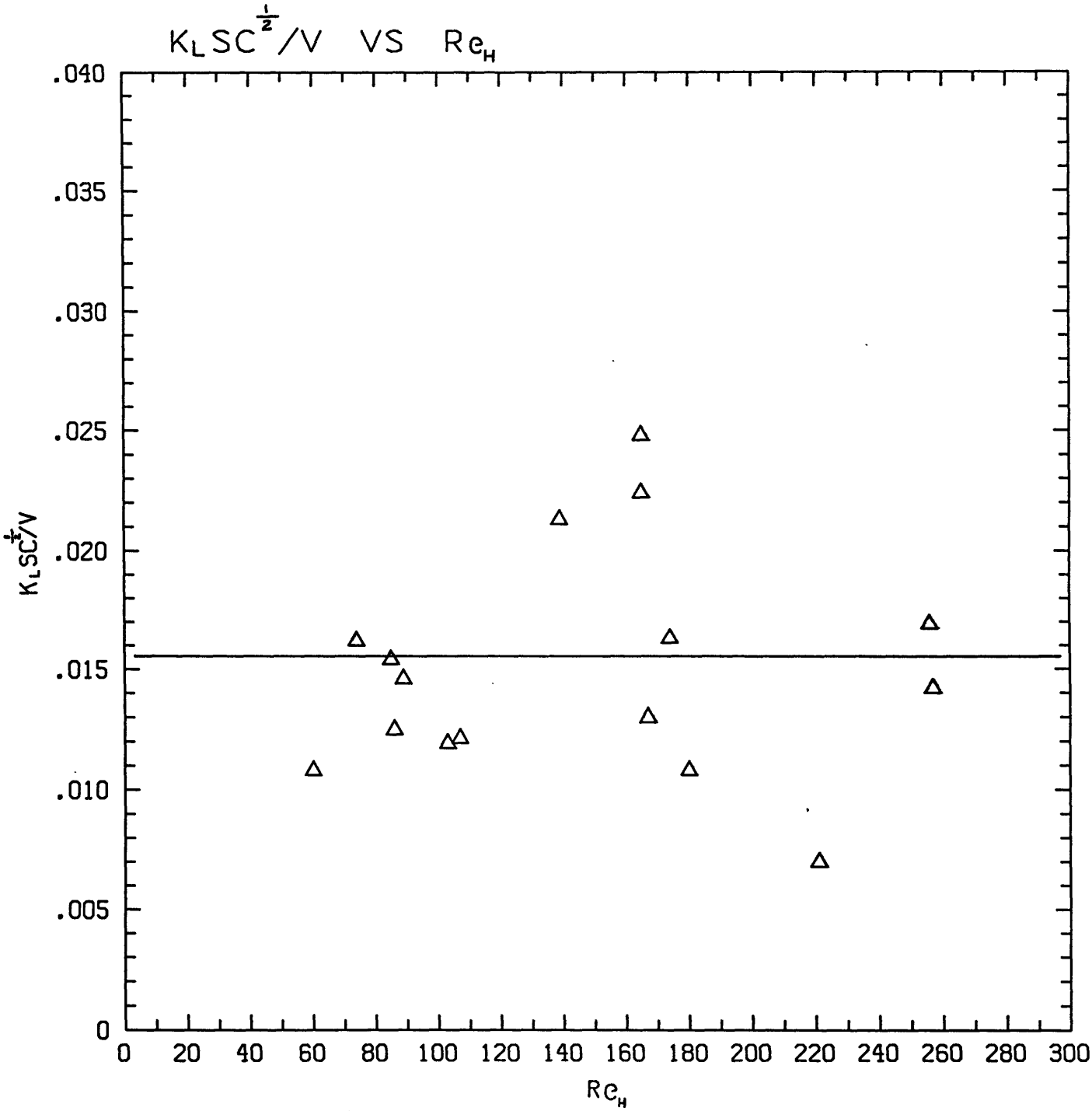
$K_L SC^{\frac{1}{2}}/V$ VS Re_H
.040
.035
.030
.025
.020
.015
.010
.005
0
$K_L SC^{\frac{1}{2}}/V$
0 20 40 60 80 100 120 140 160 180 200 220 240 260 280 300
Re_H

Figure 4.3.2

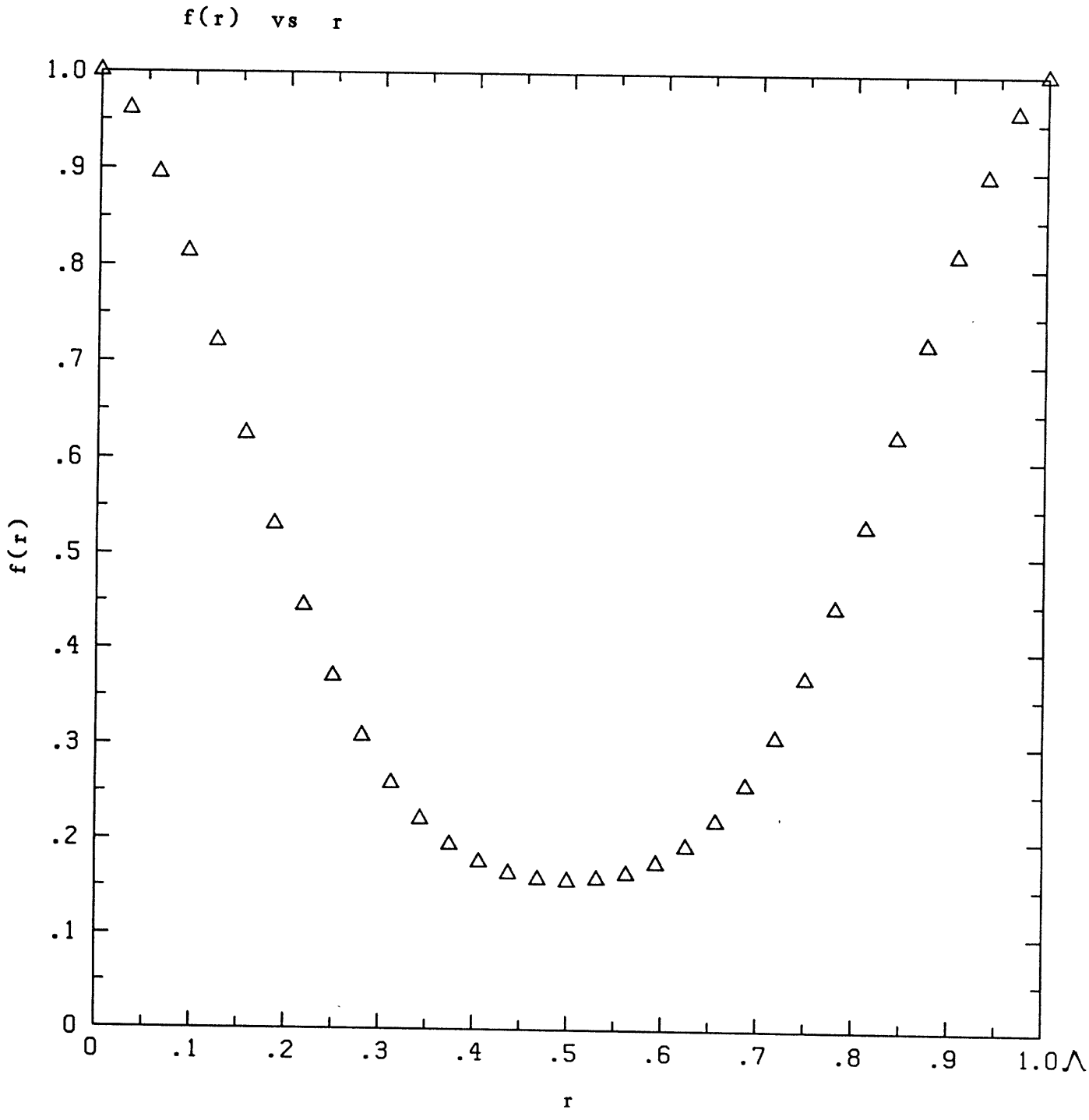

Figure 6.3.1

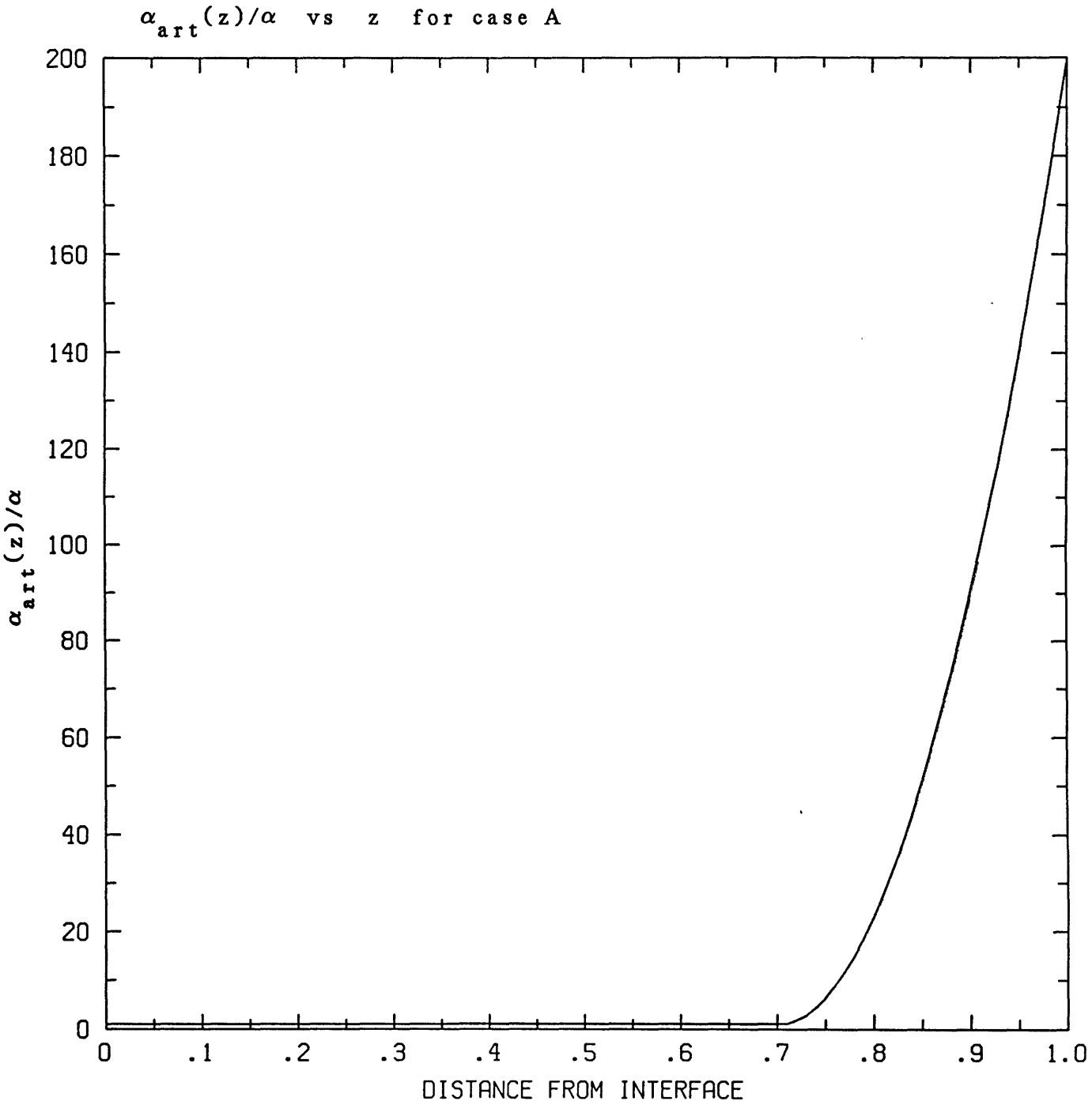
$\alpha_{art}(z)/\alpha$ vs z for case A
200
180
160
140
120
100
80
60
40
20
0
$\alpha_{art}(z)/\alpha$
0
.1
.2
.3
.4
.5
.6
.7
.8
.9
1.0
DISTANCE FROM INTERFACE

Figure 6.3.2

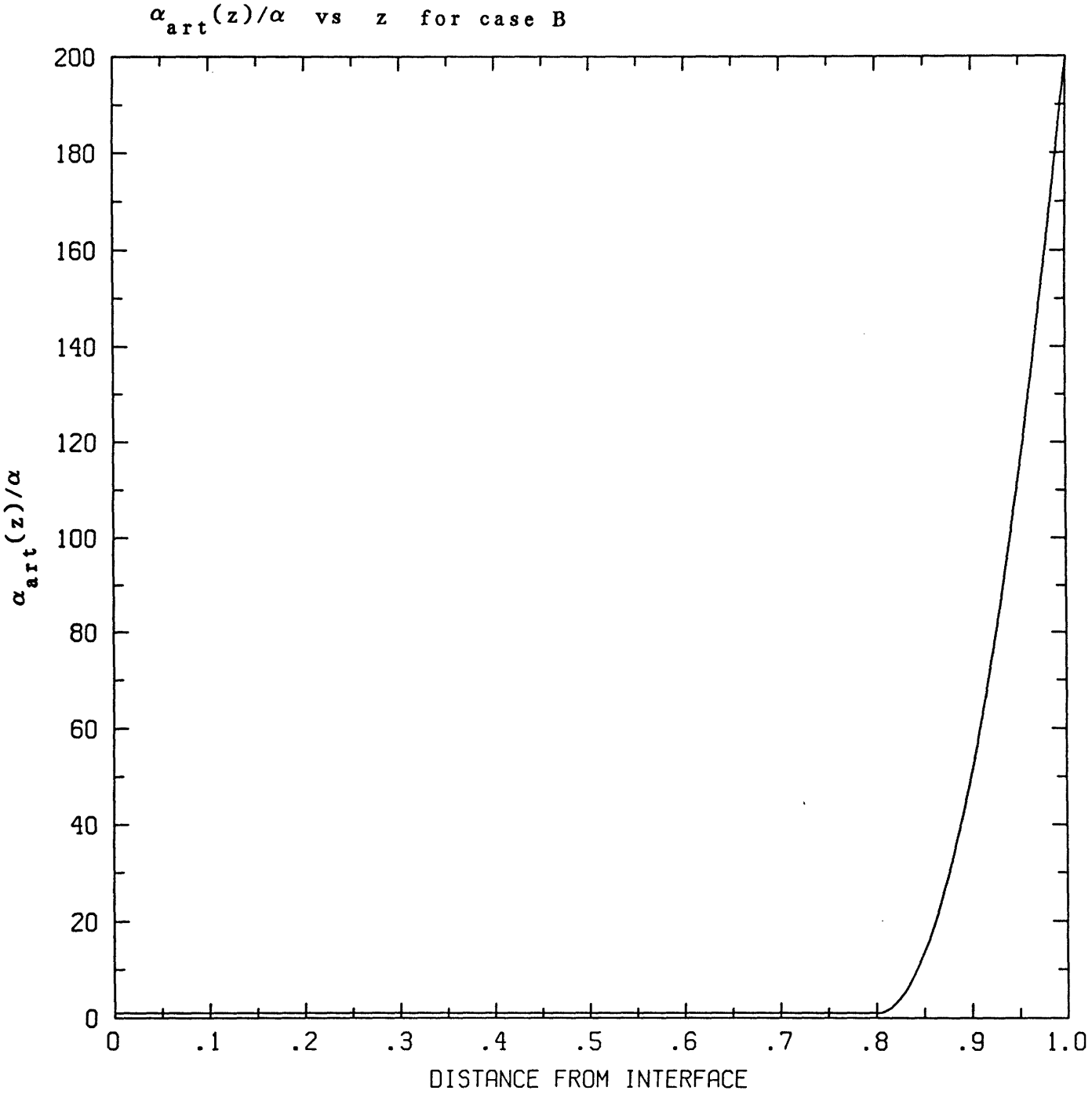
$\alpha_{art}(z)/\alpha$ vs z for case B
200
180
160
140
120
100
80
60
40
20
0
$\alpha_{art}(z)/\alpha$
0
.1
.2
.3
.4
.5
.6
.7
.8
.9
1.0
DISTANCE FROM INTERFACE

Figure 6.3.3

Computational grid arrangment for Case A

Interface

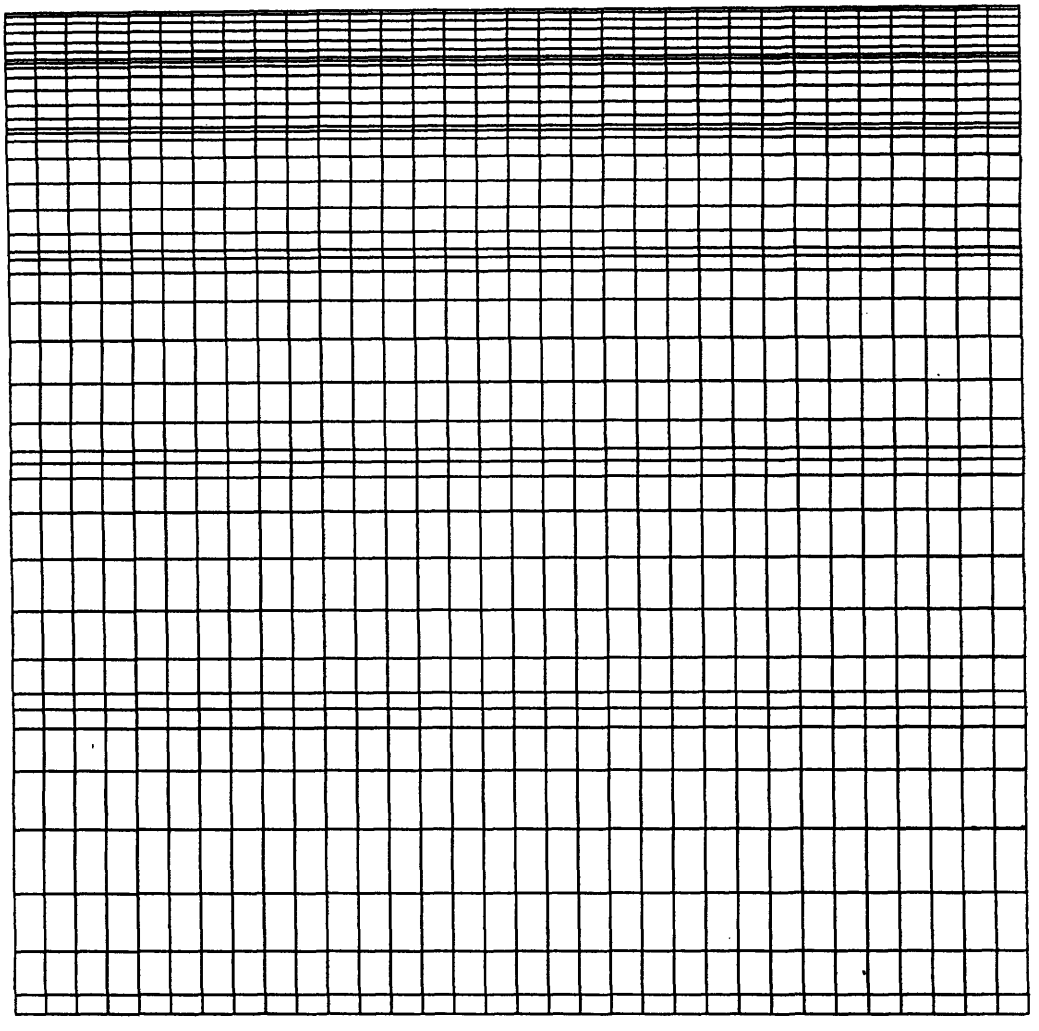

Lower Boundary

Figure 6.4.1

Computational grid arrangment for Case B

Interface

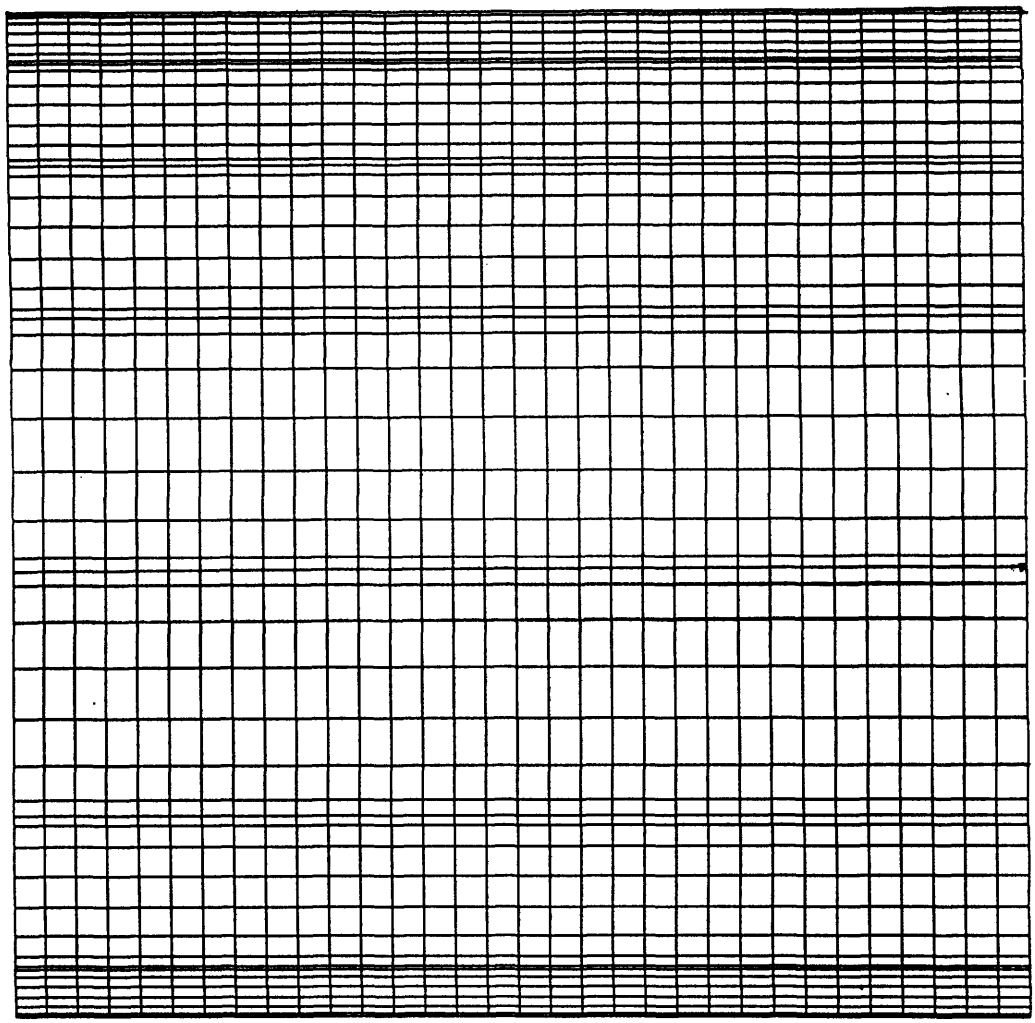

Lower Boundary

Figure 6.4.2

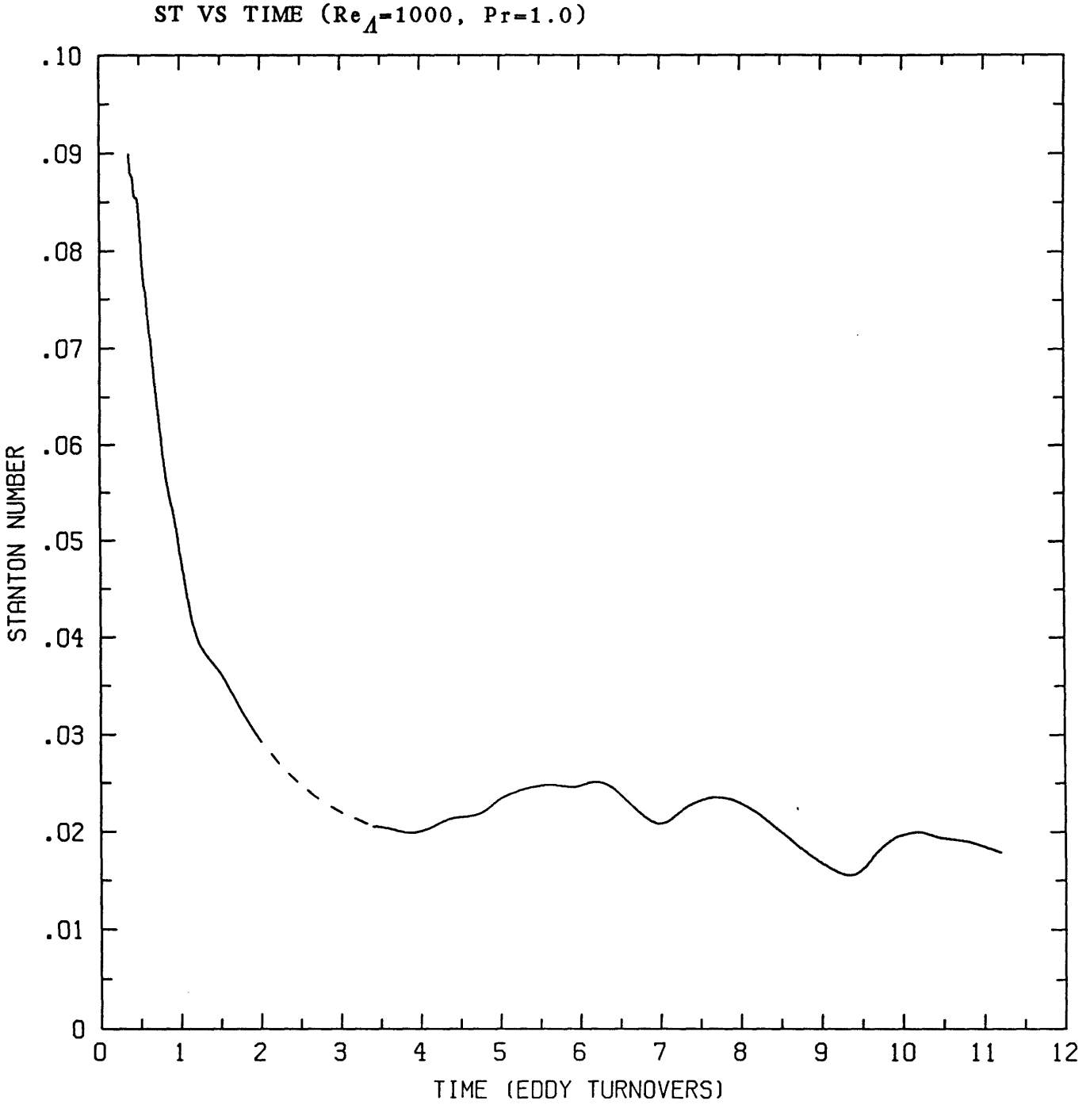
ST VS TIME (Re_Δ=1000, Pr=1.0)
STANTON NUMBER
.10
.09
.08
.07
.06
.05
.04
.03
.02
.01
0
0
1
2
3
4
5
6
7
8
9
10
11
12
TIME (EDDY TURNOVERS)

Figure 7.1.1

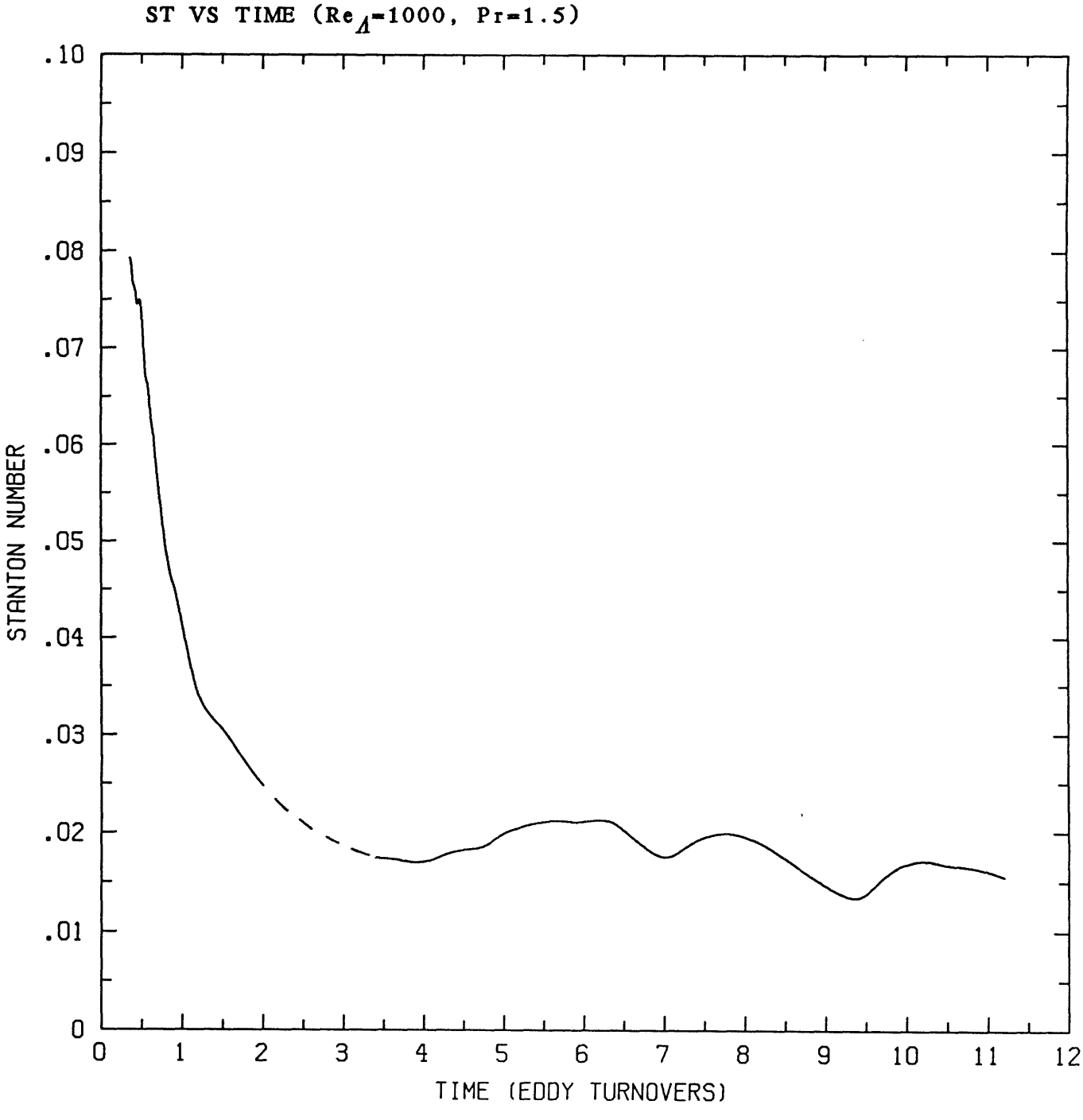
ST VS TIME (Re_Δ=1000, Pr=1.5)
STANTON NUMBER
.10
.09
.08
.07
.06
.05
.04
.03
.02
.01
0
0
1
2
3
4
5
6
7
8
9
10
11
12
TIME (EDDY TURNOVERS)

Figure 7.1.2

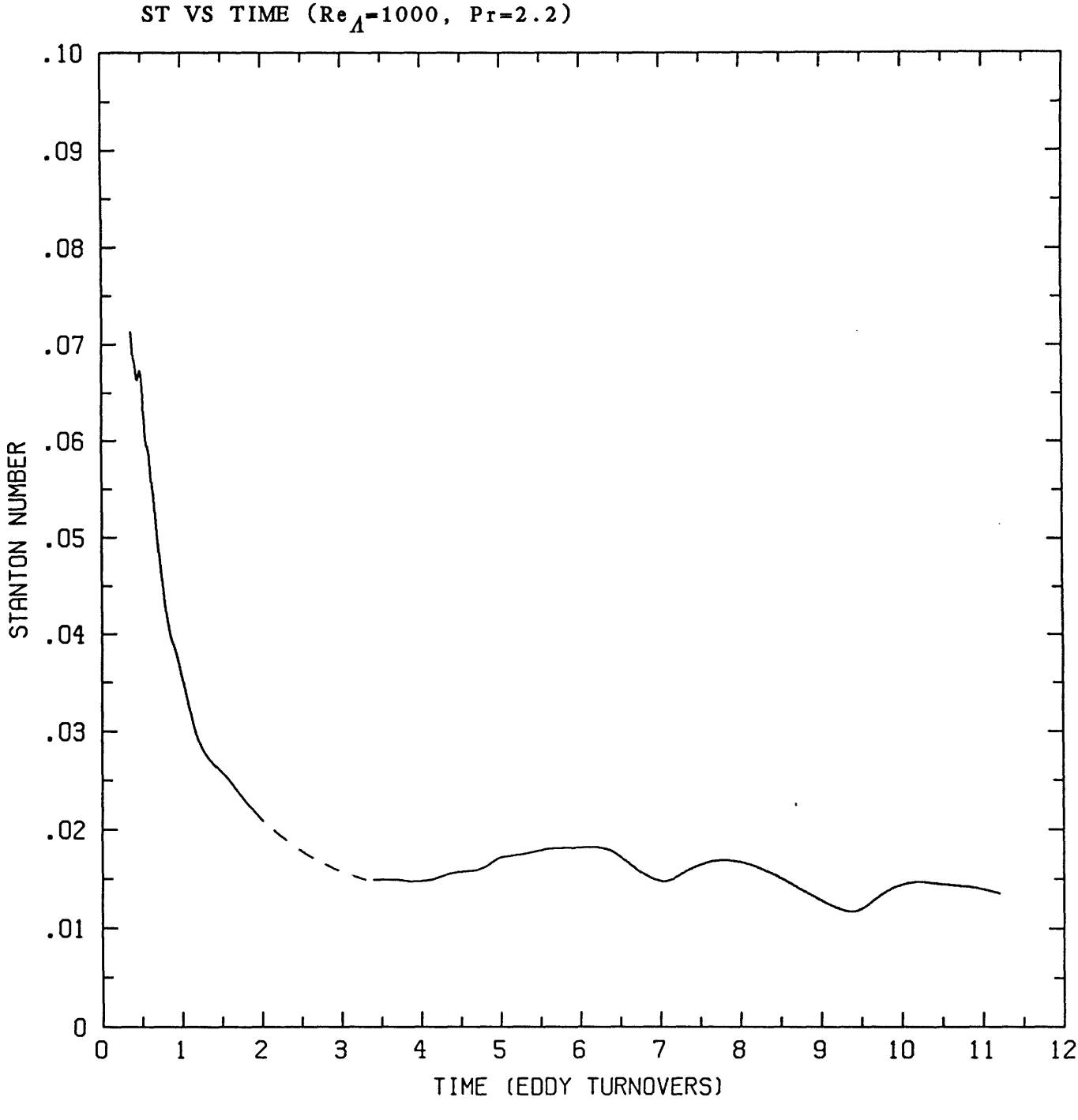
ST VS TIME (Re_Δ=1000, Pr=2.2)
STANTON NUMBER
.10
.09
.08
.07
.06
.05
.04
.03
.02
.01
0
0
1
2
3
4
5
6
7
8
9
10
11
12
TIME (EDDY TURNOVERS)

Figure 7.1.3

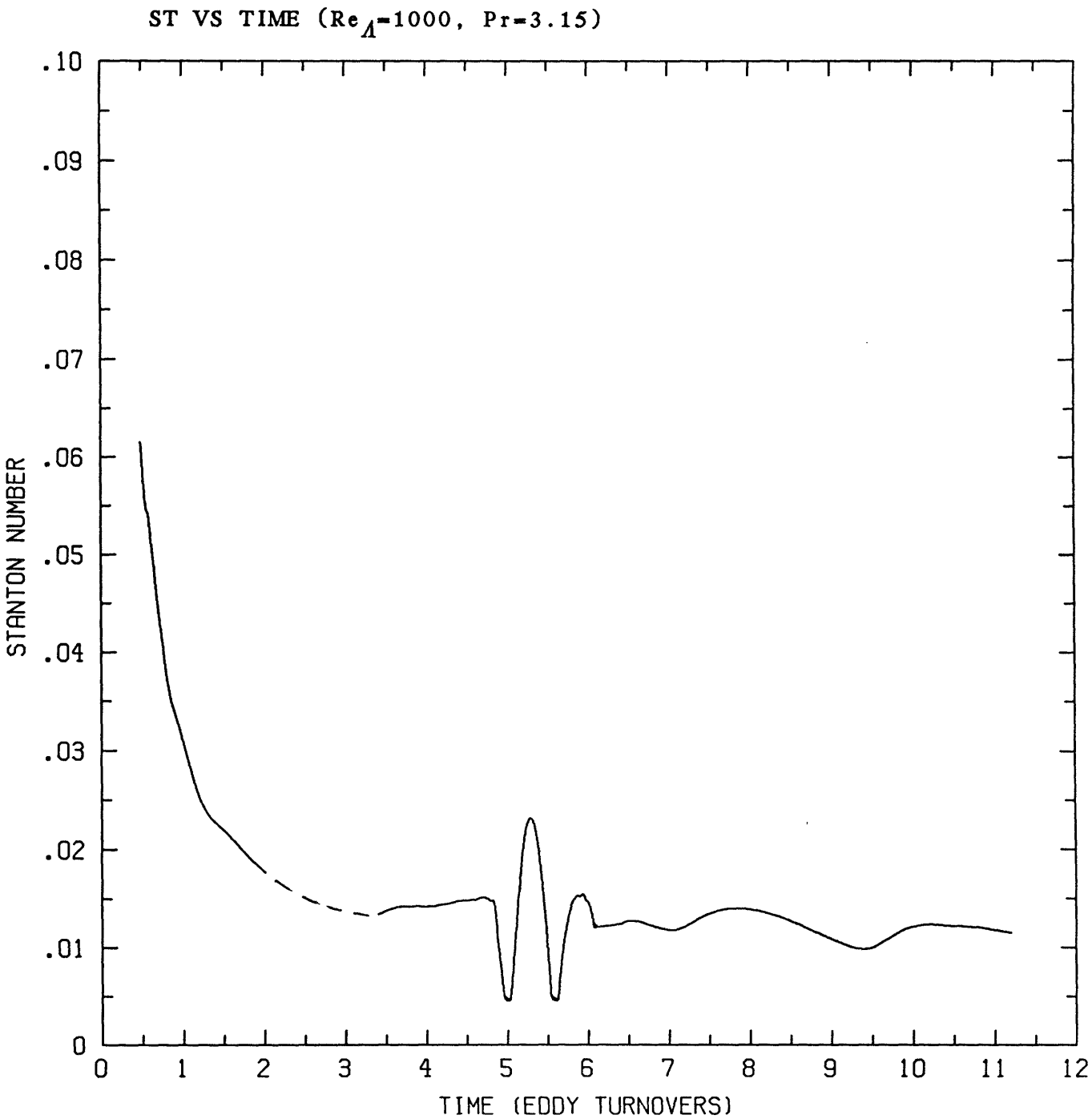
ST VS TIME (Re_Δ=1000, Pr=3.15)
STANTON NUMBER
.10
.09
.08
.07
.06
.05
.04
.03
.02
.01
0
0
1
2
3
4
5
6
7
8
9
10
11
12
TIME (EDDY TURNOVERS)

Figure 7.1.4

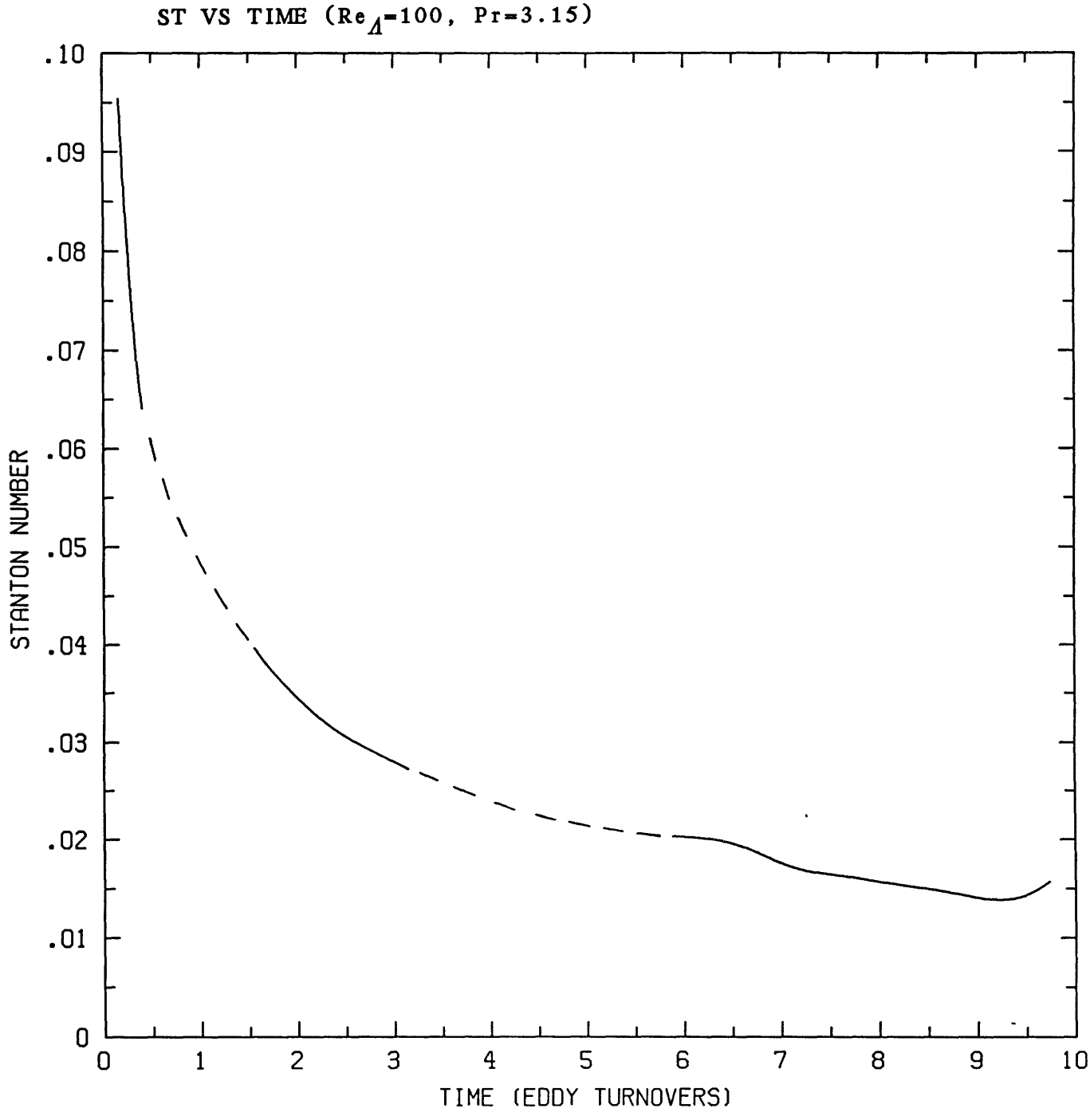
ST VS TIME (Re_Δ=100, Pr=3.15)
STANTON NUMBER
.10
.09
.08
.07
.06
.05
.04
.03
.02
.01
0
0
1
2
3
4
5
6
7
8
9
10
TIME (EDDY TURNOVERS)

Figure 7.1.5

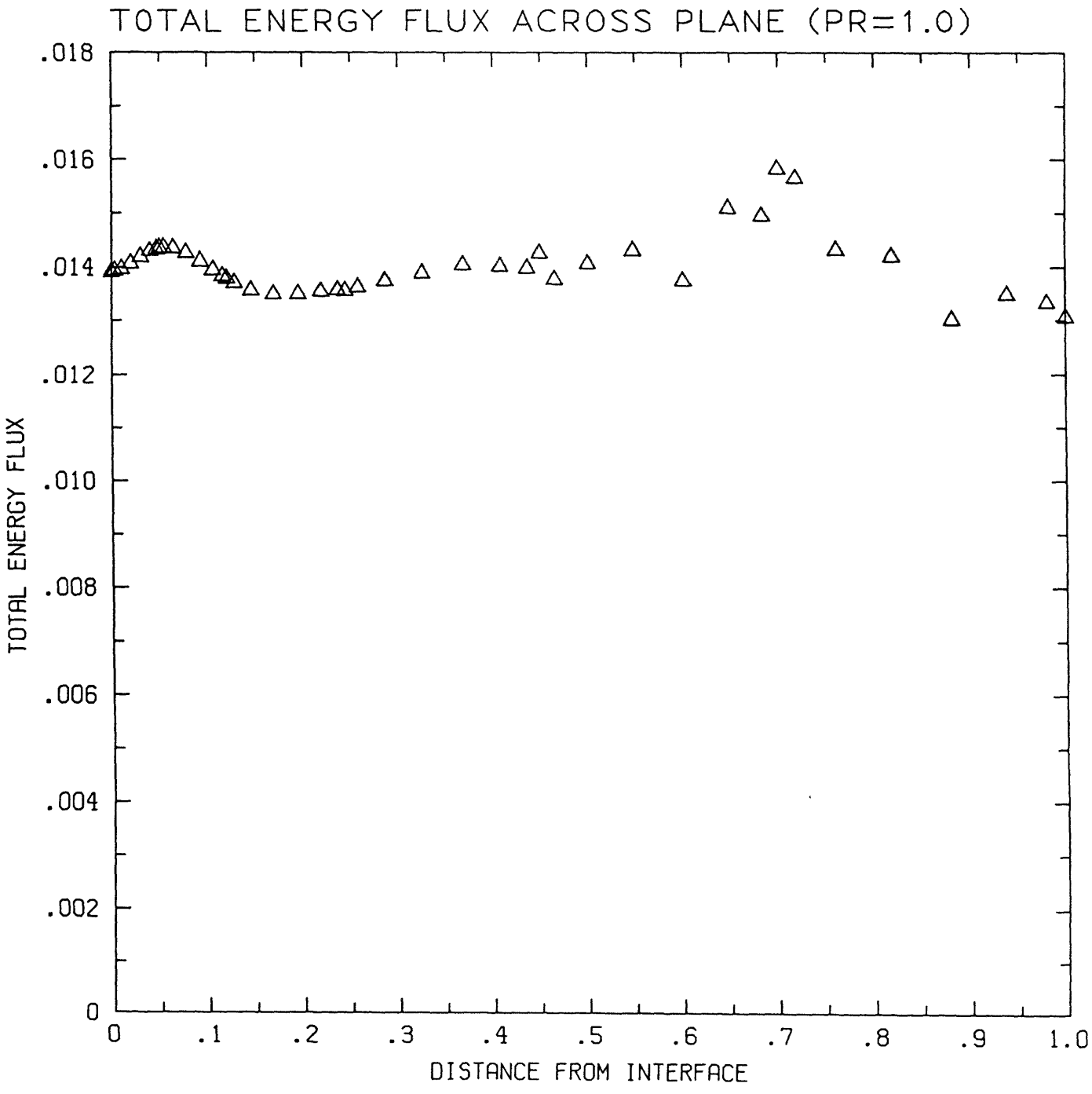
TOTAL ENERGY FLUX ACROSS PLANE (PR=1.0)
TOTAL ENERGY FLUX
.018
.016
.014
.012
.010
.008
.006
.004
.002
0
0
.1
.2
.3
.4
.5
.6
.7
.8
.9
1.0
DISTANCE FROM INTERFACE

Figure 7.1.6

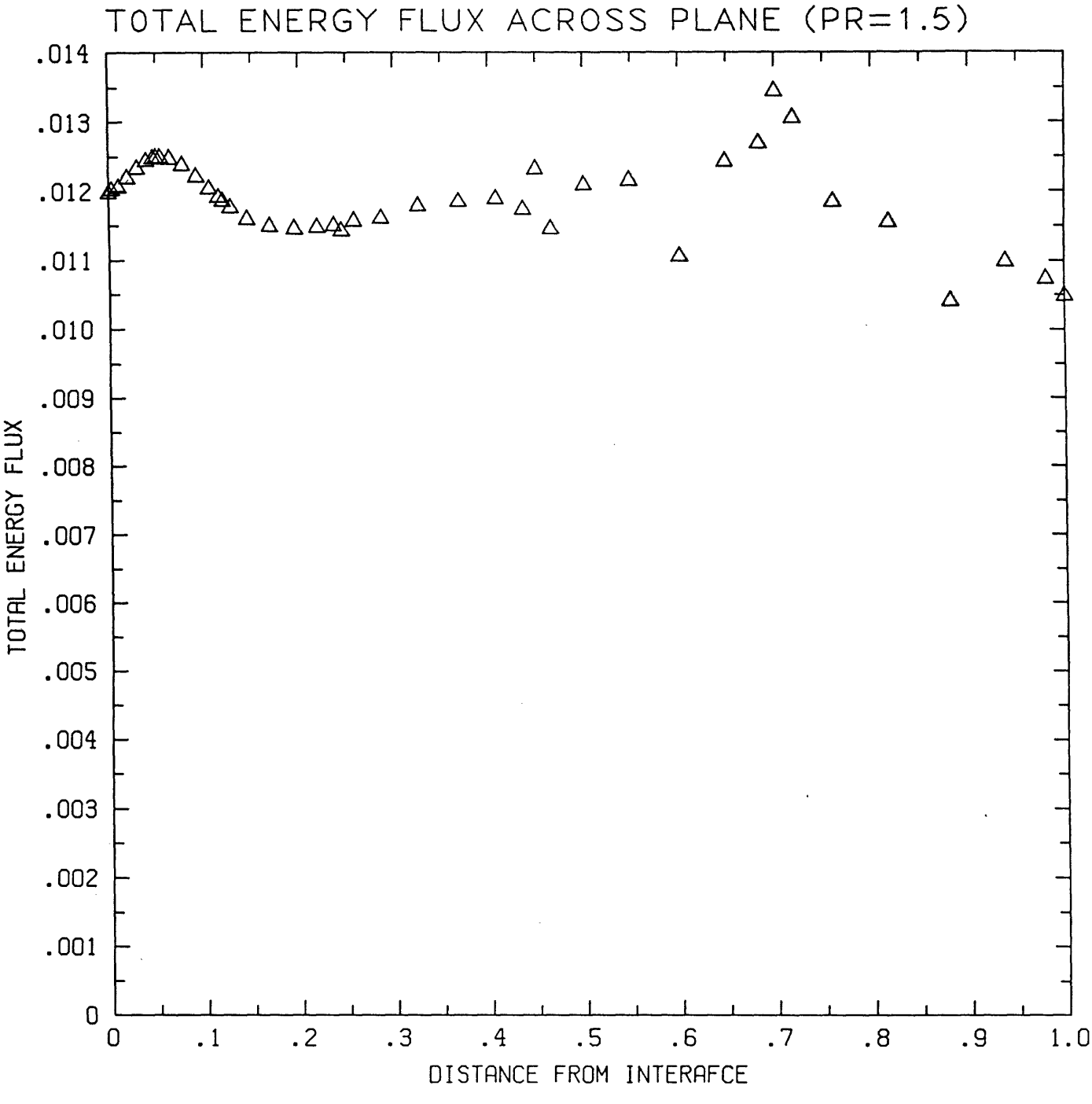
TOTAL ENERGY FLUX ACROSS PLANE (PR=1.5)
TOTAL ENERGY FLUX
.014
.013
.012
.011
.010
.009
.008
.007
.006
.005
.004
.003
.002
.001
0
0
.1
.2
.3
.4
.5
.6
.7
.8
.9
1.0
DISTANCE FROM INTERAFCE

Figure 7.1.7

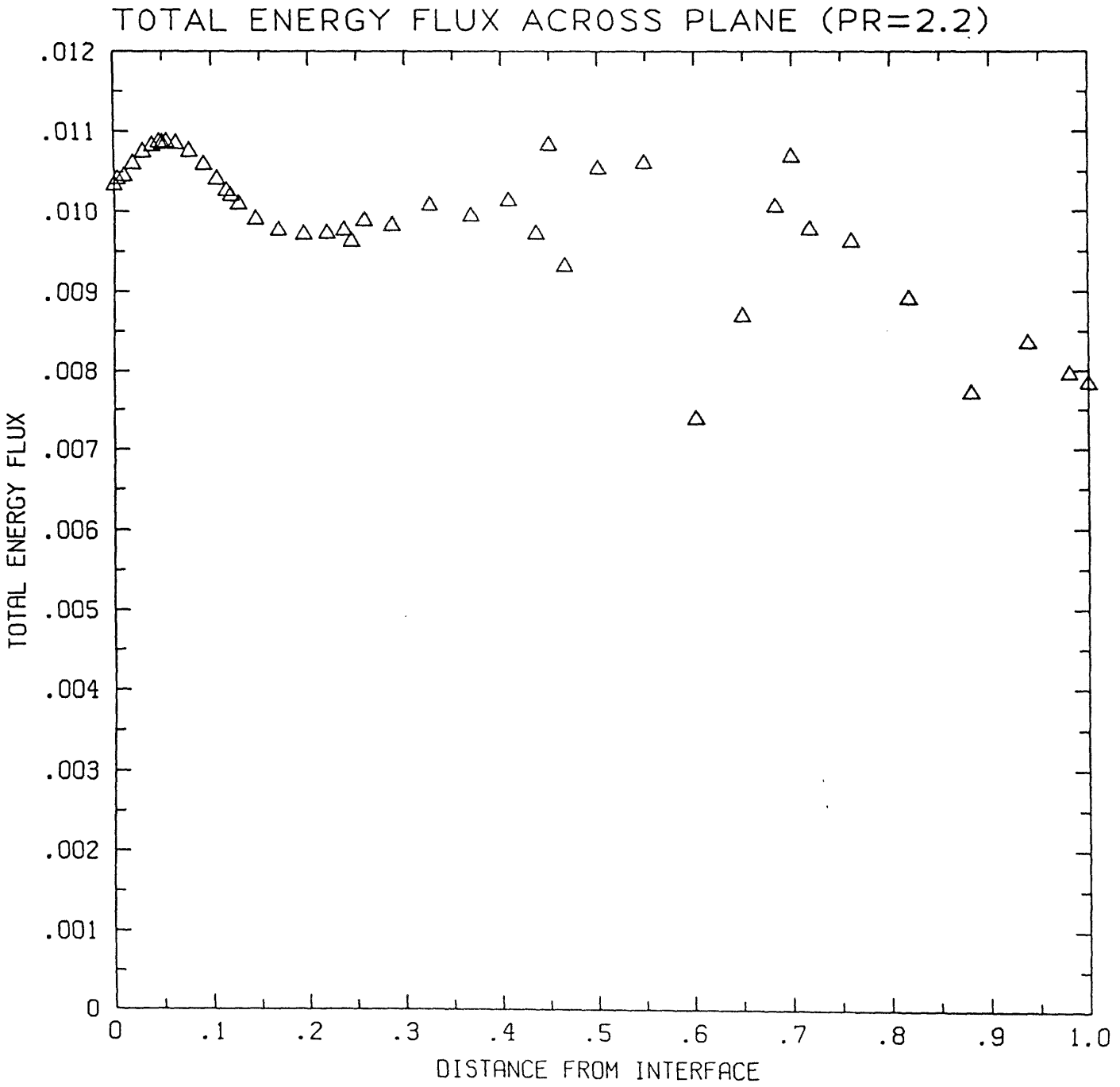
TOTAL ENERGY FLUX ACROSS PLANE (PR=2.2)
TOTAL ENERGY FLUX
.012
.011
.010
.009
.008
.007
.006
.005
.004
.003
.002
.001
0
0
.1
.2
.3
.4
.5
.6
.7
.8
.9
1.0
DISTANCE FROM INTERFACE

Figure 7.1.8

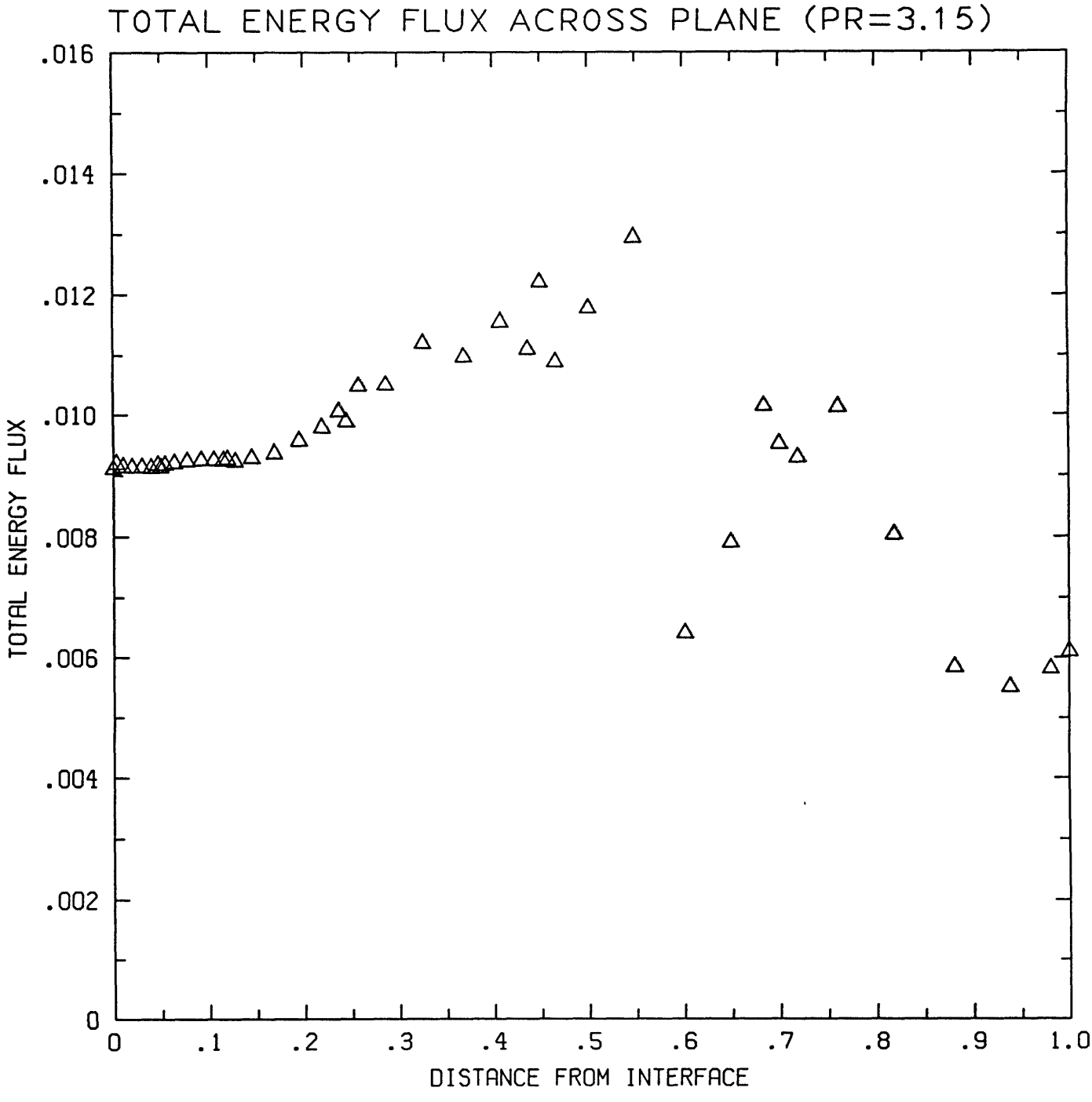
TOTAL ENERGY FLUX ACROSS PLANE (PR=3.15)
TOTAL ENERGY FLUX
.016
.014
.012
.010
.008
.006
.004
.002
0
0
.1
.2
.3
.4
.5
.6
.7
.8
.9
1.0
DISTANCE FROM INTERFACE

Figure 7.1.9

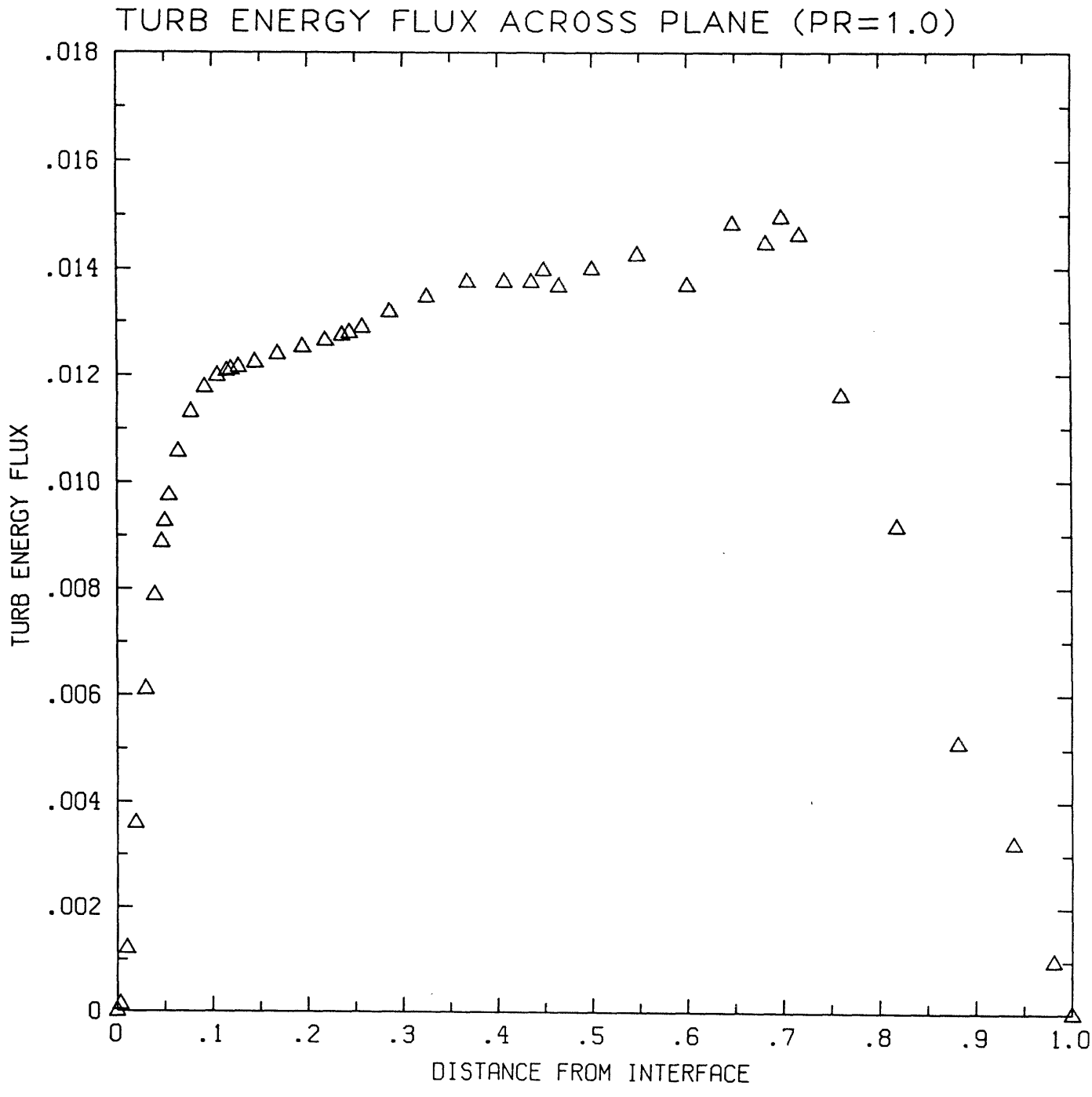
TURB ENERGY FLUX ACROSS PLANE (PR=1.0)
TURB ENERGY FLUX
.018
.016
.014
.012
.010
.008
.006
.004
.002
0
0
.1
.2
.3
.4
.5
.6
.7
.8
.9
1.0
DISTANCE FROM INTERFACE

Figure 7.1.10

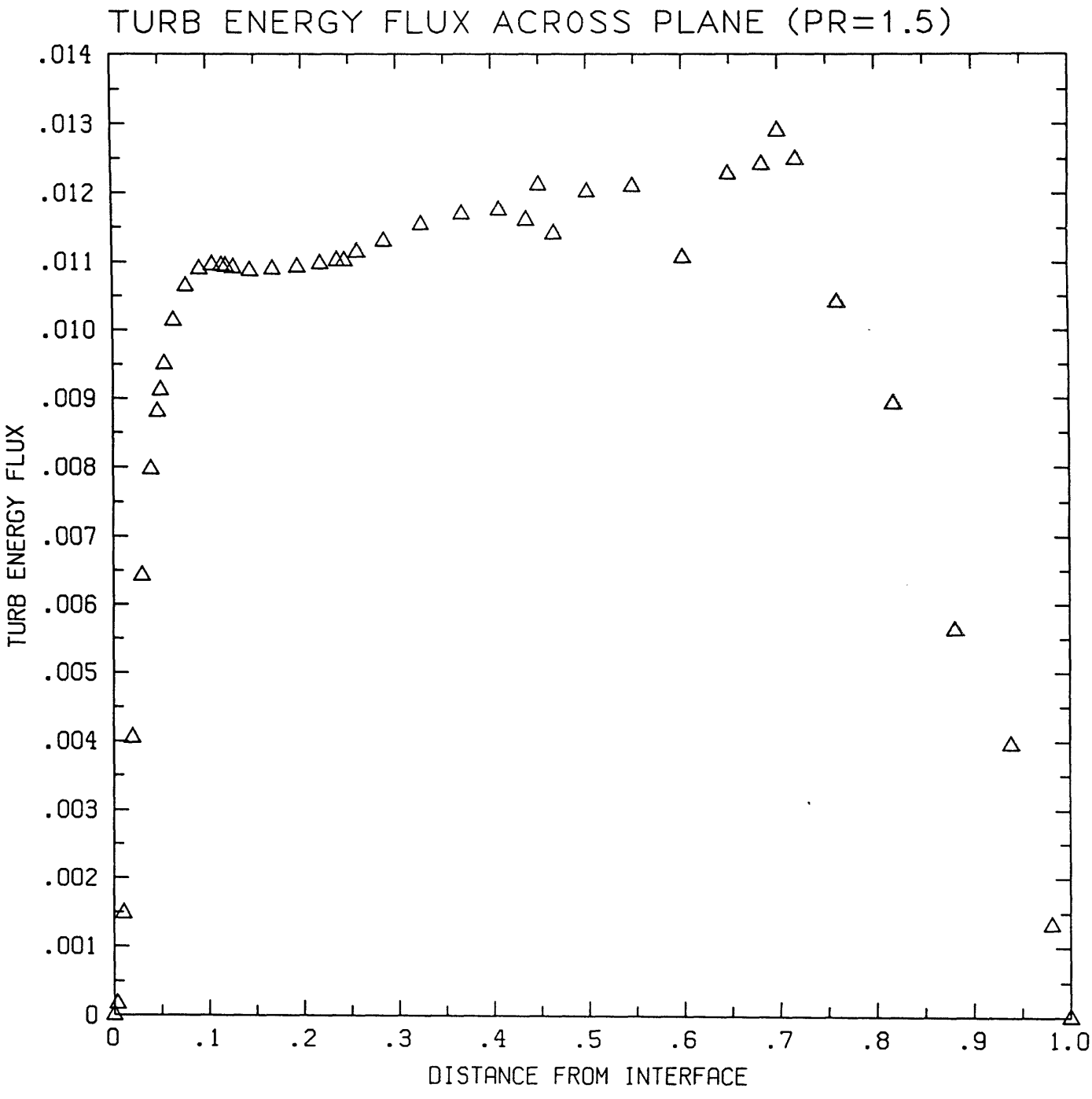
TURB ENERGY FLUX ACROSS PLANE (PR=1.5)
TURB ENERGY FLUX
.014
.013
.012
.011
.010
.009
.008
.007
.006
.005
.004
.003
.002
.001
0
0
.1
.2
.3
.4
.5
.6
.7
.8
.9
1.0
DISTANCE FROM INTERFACE

Figure 7.1.11

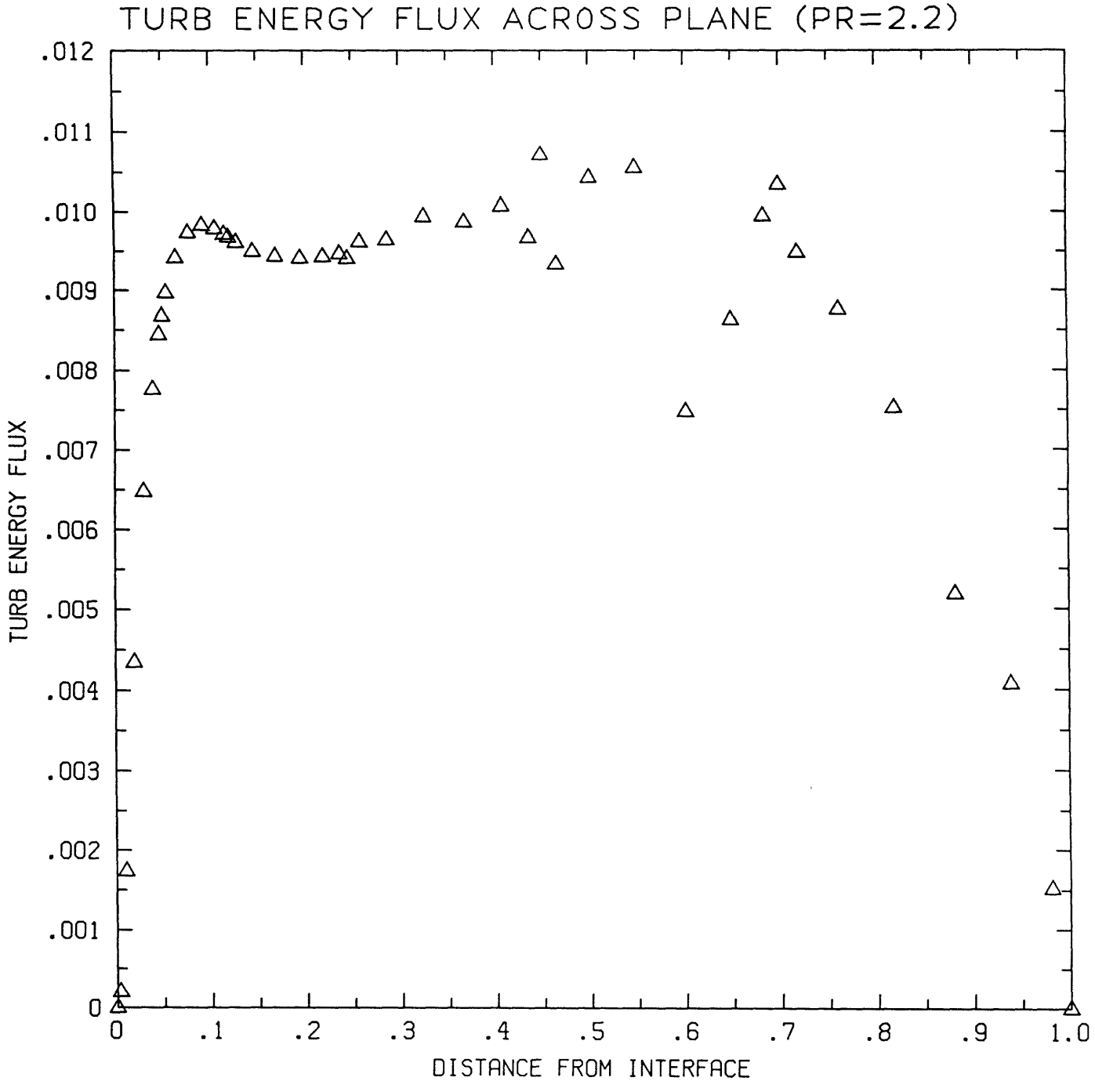
TURB ENERGY FLUX ACROSS PLANE (PR=2.2)
TURB ENERGY FLUX
.012
.011
.010
.009
.008
.007
.006
.005
.004
.003
.002
.001
0
0
.1
.2
.3
.4
.5
.6
.7
.8
.9
1.0
DISTANCE FROM INTERFACE

Figure 7.1.12

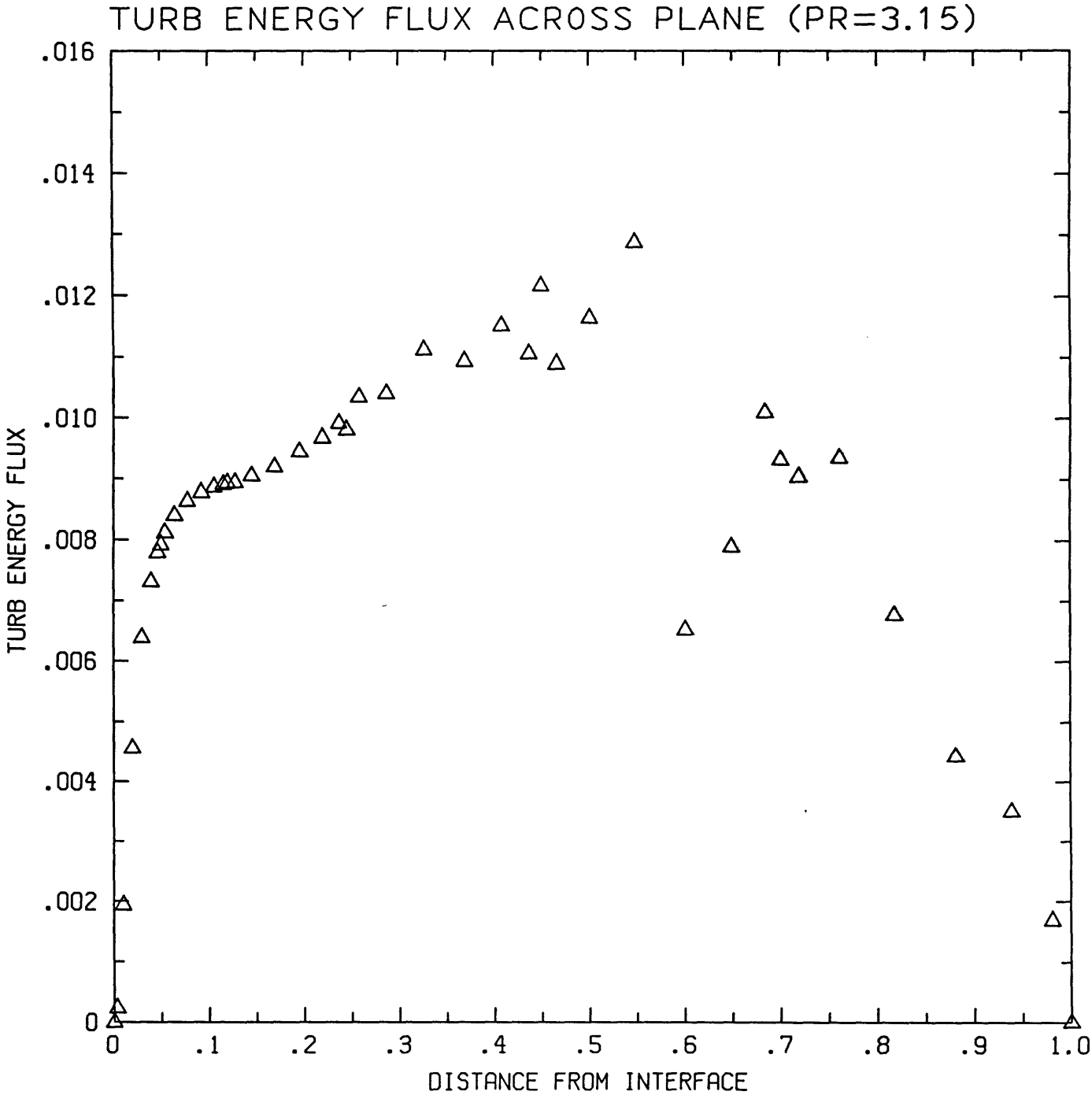
TURB ENERGY FLUX ACROSS PLANE (PR=3.15)
TURB ENERGY FLUX
.016
.014
.012
.010
.008
.006
.004
.002
0
0
.1
.2
.3
.4
.5
.6
.7
.8
.9
1.0
DISTANCE FROM INTERFACE

Figure 7.1.13

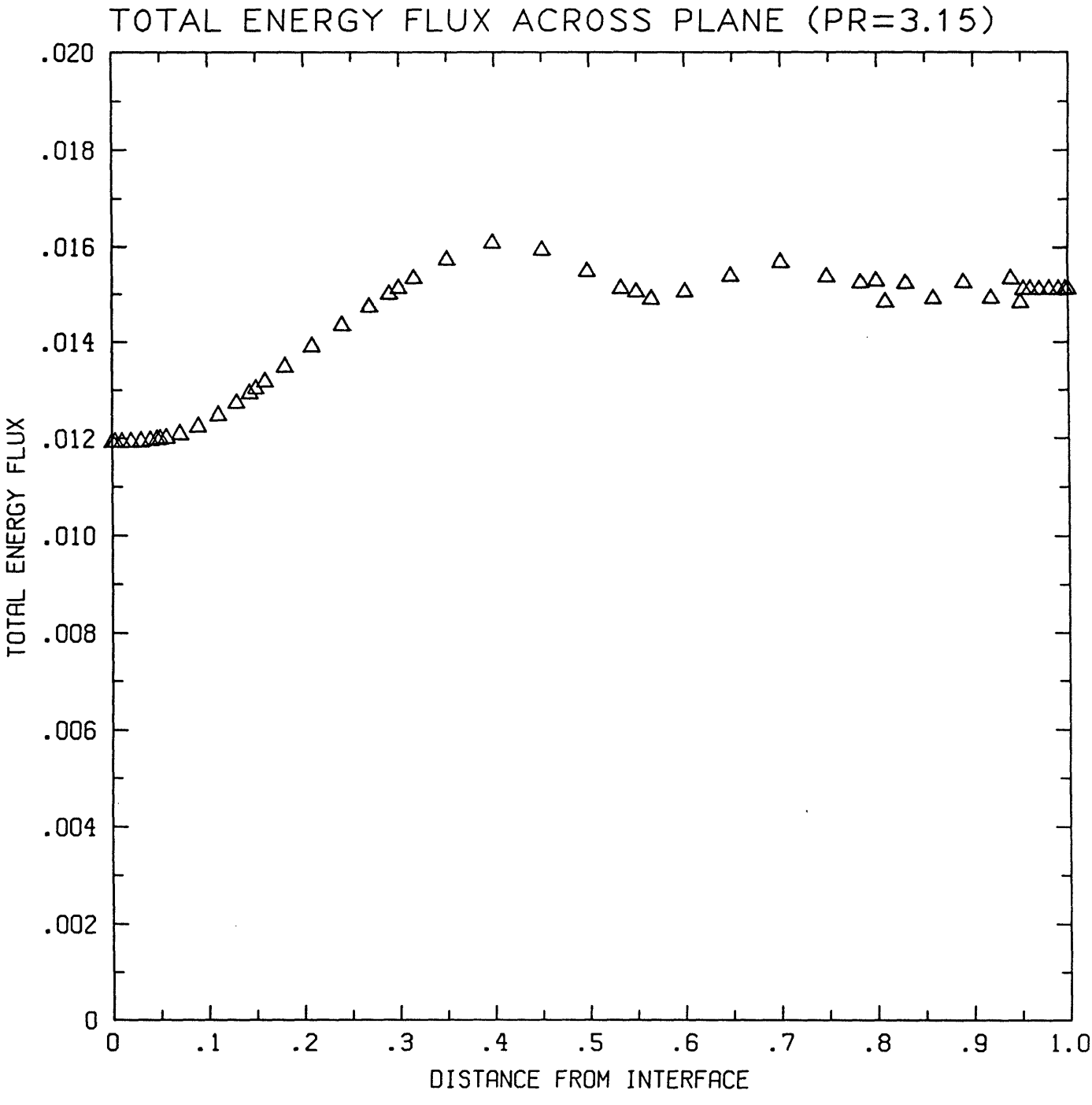
TOTAL ENERGY FLUX ACROSS PLANE (PR=3.15)
TOTAL ENERGY FLUX
.020
.018
.016
.014
.012
.010
.008
.006
.004
.002
0
0
.1
.2
.3
.4
.5
.6
.7
.8
.9
1.0
DISTANCE FROM INTERFACE

Figure 7.1.14

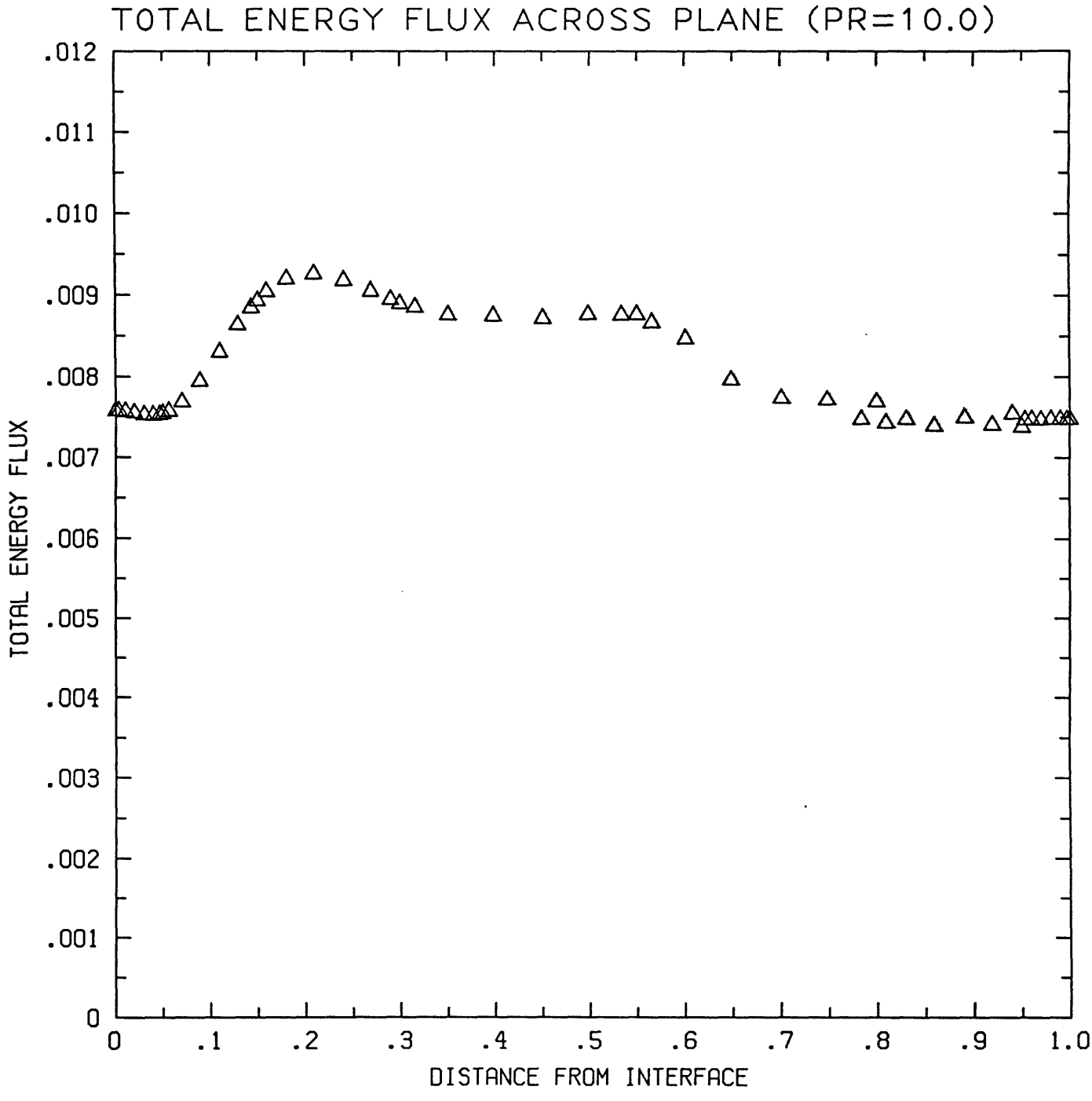
TOTAL ENERGY FLUX ACROSS PLANE (PR=10.0)
TOTAL ENERGY FLUX
.012
.011
.010
.009
.008
.007
.006
.005
.004
.003
.002
.001
0
0
.1
.2
.3
.4
.5
.6
.7
.8
.9
1.0
DISTANCE FROM INTERFACE

Figure 7.1.15

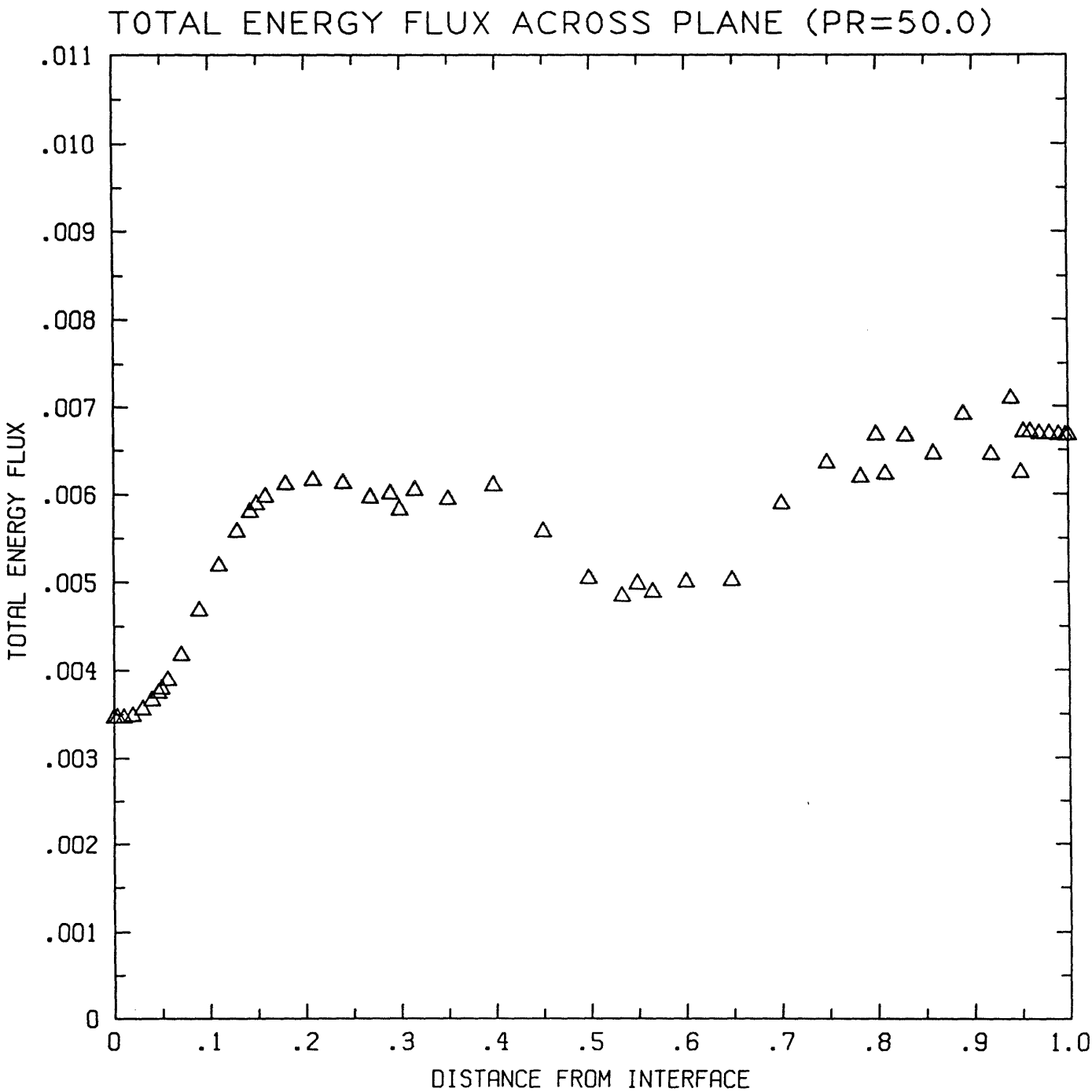
TOTAL ENERGY FLUX ACROSS PLANE (PR=50.0)
TOTAL ENERGY FLUX
.011
.010
.009
.008
.007
.006
.005
.004
.003
.002
.001
0
0
.1
.2
.3
.4
.5
.6
.7
.8
.9
1.0
DISTANCE FROM INTERFACE

Figure 7.1.16

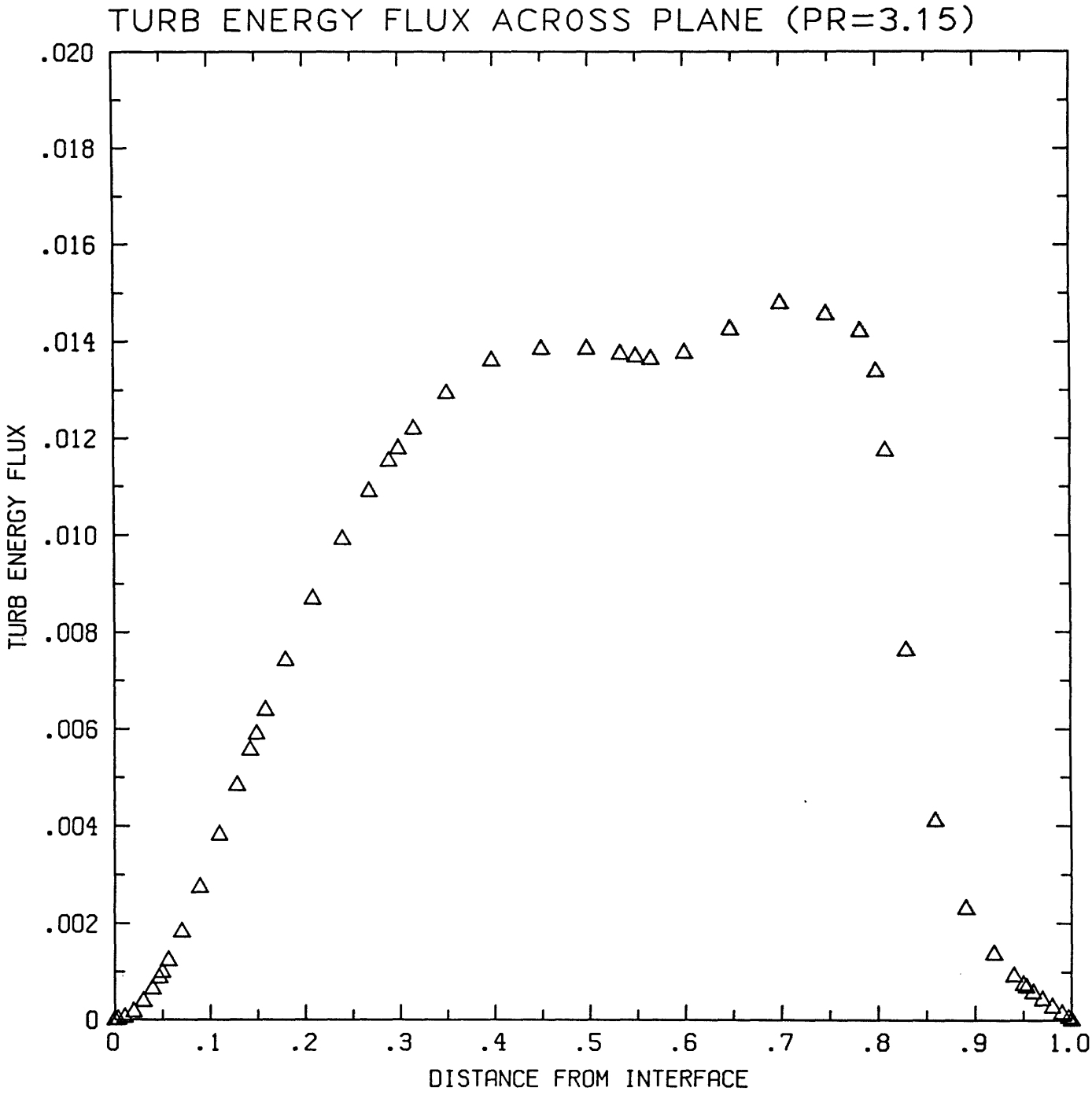
TURB ENERGY FLUX ACROSS PLANE (PR=3.15)
TURB ENERGY FLUX
.020
.018
.016
.014
.012
.010
.008
.006
.004
.002
0
0
.1
.2
.3
.4
.5
.6
.7
.8
.9
1.0
DISTANCE FROM INTERFACE

Figure 7.1.17

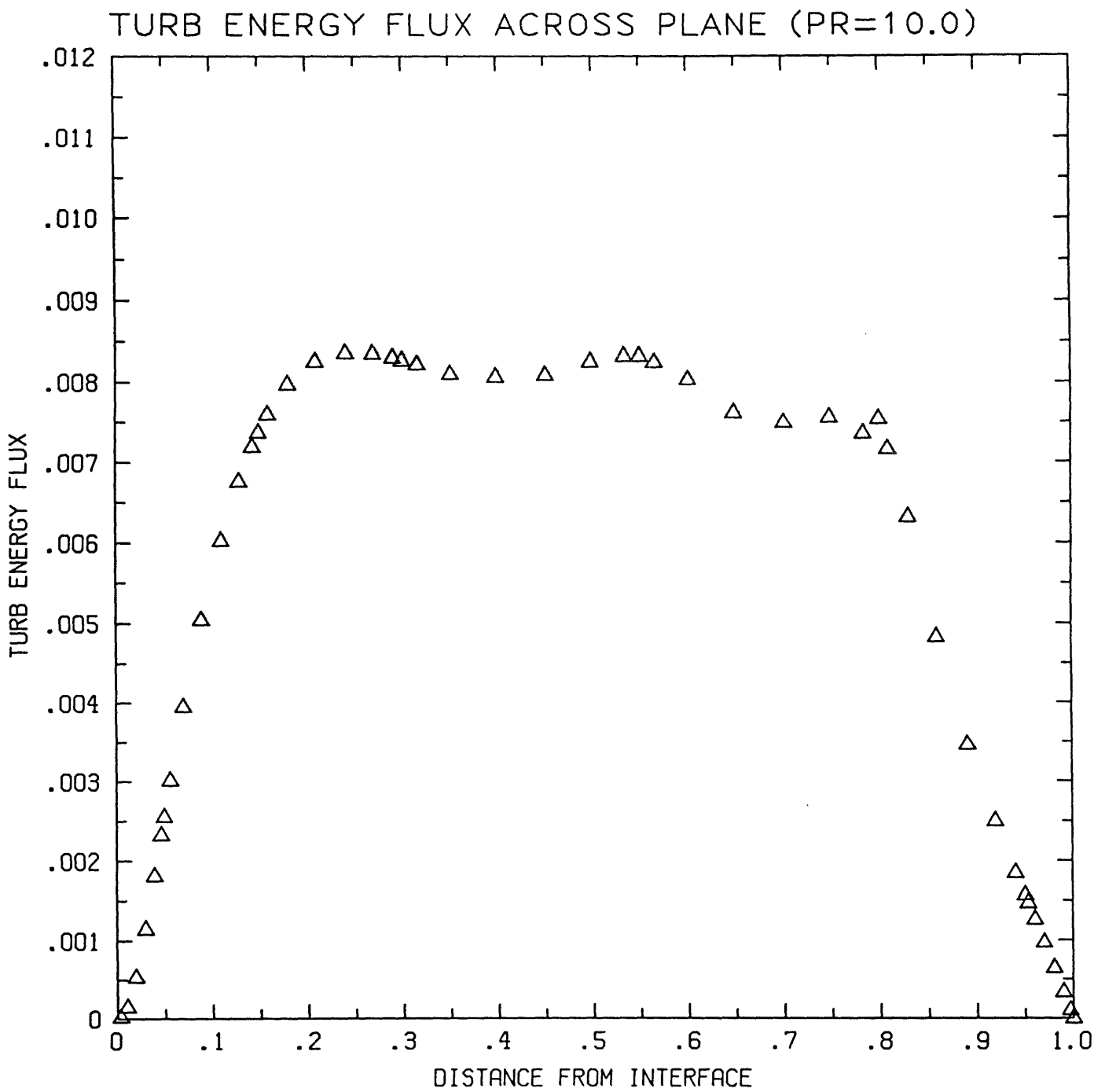
TURB ENERGY FLUX ACROSS PLANE (PR=10.0)
TURB ENERGY FLUX
.012
.011
.010
.009
.008
.007
.006
.005
.004
.003
.002
.001
0
0
.1
.2
.3
.4
.5
.6
.7
.8
.9
1.0
DISTANCE FROM INTERFACE

Figure 7.1.18

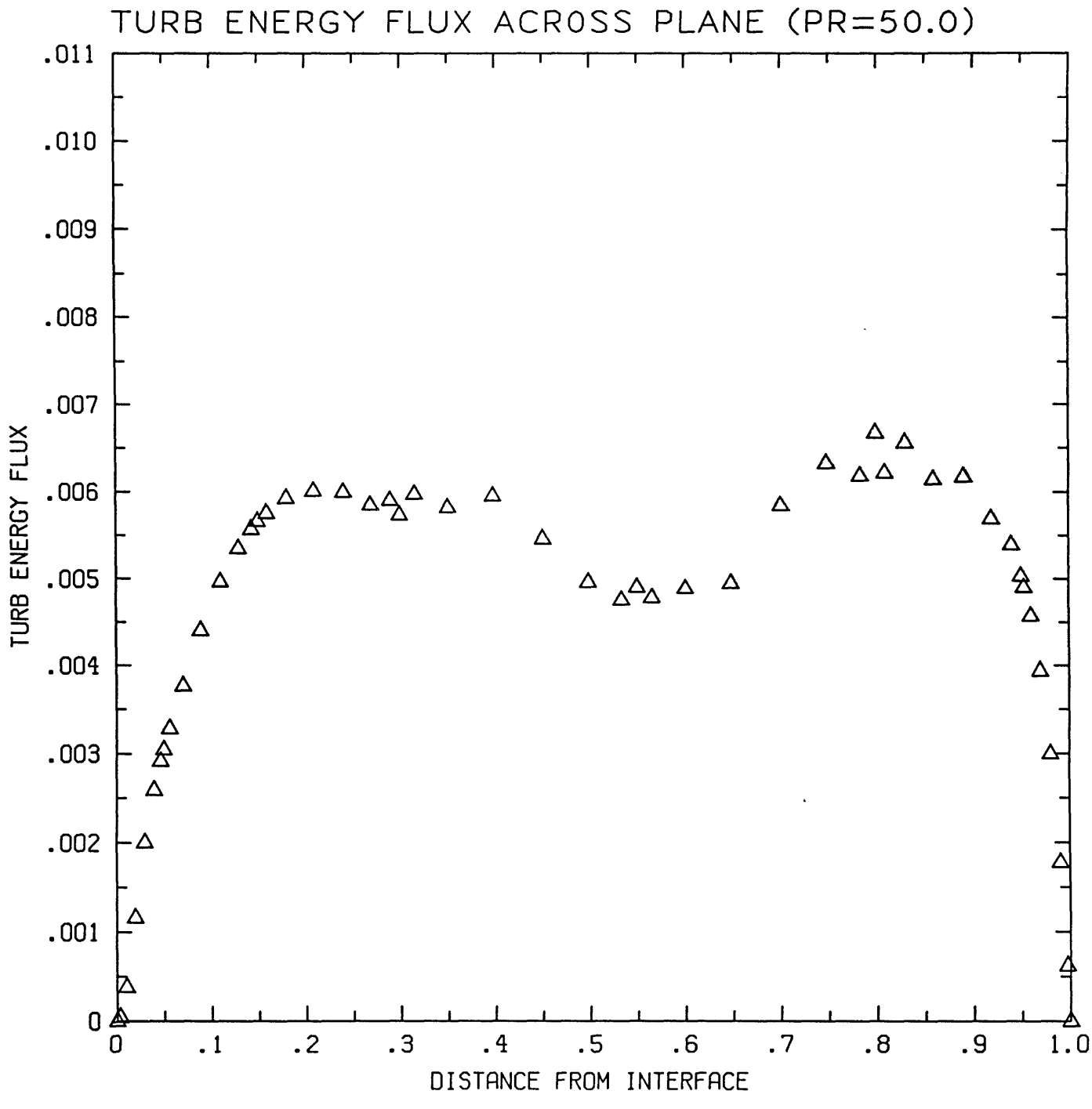
TURB ENERGY FLUX ACROSS PLANE (PR=50.0)
TURB ENERGY FLUX
.011
.010
.009
.008
.007
.006
.005
.004
.003
.002
.001
0
0
.1
.2
.3
.4
.5
.6
.7
.8
.9
1.0
DISTANCE FROM INTERFACE

Figure 7.1.19

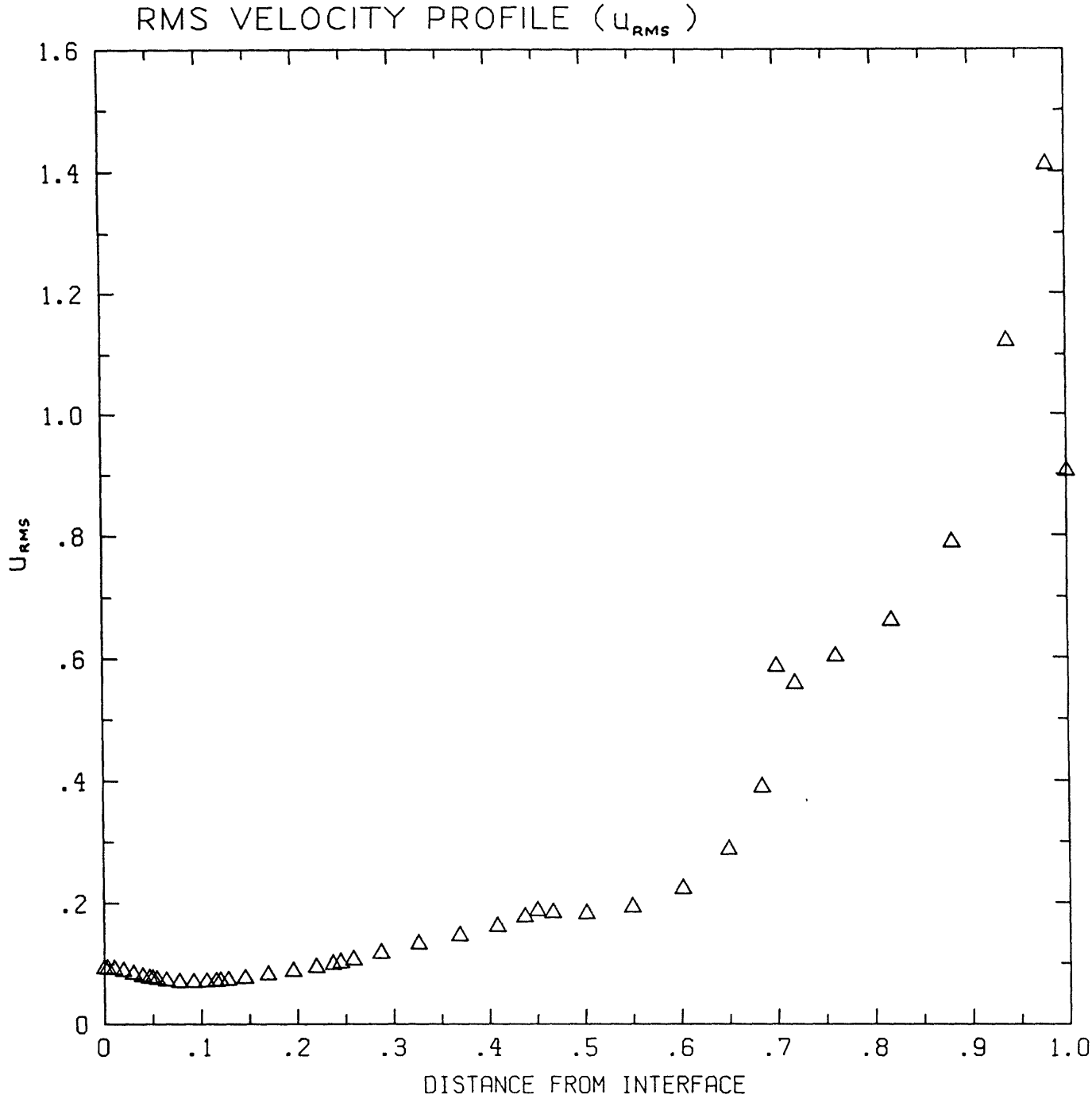
RMS VELOCITY PROFILE (u_{RMS})
1.6
1.4
1.2
1.0
.8
.6
.4
.2
0
U_{RMS}
0
.1
.2
.3
.4
.5
.6
.7
.8
.9
1.0
DISTANCE FROM INTERFACE

Figure 7.2.1

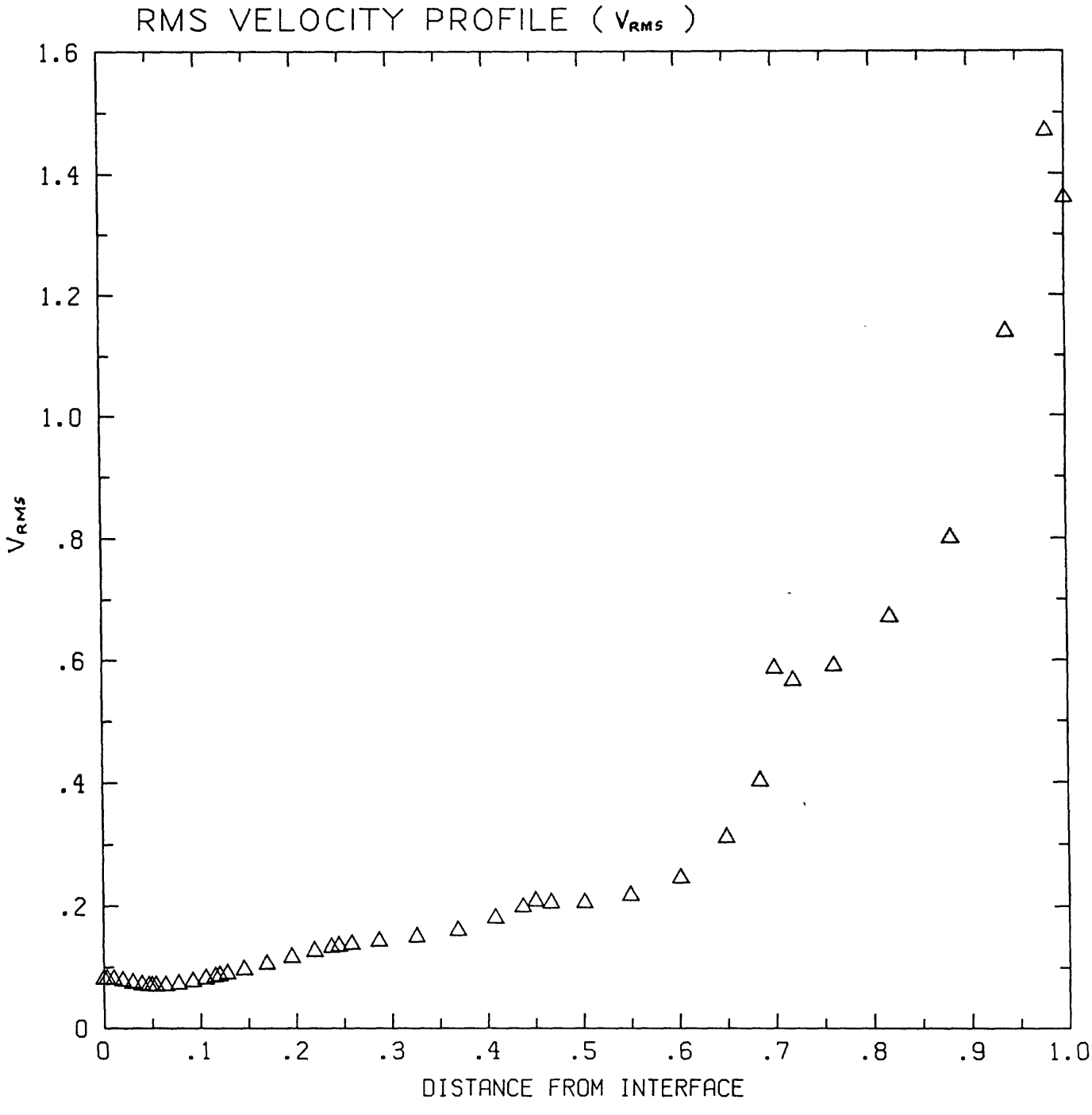
RMS VELOCITY PROFILE (V_{RMS})
1.6
1.4
1.2
1.0
.8
.6
.4
.2
0
V_{RMS}
0
.1
.2
.3
.4
.5
.6
.7
.8
.9
1.0
DISTANCE FROM INTERFACE

Figure 7.2.2

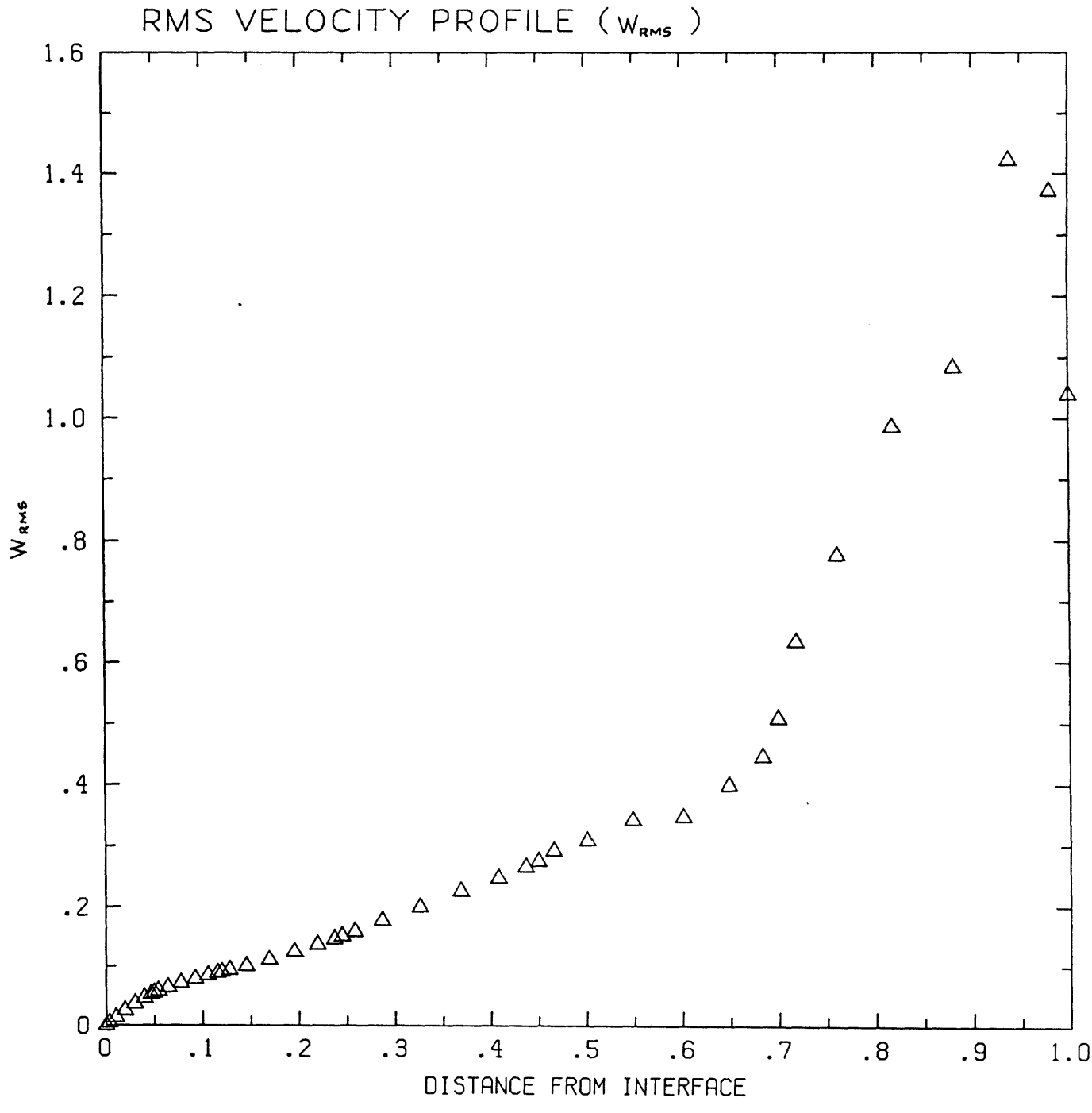
RMS VELOCITY PROFILE (W_{RMS})
1.6
1.4
1.2
1.0
.8
.6
.4
.2
0
W_{RMS}
0
.1
.2
.3
.4
.5
.6
.7
.8
.9
1.0
DISTANCE FROM INTERFACE

Figure 7.2.3

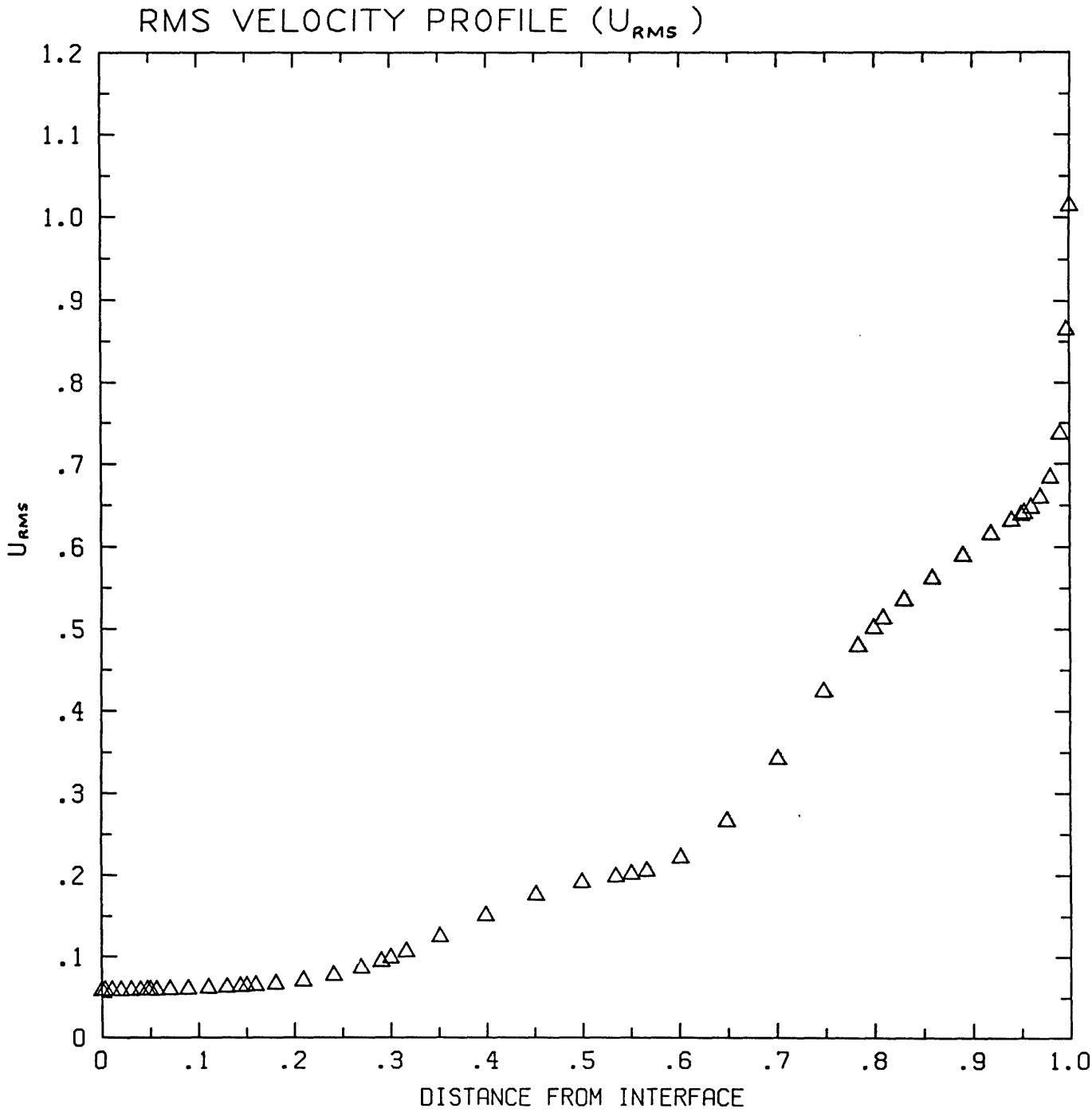
RMS VELOCITY PROFILE (U_{RMS})
1.2
1.1
1.0
.9
.8
.7
.6
.5
.4
.3
.2
.1
0
U_{RMS}
0
.1
.2
.3
.4
.5
.6
.7
.8
.9
1.0
DISTANCE FROM INTERFACE

Figure 7.2.4

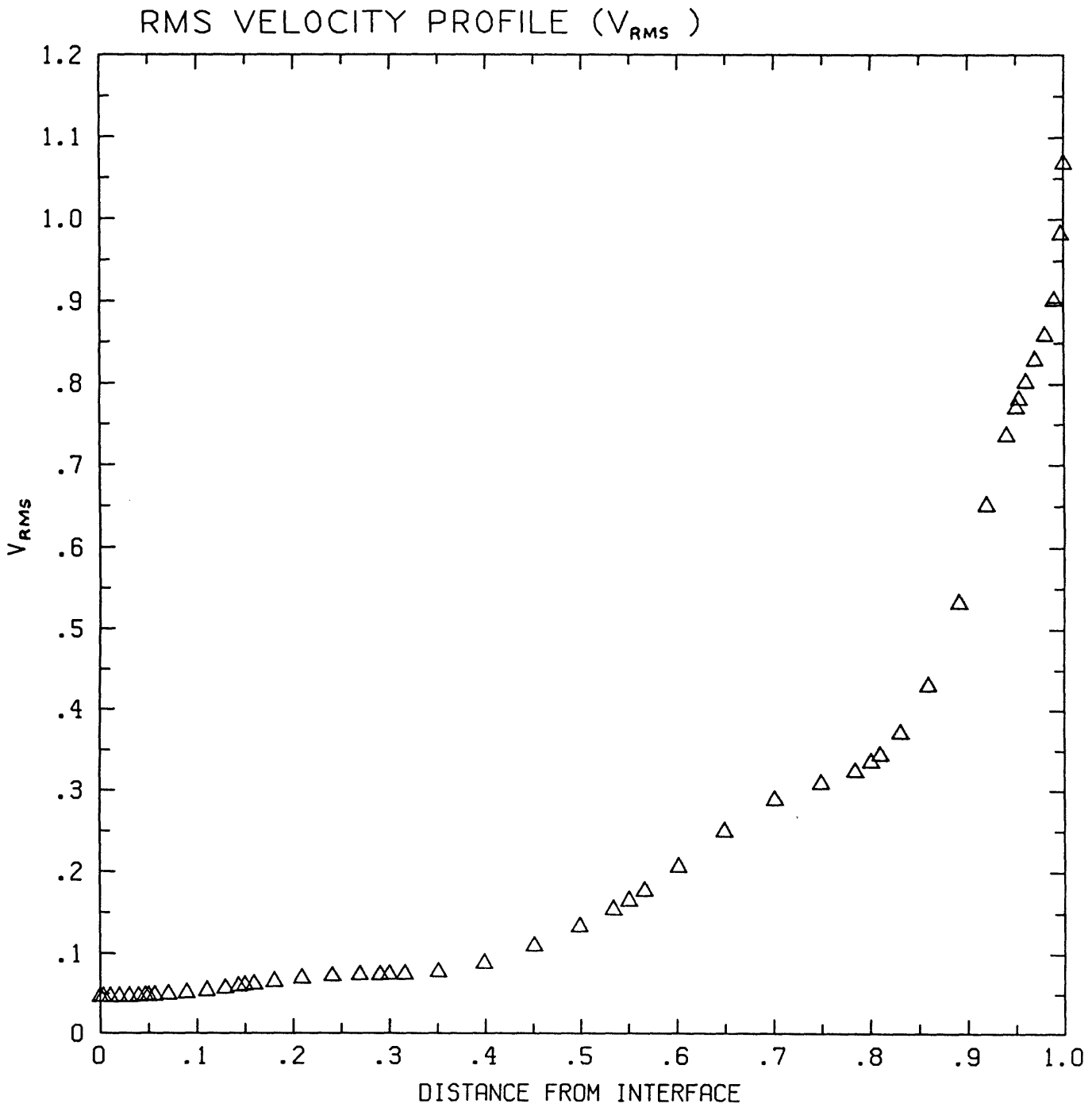
RMS VELOCITY PROFILE (V_{RMS})
1.2
1.1
1.0
.9
.8
.7
.6
.5
.4
.3
.2
.1
0
V_{RMS}
0
.1
.2
.3
.4
.5
.6
.7
.8
.9
1.0
DISTANCE FROM INTERFACE

Figure 7.2.5

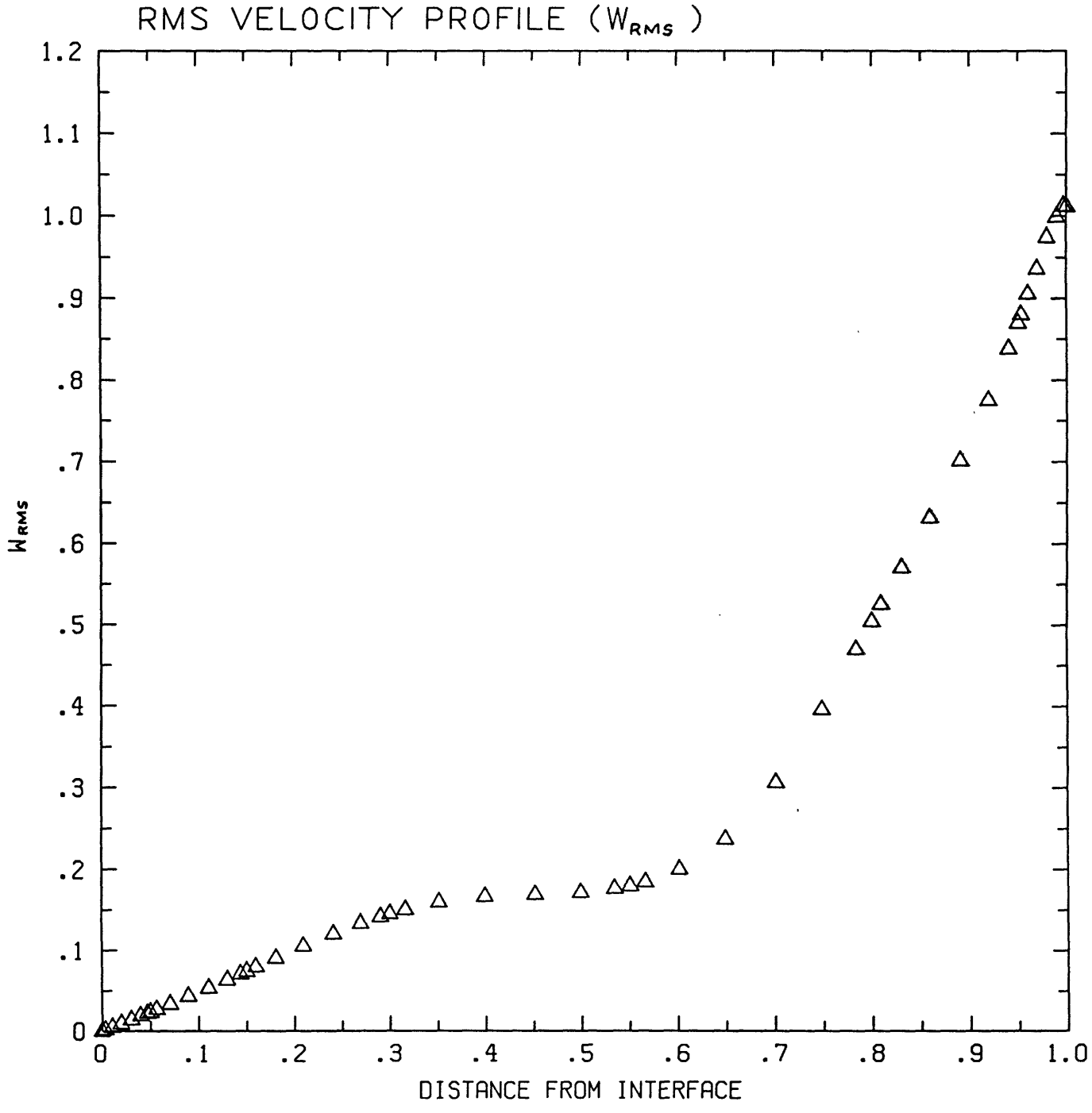
RMS VELOCITY PROFILE (W_{RMS})
1.2
1.1
1.0
.9
.8
.7
.6
.5
.4
.3
.2
.1
0
W_{RMS}
0
.1
.2
.3
.4
.5
.6
.7
.8
.9
1.0
DISTANCE FROM INTERFACE

Figure 7.2.6

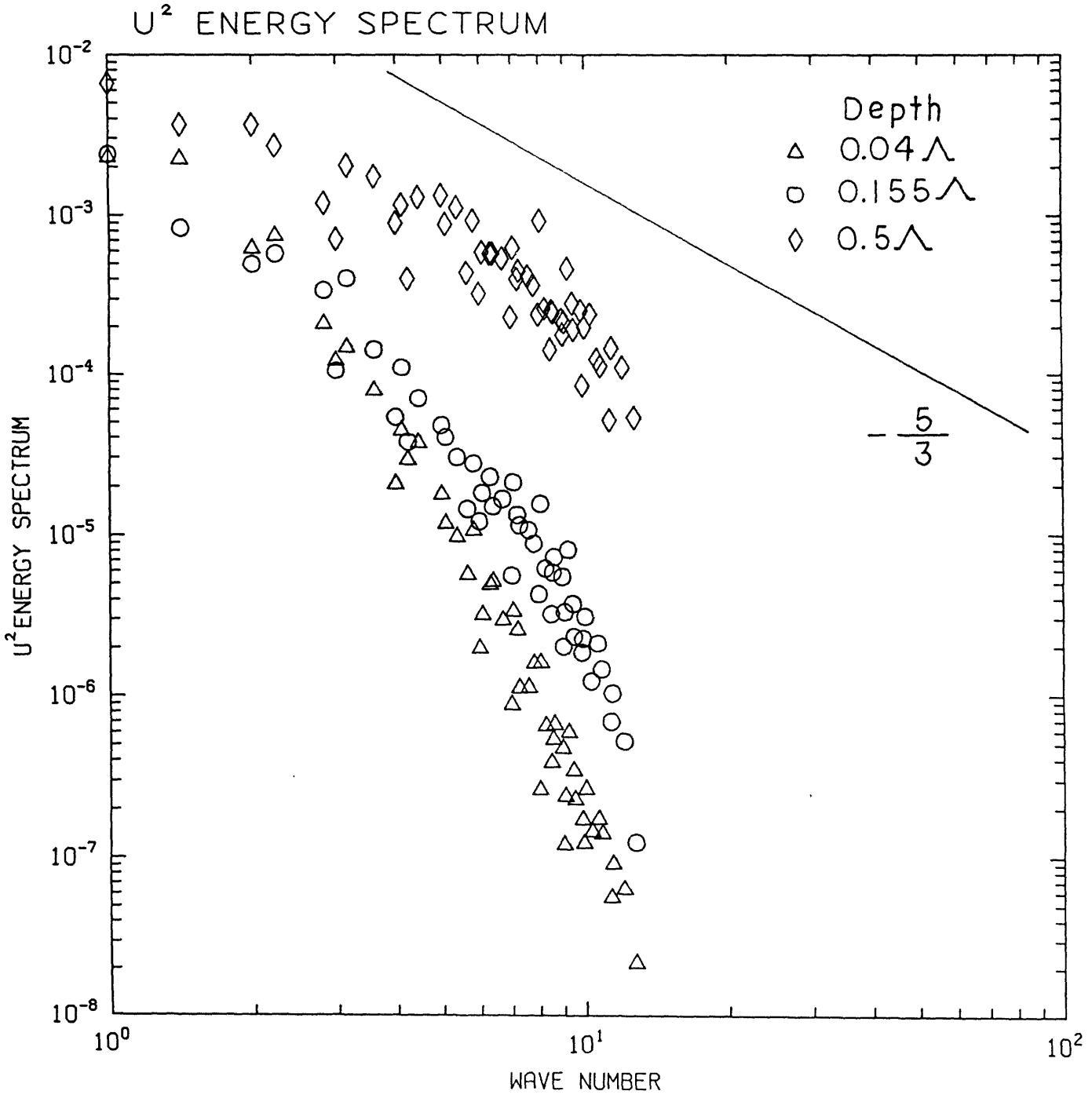
U² ENERGY SPECTRUM
Depth
0.04Λ
0.155Λ
0.5Λ
-5/3
U²ENERGY SPECTRUM
WAVE NUMBER
10⁻²
10⁻³
10⁻⁴
10⁻⁵
10⁻⁶
10⁻⁷
10⁻⁸
10⁰
10¹
10²

Figure 7.2.7

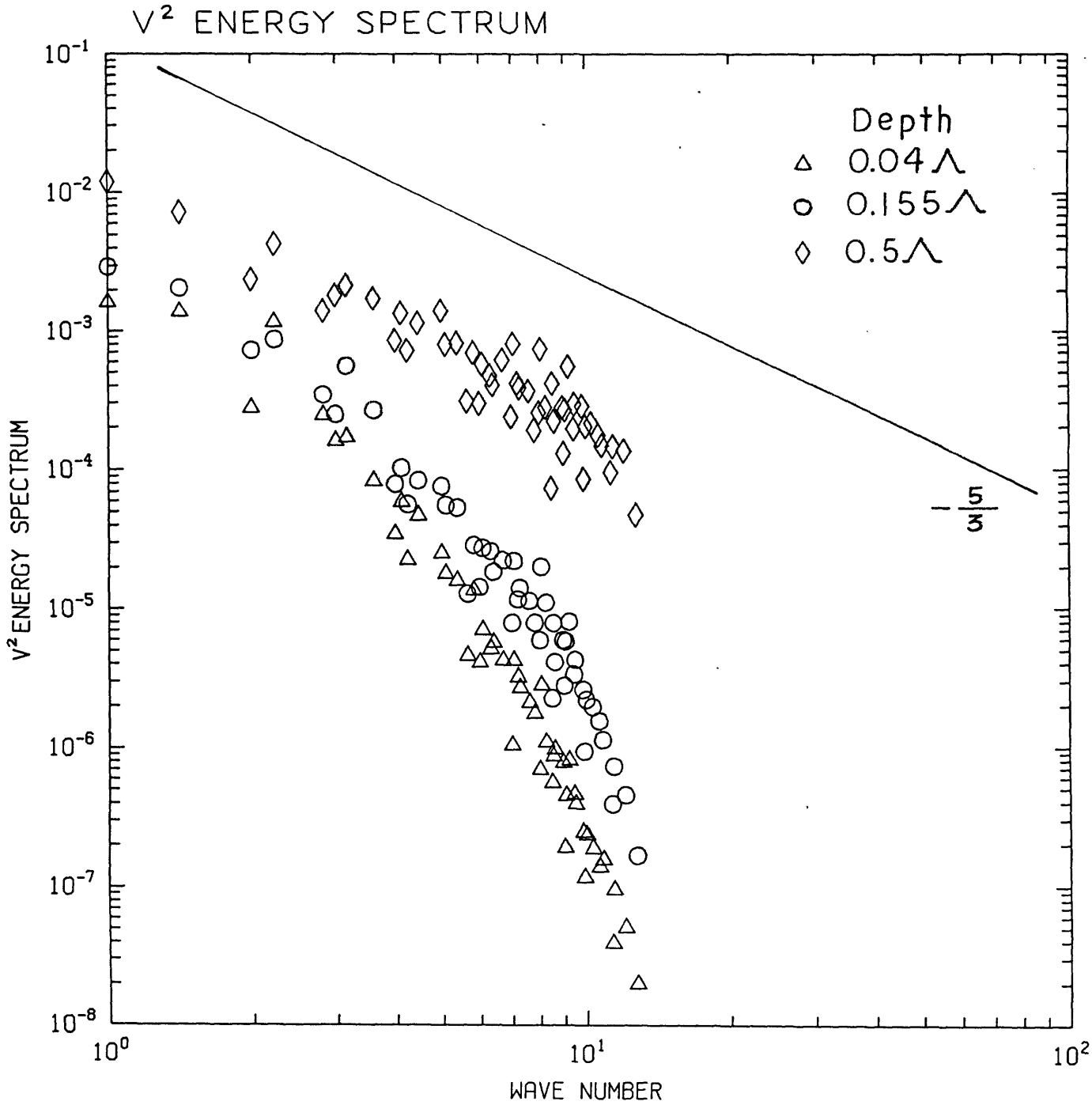
V² ENERGY SPECTRUM
Depth
0.04Λ
0.155Λ
0.5Λ
-5/3
V²ENERGY SPECTRUM
WAVE NUMBER
10⁻¹
10⁻²
10⁻³
10⁻⁴
10⁻⁵
10⁻⁶
10⁻⁷
10⁻⁸
10⁰
10¹
10²

Figure 7.2.8

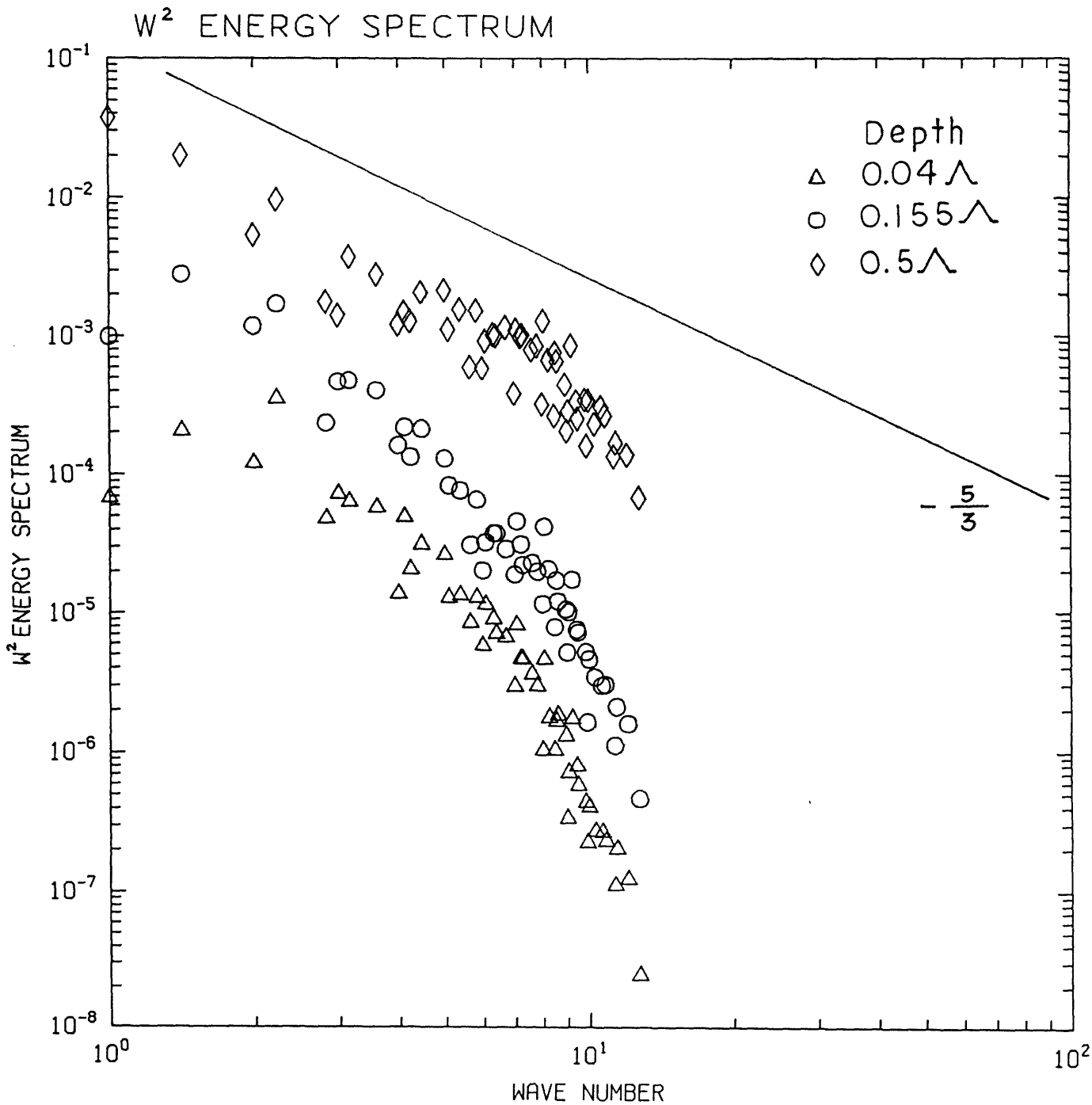
W² ENERGY SPECTRUM
Depth
0.04Λ
0.155Λ
0.5Λ
- 5/3
W² ENERGY SPECTRUM
WAVE NUMBER
10⁻¹
10⁻²
10⁻³
10⁻⁴
10⁻⁵
10⁻⁶
10⁻⁷
10⁻⁸
10⁰
10¹
10²

Figure 7.2.9

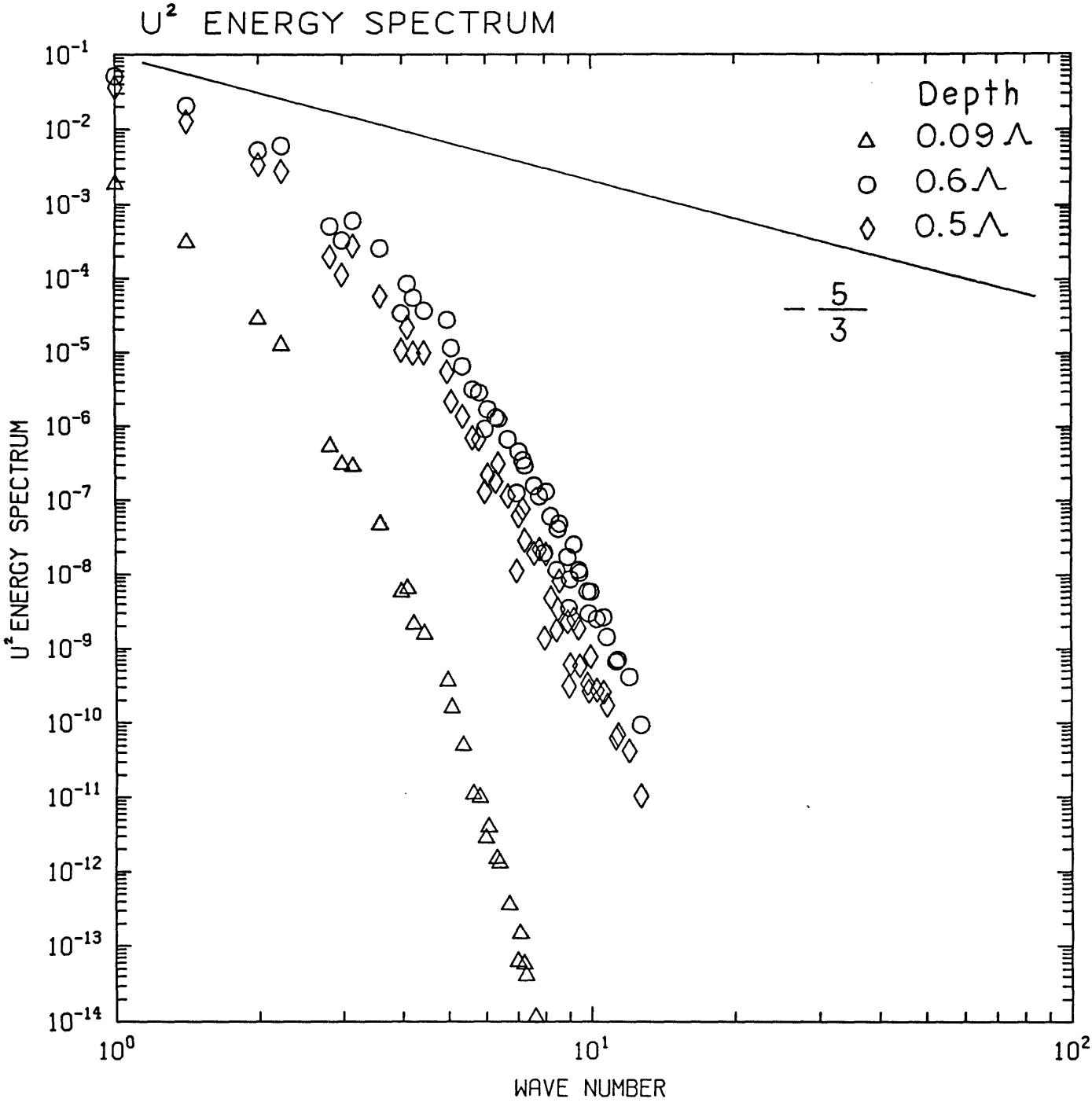
U² ENERGY SPECTRUM
Depth
0.09 Λ
0.6 Λ
0.5 Λ
- 5/3
U²ENERGY SPECTRUM
WAVE NUMBER
10⁻¹
10⁻²
10⁻³
10⁻⁴
10⁻⁵
10⁻⁶
10⁻⁷
10⁻⁸
10⁻⁹
10⁻¹⁰
10⁻¹¹
10⁻¹²
10⁻¹³
10⁻¹⁴
10⁰
10¹
10²

Figure 7.2.10

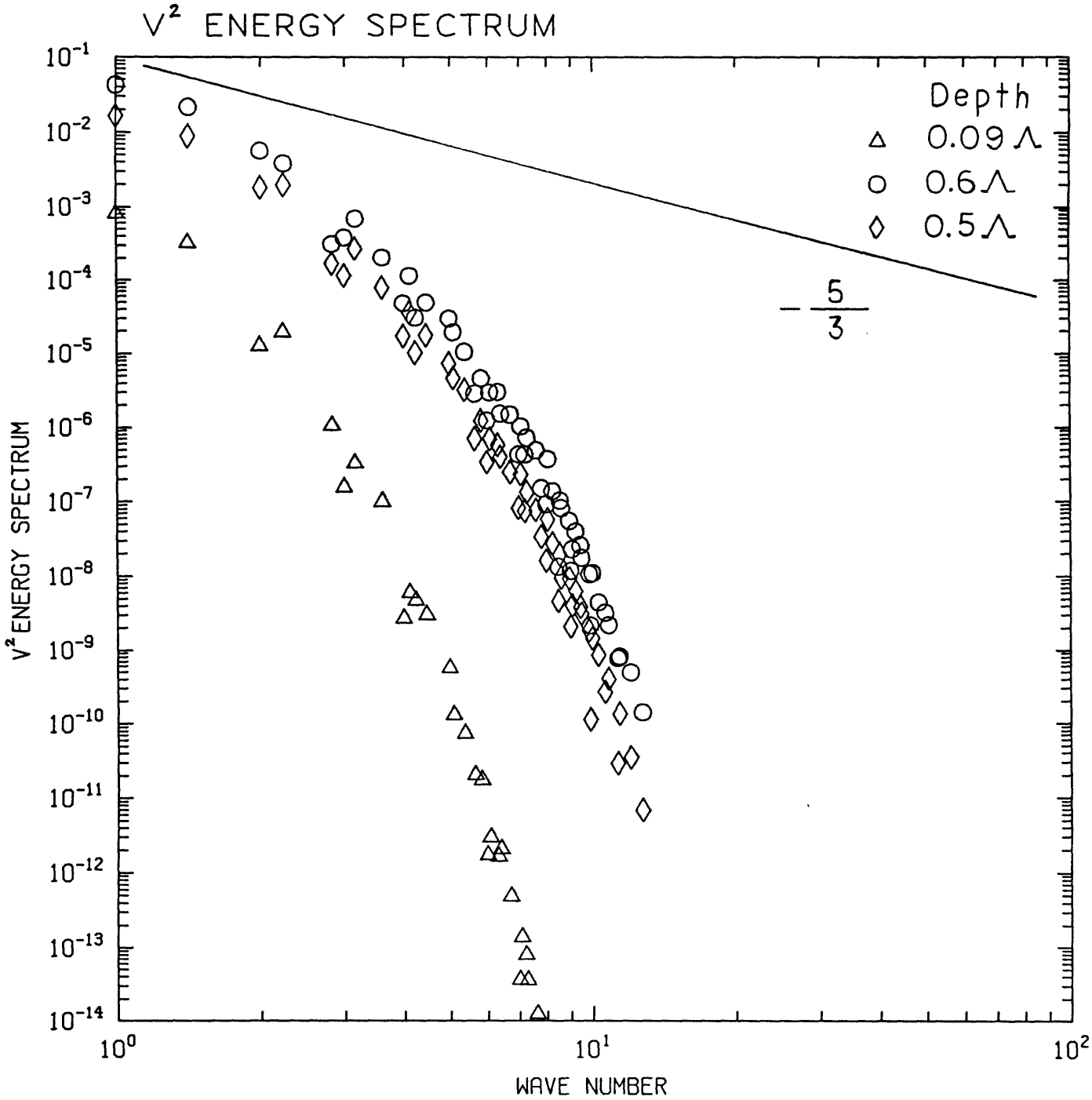
V² ENERGY SPECTRUM
Depth
0.09Λ
0.6Λ
0.5Λ
-5/3
V² ENERGY SPECTRUM
WAVE NUMBER
10⁻¹
10⁻²
10⁻³
10⁻⁴
10⁻⁵
10⁻⁶
10⁻⁷
10⁻⁸
10⁻⁹
10⁻¹⁰
10⁻¹¹
10⁻¹²
10⁻¹³
10⁻¹⁴
10⁰
10¹
10²

Figure 7.2.11

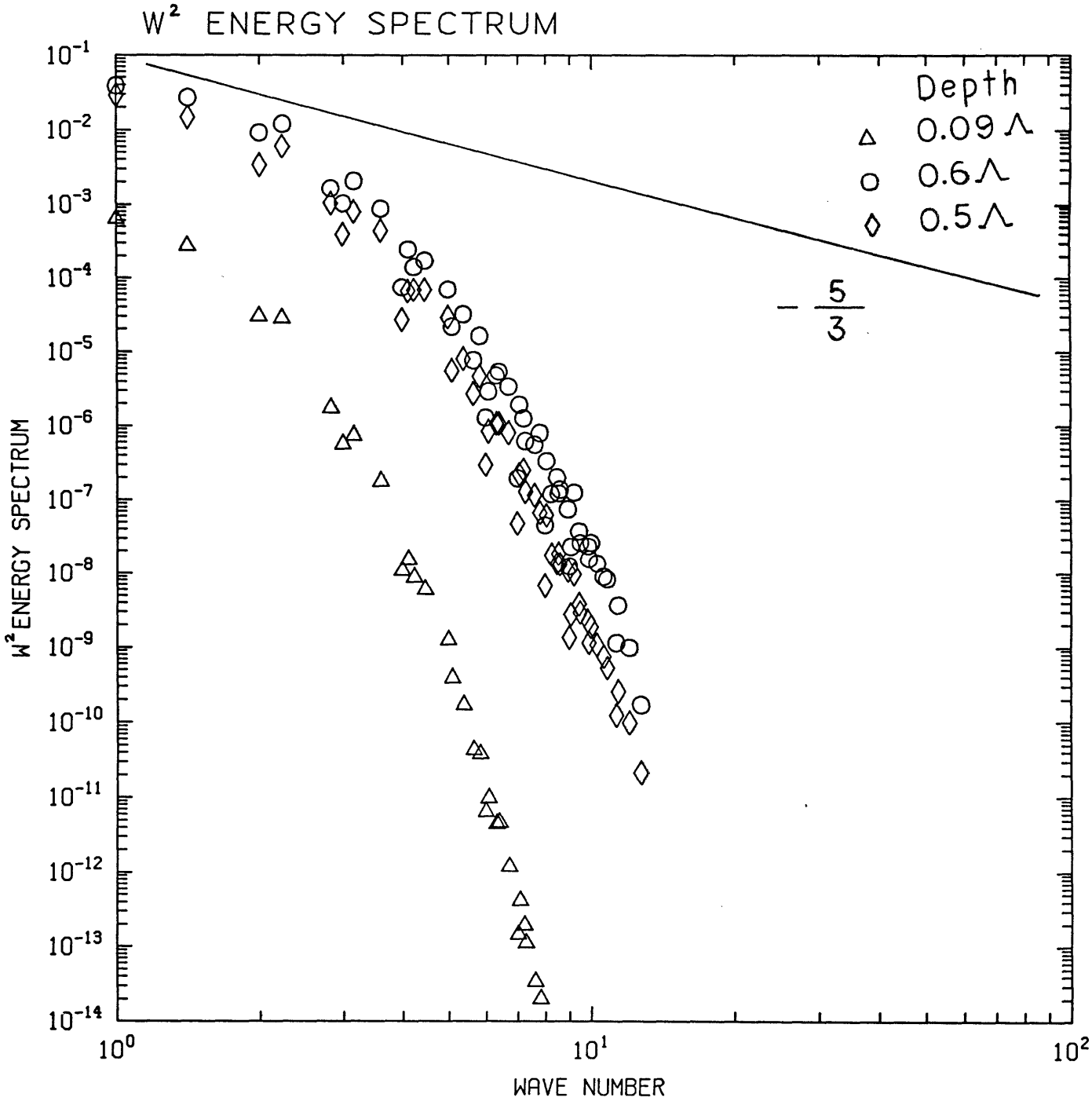
W² ENERGY SPECTRUM
Depth
0.09 Λ
0.6 Λ
0.5 Λ
- 5/3
W²ENERGY SPECTRUM
WAVE NUMBER
10⁻¹
10⁻²
10⁻³
10⁻⁴
10⁻⁵
10⁻⁶
10⁻⁷
10⁻⁸
10⁻⁹
10⁻¹⁰
10⁻¹¹
10⁻¹²
10⁻¹³
10⁻¹⁴
10⁰
10¹
10²

Figure 7.2.12

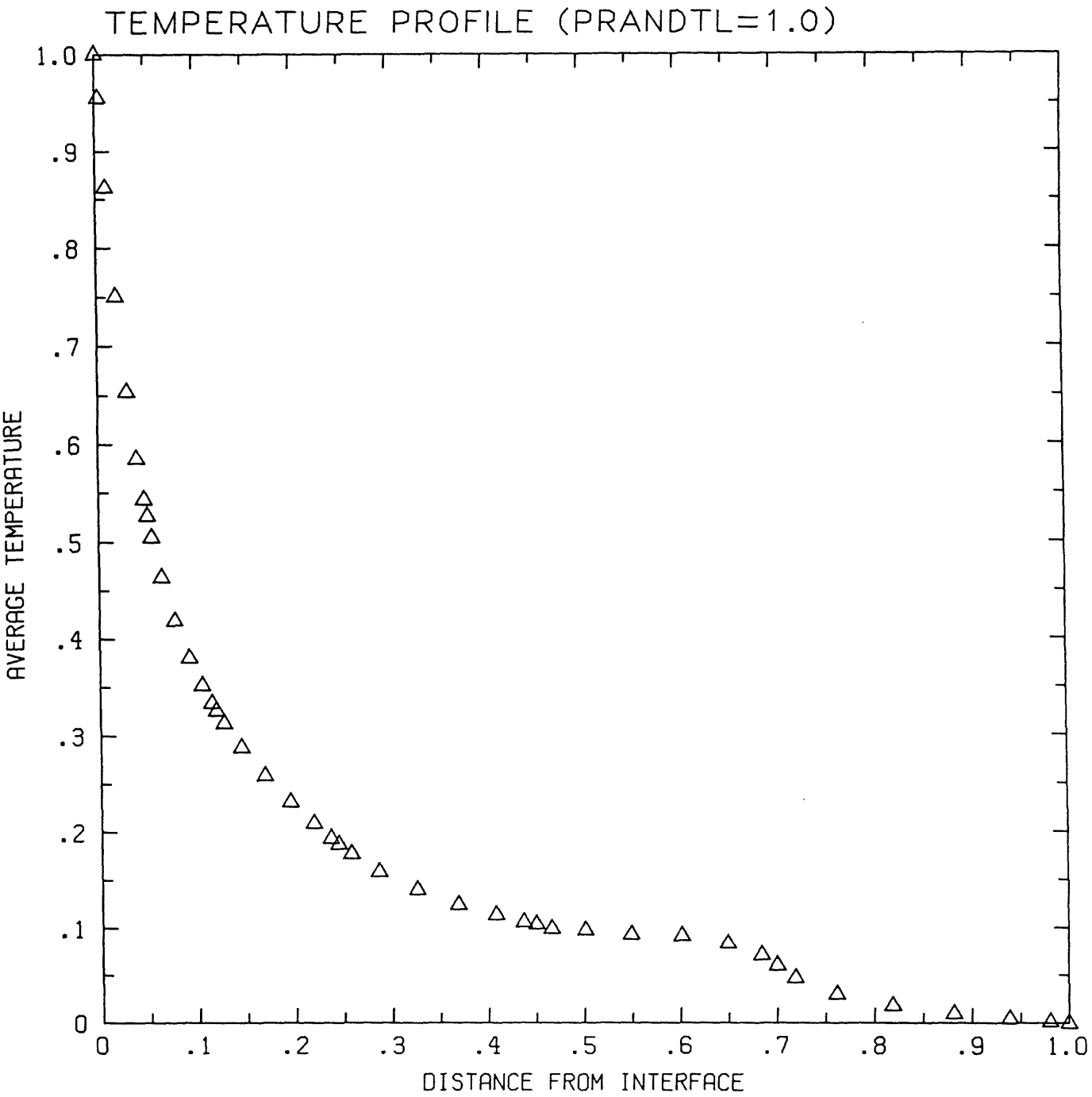
TEMPERATURE PROFILE (PRANDTL=1.0)
AVERAGE TEMPERATURE
DISTANCE FROM INTERFACE
1.0
.9
.8
.7
.6
.5
.4
.3
.2
.1
0
0
.1
.2
.3
.4
.5
.6
.7
.8
.9
1.0

Figure 7.3.1

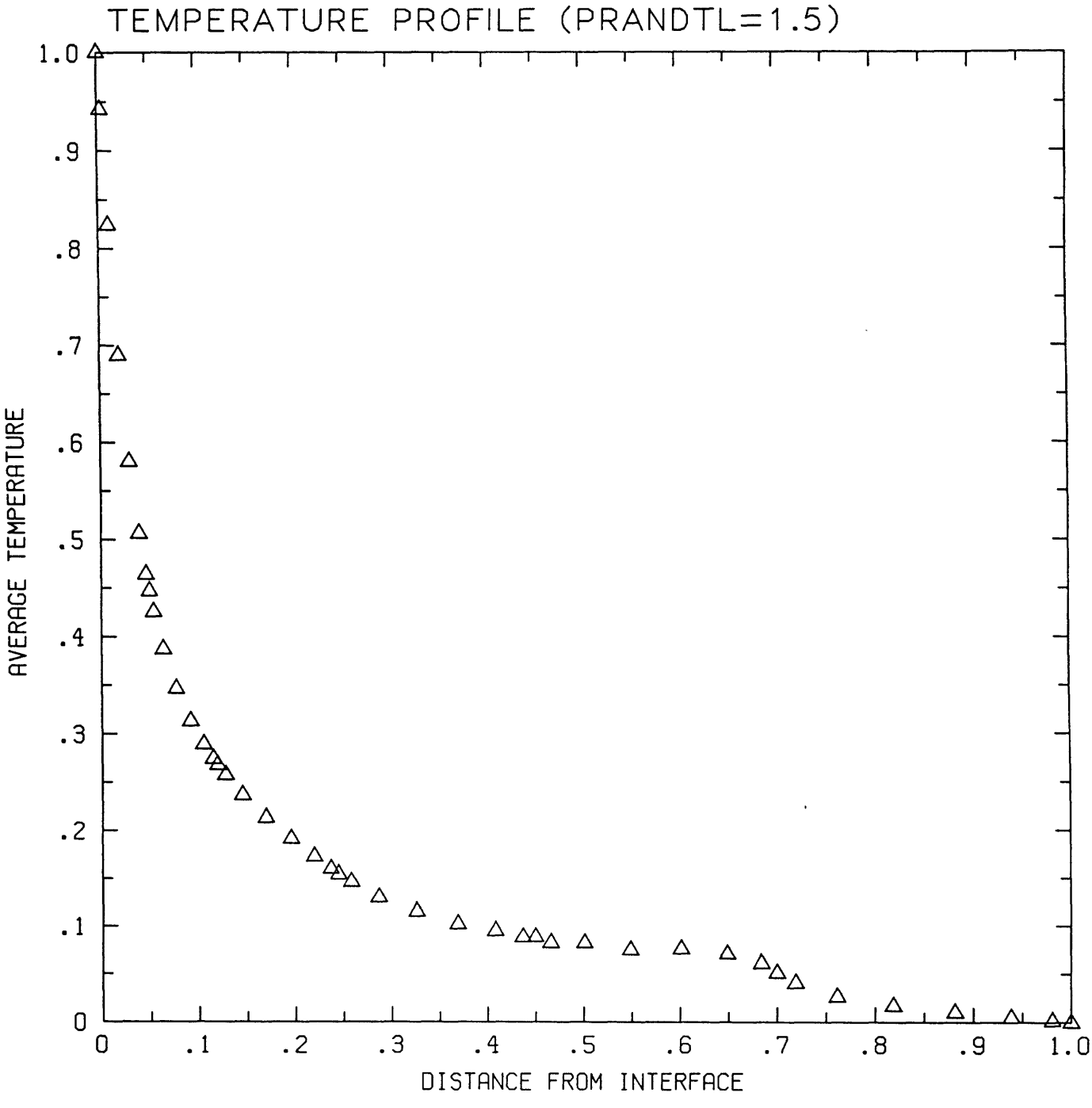
TEMPERATURE PROFILE (PRANDTL=1.5)
AVERAGE TEMPERATURE
DISTANCE FROM INTERFACE
1.0
.9
.8
.7
.6
.5
.4
.3
.2
.1
0
0
.1
.2
.3
.4
.5
.6
.7
.8
.9
1.0

Figure 7.3.2

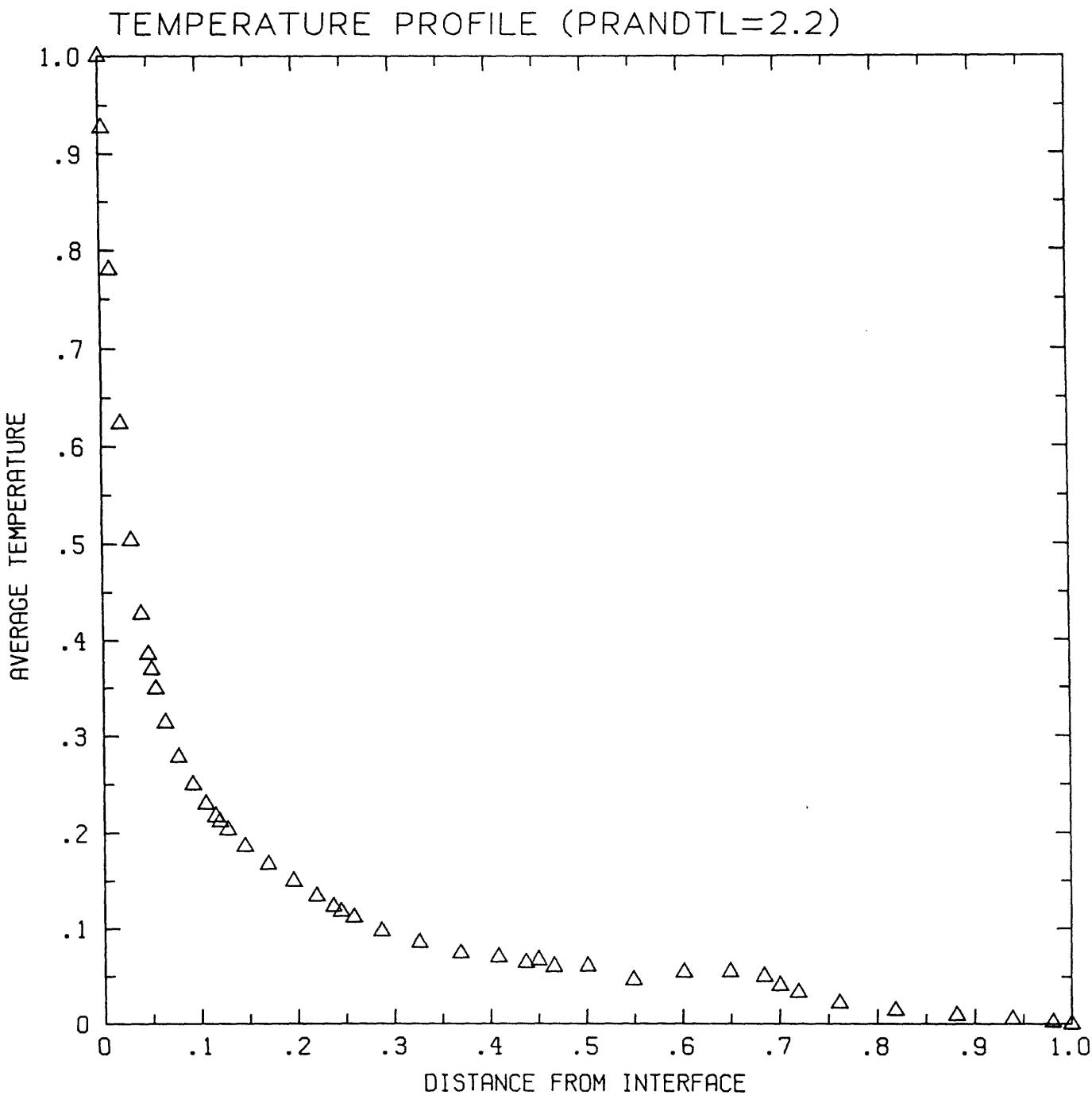
TEMPERATURE PROFILE (PRANDTL=2.2)
AVERAGE TEMPERATURE
DISTANCE FROM INTERFACE
1.0
.9
.8
.7
.6
.5
.4
.3
.2
.1
0
0
.1
.2
.3
.4
.5
.6
.7
.8
.9
1.0

Figure 7.3.3

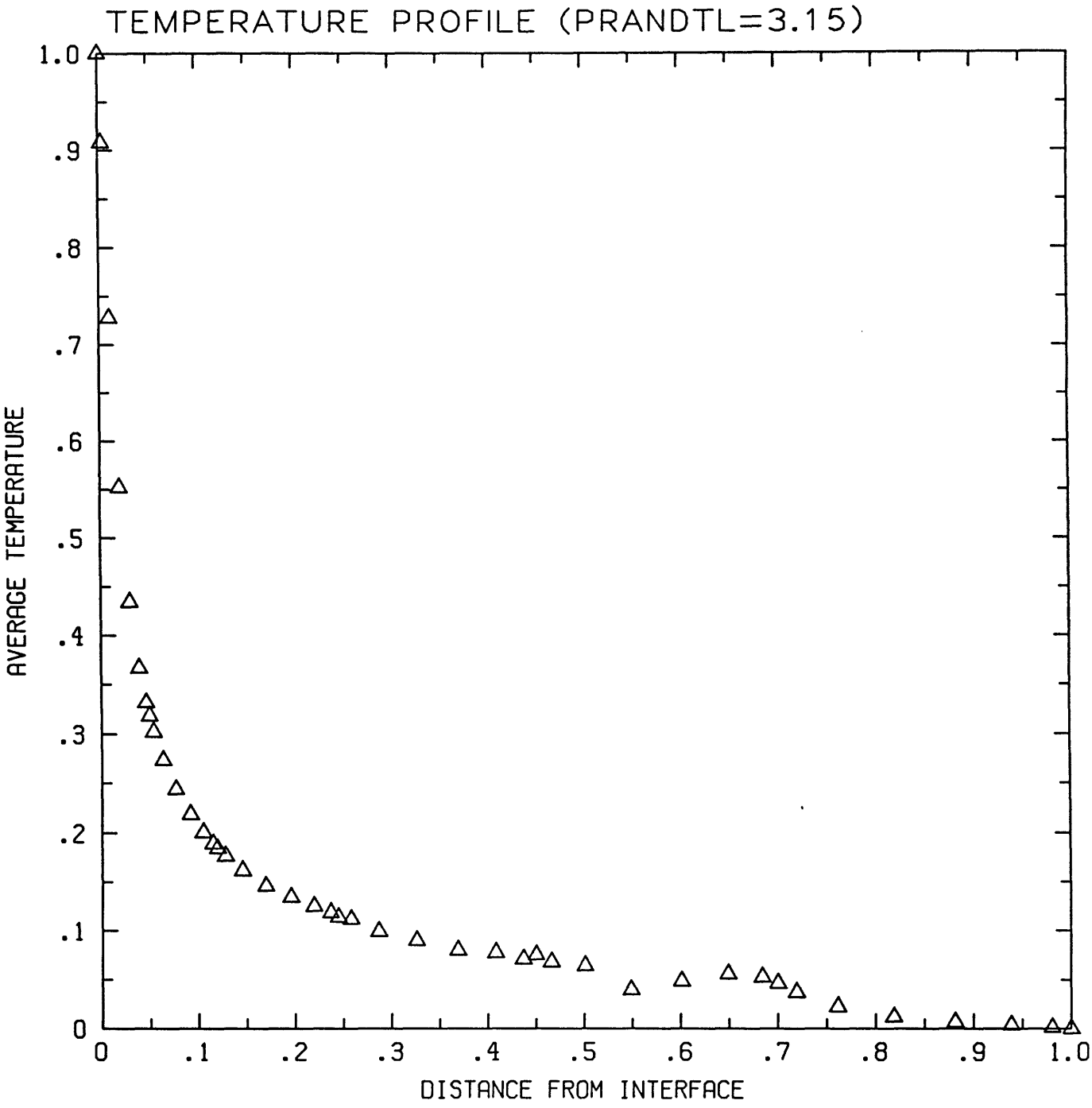
TEMPERATURE PROFILE (PRANDTL=3.15)
AVERAGE TEMPERATURE
1.0
.9
.8
.7
.6
.5
.4
.3
.2
.1
0
0
.1
.2
.3
.4
.5
.6
.7
.8
.9
1.0
DISTANCE FROM INTERFACE

Figure 7.3.4

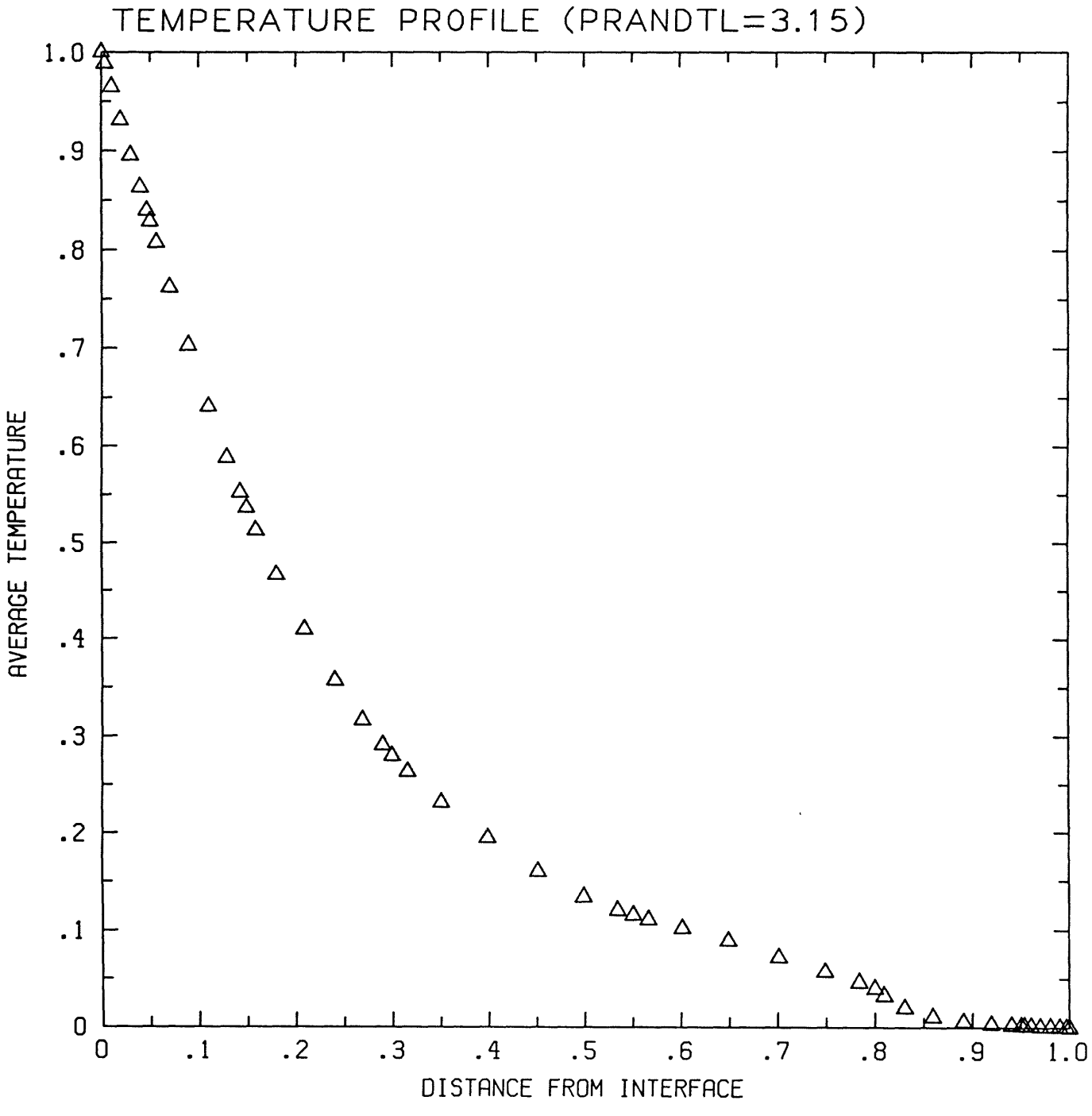
TEMPERATURE PROFILE (PRANDTL=3.15)
AVERAGE TEMPERATURE
1.0
.9
.8
.7
.6
.5
.4
.3
.2
.1
0
0
.1
.2
.3
.4
.5
.6
.7
.8
.9
1.0
DISTANCE FROM INTERFACE

Figure 7.3.5

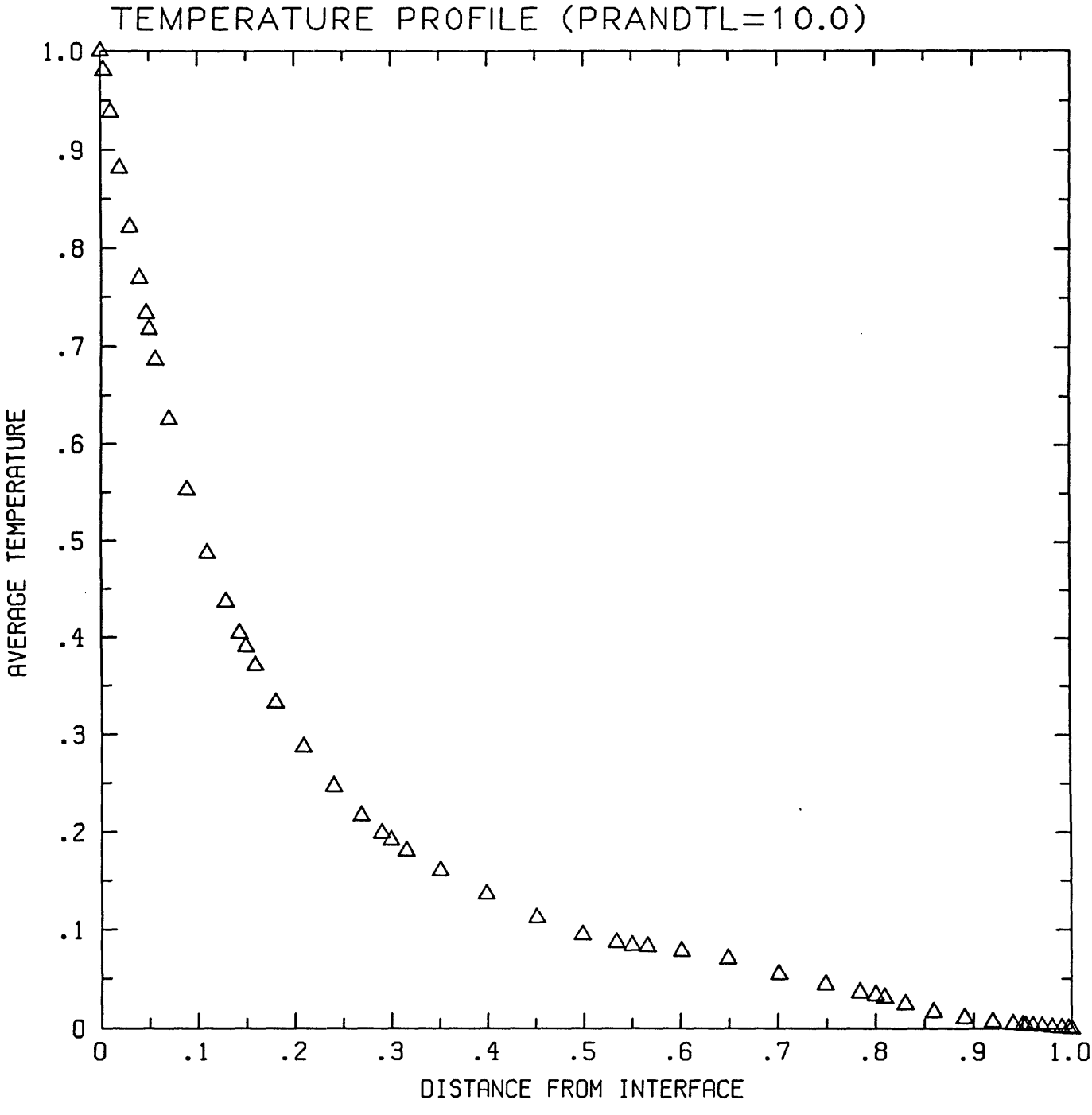
TEMPERATURE PROFILE (PRANDTL=10.0)
AVERAGE TEMPERATURE
DISTANCE FROM INTERFACE
0
.1
.2
.3
.4
.5
.6
.7
.8
.9
1.0

Figure 7.3.6

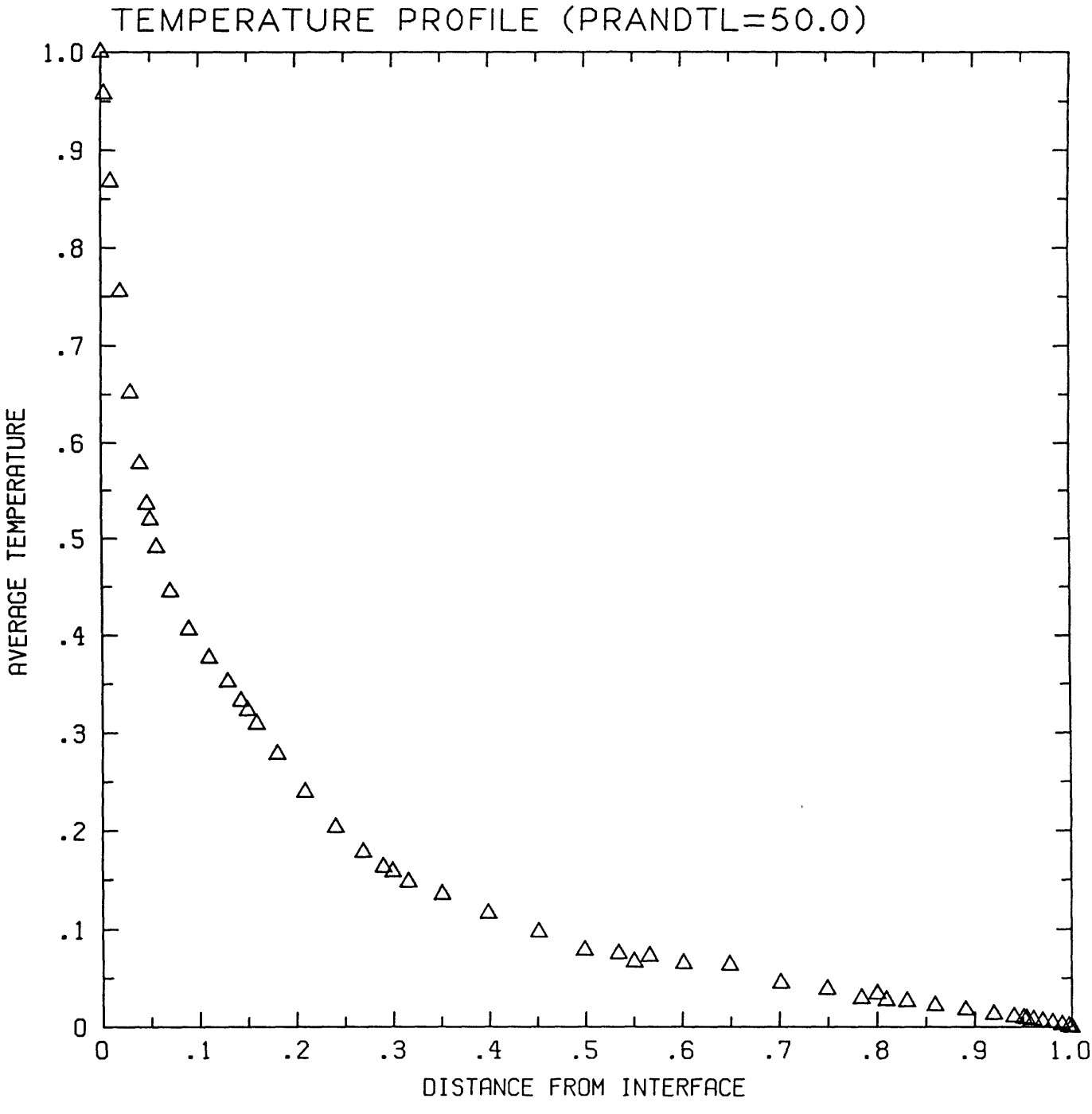
TEMPERATURE PROFILE (PRANDTL=50.0)
AVERAGE TEMPERATURE
1.0
.9
.8
.7
.6
.5
.4
.3
.2
.1
0
0
.1
.2
.3
.4
.5
.6
.7
.8
.9
1.0
DISTANCE FROM INTERFACE

Figure 7.3.7

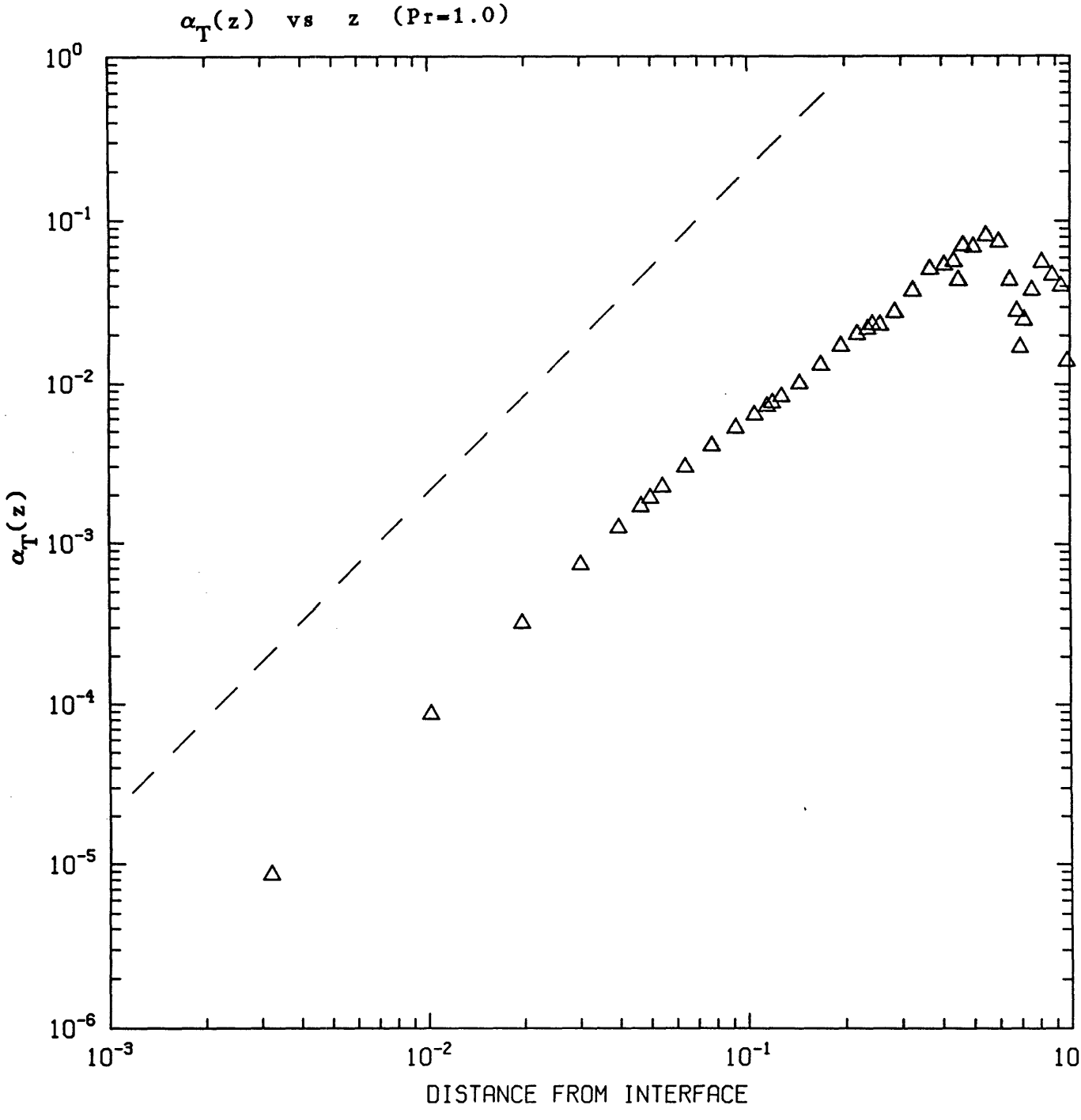
$\alpha_T(z)$ vs z (Pr=1.0)
10^0
10^{-1}
10^{-2}
10^{-3}
10^{-4}
10^{-5}
10^{-6}
$\alpha_T(z)$
10^{-3}
10^{-2}
10^{-1}
10^0
DISTANCE FROM INTERFACE

Figure 7.4.1

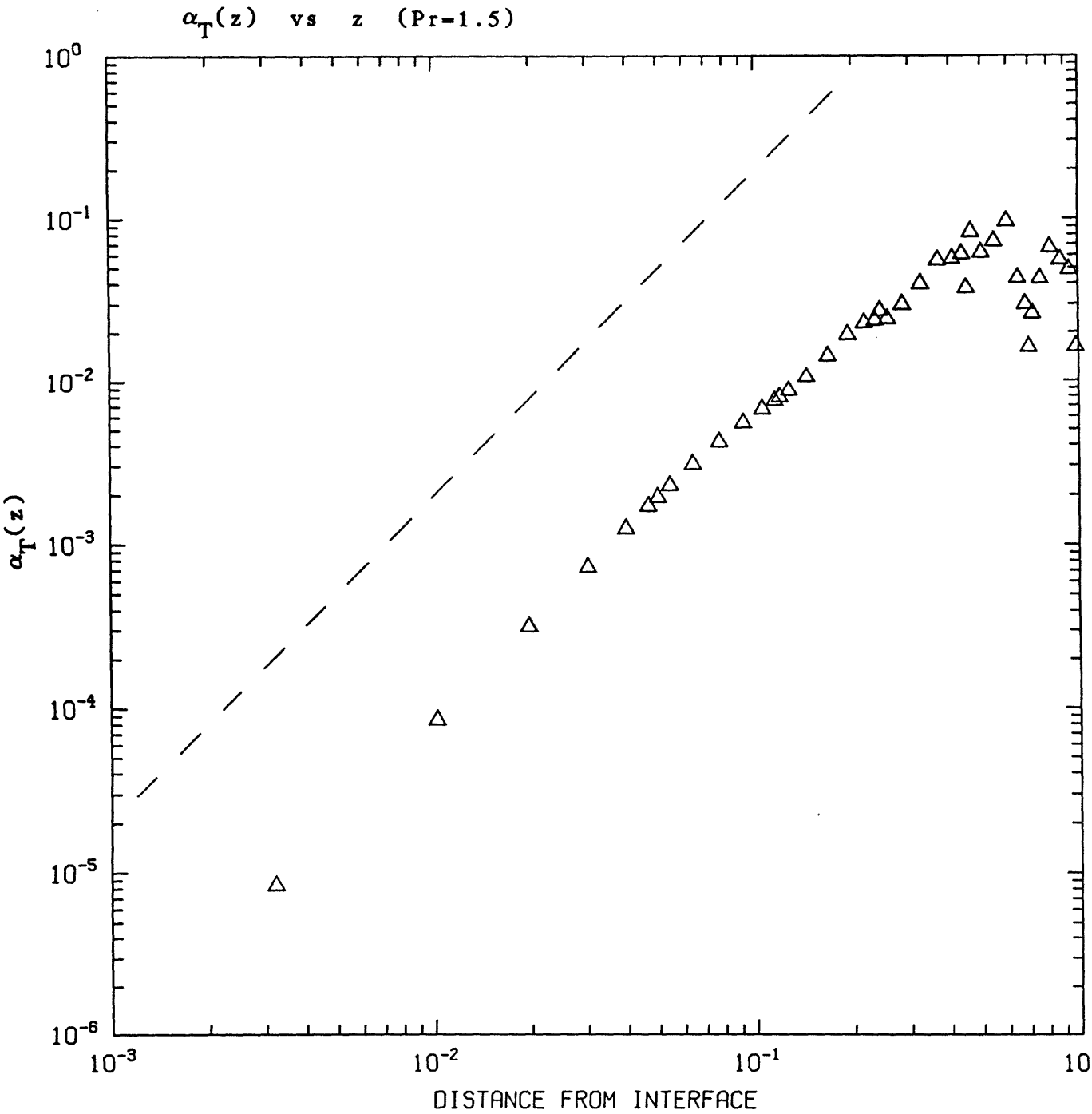
$\alpha_T(z)$ vs z (Pr=1.5)
10^0
10^{-1}
10^{-2}
10^{-3}
10^{-4}
10^{-5}
10^{-6}
$\alpha_T(z)$
10^{-3}
10^{-2}
10^{-1}
10^0
DISTANCE FROM INTERFACE

Figure 7.4.2

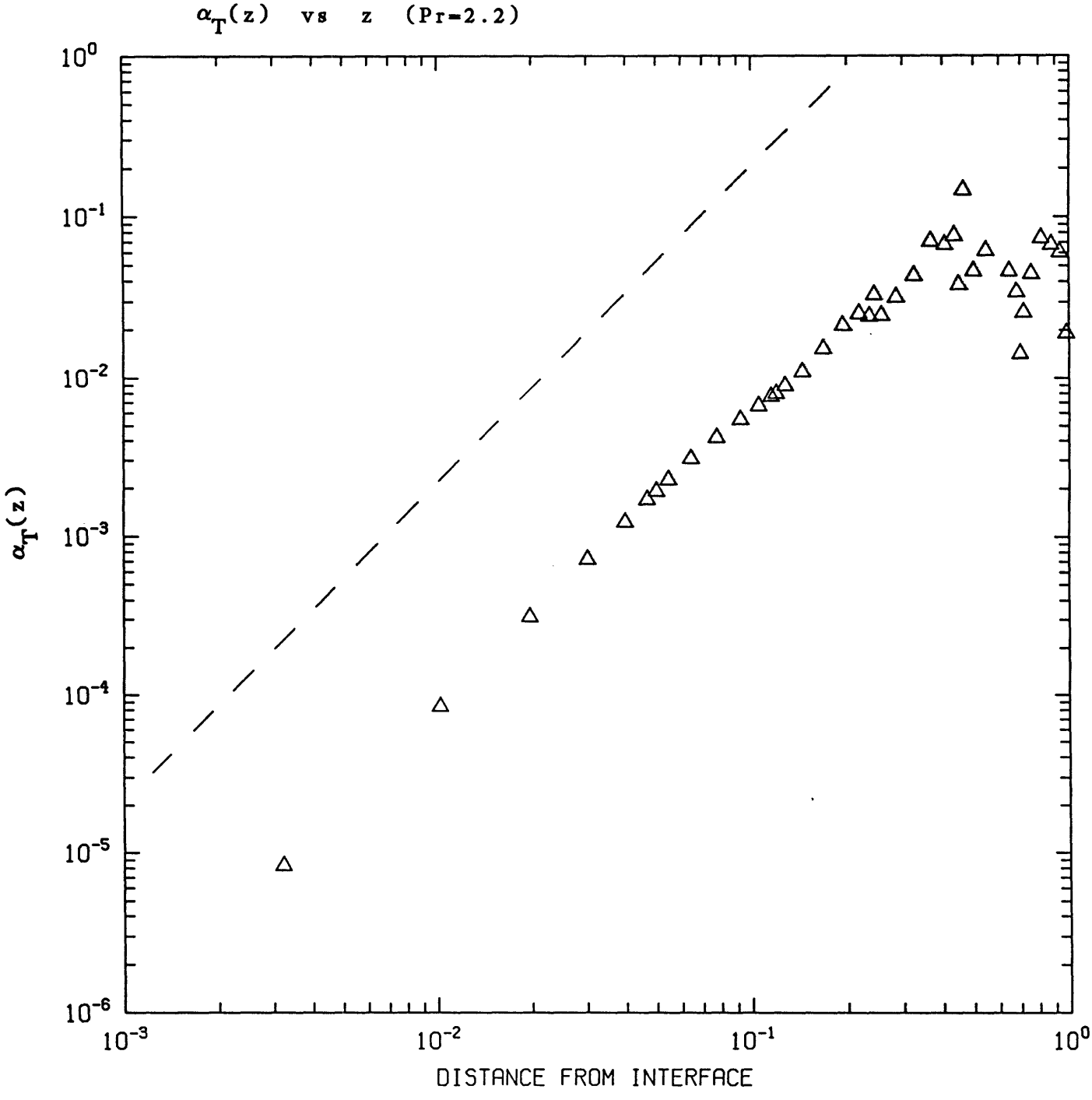
$\alpha_T(z)$ vs z (Pr=2.2)
10^0
10^{-1}
10^{-2}
10^{-3}
10^{-4}
10^{-5}
10^{-6}
$\alpha_T(z)$
10^{-3}
10^{-2}
10^{-1}
10^0
DISTANCE FROM INTERFACE

Figure 7.4.3

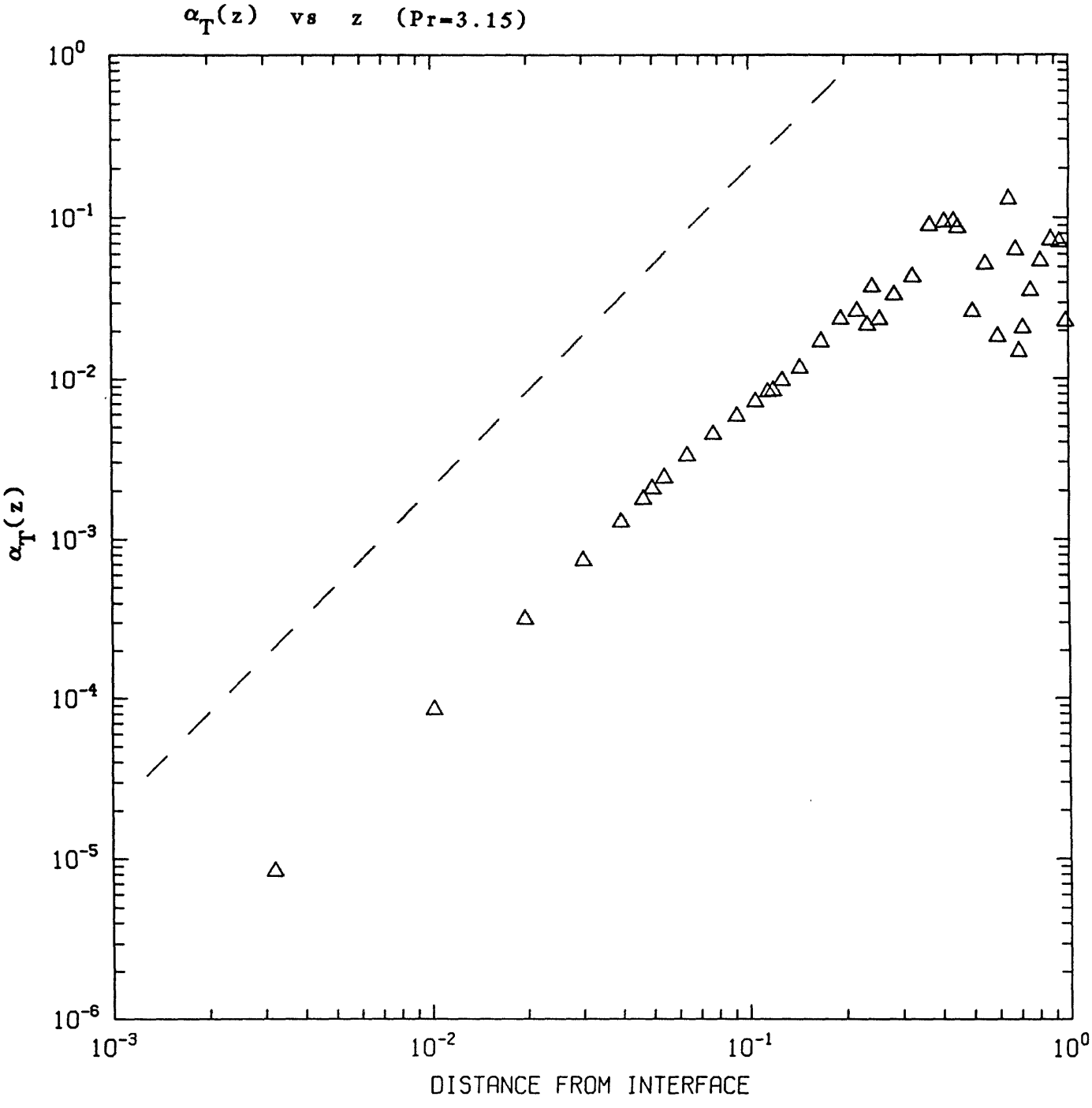
$\alpha_T(z)$ vs z (Pr=3.15)
10^0
10^{-1}
10^{-2}
10^{-3}
10^{-4}
10^{-5}
10^{-6}
$\alpha_T(z)$
10^{-3}
10^{-2}
10^{-1}
10^0
DISTANCE FROM INTERFACE

Figure 7.4.4

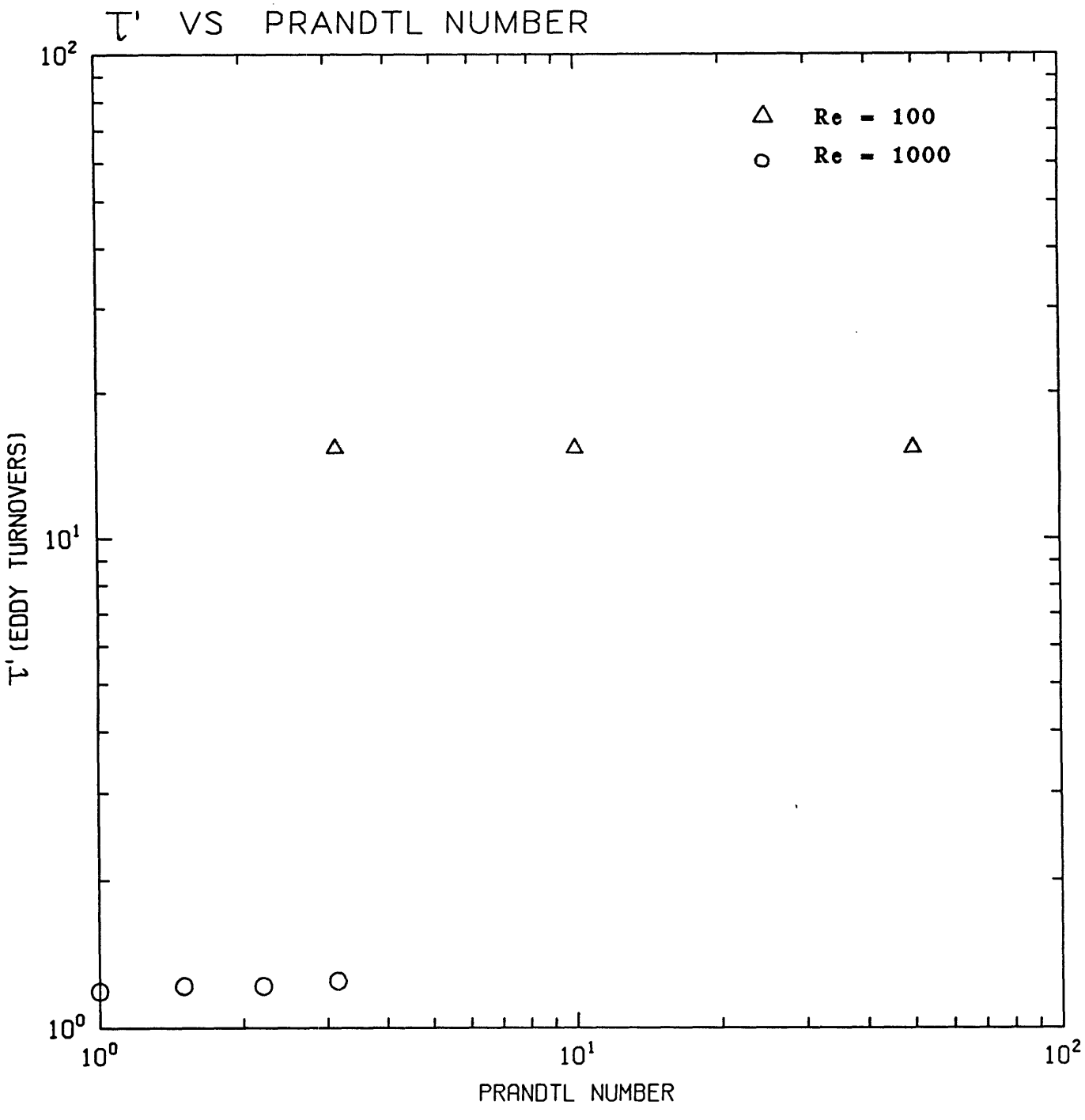
τ' VS PRANDTL NUMBER
Re = 100
Re = 1000
τ' (EDDY TURNOVERS)
PRANDTL NUMBER
10^2
10^1
10^0
10^0
10^1
10^2

Figure 7.4.5

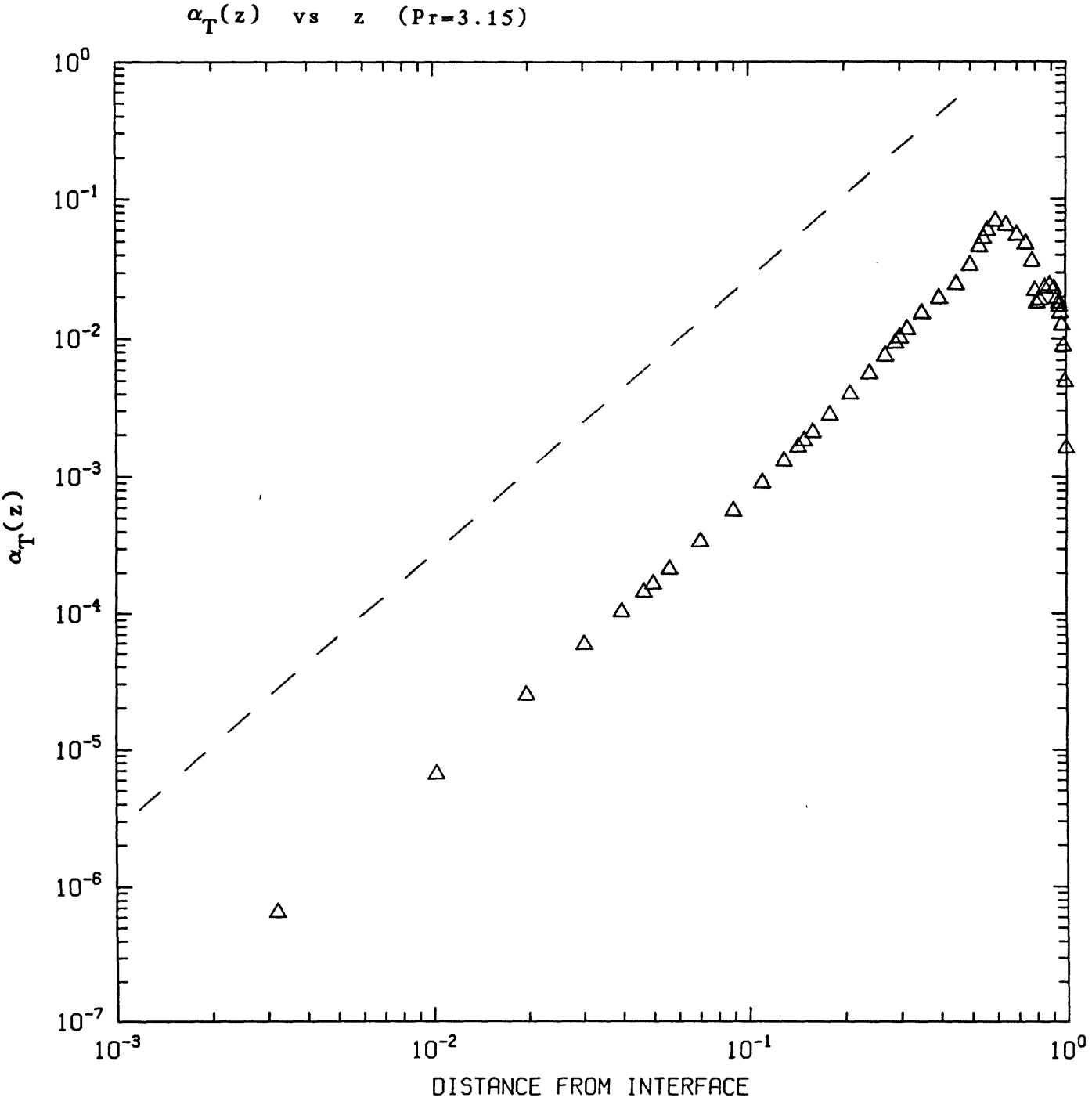
$\alpha_T(z)$ vs z (Pr=3.15)
10^0
10^{-1}
10^{-2}
10^{-3}
10^{-4}
10^{-5}
10^{-6}
10^{-7}
$\alpha_T(z)$
10^{-3}
10^{-2}
10^{-1}
10^0
DISTANCE FROM INTERFACE

Figure 7.4.6

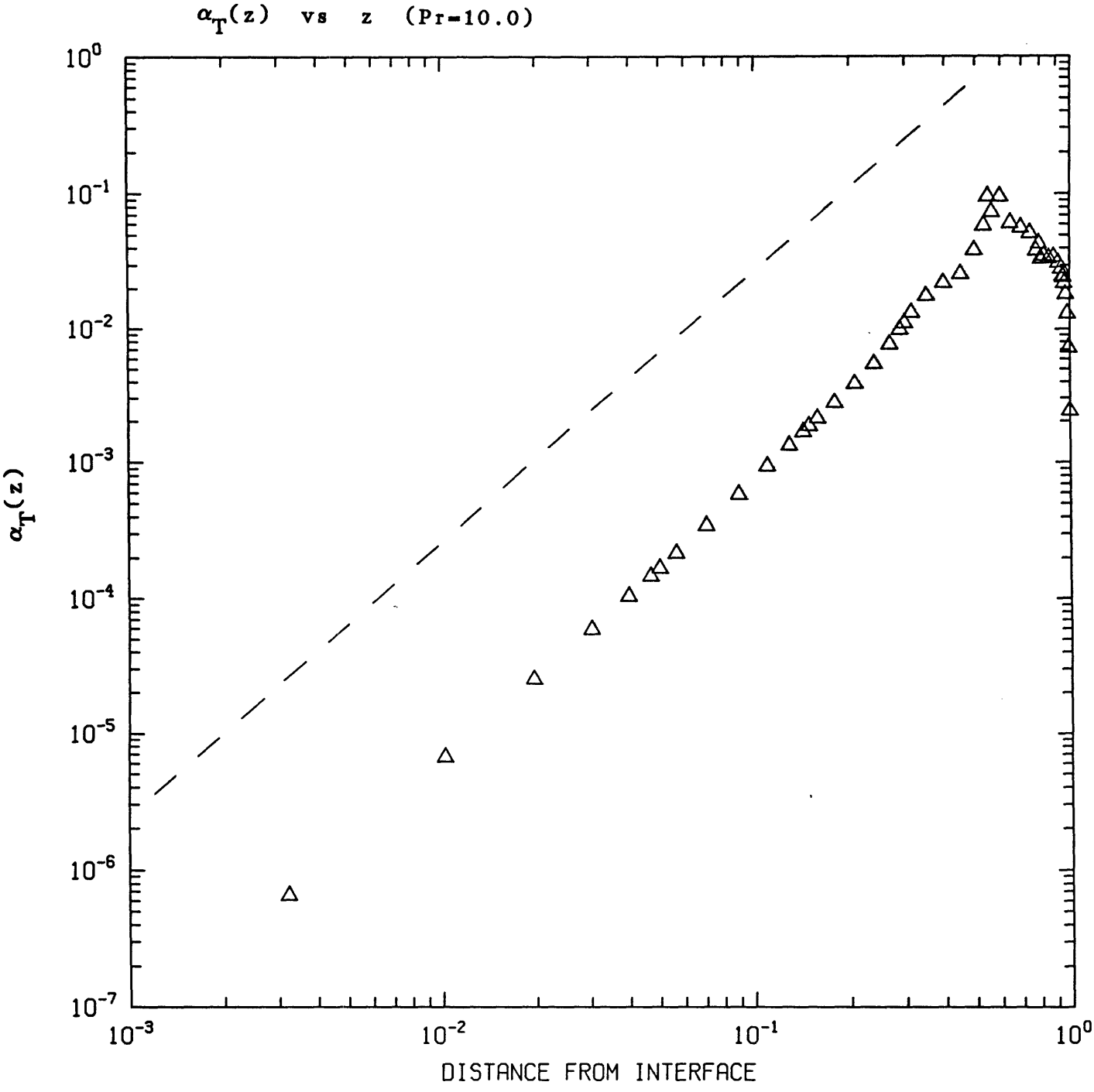
$\alpha_T(z)$ vs z (Pr=10.0)
10^0
10^{-1}
10^{-2}
10^{-3}
10^{-4}
10^{-5}
10^{-6}
10^{-7}
$\alpha_T(z)$
10^{-3}
10^{-2}
10^{-1}
10^0
DISTANCE FROM INTERFACE

Figure 7.4.7

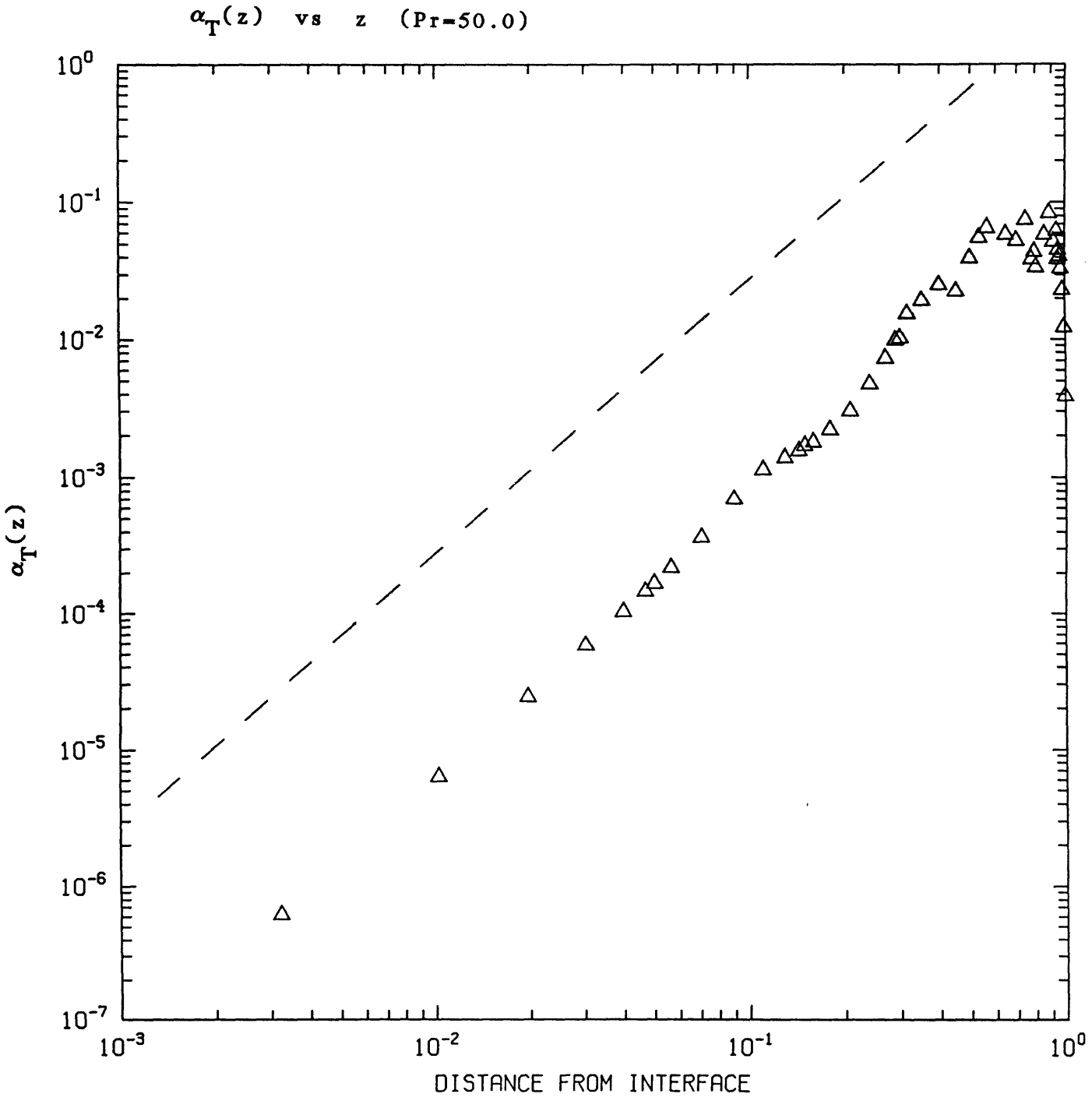
$\alpha_T(z)$ vs z (Pr=50.0)
10^0
10^{-1}
10^{-2}
10^{-3}
10^{-4}
10^{-5}
10^{-6}
10^{-7}
$\alpha_T(z)$
10^{-3}
10^{-2}
10^{-1}
10^0
DISTANCE FROM INTERFACE

Figure 7.4.8

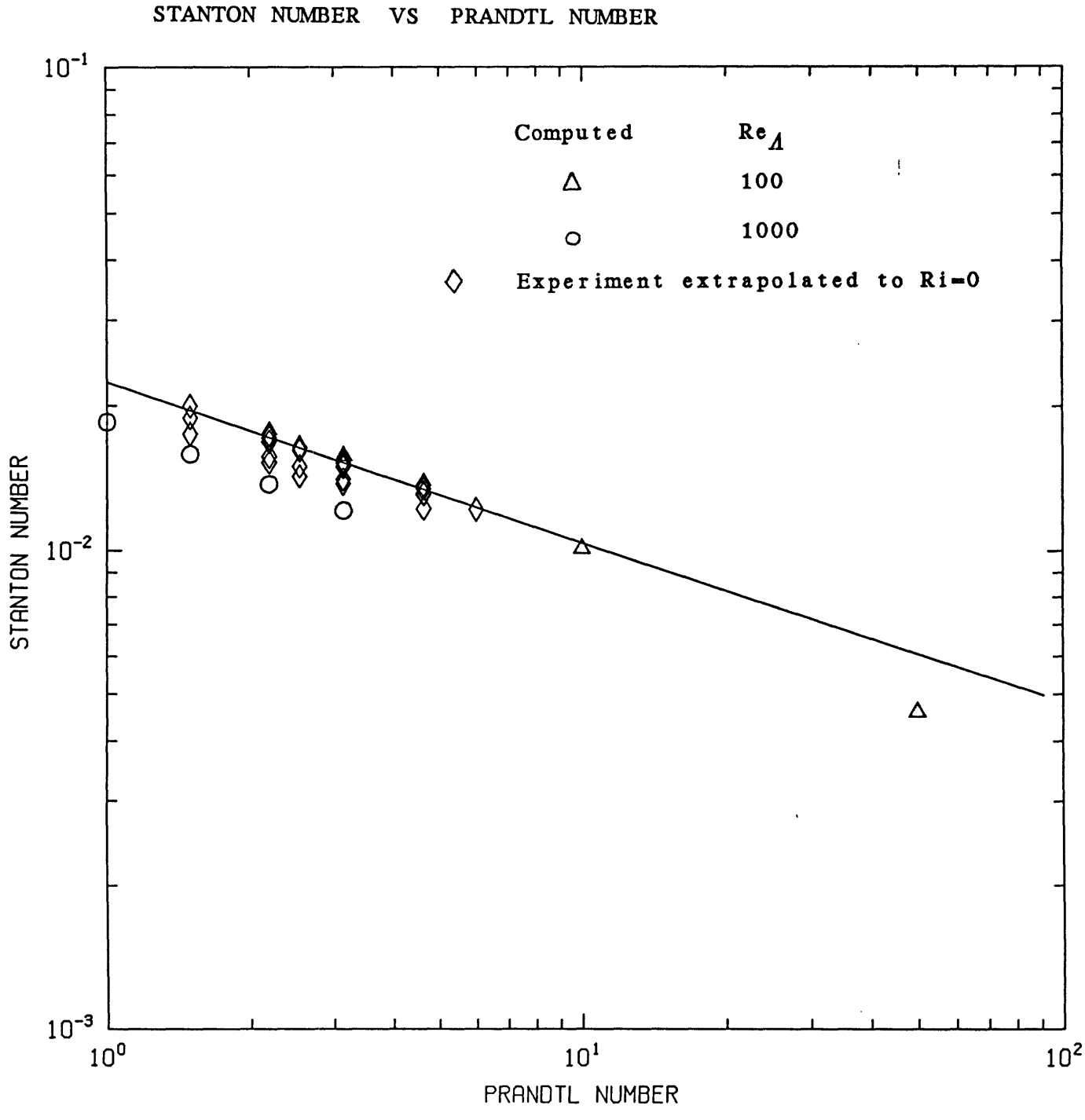
STANTON NUMBER VS PRANDTL NUMBER
Computed
Re_Δ
100
1000
Experiment extrapolated to Ri=0
STANTON NUMBER
PRANDTL NUMBER
10^{-1}
10^{-2}
10^{-3}
10^{0}
10^{1}
10^{2}

Figure 7.5.1

Appendix 1

A schematic view of the laser set-up is given below.

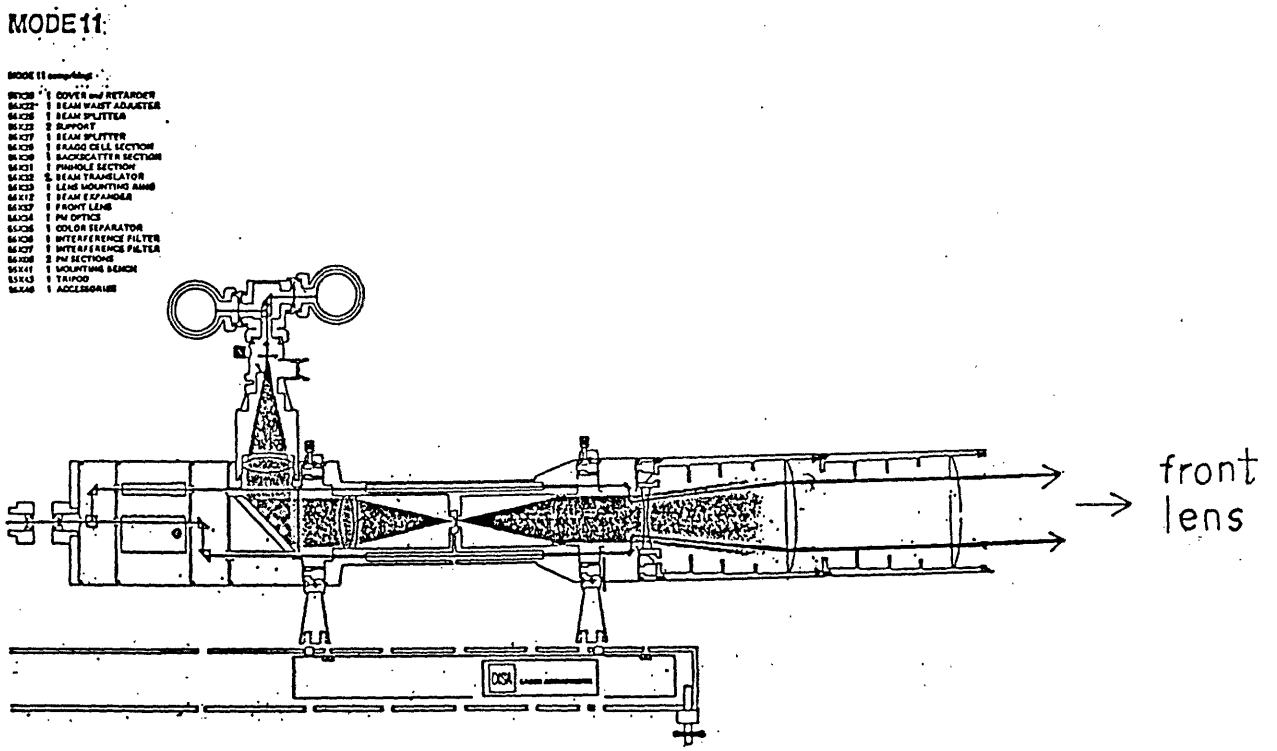

The 3 beams coming out of the expanders go through a series of mirror reflections to reach the desired location before converging through the 310mm focal length front lens.

The equation of the velocity in a LDA measurement is given nominally as

$$V = f_D \lambda / (2 \sin \theta / 2) \qquad \text{A.1}$$

where V is the fluid velocity in m/s

f_D is the doppler frequency in Hertz

λ is the wavelength of laser beams in metres

θ is the angle between the intersecting laser beams.

Boadway and Karahan (1981) have found that equation A.1 is still applicable when the beams refracted through a flat surface into another medium, in which λ is taken to be the wavelength in air and θ is the unrefracted angle of intersection.

Appendix 2

In order to make better comparison with our critical number, we need to have a fair estimate of the macroscale near the interface for the flow in an open channel of constant water height. In the absence of any data on direct measurement of macroscale, we state that the macroscale should not be very different from the Prandtl mixing length L, given by

$$\nu_T = L^2 \partial u/\partial y \qquad \text{A.2.1}$$

where ν_T is the turbulent eddy viscosity and $\partial u/\partial y$ is the average velocity gradient. Jobson et al (1970) made some detailed velocity measurements in a open channel flow and their experimental data can be fitted empirically by the expression,

$$\nu_T = k u_* y(1-y/h)(1+0.4(y/h)^2)^{-1} \qquad \text{A.2.2}$$

where k is the von Karman constant, u_* is the friction velocity based on water density, y is the distance measured from the base up and h is the water height. In a separate experiment by Ueda et al (1977), it was found that the velocity profile fit the logarithmic law quite well except for regions very close to the interface. Hence for regions further away from the interface, velocity can be taken to be

$$u/U = (\ln(y u_*/\nu))/k + 5.75 \qquad \text{A.2.3}$$

The expression for L^2, not very close to the interface, can then be expressed as

$$L^2 = k^2 y^2 (1-y/h)/(1+0.4y^2/h^2) \qquad \text{A.2.4}$$

The maximum value of L obtained is 0.174h at about y=0.6h and decreases toward the interface. So taking the mixing length to be 0.1h should give us a reasonable estimate of the macroscale which is responsible for characterising the turbulence near the interface.